MINISTRY OF EDUCATION AND TRAINING

VIETNAM ACADEMY OF SCIENCE AND TECHNOLOGY

GRADUATE UNIVERSITY OF SCIENCE AND TECHNOLOGY

AUTHOR'S FULL NAME: DANG THI LE HANG

DISSERTATION'S TITLE
INJECTABLE ALGINATE AND PLURONIC-BASED HYDROGELS WITH ON-DEMAND BIOACTIVE COMPOUNDS FOR SPECIFIC TISSUE REGENERATION

DOCTORAL DISSERTATION ON ORGANIC CHEMISTRY
Code: 9.44.01.14

TP. Hồ Chí Minh – 2023

MINISTRY OF EDUCATION AND TRAINING

VIETNAM ACADEMY OF SCIENCE AND TECHNOLOGY

GRADUATE UNIVERSITY OF SCIENCE AND TECHNOLOGY

Author's full name: Dang Thi Le Hang

DISSERTATION'S TITLE
INJECTABLE ALGINATE AND PLURONIC-BASED HYDROGELS WITH ON-DEMAND BIOACTIVE COMPOUNDS FOR SPECIFIC TISSUE REGENERATION

DOCTORAL DISSERTATION ON ORGANIC CHEMISTRY
Code: 9.44.01.14

Graduation University of Science and Technology's confirmation

Supervisor 1
(Sign, write full name)

TP. Hồ Chí Minh – 2023

DECLARATION

The work was conducted at the Department of Pharmaceutical Biomaterials - Institute of Applied Materials Science (IAMS) - Vietnam Academy of Science and Technology (VAST) in Ho Chi Minh City.

I hereby declare that this is my research work, conducted under the scientific guidance of Associate Professor Dr. Tran Ngoc Quyen. The research content and data obtained are honest and come from my research. The results of this study have not been published in any thesis of the same level.

Ho Chi Minh, September 12th, 2023

ACKNOWLEDGEMENTS

As a member of the Department of Pharmaceutical Biomaterials—IAMS-VAST since 2015, I have made a remarkable academic journey. I have completed my theses from this lab for my bachelor's, master's, and now doctoral research degrees. First, I would like to express my deepest gratitude to my supervisor, Associated Professor Tran Ngoc Quyen, for meaningful work.

I want to thank all the fantastic collaborations with the Department of Pharmaceutical Biomaterials – IAMS-VAST member. I wish to express special thanks to Associated Professor Tien Dung Le and Dr. Thi Phuong Nguyen (now a lecturer at HCM University of Industry and Trade), BSc. Nhat Anh Tong (now a postdoc at Washington University), Professor Cuu Khoa Nguyen (now a lecturer at GUST), BSc. Tuong Van Vo (now PhD candidate at Sydney University), BSc. Thanh Tuyen Nguyen (now working in a Pharmaceutical company), etc., for delightful collaboration on thermal responsive hydrogel for tissue regeneration projects; Dr. Trung Phung (IAMS), Dr. Dinh Phong Tran (IAMS), Dr. Thuy Trang Nguyen (IAMS), Ph.D. candidate Hong Ngoc Pham, MSc. Son Pham (IAMS), MSc. Chieu An Tran (IAMS), etc., for exciting collaboration on this project.

I would also like to express my sincerest gratitude to collaborators outside my institute for their help during the enjoyable PhD research. In particular, Dr. Ngoc Hoa Nguyen and MSc. Truc Lam Nguyen at HCM University of Industry and Trade offered an excellent collaboration on material characterization, such as scanning electron microscope (SEM), X-ray diffraction, etc. BSc. Minh Ty Nguyen at ICT-VAST provided the opportunity to use Fluorescence spectra (Fluoromax Plus C (Horiba-Janpan)). Dr. Liem Chau Pham and Assoc. Prof Huu Hieu Nguyen at HCM University of Technology allowed me to use a rheometer to identify the thermal sensitive feature of the hydrogel. Assoc. Prof. Hong Tuoi Do at the University of Medicine and Pharmacy at Ho Chi Minh City and Assoc. Prof. Ha Tran at VNUHCM - University Of Science, as well as the staff in the Department of Pathology at Military Hospital 175, offered an excellent collaboration on diabetic wound healing as well as immunological response. Dr. Tuan Tran at VNUHCM - University Of Science allowed me to explore the ani-bacteria function of the design hydrogel. Dr. Bich Tram Nguyen at the Ho Chi Minh City Biotechnology Center offered a tremendous opportunity to perform cell tests.

My journey in the Ph.D. program would not be possible without generous support from various funding agencies, shared facilities and managers, and services in IAMS and GUST. I wish to express my sincere thankfulness for the financial support from VATS (Support for young scientists of VAST; VAST 7 priority directions Grant Number ĐLTE.07/22-23; Program to

Develop the excellent research group of VAST Grant Number NCX.01.01/23-25), Ho Chi Minh Department of Science and Technology (number of contract 47/2019/HĐ-QPTKHCN), for shared facility uses at Center for Biological, Chemical and Physical Analysis Instruments; for spiritual encouragement from staff at MSc. Dong Yen Pham, MSc. Cong Truc Nguyen, Hong Thanh Nguyen (chief accountant), Hanh Thai (Treasurer), Thuy Hang Le (accountant), Lan Ngo (archivist) and Dr. Tien Dang. I would also like to give special thanks to MSc. Hoang Hanh Huynh, MSc. Tong Hung Quach and Dr. Minh Nhat Ho helped tremendously by giving me relaxing moments on hard and busy days throughout my graduate studies. Besides, I would like to acknowledge my academic affairs (MSc. Ngan Nguyen and MSc. Khanh Pham) for preparing my educational documents.

Finally, I am deeply grateful for my family's endless love and support: my mother, Chau Trinh, my young brother, Trong Dang, and my older brother, Quan Nguyen. This dissertation is the initial step toward starting the new grand journey in the academy.

Above all, I have a good time that I will never forget. I couldn’t have done it without all of you.

Le Hang Dang

Ho Chi Minh City, Viet Nam

CONTENT

LIST OF ABBREVIATIONS

^{1}H-NMR: Proton nuclear magnetic resonance

AALG: Aminated alginate

AC: alginate-cystamine or Na Alg-cys

ACP: Alginate-cys-Pluronic

ADA: Alginate-dopamine

AIC: Akaike Information Criterion

Alg= Alginate

AO: Acridine orange

APC 1: Alginate-cys-Pluronic F127 with Pluronic accounting for 87.5% by mass

APC 2: Alginate-cys-Pluronic F127 with Pluronic accounting for 91% of the mass

APC 3: Alginate-cys-Pluronic F127 with Pluronic accounting for 93% of the mass

APC 4: Alginate-cys-Pluronic F127 with Pluronic accounting for 95% of the mass

AR-ACP: L-arginine and Resveratrol loading ACP hydrogel

BG: Bioactive Glasses

BJ cells: Fibroblasts established from skin

BMSCs: Bone Mesenchymal stem cells

CaNT: calcium nitrate tetrahydrate

CGC: Critical gelation concentration

CMC: Carboxymethyl cellulose

CMPI: 2-chloro-1-methyl pyridinium iodide

CS: Chitosan

CST: Critical solution temperature

CTAB: Hexadecyltrimethylammonium bromide

DCC: N, N′-dicyclohexylcarbodiimide

DI water: Deionized Water

DLS: Dynamic light scattering

DMAP: 4-(N,N′-dimethylamino)pyridine

DMEM: Dulbecco's modified Eagle's medium

DOPA: Dopamine = 3,4-dihydroxy phenyl-L-alanine

DPPH: 2,2-diphenyl-1-picryl-hydrazine-hydrate

DS: Degree of substitution

ECM: Extracellular matrix

EDC: 1-ethyl-3-(3-dimethyl aminopropyl) carbodiimide

ELSD: Evaporative light scattering detector

eNOS: Endothelial NO synthase

FDA: Food and Drug Administration

FT-IR: Fourier-transform infrared spectroscopy

G': Storage moduli

G'': Loss moduli

GRAS: Generally Recognized as Safe

GT: gelation temperature

hBMSCs: Human bone mesenchymal stem cells

HCA: Hydroxycarbonate apatite

HNP BG: Hemin nanoparticles incorporated bioglass

HNP: Hemin nanoparticles

HPLC: High-performance liquid chromatography

HRP: Horseradish peroxidase

KP: Korsmeyer-Peppas

LCST: Lower critical solution temperature

LVR: Linear viscoelastic range

MES: Morpholinoethanesulfonic acid sodium salt

MG63: Human osteosarcoma cells

MSCs: Mesenchymal stem cells

MTT: 3-[4,5-dimethylthiazol-2-yl]-2,5 diphenyl tetrazolium bromide

NHS: N-hydroxysuccinimide

NMR: Proton nuclear magnetic resonance

NO: nitric oxide

pBMSCs: Porcine bone marrow-derived mesenchymal stem cells

PBS: Phosphate-buffered saline

PDA: Pluronic-dopamine

PI: Propidium iodide

Pluronic F127: F127

Pluronic= poly(ethylene oxide)- Poly(1,2-butylene oxide)– poly(ethylene oxide) triblock copolymers (PEO–PPO–PEO)

p-NPC: 4-Nitrophenyl chloroformate

PolyNIPAM: poly(N-isopropyl acrylamide)

R-ACP: Resveratrol loading ACP hydrogel

ROS: Reactive oxygen species

SANS: Small-angle neutron scattering

SAO: Small amplitude oscillatory shear

SAXS: Small-angle X-ray scattering

SEM: Scanning electron microscopes

SRB: Sulforhodamine B

STZ: Streptozotocin

TBA: tetrabutylammonium

TBNS: 2,4,6-trinitrobenzene sulfonic acid

TE: Tissue engineering

TEM: Transmission electron microscopes

TEOS: Tetraethyl orthosilicate

TEP: Triethyl phosphate

TNBS: 2,4,6-trinitrobenzene sulfonic acid

UCST: Upper critical solution temperature

XRD: X-ray diffraction

β-TCP: β-tricalcium phosphate

LIST OF FIGURE

LIST OF TABLE

LIST OF SCHEMATIC

CHAPTER 1: INTRODUCTION

1.1 Motivation: the importance of thermal-responsive hydrogel in tissue engineering and the current challenge

Millions of deaths occur globally each year due to injuries and diseases causing tissue damage, with a profound impact on the quality of life and a substantial healthcare burden [1-4]. Despite the introduction of organ transplantation, conventional reconstruction may not be suitable in many cases [5, 6]. Allograft faces limitations such as the availability of appropriate human grafts, the necessity for immunosuppression, and technical challenges [7, 8]. The immunosuppressive measures for graft recipients carry significant risks, including susceptibility to infections, an elevated risk of cancer, and reduced life expectancy [6, 8]. In response to these challenges, there has been a rapid development of studies in the field of tissue regeneration [1, 3, 5]. The primary objective of these studies is to create functional human tissue equivalents for organ repair and replacement [9, 10].

A fundamental concept in tissue regeneration involves the utilization of biomaterials that mimic the structure of the extracellular matrix (ECM) to support new cell growth and promote repair [1, 5, 10]. While decellularized techniques initially provided ideal biomaterials (dECM) for tissue regeneration [4, 11-14], concerns regarding relevance, ethical approval, scaling-up, and cost have prompted a shift towards the use of safe and effective tissue-engineered scaffold alternatives [2, 3, 10]. Among them, hydrogels have emerged as prominent and versatile materials in tissue regeneration [1, 3, 5]. Hydrogels are characterized by highly hydrated three-dimensional (3D) networks of water-soluble polymers [1, 3]. Their swollen and hydrated structure closely resembles the ECM in the native tissues, creating a microenvironment favorable for regenerated cells [15, 16]. The porous structure of hydrogels supports the encapsulated process. It can act as the cargo for sensitive biological cues, making it an excellent selection for carrying and releasing drugs/ therapeutic agents [2, 3, 16]. The soft feature of the hydrogel can help reduce the surrounding tissue's inflammatory response, enhancing its biocompatibility [1, 15]. Hydrogels easily adjust their shape following private requirements, making them preferred for implantable materials and devices [2, 10].

In recent years, injectable hydrogels have gained more attention than conventional gels due to their advantages in low-invasive surgical procedures and real-time adaptability in shape [17, 18]. Injectable gels, essentially a type of in situ forming hydrogel, simplify cargo incorporation, making them preferable as delivery vehicles [19]. This hydrogel form is particularly suitable for applications where the final form or shape is either unimportant or defined by the void or space into which they are injected [17, 18]. Apart from the in situ gelling characteristic, the term "injectable" implies that the hydrogel is created through a process that

primarily involves the transport of the sol or the prequel to a targeted site for gelation via an injection device [15, 17]. The need for injectable hydrogels has spurred using smart hydrogels that exhibit a structural response to temperature changes [17, 19-21]. In such hydrogels, at a critical gelation concentration (CGT), the hydrogel displays the behavior of the fluid, transforming from a sol to a gel state above that temperature [17, 22]. Polymers with a low critical solution temperature or phase transition between room and body temperature have been employed to create injectable in situ hydrogels [17]. After injection into the body, the polymer solution undergoes thermally induced self-assembly to form a hydrogel at body temperature [20]. A significant focus has been developing thermosensitive hydrogels by combining thermo-responsive polymers with natural-based polymeric components, such as polysaccharides[20, 23]. This combination allows for the rational design of artificial environments conducive to cell growth and differentiation [24]. Polysaccharides, either conjugated with a thermosensitive polymer or through crosslinking a combination of both polysaccharide and thermosensitive polymers, have been utilized to prepare thermally responsive hydrogels with an optimal critical solution temperature suitable for injection into the body [20, 22, 23]. This combination also offers new possibilities for developing suitable mechanical strength for each tissue application [15, 16].

It is often hard to gather all essential features in a single hydrogel to fulfill the fundamental requirements for the desired clinical application. Recognizing the limitations of hydrogels has led to the development of hybrid systems with different biological cues [25, 26]. By incorporating bioactive compounds like amino acids [27-29], plant-derived bioactive substances [30-32], and/or bioglass [27, 33] into hydrogels, these systems acquire characteristics that the bare form of the scaffold cannot achieve on their own. Interestingly, strengthening hydrogels through biophysical factors may even outperform or replace the effects of biochemical cues [34], particularly in applications where such factors effectively encourage cultured and/or recruited cells to form functional tissues [29, 31, 32]. As a result, there is a compelling need to explore the application of innovative synthetic designs to address these challenges and create materials that offer greater programmability.

1.2 Aims and object

The project aimed to identify and develop innovative injectable scaffolds with thermal-responsive properties and on-demand requirements for tissue regeneration. This was achieved using hybrid polymer materials, specifically polysaccharide, alginate, and thermal-responsive polymer pluronic F127. The objective was to create scaffolds that provide a well-defined and suitable microenvironment for guiding cells predictably, thus facilitating tissue regeneration. In addition, the delicate combination of biological cues (plant-driven compound- Resveratrol,

amino acids (arginine), or inorganic nanoparticles (bioglass) would be involved as singling regulators in the designed hydrogel systems, resulting in promoted and synergetic efficacy of these materials in tissue regeneration.

Two common strategies for designing thermally responsive hydrogel from Pluronic F127 and alginate, grafting, and crosslinking, were involved in this study. Therefore, this thesis would involve two main detail objects:

The project aims 1: To develop a thermally responsive hydrogel from alginate and Pluronic F127 via grafting techniques. The hypothesis was that after Pluronic grafting on alginate, the biocompatible scaffold would form with the reversible sol-gel transition following the function of temperature. This scaffold would carry the on-demanded biological cues for the specific tissue in a suitable release manner to support this tissue's regenerative process.

The project aims 2: To develop a thermally responsive hydrogel from alginate and Pluronic F127 by employing crosslinking techniques. Inheriting from the oxidative crosslinking of the catechol group, the 3,4-dihydroxyphenyl-L-alanine (DOPA) would be introduced on the alginate and pluronic F127, forming alginate-DOPA (ADA) and Pluronic F127- DOPA (PDA) respectively. Rather than using peroxidase enzyme as the catalytic agent for the oxidative reaction, bioglass would be modified in this study to mimic the catalytic activity of peroxidase. The hypothesis was that the peroxidase-mimicking enzyme based on bioglass would act as a catalyst to facilitate the catechol oxidation, resulting in the formation of crosslinking in alginate and Pluronic with suitable sol-gel transition and provide the biomimetic scaffold for bone regeneration.

CHAPTER 2: STATE OF THE ART AND LITERATURE REVIEW

2.1 The concept of injectable thermal responsive hydrogel in tissue regeneration

2.1.1 Tissue regeneration and tissue engineering

A tissue or organ's loss or failure function is a costly problem in the human health care system [3, 7, 9]. Many reasons can induce damage to the body during life, such as injury, trauma, or cancer. Consequently, the tissue can lose its function [8]. Humans have innate regenerative potential in the body [35]. Regeneration is the coordinated migration of cells, differentiation of progenitor cells, and tissue morphogenesis [2, 8, 10]. The concept of tissue regeneration follows the intricate biological phenomena encompassing diverse cell types, growth factors, cytokines, and metabolites [35]. The multiple signaling messages generate billions of new cells to respond to the biological feedback systems to remove the injured cells/ tissues [2, 9, 36]. Although different tissues have different regenerative mechanisms, this process can be categorized into three distinct stages for all types of tissues: inflammation (both acute and chronic), neotissue formation, and tissue remodeling. In the first stage of tissue regeneration, the immune system undertakes various tasks (e.g., damaged tissue debridement, releasing chemokines, enzymes, etc.) as inflammatory cells eliminate damaged cells and infective microorganisms, ultimately diminishing local inflammation reaction and triggering tissue-repair signals. In the next phase, the endogenous tissue stem cells migrate to the injury site and increase, resulting in the replacement of the damaged extracellular matrix (ECM) and the development of vascularized networks. In the final phase, tissue remodeling is focused on the biophysical integrity of the newly formed extracellular matrix (ECM) via reorganization, degradation, and resynthesis of the tissue. However, the degree and duration of this repair response depend on the tissue location and development stage [4, 6, 9, 24, 35, 36]. The regenerative ability is inferior in adults or patients with underlying disorders [35]; consequently, clinical assistance should be applied to restore the body’s regenerative capacity [9]. Through the knowledge about how individual cells respond to signals, interact with their environment, and organize into tissues and organisms, researchers have been able to manipulate these processes to mend damaged tissues or even create new ones, leading to the debut of tissue regeneration [2, 3, 8, 10]. Tissue regeneration appears to be one of the most critical methods to improve the tissue of patients suffering from various tissue damage worldwide [37]. Now, tissue regeneration is also known as regenerative medicine [10, 38]. Regenerative medicine is an interdisciplinary field aiming to maintain a stable state, improve the function, or replace the biological function of the tissue [38]. Regenerative medicine is primarily related to the development of biological substitutes, including scaffolds and decellularized tissues and/ or their combination with cells and biological cues/signals, to

Support the regeneration of damaged tissue[37]. Regenerative medicine is a broad range of tissue engineering [5]. In tissue engineering, cells, scaffolds, and growth factors combine to regenerate or replace damaged or diseased tissues [10, 39]. The terms “tissue engineering” and “regenerative medicine” have become largely interchangeable, as the field hopes to focus on cures instead of treatments for complex, often chronic, diseases [37, 38].

2.1.2 Hydrogel as biomimetic ECM

Cells are critical responders in tissue regeneration [35, 37, 39]. As a result, cell-based therapies have become a potential strategy for tissue regeneration. Nevertheless, significant challenges have arisen due to inadequate control over cell delivery and retention at the injury site [1-3], prompting a shift in focus to another pivotal element in tissue engineering and regenerative medicine strategies: the extracellular matrix (ECM) [15].

ECM assemblies exhibit high dynamism, serving as a three-dimensional support structure for cells and actively influencing their behavior [5, 9, 10]. Tissue-specific characteristics primarily arise from the dynamic biophysical and biochemical interactions among diverse cell types and their microenvironment [40-43]. Mature ECM, responsive to environmental cues, can undergo dynamic remodeling through reciprocal interactions between cells and ECM, facilitating tissue homeostasis and response to stress [44-46]. During the regeneration, the migration and the proliferation of endogenous progenitor and stem cells to the injury site result in the replacement of the damaged ECM [5, 9, 10]. However, the human organism's ability to regenerate and repair damaged tissues is limited, dependent on age, health conditions, etc [10, 37, 39]; consequently, endogenous progenitor and stem cells could not wholly reform the ECM [35]. Therefore, it cannot provide instructive cues to direct cell phenotype for tissue regeneration.

In theory, the ideal regenerative scaffold would be the natural extracellular matrix (ECM), leading to the emerging development of decellularized tissue for harvesting ECM (dECM) in tissue regeneration [4, 7, 9]. The primary advantage of using dECM as a scaffolding material lies in its ability to support and promote the formation of more specific tissue while minimizing scar tissue [2]. The decellularization process should eliminate all potentially immunogenic components while preserving the original composition and structure of the native ECM as much as possible [46, 47]. Ineffectual decellularization is often associated with intense inflammatory responses that can impede proper remodeling [48]. Different tissues from various donors, even when subjected to similar decellularization protocols, may exhibit significantly different dECM compositions post-process [49]. Despite advancements in the field, the therapeutic application of dECM still encounters challenges related to standardization, scaling up, and ethical and regulatory constraints [10, 37, 39, 48].

Artificial ECMs provide a viable alternative [3-5] to address drawbacks associated with dECM. These structures, typically based on 3D configurations, can be composed of either (i) materials derived from naturally occurring molecules or (ii) synthetic materials with biomimetic features [10, 17, 19]. In comparison to native ECM, artificial structures are more straightforward, facilitating large-scale industrial production with lower batch-to-batch variation [5, 6, 10, 16]. They encounter fewer regulatory issues and are more amenable to manipulation, including tailoring mechanical and degradation properties, making them easier to process [19, 23, 24, 37]. In addition, the structure of decellularized ECM (ECM) of all organs is heterosporous morphology with a high degree of interconnectivity (figure 1). Inspired by this discovery, hydrogels have emerged as favored candidates due to their intrinsic ability to closely mimic several features of the native ECM [15-18]. Hydrogels, which are hydrophilic 3D cross-linked polymeric networks with interconnected microscopic pores, can absorb biological fluid up to 99% of their volume [10, 19, 22]. Hydrogels create a highly hydrated environment, resembling the aqueous conditions experienced by cells in the native ECM [10]. These hydrogels can be formed from both natural and synthetic polymers, offering high adaptability to chemical modification and process engineering techniques for the controlled modulation of their properties [16, 41, 44, 50, 51]. The compliant nature of hydrogels allows for the presentation of embedded cells in suitable viscoelastic microenvironments, the properties of which can be adjusted to match those of various native tissues [47, 52-55]. To further tailor their degradation, stimulative bonds (e.g., temperature stimuli bond, pH stimuli bond, redox stimuli bond, etc.) can be incorporated into hydrogels based on the requirements of specific tissues [56-60]. Additionally, these hydrogels may contain specific biochemical cues to instruct cells and stimulate host cells [51, 61-64]. In comparison to dECM, hydrogel structures are more straightforward and easy to facilitate large-scale industrial production with lower batch-to-batch variation [1-3, 15, 16]. They encounter fewer regulatory issues and are more amenable to manipulation, including tailoring mechanical and degradation properties, making them easier to process [16]. Through rational design, hydrogels, serving as artificial matrices, should offer appropriate mechanical, chemical, and biological support for optimal cell growth and maintenance [65].

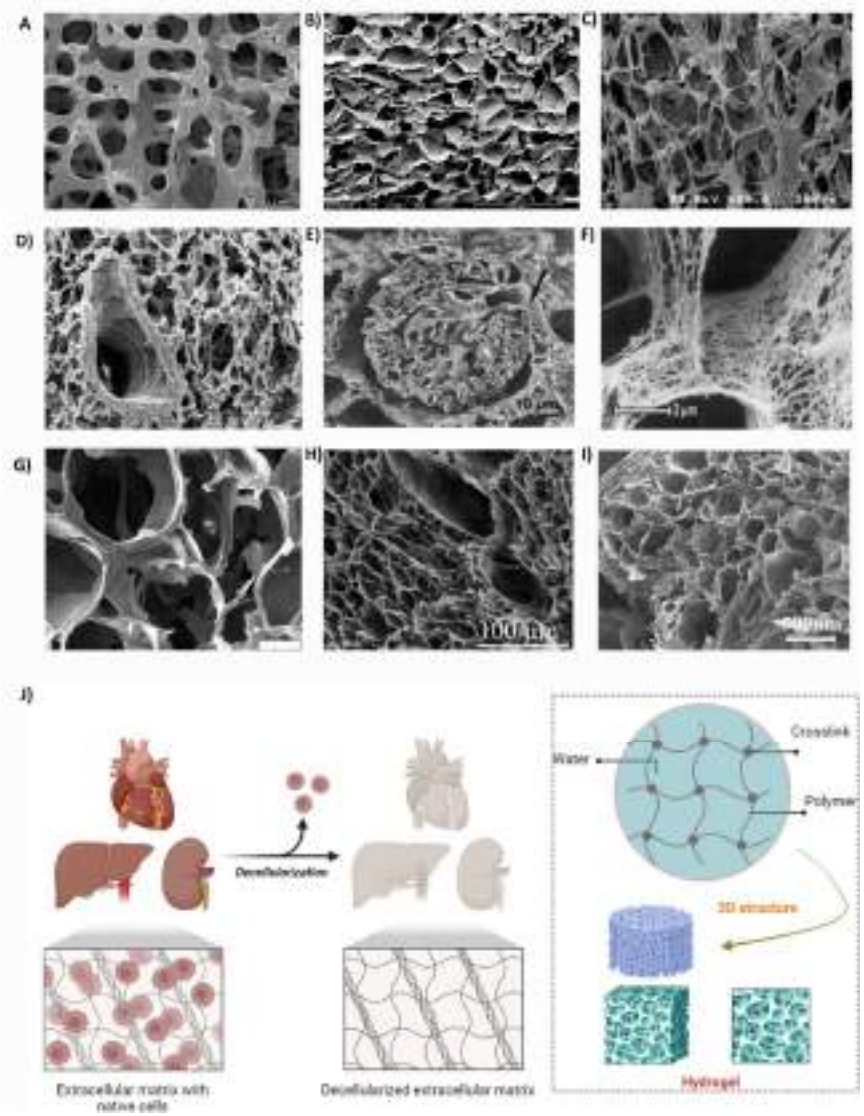

Figure 2.1: The similar structure between native ECM and hydrogel.

A-I: The morphology of dECM from A) bone [66], B) Skeletal muscle [67], C) Skin [68], D) Lung [14], E) Kidney [13], F) Heart [69], G) Placenta [12], H) Ovary [11], I) testis [70]. J) The illustration of the similarity between native ECM and hydrogel.

2.1.3 Injectable thermal responsive hydrogel – ideal performance for tissue regeneration

2.1.3.1 Injectable hydrogel

As an emerging hydrogel in tissue regeneration, hydrogels with injectability have been widely investigated [17, 19, 20, 22]. The concept behind injectable hydrogels is to inject a polymer solution into the treatment site and then allow it to gel (figure 2). Injectable materials can be introduced into the body much faster and have a better affinity for the host tissue [71-75]. Also, injectable formulations can fill a void or defect area with various shapes [10]. These injectable scaffolds typically comprise materials, cells, and biological signals (growth factor,

protein, drug, or bioactive compounds) to facilitate neo-tissue formation. Various studies with injectable hydrogel have shown advantages in inner tissue regenerative, including cardiovascular, cartilage, and bone, in terms of minimally invasive means [51, 54, 74-77]. Further, injectable hydrogel shows the best suitable performance for the new manufacturing processes [5]. The injectable hydrogel, which can inject through a needle or catheter, has become interested in this field [1, 20-22, 24].

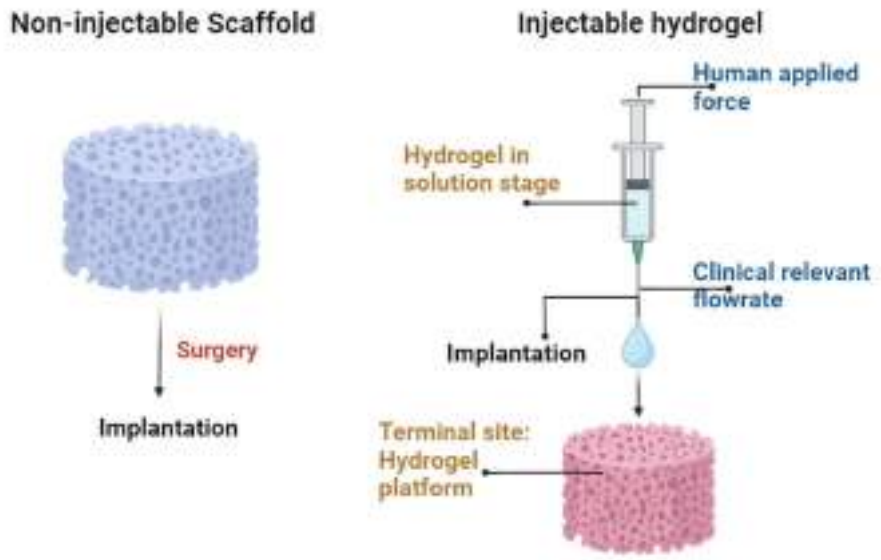

***Figure 2.2**: The illustration of non-injectable hydrogel and injectable hydrogel.*

The primary requirement of these materials is due to the necessity for polymer design [78]. The initial success of injectable systems is achieved through formulations that can undergo gelation in situ, injecting liquid polymer solutions into tissues, where they solidify [17, 18]. Dual-syringe devices for co-injecting two solutions that react to form a hydrogel upon mixing are commonly used [79]. However, the dual solutions require conditions, such as each component's concentration and the mixing solution's flow rate. The poor mixing can further contribute to heterogeneous gelation [78, 79]. Moreover, as injectable hydrogels form in the body, crosslinking methods are limited to biocompatible mechanisms feasible under physiological conditions [24, 60, 75, 80]. In Tosy for injection, the stimuli-responsive polymers are the strategy to design the single injection [21, 24]. Stimuli-responsive polymers have been engineered to undergo sol-gel transitions based on environmental factors such as temperature, pH, and ionic strength [17, 21, 24]. These polymers are designed to remain liquid under nonphysiological conditions (e.g., room temperature, acidic pH, salt-free) but solidify upon introduction into the body (e.g., 37 °C, neutral pH, millimolar salt concentration) [24, 60, 75, 80]. While these injectable systems have shown promise in animal studies [43, 57, 58, 75,

80], challenges with gelation kinetics persist [78, 79]. Issues related to gelation kinetics may lead to solidification within the syringe or slow gelation, resulting in premature cargo release in vivo [1]. Despite these limitations, ongoing research aims to enhance the performance of injectable hydrogels.

2.1.3.2 Thermal responsive hydrogel

Temperature-sensitive hydrogels can be divided into positively and negatively thermosensitive, according to their temperature-sensitive structure of polymer [62, 76, 81-85]. Negative thermo-responsive hydrogels are identified by their lower critical solution temperature (LCST) [22, 24]. Below the LCST, the hydrogel structure relaxes, and above this temperature, the polymer in the hydrogel structure is compacted [86]. On the other hand, positive temperature-sensitive hydrogels are identified by their upper critical solution temperature (UCST) [24, 87]. Below UCST, the polymers compact, and above UCST, it relaxes [87]. Following the hydrogel structure, temperature-sensitive hydrogels can be divided into volume and sol-gel phases [59, 85]. The volume phase transition focuses on the hydrogel with the control degree of swelling based on temperature [85, 86, 88]. A sol-gel phase transition is the group of hydrogel that can transition from the solution phase to the gel phase as a function of temperature [89-94]. Among them, a thermosensitive hydrogel with reversible properties and LCST is one of the most widely applied systems for making injectable hydrogel [22, 23, 90, 91], which is the solution state upon injection at a lower temperature and transforms into a gel state immediately at body temperature [94, 95].

While temperature-responsive and injectable hydrogels exhibit significant promise in various biomedical applications, their preparation and injection processes still pose specific challenges [78, 79]. The polymer network in thermoresponsive hydrogels, and hydrogels in general, is established through polymerization reactions involving crosslinking agents that can be either non-biodegradable or biodegradable [88, 96]. Chemical or physical interactions are employed for crosslinking, impacting the final hydrogel properties and stability crucial for the intended application [97]. Chemical crosslinkers, forming covalent bonds, often yield stiffer hydrogels but may introduce some level of toxicity and may disrupt injectability [23]. Conversely, physical crosslinking through chain entanglement or secondary forces can result in hydrogels with reduced stiffness [22]. Careful consideration of material selection, polymerization reaction, and gelation conditions is imperative to ensure biocompatibility, particularly in injectable systems [15-18].

Thermoresponsive hydrogels can be designed to be biodegradable by incorporating weak bonds susceptible to hydrolysis or other forms of lysis, with cell metabolism and byproduct excretion influencing overall safety [1, 3, 17, 20, 22]. This modified hydrogel class

should be a freely flowing solution into a target region, undergoing in situ gelation in response to increasing temperatures above ambient values and conforming to the surrounding environment [56, 63, 87, 98]. Parameters such as hydrogel lower critical solution temperature (LCST), gelation rate, viscosity, and mechanical strength are crucial and should be characterized and tuned for biological applications [58, 84, 99]. For instance, adjusting polymer concentration and copolymerization ratio of hydrophobic and hydrophilic monomers can alter LCST and viscosity [43, 87]. Importantly, thermoresponsive hydrogels for tissue regeneration must possess mechanical stiffness matching native tissues to modulate target adhesion, proliferation, differentiation, and proper functioning [100]. Adequate mechanical stiffness is fundamental to withstand in vivo forces, ensuring structural integrity and transmitting physiological forces until the hydrogel is entirely replaced by native tissues, minimizing immune system response [17, 19, 23, 38, 79, 100]. Generally, hydrogel mechanical stiffness can be easily modulated by tuning polymer concentration, modifying polymer, and adjusting crosslinking density to achieve optimal mechanical properties for tissue regeneration applications [2, 3, 10].

2.1.4 Emerging trend of injectable hydrogel developing from the hybrid system of polysaccharides and thermo-responsive polymers.

2.1.4.1 The advance of hybrid hydrogels developing from polysaccharides and thermo-responsive polymers

In recent years, a notable body of research has emerged discussing stimuli-responsive hydrogels that incorporate polysaccharides [101]. Integrating biopolymers with thermo-responsive materials has garnered significant attention across various fields [56, 63]. Polysaccharides constitute a substantial category of natural polymers featuring a linear or branched arrangement of sugar monomers connected through glycosidic linkages [102]. These polymers have been sourced from various origins, including plants (such as cellulose, starch, Arabic gum, pectin, guar gum), animals (hyaluronan, chitosan, heparin), microbes (pullulan, gellan, levan, dextran, xanthan), and algae (agar, alginate, carrageenan, fucoidan, agarose) [24, 42, 61, 86, 101]. In recent times, naturally derived polysaccharides have gained prominence over synthetic polymers due to their biocompatibility, biodegradability, low or negligible cytotoxicity, extensive diversity, cost-effectiveness, and approval by the US Food and Drug Administration (FDA) for a wide range of applications in pharmaceutical and food industry [61, 101, 103]. Additionally, their numerous active functional groups make them amenable to tailoring and chemical modifications [42, 103]. The intricate structures and high molecular weight of these polymers confer stability in harsh environmental conditions [61]. Furthermore, polysaccharides serve as rheological modifiers, influencing viscosity, gelling, elasticity, and stiffness properties, following their structure and molecular weight [52, 101]. Incorporating

Polysaccharide with thermal responsive polymer possesses resultant hydrogel, customized thermo-sensitive characteristics, and well-adaptation to the cell environment [24, 51].

For instance, PNIPAM is inherently a thermoresponsive hydrogel [85-87, 98]. However, using unmodified PNIPAM comes with several challenges, including low biodegradability, limited drug loading capacity, slow response to thermal stimuli, and insufficient mechanical strength [85, 98]. The abovementioned limitations have increased the research to adjust the hydrogels' properties and improve their position as an active system for different biomedicine and tissue engineering applications. Additionally, copolymers of PNIPAM and biopolymers generally yield hydrogels with increased strength and improved mechanical properties compared to homopolymer PNIPAM gels [103, 104]. While studies have been conducted to assess the biocompatibility of PNIPAM, most of these studies have focused on specific narrow applications [87]. The NIPAM monomer is toxic to humans, particularly to neural tissue; PNIPAM is generally considered cytocompatible [44]. However, hydrogels based solely on PNIPAM can produce structures unsuitable for tissue regeneration in terms of the resulting scaffold's pore size and mechanical properties [86, 98]. Incorporating natural polysaccharides in combination with PNIPAM aims to address these limitations and create materials that exhibit dual functionality by combining the properties of the thermal responsive feature and the biological/chemical feature of polysaccharides [86].

Gupta et al. [105] proved the excellent performance of PNIPAM hydrogel after modification with carboxymethyl guar. The hybrid hydrogel exhibited a softer consistency than a pure PNIPAM hydrogel, which was easy to support cell viability and proliferation. Similarly, incorporating carboxymethyl cellulose (CMC) into the PNIPAM hydrogel introduced by Vasile et al. [70] showed an outstanding presentation in reversible thermal trigger gelling systems. They reported that the hybrid system showed a temperature-responsive sol-gel transition, which was not observed in the pure PNIPAM hydrogel. Along with thermal responsive property, the hybrid system exhibited a new function, a sensitive hydrogel system inherited from CMC [70]. In other words, the viscosity of the hybrid system could be controlled by both temperature and pH, while this feature was lacking in the single system. In addition, the authors also noted the excellent biocompatibility of the hybrid hydrogel system rather than a single PNIPAM system. Surprisingly, preliminary enzymatic degradation studies indicated that the hybrid system consisting of PNIPAM and CMC could control the degradation by adding cellulases, while PNIPAM hydrogel could not.

The introduction of alginate (Alg) into the PNIPAM structure also achieved inventiveness [47, 88, 106]. An assessment of rheological data of this hybrid hydrogel showed the sol-gel transition as a function of temperature [88]. In particular, the stiffness of the

PINPAM hydrogel was improved following the addition of Alg. Additionally, Lee et al. [82] discovered that hybrid systems PNIPAM- Alg could self-assemble into micelle structures at temperatures close to physiological conditions by controlling the concentration of Alg. Furthermore, alterations in the molecular weight of the PNIPAM grafted onto the alginate backbone caused variations in the micelle morphology. The authors pointed out that these changes in morphology could have substantial implications for the copolymer's utility in applications like disease targeting, cellular uptake, and drug release.

Tan et al. conducted a study to explore the suitability of injectable Alg-based PNIPAM hydrogel systems for tissue engineering applications [96]. In this study, PNIPAM was grafted onto an aminated alginate (AAlg) backbone, resulting in copolymer AAlg-g-PNIPAM. The introduction of AAlg induced the shift of Critical gelation temperature (CGT) to 35 °C, making it suitable for *in vivo* applications. The viscosity of the hybrid gel was sharply increased within the range of 34–36 °C, followed by a plateau, resulting in the easy process of cell incorporation. Human bone mesenchymal stem cells (hBMSCs) laden AAlg-g-PNIPAM gel showed significantly higher viability than native PNIPAM. Based on these findings, Tan et al. concluded that modifying PINIPAM with AAlg provided the potential material for tissue engineering applications [96]. Pentlavalli et al. conducted a similar investigation with a hybrid system, PNIPAM, and Alg [107]. They discovered that the hybrid gel did not exhibit cytotoxic effects on human osteosarcoma cells (MG63) and porcine bone marrow-derived mesenchymal stem cells (pBMSCs), while PNIPAM did. These studies collectively suggest that Alg-g-PNIPAM is a promising candidate for cell encapsulation and may find applications in injectable cell therapies or 3D bioprinting of cells[88, 96, 107].

Another instance of hydrogels incorporating polysaccharides with thermo-responsive polymers involves using Pluronic. Lin et al. [54] devised a hybrid system by combining Pluronic F127 with dextran, resulting in dextran-g-Pluronic F-127. The incorporation of dextran induced the more comprehensive CGT range of pluronic F127. Further, the degradation of pluronic F127 hydrogel was remarkably increased after modification with dextran. Similarly, Park et al. employed a coupling reaction to synthesize Chitosan-g-Pluronic F-127 [76, 81]. Both of these copolymers have demonstrated potential applications in the biomedical field, unlike pure Pluronic F127. Chitosan-g-Pluronic F-127, in particular, has shown promise as a carrier for cartilage regeneration [71, 80]. Chitosan-g-Pluronic F127 exhibited an LCST of approximately 25 °C, which could be adjusted by varying the amount of chitosan. However, using the single Pluronic F127 exhibited quick erosion, increasing viscosity and, consequently, reducing the viability of the encapsulated cells. Interestingly, Chitosan-g-Pluronic F127 was found to be biocompatible and capable of supporting the

proliferation of bovine chondrocytes[56]. The morphology of the Chitosan-g-Pluronic F127 hydrogel had more pore interconnection than pure F127, confirming a suitable environment for cell growth. All these findings suggest that combining polysaccharides into thermo-responsive materials results in the thermo-sensitive hydrogel as a promising technology for tissue regeneration.

2.1.4.2 Technologies adopted in Hydrogels Based on Polysaccharides Incorporated with Thermo-Responsive Polymers

2.1.4.2.1 Physical strategy vs chemical strategy

Three techniques are available for producing hydrogels that combine polysaccharides with thermo-responsive polymers: physical blending, grafting approaches, and cross-linking techniques [24, 44, 51, 77, 81, 108]. In physical blending, ionic crosslinking and thermoregulation methods have created combinations of polysaccharides and thermo-sensitive polymers[65, 97]. However, the non-covalent interactions between polysaccharides and thermo-sensitive polymers result in less stable entities than those bound covalently. This instability can lead to phase separation within the resulting hydrogel[86].

Polysaccharides typically have a high crystalline level due to their abundance of intramolecular bonds[42, 101, 103]. As a result, polysaccharides often have low solubility, presenting a significant challenge when blending with another polymer[103]. The solubility of polysaccharides is frequently pH-dependent; for example, chitosan (CS) dissolves in acidic environments, while hyaluronic acid solubilizes in primary conditions. Their varying solubility complicates the mixing process, particularly in multi-step reaction procedures. To create a stable structure for thermo-sensitive hydrogels, it is necessary to employ two independent cross-linked polymer systems that form a single polymeric network[24, 42, 86, 103]. In the following section, chemical methods, including grafting approaches and chemically induced cross-linking techniques, will be discussed.

2.1.4.2.2 Grafting approach

Graft copolymerization is a common strategy for preparing materials for a hybrid hydrogel system[61, 103]. To synthesize polysaccharide-polymer conjugates, three primary routes are available: the "graft-to," "graft-from," and "graft-through" strategies[103] (figure 2.3). In brief, the "graft-to" strategy involves grafting pre-existing polymers onto polysaccharides through a one-step process. The "graft-from" strategy entails the continuous in situ growth of polymer chains from the surfaces of polysaccharides or the utilization of pre-existing polymers as initiators. The "graft-through" strategy involves attaching polymerizable groups to polysaccharides, followed by polymerization to generate polymer-grafted polysaccharides.

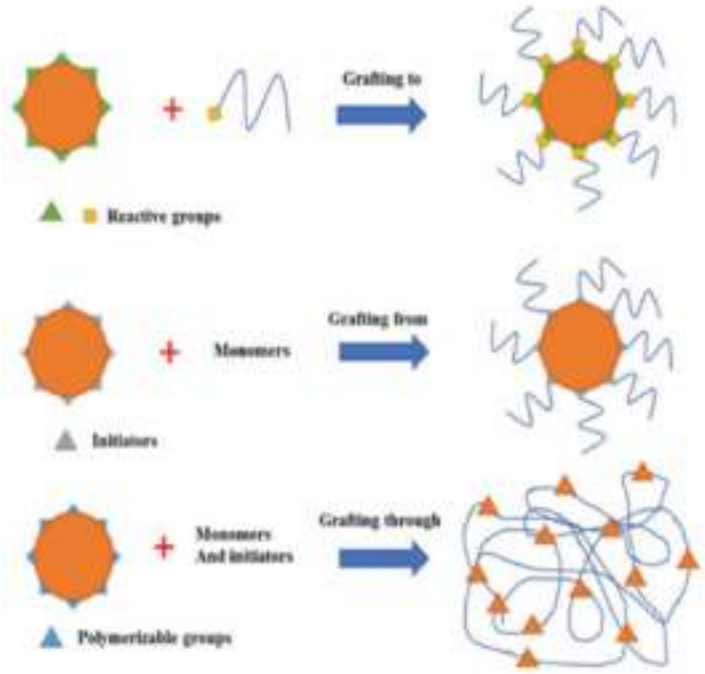

***Figure 2.3**: Graft polymerization techniques.*

Adapted from the reference [41]

Polymerization techniques play a crucial role in these strategies[53]. Controlled polymerization techniques, such as atom transfer radical polymerization, reversible addition−fragmentation chain-transfer polymerization, nitroxide-mediated polymerization, and ring-opening metathesis polymerization, provide effective means to produce polymer-modified polysaccharides with tailored structures and properties[53, 108]. The reduced viscosity of the hybrid hydrogel barely changed over a 40°C interval, attributed to the uncharged nature of the CMC backbone at low pH values [109]. This method does not guarantee the presence of the desired functional group at the end of every polymer chain. On the other hand, the direct polymerization of functional monomers can yield high functional group densities throughout the polymer backbone, which can be further utilized for preparing polymer brushes or conjugating sensor moieties for susceptible chemical detection[110, 111]. This approach ensures the desired functional group's presence in each polymer backbone's repeat unit. However, employing protective measures for the functional group may be necessary if it hinders the polymerization process. Additionally, the desired functional monomer may not always be commercially available[108].

To solve these obstacles, a pre-required modification of the polymers using bifunctional reagents is often necessary[110]. These reagents are used as linkers, and they might bring new

Functionalities into molecules or act just as spacers, improving the spatial availability of functional groups[111, 112]. Functional modification of polymer molecules with high selectivity or specificity is needed. A suitable method for functional modification should be generally applied. This approach involves the attachment of a synthetic polymer, exhibiting a well-defined end-functionality to a complimentary functionality of polysaccharide.

Various coupling techniques have been developed to desire the reactive groups, as illustrated in Figure 2.4.

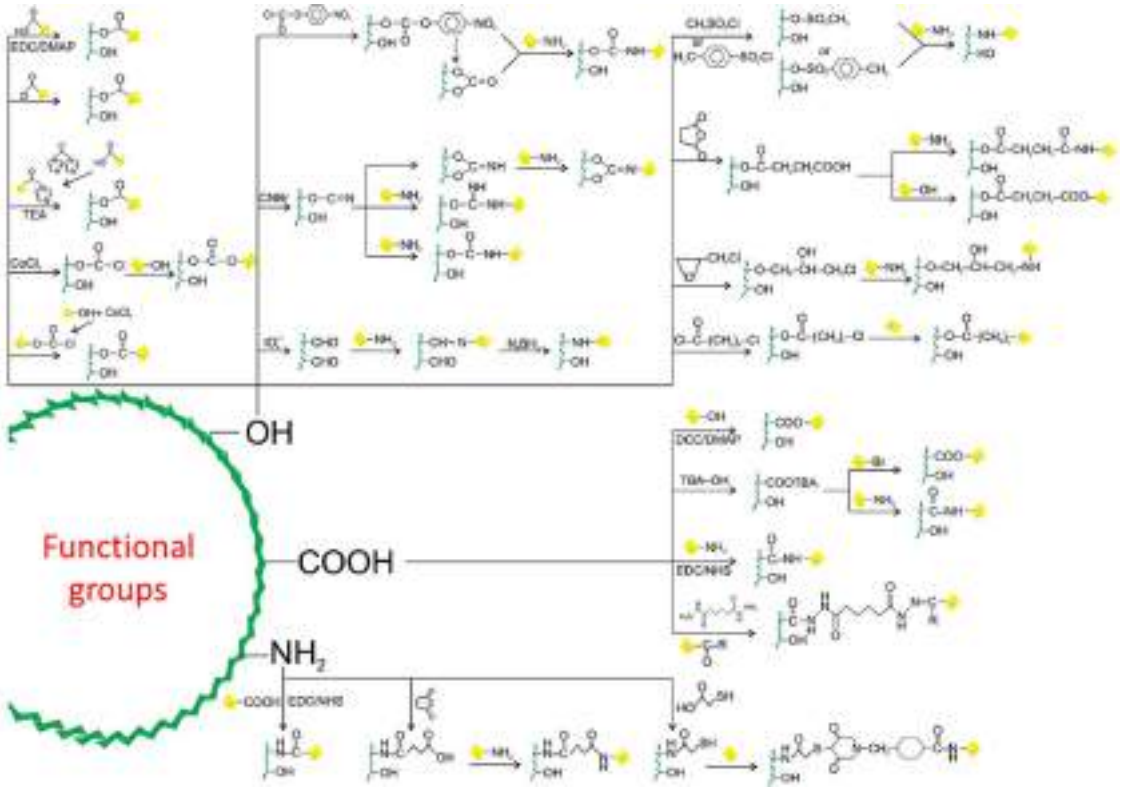

Figure 2.4*: The illustration of the coupling chemistry for different reactive functional groups of the polymers.*

Adapted from the references [10, 84-92]

The carboxylate groups can use carbodiimide derivatives as the coupling agents to make conjugated bonds with nucleophilic functional groups such as primary amino groups, hydroxyl groups,…[113]. The carbodiimide coupling agents include N, N′-dicyclohexylcarbodiimide (DCC), Carbonyldiimidazole (CDI), 1-ethyl-3-(3-dimethylaminopropyl) carbodiimide (EDC) [24, 82, 96, 113]. DCC and CDI can used in organic solvents, while EDC is used in water solvents only. The introduction of a carbodiimide bond would provide a good leaving group; therefore, the compound containing primary Amine/hydroxyl could form the amide, esters,

ureas, etc, with the carbodiimide-activated groups following the nucleophilic substitution [114-115]. To increase the yield of the reaction, the strong nucleophilic components such as pyridine (in organic solvent), 2-chloro-1-methylpyridinium iodide, 4-(N, N′-dimethylamino)pyridine (DMAP), triethyl amine,.. should be supported. In terms of EDC, the use of N-hydroxysuccinimide (NHS) is preferred. EDC forms the O-acylisourea intermediate, which is very sensitive to nucleophilic functional groups. The reaction occurs in aqueous physiological pH, while the o-acylisourea intermediate is unstable in this condition. Therefore, N-hydroxysuccinimide (NHS) is recombined in this case [116]. Another strategy to activate carboxylic groups is the use of the tetrabutylammonium (TBA) salt, specialized in the case of polysaccharides. With the help of TBA, polysaccharides can react in the organic solvent. Also, with the help of TBA, these carboxylate groups can be activated with alkyl halides[114]. Additionally, hydrazination reactions have been utilized for efficiently conjugating the carboxyl groups of polysaccharides to polymer-containing amino or hydroxyl functional groups [115].

There are many methods to improve the nucleophilicity of hydroxyl groups. The introduction of the arylation or acylation is generally focused due to the ease of reaction with the amine compounds. However, this strategy is only available to allyl alcohols or β-amino alcohols. The use of phosgene to increase the nucleophilicity of the hydroxyl group has been introduced in some research [116, 117]. Although phosgene creates chloroformate intermediates sensitive to amino groups, phosgene is very toxic and can make the cyclic [116]. Another strategy is the use of p-nitrophenyl chloroformate. The hydroxyl group forms aromatic carbonate esters with p-nitrophenyl chloroformate. This bond will be cleavage in the presentation of amino groups. Cyanogen halide activation is another method employed for the covalent attachment of amine polymers to the polysaccharide backbone via hydroxyl [118]. The reactive cyanate esters in this reaction may undergo hydrolysis to yield inert carbamates or rearrange to produce intra-/interchain and cyclic imidocarbonate structures. The parallel reactions of these products with the amine polymer can form an isourea derivative[119]. Moreover, dialdehyde polysaccharides obtained after periodate oxidation can form Schiff bases when conjugated with amine polymers[120]. Subsequent reduction using sodium borohydride can enhance the stability of these conjugates[121]. Another approach involves activating polysaccharides using sulfonyl chlorides to create corresponding sulfonyl esters, which can react with polymers containing carboxylic or amino groups[122].

Rather than direct conjugation, introducing spacers showed some advances [113]. Introducing these spaces helps support the new function of polysaccharides, including the biological functions and/ or solubility [123]. Also, with spacer groups, the reduction in the

yield of conjugation due to the steric hindrance following the self-assembly of the polysaccharide could be solved [124, 125]. The introduction of spacer groups could use the coupling agent presented in Figure 2.4 [126]. The amino acids and peptides are typically used as spacers[124]. Further, by the introduction of spacers, the degradation could be controlled by external stimuli such as pH, redox, …[127]

Generally, the different routes reported for the grafting approach using coupling chemistry. They can be typically classified into some routes: (i) identify the functional groups at the grafting site, (ii) select the complementary functional groups on the crosslinker, and then (iii) select the activating methods. For this method, copolymer solution creates only physically interconnected, without any chemical bonding, so individual components retain their original properties [103-105, 107, 108, 128].

2.1.4.2.3 Cross-linking technique

Recently, crosslinking technology has gained significant attention as an effective method for developing thermal-responsive hydrogels that incorporate polysaccharides[24, 86]. Like the grafting approach, covalent linkages between polymer chains can be established by reacting functional groups with complementary reactivity[76, 112, 129]. Derived from the fabrication of in situ-forming hydrogels, this approach connects the functional groups of polymer chains via supramolecular interactions (such as hydrogen bonding, ionic bonding, etc.) or covalent bonding. Initially, the polysaccharide backbone undergoes chemical pretreatment to introduce active groups, such as catechol or phenol[130]. These treatments create crosslinking regions, initiating the termination phase and resulting in crosslinking between different polymers[131].

The chemical crosslinking mediated hydrogel can synthesized under click chemistry, Schiff base, photo-crosslinking, Michael-type addition reaction, and redox reaction[130, 131]. Among them, redox reactions have recently emerged as a promising triggering motif for designing a novel type of responsive polymers[132]. By introducing the redox reactive moieties on the polymer backbone, two polymers are spontaneously cross-linked in the presentation of the oxidative reagent [131, 132], such as H_2O_2 or O_2. Phenolic moieties (e.g., tyrosine, catechol, and polyphenols) are commonly targeted for this method[133].

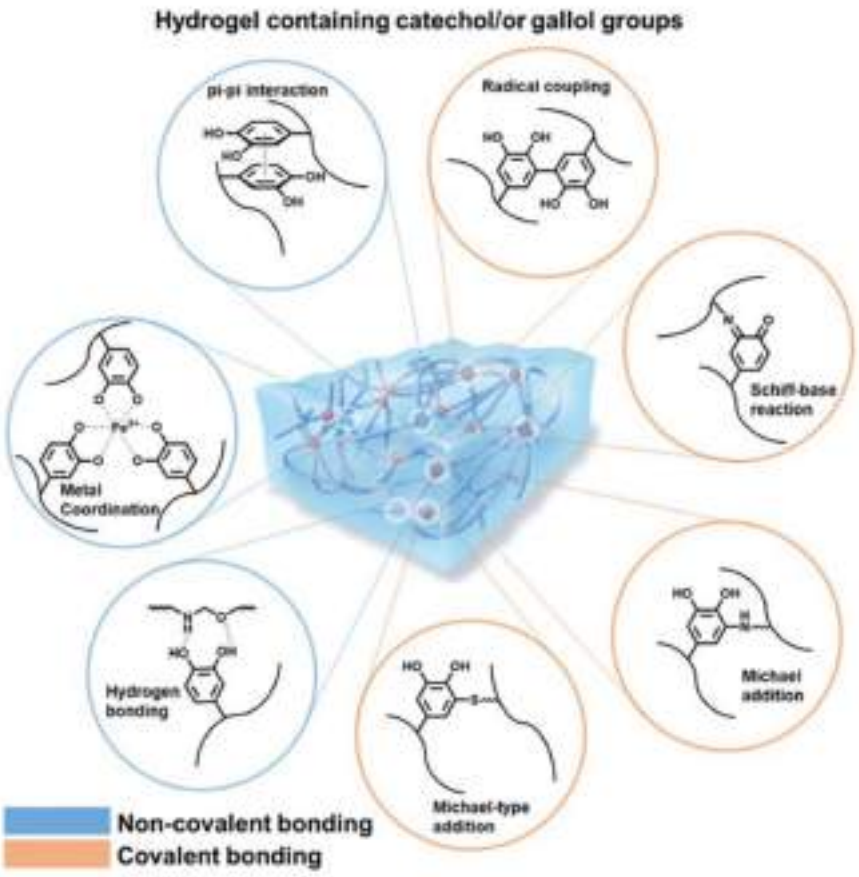

Figure 2.5: *Crosslinking mechanisms of catechol-conjugated polymers for hydrogel formation.*

Blue circle: Noncovalent crosslinking, orange circle: Covalent crosslinking. Adapted from the reference [134].

Catechol oxidation chemistry has demonstrated an excellent example of a hybrid network between polysaccharides and thermally responsive polymers [139-140]. The oxidative polymerization of catechol forms the crosslinking between two polymers [76, 112, 129]. This allows for control over the ratios of the two networks and is less time-consuming since diffusion is not required. It provides a straightforward, one-pot method for hydrogel formation (figure 2.5).

Inspired by this strategy, Park and colleagues[135] developed an injectable hybrid hydrogel from polysaccharide (hyaluronic acid) and thermal responsive polymer (Pluronic). This study modified hyaluronic acid with catechol while thiol groups from cysteamine were introduced at the end group of pluronic F127. Via the Michael addition reactions between thiol and catechol, the crosslinking between hyaluronic acid and pluronic F127 was formed,

resulting in a cross-linked adhesive hydrogel. Taking the same idea, Park et al. [130] developed a hybrid hydrogel-based pluronic with another polysaccharide, chitosan. Both precursors were soluble and could be pre-mixed at 4°C, and the resulting viscous solution rapidly solidified into a gel state when the temperature was raised to 37°C. In addition, chemical and physical crosslinking induced the resultant hydrogel with high mechanical features compared to the thermal responsive hydrogel based on physical crosslinking only [129-130].

The formation of the crosslinking between catechol motifs could be based on their auto-oxidation, catalyzed by native oxygen molecules, to facilitate catechol oxidation without additional supplements [76, 112, 136]. Polymers modified with catechol or tri-hydroxyl phenol residues (e.g., gallon, polyphenols) can be quickly injected into native tissue and form the hydrogel stage without adverse effects[137]. However, the reaction kinetics are relatively slow and highly dependent on environmental factors such as pH. This approach is not suitable for applications requiring rapid crosslinking[136]. Adding oxidative compounds such as sodium periodate could enhance the crosslinking kinetic. The crucial aspect of the crosslinking strategy relies on the oxidation of tyrosine and catechol to ortho-quinones[137]. Ortho-quinones possess high electrophilicity, enabling their participation in various reactions, including Schiff-base reactions, Michael-type additions, and coupling reactions[137, 138]. In the Schiff-base reaction, an electron donor group, such as a primary amine, attacks the C=O bond in the ortho-quinone. This results in the formation of ortho-quinone imines containing a C=N bond. When ortho-quinone acts as an electrophilic acceptor, the primary amine and thiol groups can attach to the meta-position (1,4-Michael reaction) and ortho-position (1,6-Michael reaction). Additionally, ortho-quinone can interact with neighboring catechol groups, leading to coupling reactions[137, 138]. In the case of sodium periodate-mediated oxidation, catechol-periodate intermediates break down to form ortho-quinone. However, there are limitations to using sodium periodate-mediated crosslinking in tissue engineering. Firstly, the reaction occurs under alkaline pH conditions. Secondly, sodium periodate causes a ring-opening reaction in polysaccharides (e.g., alginate, hyaluronic acid), producing cytotoxic aldehyde groups. Lastly, sodium periodate itself possesses intrinsic cytotoxicity[137, 138].

Biological peroxidase enzymes are known to regulate this process, with various types of peroxidase enzymes demonstrating this function[132, 138, 139]. Horseradish peroxidase (HRP) offers advantages over other peroxidases due to its narrow range of phenol coupling reactions [139]. HRP-mediated coupling is limited to the coupling reaction, as it cannot occur with primary amine and thiol groups[140]. HRP is an enzyme containing heme derived from a plant source[141-143]. The heme group in the HRP structure captures the oxygen molecules from the hydrogen peroxidase ((H_2O_2), forming the hem groups with high oxidation states.

This Fe (IV) = O initiates the phenolic oxidative reaction. Indeed, Fe (IV) = O takes the hydrogen atom from the phenolic motif, forming the highly reactive phenolic radical. The complex oxidizes phenolic moieties from the couple via a C-O bond between the ortho-carbon of phenolic groups and the phenolic radical and a C-C bond between the ortho-carbon of phenolic groups[132]. Despite the advantage of HRP in the redox reaction for making hydrogel, there are significant concerns associated with HRP due to an immunological response in some animal studies[143, 144].

An alternative to the HRP enzyme is peroxidase-mimicking enzymes[142, 143]. When designing these peroxidase-mimicking catalysts, it's essential to consider the peroxidase-like spatial arrangement of the hemin ligands and activating groups, which serve as the proximal and distal residues of heme[142]. This approach aims to enhance control over the oxidative catechol crosslinking process, addressing issues such as pH sensitivity and immune responses[145]. Ultimately, it enables the broader utilization of catechol oxidative chemistry as a crosslinking strategy to incorporate polysaccharides with thermal-sensitive polymers, facilitating the development of suitable thermal-responsive hydrogels for tissue regeneration.

It's important to emphasize that in the context of thermal-responsive hydrogels incorporating polysaccharides, the primary goal of crosslinking reactions is to enhance hydrogel strength without compromising the phase transition due to the presence of polysaccharides[24, 86]. Unlike grafting techniques, crosslinking methods focus on establishing stable polymeric networks, forming the hydrogel structure. In other words, these methods randomly create covalent bonds between adjacent polymer chains. Typically, polysaccharides can engage in chemical crosslinking with each other, while thermal-responsive polymers are part of the mix. However, the heterogeneity within the networks may disrupt the thermal-responsive property. Therefore, the challenge remains to create thermoresponsive hydrogels incorporating polysaccharides using crosslinking techniques with an entirely predictable and controllable phase transition temperature.

2.2 Encoding the hydrogel for specific tissue regeneration

2.2.1 The stiffness of the hydrogel

Understanding the vital role of hydrogel stiffness in guiding tissue regeneration [100], it is evident that initial interactions between cells and the scaffold surface, mediated by focal adhesions with the matrix [146-153], trigger the recruitment and activation of proteins Associated with mechano-signaling pathways [154-157]. This cascade of events leads to adaptive cellular responses, encompassing gene and protein expression changes, influencing cell growth and differentiation [100, 154, 156, 158]. As revealed in prior studies, the

interconnection between hydrogel stiffness and cellular response is pivotal in substrate-guided tissue regeneration [155, 156, 158]. For example, in the case of wound healing, the change in the hydrogel stiffness induced the various regenerative capacity [100]. Medium stiff hydrogels (~10^3 Pa) have been shown to mitigate scar formation, enhance wound healing, and facilitate myofibroblast transformation, keratinocyte proliferation, extracellular matrix synthesis, and remodeling. The impact of hydrogel stiffness extends to the secretion of crucial factors like TGF-β1 and bFGF, critical players in skin wound healing. This correlation suggests that the therapeutic effects of hydrogels in skin wound healing can be finely tuned by adjusting the stiffness of the hydrogel. Hydrogel stiffness regulates cell behavior and fate, while cells reciprocally contribute to the remodeling of the substrate, influencing the overall tissue regeneration process [100, 156, 158]. In addition, in the human body, different tissues exhibit differences in rigidities, as demonstrated in Table 2.1. Therefore, careful consideration is essential to ensure optimal outcomes when designing hydrogels tailored for specific tissue regeneration applications [155, 157].

Table 2.1: *The stiffness of living tissues.*

Tissue	Organ	Stiffness range (kPa)	Reference
Connective tissue	Fat	0.02	[153]
	Skin	4.5-8	[152]
	Tendon	310.000	[159]
	Ligament	25.000-93.000	[151]
Vascular	Carotid artery	90	[159]
Nervous	Brain	0.2 -3	[159]
	Spinal cord	27-89	[159]
	Nerve	5000	[150]
Musculoskeletal	Cardiac muscle	20-150	[159, 160]
	Skeletal muscle	10-170	[149]
	Cartilage	20	[149, 161]
	Pre-calcified bone	30-50	[149]
Kidney	Cortex	4	[146, 162]
	Medulla	5	[148]
	Sinus	8	[148, 162]
Pancreas		2.9	[146, 147]
Eye	Cornea	7.5–109.8	[163]
	Lens	0.2-10.3	[164]

2.2.2 The biological cues

In tissue engineering, along with stiffness, manipulating the microenvironment with biological cues, such as mitogens, growth factors, and morphogens, is crucial for guiding cells in tissue regeneration [32, 33, 165-168]. These cues can activate specific signaling pathways or sets of genes to direct and control cellular responses [134, 169-173]. Hydrogels have been specifically engineered to deliver various growth factors or chemoattractant signals locally, aiming to recruit stem cells and expedite healing [174-177]. It is essential to highlight that the scaffold's appropriate design is paramount for programmed morphogenesis in the intricate environment where neotissue formation occurs [10, 24, 36, 38] (figure 2.6). Careful consideration of signals' spatial and temporal evolution throughout the regeneration process is necessary [8, 10, 18], involving predicting transport phenomena and monitoring mass transport parameters [15, 19, 21, 23, 35]. The selection of biological cues should align with the pathology of the damaged tissue [168, 172, 178-181], emphasizing the importance of designing systems that can provide these biological cues in a time-controlled manner to mimic the normal healing process [182] closely. This section will further discuss this concept, focusing on selecting biological cues for diabetic wound healing and bone regeneration.

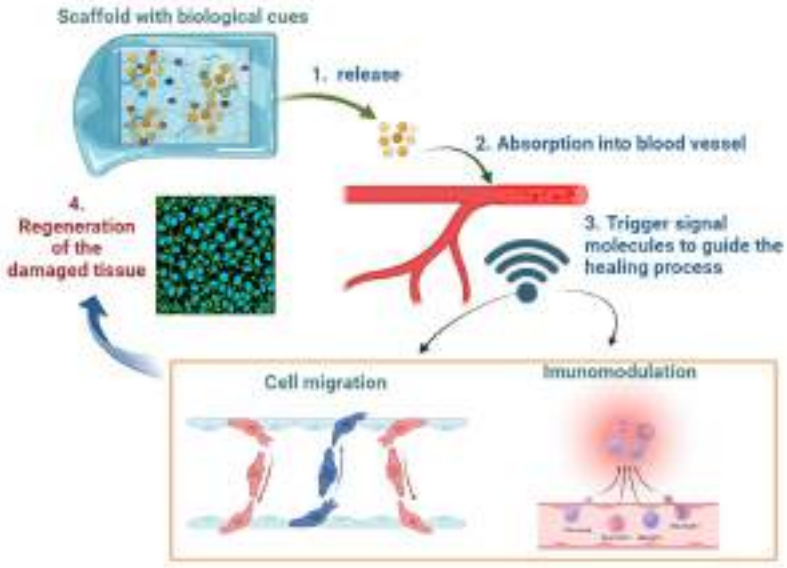

Figure 2.6: *The illustration of the function of biological cues in developing the functional scaffold.*

To activate resident cells for the regeneration process, the ideal design of the scaffold follows the addition of the homing factors to guide cells. These factors would (1) release from the hydrogel scaffold, (2) go into the bloodstream, and (3) make these signals to guide the

migration of cells and to guide the difference process of cells in support of new tissue growth (4).

2.2.2.1 Diabetic wound

2.2.2.1.4 The wound healing process and the alterations in diabetic conditions

The wound healing process includes several sequential phases: inflammation, proliferation, granulation, and tissue remodeling [28, 167, 169, 180, 183]. It is a complex cellular response to injury involving the activation of various cell types, including fibroblasts, endothelial cells, macrophages, and platelets [3, 19, 24, 36]. The initial step in wound healing is clot formation, which recruits fibroblasts and immune cells to the injured area [36]. The inflammatory phase, lasting approximately four days, is significantly influenced by macrophages [35, 36]. Macrophages migrate to the wound, explicit necrotic material, and produce factors that induce angiogenesis by endothelial cells, epithelialization by keratinocytes, and matrix deposition by fibroblasts, leading to the reconstruction of ECM [36]. Subsequently, re-epithelialization involves migrating epithelial cells and keratinocytes across the wound barrier and granulation tissue [35].

Nitric oxide, a gaseous molecule, is widely recognized in treatments for wound healing [170, 171, 184-187]. Typically, NO is involved in the natural process of wound healing [184-187]. During hemostasis, NO is produced by endothelial cells to activate the cyclic c-GMP pathway; consequently, it prevents platelet aggregation and then increases vasodilation[169, 171, 187]. The vasodilation helps to increase the blood flow to the wound site and then increases the influx of inflammatory cells[35]. The concentration of NO at the wound site is increased due to the activation of iNOS in neutrophils and macrophages[36]. This way, the phagocytosis pathway is increased to clean the wound site[187, 188]. In the inflammatory phase, M1 macrophages produce significant amounts of NO (>0.5mM) to combat microbes and prevent wound infection [188]. As the wound transitions to the proliferation stage, NO levels decrease significantly (0.01-0.25mM) [188, 189]. M1 macrophages convert to M2 macrophage cells, which do not produce NO [36]. During this phase, NO production depends on fibroblasts and keratinocytes, stimulating the proliferation and migration of more keratinocytes within the wound [188, 189].

In a diabetic state, persistent hyperglycemia triggers the overproduction of superoxide through various pathways, including the polyol pathway, xanthine and NADPH oxidases, cyclooxygenases, uncoupled nitric oxide synthase, glucose auto-oxidation, and the mitochondrial respiratory chain [188-191]. This results in elevated levels of reactive oxygen species (ROS) and diminished antioxidants, defining a state of oxidative stress [192]. The

excess superoxide activates the NF-κB transcription factor, leading to the upregulation NOS-2 and subsequent nitric oxide (NO) production [190, 193]. In the presence of high superoxide and low levels of superoxide scavenger molecules, NO rapidly reacts with superoxide to generate peroxynitrite [192], thereby reducing the bioavailability of NO [188, 189]. Additionally, heightened ROS and peroxynitrite levels in hyperglycemia limit the production of BH4 (an essential co-factor for NO production) and induce the uncoupling of NOS, resulting in superoxide production instead of NO [192]. Another contributing mechanism is the concentration of arginase, which competes with NOS enzymes for the substrate arginine, reducing NO availability and favoring superoxide production [194]. In diabetic wounds, increased arginase activity levels were observed, correlating with delayed healing in various studies [28, 166-168, 176, 181, 194, 195]. The NO deficiency disrupts endothelial vascular function, impacting vessel functionality [190, 192, 193].

Furthermore, in diabetic patients with elevated cholesterol levels, peroxynitrite promotes lipid peroxidation and triggers an inflammatory response, leading to platelet aggregation [196]. These effects are particularly pronounced in small blood vessels, contributing to the progression of neuropathy [190, 192, 194]. Vascular impairment can result in persistent ischemia and wounds in diabetic individuals are often associated with low oxygen tension [197]. Under physiological conditions, cells express HIF-1α, a pivotal transcription factor enabling cells to adapt to hypoxic conditions by promoting angiogenesis, cell proliferation, survival, and energy metabolism [196]. Nitric oxide (NO) is a crucial regulator in expressing HIF-1α [191, 192]. During the initial phases of wound healing, when M1 macrophages are predominant, the high NO production from cells may facilitate the stabilization of HIF-1α to generate an adaptive response to injury [193, 194, 197]. As the resolution phase begins, lower NO levels from other cells resolve the wound environment and restore its normal state [188, 189]. Fibroblast-produced NO regulates collagen production and may act as the initial response before immune cells arrive at the wound site [190]. Low NO levels influence extracellular matrix remodeling/turnover [192, 193]. The dynamic modulation of NO doses at the wound site over the healing process ensures the expected production and regulation of growth factors to maintain cell phenotype and function at each stage [189-191]. Due to its reactivity and short lifespan, NO's overall effect on cells is influenced by aggravating factors, with mechanisms in place to maximize its biological effect for an appropriate host response [171, 184, 187, 198]. Maintaining nitroso-redox balance is crucial, and any persistence of stimuli or inadequate feedback can disrupt the equilibrium of the wound environment, which is characteristic of dysregulated healing in diabetic wounds [199].

2.2.2.1.5 L-arginine

The most straightforward method for assessing the impact of NO on wound healing is to administer the molecule in its gaseous form [188, 200-202]. The direct application of NO gas in the wound site focuses on infiltrating microorganisms using a gNO cylinder [188, 192-194, 201]. While the administration of gNO is relatively simple in a clinical context, its use restricts patient mobility due to the equipment's requirement, particularly the gNO cylinder size [203]. Additionally, the direct NO gas induces risk to the patient's health, posing substantial safety risks to the gas exchange system [201, 2023]. To overcome the drawbacks of gNO delivery, NO precursors have been introduced [204].

Among them, L-arginine has been favored over NO precursors. L-arginine is a natural amino acid classified as a semi-essential amino acid in human metabolism [166-168, 176, 181, 195, 198]. L-arginine is a substrate of the enzyme nitric oxide synthase (NOS). Through this pathway, NO and L-citrulline are formed [195]. Endothelial NOS (eNOS) uses arginine to stimulate vasodilation and act as a neurotransmitter [166]. Arginine is uptake by macrophage M1 cells to generate NO [167]. Interestingly, along with nitric oxide, L-arginine is also used by macrophages M2 to produce ornithine [193, 194, 197]. These ornithine produce the signaling for cell growth and differentiation, the synthesis of collagen fiber, and finally, the repairing process. Therefore, arginine is frequently used to increase NO production during diabetic wounds [193, 197, 204].

Nevertheless, the extracellular L-arginine raises the challenge related to the activity of immune cells [166-168]. Studies from Michaela Pekarova et al. [205] recorded the increase of superoxide anion in stimulated macrophage cells culturing with L-arginine. It is well known that the affinity binding between NO and superoxide anion (10^5 -10^6 M^{-1} S^{-1}[206]) is higher than that of superoxide anion and the scavenger agents such as proteins/metal ions (1.9×10^{10} M^{-1} S^{-1} [207]) and scavenger superoxide dismutase (2×10^9 M^{-1} S^{-1} [193]). Thus, the formation of peroxynitrite- the more reactive and toxic compound, is more pronounced. Peroxynitrite is a signaling molecule that controls cell proliferation and anti-bacteria [190, 192, 193, 208]. However, the higher concentration of peroxynitrite induces significant toxicity to renew cells. The addition of ROS scavengers could dismiss this effect [189, 203, 204]. In diabetic patients, the formation of peroxynitrite is alarming. Due to the elimination of peroxynitrite in blood plasma, the nitrotyrosine level is very high in patients with diabetes [209, 210]. The higher concentration of peroxynitrite in the blood plasma is also the main reason for delayed wound healing in diabetic patients [205]. Thus, the combination with the ROS scavenging agents is necessary to exploit the therapeutic value of L-arginine in wound healing.

2.2.2.1.6 Resveratrol

Resveratrol (trans-, 3,5,4′-trihydroxystilbene) is a naturally occurring polyphenol present in, among others, red wine [180, 185, 199, 211-215]. Interest in resveratrol increased tremendously in diabetic wounds due to its multiple therapeutic values [180, 211, 212]. Resveratrol has an anti-oxidant-based structure. Resveratrol has a central carbon-carbon double bond connecting the phenolic ring and is responsive to antioxidant capabilities [215]. These functional moieties help to quench harmful radicals via hydrogel atom transfer or electron transfer process [180]. The formation of resveratrol dimers during this process also helps to stabilize the radical [215]. Also, resveratrol is a bioactive compound that can regulate the activity of SIRT1 to combat oxidative stress [216, 217]. The expression of SIRT1 helps to enhance the activity of nuclear factor erythroid 2–related factor 2 in controlling the balance between reduction and oxidation inside the cells [217]. Further, SIRT1 activates the deacetylation of the X-box, consequently promoting the transcription of the collagen gene and assisting in the remodeling of the damaged tissue [218, 219]. Additionally, many studies have proved the function of resveratrol in the increase in the expression of the eNOS enzyme, leading to the indirect support of the increase in NO concentration[180, 214, 220]. Furthermore, resveratrol can be the homing factor for immune cells into the vascular wall and mitigates vascular inflammation [199, 211, 213]. These multifaceted mechanisms collectively contribute to the in vivo effects of resveratrol on vascular function and blood pressure [213]. Based on these advances, various studies [31, 32, 180, 213, 215] have developed a topical product based on resveratrol for diabetic wounds.

2.2.2.2 Bone

Bone is hard tissue with a highly vascularized system that can heal and remodel considerably [27, 178, 179, 183, 220, 221]. The critical roles of bone are to support the body, serve as a mineral reservoir, support muscular contractions, and protect the internal organs [174, 221, 222]. The bone healing process is complicated and requires various cell messages signal cascade [27, 220]. Usually, its process could be divided into 3 phases: inflammation, neo-tissue formation, and remodeling [174]. The hierarchical structure of bone matrix has provided significant bioinspired motifs for biomaterial and scaffold design [66]. The extracellular matrix (ECM) of this tissue is made up of both a non-mineralized phase (osteoid) and a mineralized phase comprising calcium phosphate salts [161, 222, 223]. Therefore, the hydrogel scaffold should be involved in the biological cues with osteoconductive features to assist the healing process of bone; along with the stiffness, the hydrogel scaffold should be involved in the biological cues [90, 174, 221, 222]. In this section, we will pay attention to bioglass, an osteo-friendly environment.

Bioactive Glasses (BGs), classified as bioceramics, were originally developed by Professor Hench in 1969 and introduced as 45S5 Bioglass® by Novabone in Florida[174]. Bioglass® is a quaternary system composed of 45 wt.% SiO_2, 24.5 wt.% CaO, 24.5 wt.% Na_2O, and 6.0 wt.% P_2O_5. Since their inception, numerous studies have explored the application of BGs in bone regeneration repair of bone defects [222]. When implanted, BGs undergo dissolution, forming hydroxycarbonate apatite (HCA) on their surface. HCA has a composition and structure similar to that of bone mineral, facilitating the bonding of bone to the material [222]. The presence of HCA on BG-containing materials can influence protein adsorption, ultimately promoting osteoblast-like cell adhesion and differentiation through fibronectin mediation[27]. Additionally, it is widely recognized that the ionic dissolution products of BGs can stimulate both osteogenesis and angiogenesis, both *in vitro* and *in vivo*[174]. In recent years, several BG products have been commercialized for bone regeneration, such as PerioGlas®, Biogran®, and BonAlive®, as well as for addressing tooth hypersensitivity, as seen with NovaMin®[178]. These products benefit from BGs' remarkable bioactivity and biocompatibility[174, 179, 221]. Beyond their excellent osteoconductivity and osteostimulatory properties, numerous studies have highlighted that the controlled release of specific therapeutic ions, including silver (Ag^+), gallium (Ga^{3+}), zinc (Zn^{2+}), copper (Cu^{2+}), and cerium (Ce^{3+}), when incorporated into the glass network, can confer antibacterial properties[178]. The attractive characteristics of BGs, resulting from the biological effects of released ions, have expanded their applications, including soft tissue repair, notably in the context of healing skin wounds, as exemplified by Mirragen™ from Avalon Medical in the USA [183, 224]. Intriguingly, the ionic dissolution products of BGs have been observed to enhance vascularization by stimulating the release of angiogenic growth factors from fibroblasts [27, 33, 222].

It is paramount to assess the concentration of released ions from biomaterials containing BGs before considering them as potential products for tissue regeneration [90, 174, 221, 222]. Multifunctional BGs and their composites are continuouscontinuously evolve insynthesis methods, and structural properties [173]. They aim to address the unmet requirements for the controlled release of therapeutic ions into the defect area to facilitate the tissue regeneration process. Chemical interactions bet particles and hydrogel matrix can be of marked significance for better controlling the composite properties [172, 224]. Enhancing BG particles with biopolymers like polydopamine and integrating these modified particles into hydrogels represents a promising approach for fine-tuning degradation behavior, mechanical strength, sustained ion release, and introducing additional functionalities to the system [174, 222, 225]. This can result in a material that elicits a desirable biological response [225].

Recent advancements in incorporating bioglass (BG) into hydrogels show significant potential to transform the landscape of regenerative medicine [33, 174]. When producing hydrogels that mimic tissue properties, controlling and optimizing several key factors is crucial [178, 179, 221]. Thvital include the kinetics of gelation, biodegradability, compatibility with the host tissue's mechanical properties, and the hydrogel formulation's cytocompatibility [30, 33]. The studies reviewed within the scope of this work consistently demonstrate that BG particles can enhance the stiffness of hydrogels and confer bioactivity to non-bioactive polymeric biomaterials by promoting the formation of apatite[30]. Furthermore, including BG particles can significantly influence the gelation mechanism of hydrogels. This influence arises from the silanol groups on the surface of BG particles and the release of divalent metal ions (e.g., Ca^{2+}, Cu^{2+}, and Sr^{2+}) from these particles, strengthening the crosslinking within the hydrogel networks[172]. The ionic dissolution products of BGs may lead to the time-dependent and dynamic crosslinking of alginate-based hydrogels, resulting in changes in the physicochemical properties of these gels over time and enhancing their biological capabilities [174]. Also, introducing BG particles imparts new functionalities to hydrogels, presenting a promising application[33]. The ionic dissolution products of BGs not only confer apatite-forming bioactivity to the materials but also promote angiogenesis and osteogenesis by activating relevant genes, such as ALP, VEGF, bFGF, bFGFR, and Col-I[172, 173, 183]. Achieving controlled release of ionic species from the BG phase is essential to elicit the desired cell responses and prevent the concentration of these ions from exceeding cytotoxic levels that could negatively impact mammalian cell viability, proliferation, and differentiation [90, 174, 221, 222]. Further, BGs are also suitable carriers for growth factors like BMPs and could modulate their release, or in synergy with TGF-β, EGF, or other medication such as DFO or RLX could remarkably promote tissue growth and wound healing [174, 221, 224].

Injectable hydrogels, especially thermal responsive hydrogel with sol-gel transition, exhibit poor mechanical properties, falling significantly short of load-bearing tissues [71, 81, 226]. Including BGs can improve the strength and elastic modulus of these hydrogels' strength and elastic modulus below the ideal mechanical properties for natural tissues [27, 30, 33, 174]. To address this challenge, scientists have explored the design of novel BGs doped with active metal ions like Cu, Sr, Ag, and Zn [222, 225]. These ions offer Therapeutic potential to achieve favorable biological outcomes tailored to specific host environments [27, 174]. Importantly, BGs can exhibit diverse functionalities based on their composition. Drawing inspiration from the peroxidase-like function of cerium oxide, researchers have explored co-synthesizing ceria with bioglass to control the enzymatic activity of hybrid nanoparticles [227, 228]. In another study by Ziqi Xu, the incorporation of gold nanoclusters into the BG network revealed a novel

function for BG: peroxidase-like catalytic activity[225]. Consequently, BGs with peroxidase-mimicking properties could offer more effective strategies for designing mussel-inspired hydrogels with injectability, adhesiveness, and enhanced bioactivity.

2.3 Pluronic derived thermal responsive hydrogel-forming materials

2.3.1 Introduction to Pluronic

Poloxamers are a class of nonionic triblock copolymers first introduced by BASF in 1973. These copolymers consist of a central hydrophobic chain made of poly(propylene oxide), often referred to as PPO, flanked by two hydrophilic chains composed of poly(ethylene oxide), commonly known as PEO. They are marketed under various trade names, including Pluronics and Synpernonics [54, 81, 84, 229].

Due to the customizable chain length of PEO and PPO, Poloxamers come in various types, allowing for different PEO and PPO unit ratios[94]. BASF markets these polymers under other names, which consist of a letter "P" followed by three digits. When multiplied by 100, the first two digits represent the molecular weight of the poly(propylene oxide) chain. In contrast, when multiplied by 10, the last digit indicates the percentage of poly(ethylene oxide) in the copolymer. For instance, P188 is a non-ionic triblock copolymer composed of a poly(propylene oxide) chain with a molecular weight of 1800 g/mol and 80% poly(ethylene oxide). Pluronics – another name for poloxame, has a distinct vocabulary: the initial letter signifies the physical state of the product (e.g., P for paste, L for liquid, F for flakes). The first digit (or the first two digits in three-digit names) represents the molecular weight of the poly(propylene oxide) chain multiplied by 300, and the final digit when multiplied by 10, designates the percentage of poly(ethylene oxide) in the copolymer.

Pluronics are considered biocompatible polymers because the PEO block repels opsonizing agents in the endothelial reticular system, allowing them to circulate in the bloodstream for an extended period, reaching their target tissues[56, 62, 84]. Additionally, they have a relatively small molecular mass compared to other polymers, making them more susceptible to filtration and elimination by the excretory system[230]. These qualities have led to the FDA's classification of certain hydrophilic Pluronics like F127, F68, F88, etc., as "Generally Recognized as Safe" (GRAS)[94]. This designation streamlines the FDA approval process for formulations containing Pluronics.

2.3.2 Pluronic F127

One of the best-known and widely used Poloxamer for making hydrogel is Pluronic F-127 (also known as PF-124 or Poloxamer 407), a linear triblock copolymer made up of a 12.500 g/mol poly(propylene oxide) and 70% of poly(ethylene oxide). Pluronic F127 has

received FDA approval for various applications, including oral, ophthalmic, and topical medicines[84]. Moreover, it is less toxic to patients than typical formulation components like cremophor or Tween 80. Also, Pluronic F127 forms the sol-gel transition following the temperature change, resulting in the potential to inspire novel ideas for clinical treatment and facilitate the advancement of innovative scaffolds for tissue regeneration[83, 84].

Extensive research has been conducted on the behavior of aqueous solutions containing Pluronic F-127. Notably, solutions of Pluronic F-127 with concentrations ranging from 20% to 30% remain liquid when refrigerated but form a gel at room temperature [54, 81]. The mechanism behind the gelation of Pluronic aqueous solutions has been thoroughly explored. Studies involving ultrasonic velocity measurements and dynamic light scattering (DLS) of Pluronic F127 solutions have indicated that gelation is primarily attributed to thermally induced changes in micellar properties, precisely the aggregation number and micellar symmetry [229]. Further investigations have suggested that gelation arises from micellar association and interactions[62]. A significant contribution to this understanding came from Chu et al., who delineated three distinct temperature regions within Pluronic aqueous solutions: unimer, transition, and micelle phases[92, 93].

Research has explored the micellization and gelation behaviors of Pluronic [95, 231]. Static and dynamic light-scattering measurements have shown that the gelation of PEO/PPO block copolymers is driven by the ordered packing of micelles [231]. In summary, gels formed in these systems are predominantly micellar. At lower temperatures, they exhibit a stable liquid micellar solution phase, while an increase in temperature induces a transition to a cubic micellar structure [81, 91, 95, 232]. Further temperature elevation results in hexagonally packed cylinders [94]. The Pluronic hydrogels exhibit considerable viscosity, partial rigidity, and persistence time due to the ordered micellar packing structure and intermicellar entanglements [92, 93, 231, 232]. The above properties are convenient for incorporating hydrophilic and hydrophobic drugs [84, 94, 135]. Moreover, some concentrated Pluronic aqueous solutions exist as a sol state at room temperature but form a gel at the physiological temperature [76, 90, 233-235]. Therefore, Pluronics are widely used in the injectable in situ forming drug-delivery matrices [81, 91, 95, 232].

2.3.3 Basic potential biomedical applications of Pluronic F127 hydrogel in tissue regeneration

In recent years, Pluronic hydrogels have found extensive utility in various applications, including drug and gene delivery, as well as the prevention of tissue adhesion and burn wound dressings[54, 56, 62, 84, 229]. Advances in gene delivery using Pluronic® have been discussed elsewhere. Pluronic® polymers are known for their bio-inert characteristics, attributed to their

PEO chains' hydrophilic and flexible nature. As a result, most cells do not adhere to these polymers, which have been employed as barriers to prevent tissue adhesion [95].

Based on the intrinsic feature of pluronic, Emilia Gioffredi et al. [232] proved that Pluronic F127 could be considered the best scaffold for cell-laden in 3D printing. Pluronic F127 hydrogel with a 25% w/v concentration was chosen as the bio-ink due to its rapid gelation at 37 °C within 5 minutes, favorable viscoelastic properties (G' = 16500 Pa at 37 °C), pseudoplastic behavior, and swift viscosity recovery following shearing taking only approximately 5 seconds. Using additive manufacturing techniques, scaffolds were produced in non-cellularized and cellularized forms (with Balb/3T3 fibroblasts). These scaffolds exhibited a 0°/90° pattern. The resulting printed scaffolds demonstrated uniform cell distribution along the filament structure, and cell viability was effectively preserved during printing. Along with Balb/3T3 fibroblasts, it has been observed that Pluronic® can serve as a suitable substrate for hematopoietic stem cells, providing support for their culture and preservation, surpassing the performance of conventional tissue culture dishes[91]. Recent reports have highlighted the use of Pluronic® F127 in tissue engineering applications. This particular polymer exhibits rapid gelation at 37 °C, achieving this state after just 1 minute of incubation in a 30% solution within the cell culture medium. Nonetheless, following the comment from the authors, F127 gels exhibited significant instability under culture conditions, showing signs of dissolution within a few minutes of incubation in the culture medium. As a result, it was impossible to carry out long-term in vitro studies to evaluate cell viability and proliferation under extended culture conditions. One notable application involved using F127 as a scaffold for lung tissue engineering, which yielded promising results regarding tissue growth with minimal inflammatory response [91]. Weinand and colleagues [90] conducted an *in vitro* study focusing on bone regeneration, in which a β-tricalcium phosphate (β-TCP) scaffold was used in conjunction with an F127 hydrogel to facilitate cell delivery and distribution. It was observed that after one week in culture, F127 was no longer present in the channels of the β-TCP scaffold, indicating possible degradation. At the same time, in bone tissue growth, the constructs displayed lower stiffness than other hydrogel composites like fibrin and collagen I.

Yu Liu et al. discovered that Pluronic F127 gel could be helpful as an injectable delivery hydrogel for peptides and proteins with short half-lives to prolong their therapeutic effect, increase their bioavailability, and improve the clinic outcome [89]. They demonstrated that the *in vitro* release of rHV2 from Pluronic® F127 gel follows zero-order kinetics and does not impact the antithrombotic activity of released rHV2. Subcutaneous injection of rHV2-loaded

PF127 gel in normal rats significantly prolonged the antithrombotic effect and plasma levels of rHV2.

The concept underpinning the use of thermoresponsive hydrogels in tissue engineering involves developing hydrogel-based Pluronic with stem cells and active components for the treatment site through injection [91, 92, 232]. The temperature-triggered gelation of Pluronic leads to the formation of a 3D construct at the injected site, and then live cells can differentiate and increase [90, 232]. For tissue engineering purposes, Pluronic-based polymeric scaffolds must replicate the structure and functions of the native extracellular matrix (ECM)[44, 45, 51]. Smart hydrogels have proven instrumental in cartilage tissue engineering, bone tissue engineering, and nucleus pulposus cell encapsulation. These matrices facilitate 3D cell culture, maintain nutrient and waste exchange, and efficiently fill tissue defects as they can be injected in a liquid state [76, 84, 229]. This unique feature enables minimally invasive surgical procedures for implant delivery. However, the application of hydrogel pluronic F127 is not considered. The main problems are the weak mechanical, high CGC value, quick erosion, and non-biodegradability [94, 232].

Addressing these limitations through modification is essential to enhance the performance and applicability of Pluronic-based materials in various fields [76, 81, 232]. Modifying Pluronic with polysaccharides through chemical integration or physical blending is a widely adopted approach to address those mentioned above [81, 89, 236-239]. Conversely, in specific scenarios, it may involve the modification of a polysaccharide with Pluronic [24, 61, 83, 101, 103, 119, 131, 182, 240]. Polysaccharides are often blended with Pluronic to impart thermo-responsiveness [81, 236-238]. However, for polysaccharides, water is a suitable solvent over the entire range of composition [92]. The Pluronic F127 has a hydrophilic/hydrophobic segment structure that is less soluble in water at increasing temperatures [94]. In addition, at low temperatures, the EO block presents a polar conformation that interacts with water; by increasing the temperature, the system entropy favors the polar structures, and the interaction with water is diminished [234, 241, 242]. The miscibility gaps can be found [76, 135]. Even for compatible polymers, preparing homogeneous mixtures with an arbitrary composition is seldom possible [62, 229]. Due to the region having two phases, the experimental conditions for the design of materials by using polysaccharide and pluronic mixtures require a careful examination [226, 243]. Therefore, for making injectable hydrogel, grafting strategy or crosslinking is the preferred method [81, 89-91, 95, 232, 236-239]. This method could solve the occurrence of heterogeneous zones in the blending techniques. The development of thermal responsive hydrogel via the incorporation of polysaccharide in pluronic F127 structure under the chemical strategy is outlined in table 2.2. This modification

enables the combination of Pluronic's thermoresponsive properties with the high biodegradability of natural polymers, thereby improving mechanical strength and swelling capacity [81, 236, 237]. However, it's worth noting that natural thermo-responsive polysaccharides typically exhibit an upper critical solution temperature (UCST), which can be less suitable for biomedical applications [54, 107, 112]. To render them injectable, they would need to be heated beyond their UCST, potentially compromising the viability and functionality of living cells [43, 88, 96]. Therefore, the ratios in the grafting techniques or crosslinking should be carefully controlled to obtain the suitable sol-gel condition as well as the stiffness of the matrix.

Table 2.2: *A comprehensive review of thermal responsive hydrogel-based pluronic F127 and polysaccharide: materials, synthesis method, key findings, and application.*

Material	Synthesis method	Key Findings	Potential application	Reference
Pluronic F127/Hyaluronic acid (HA)	Dopamine-modified pluronic (PDA) Cysteamine-modified HA (HA-DN)	- Temperature-induced sol-gel transition increases from 19°C to 29°C with the addition of HA-DA. No sol-gel transition if HA-DN > 10 wt% - Pluronic F127 hydrogel degraded after three days, while the addition of HA-DN prolonged the degradation time by up to 30 days - The injection of HA-DN/PDA into mice model was stable for 21 days, while the single components started to dissolve in 3 days	Wrinkle filler, tissue engineering, and drug deliver	[135]

Chitosan (CS) / pluornic F127	Dopamine-modified chitosan (CHI-C) Thiol-terminated Pluronic F-127 (Plu-SH)	- CHI-C forms hydrogel by itself at 1% and requires 48h to complete the crosslinking - CHI-C and Plu-SH required three h for reaction - The erosion of Plu and CHI-C was three days, and the introduction of crosslinking between Plu-SH and CHI-C was over 30 days. - CHI-C/Plu-SH hydrogel showed the improvement of adhesive feature in tissue	injectable drug delivery depots, tissue engineering hydrogels, tissue adhesives, and antibleeding materials	[238]
Poloxamer 407 (PF127)/carboxymethyl chitosan (CMCS)	poloxamer 407 (PF127) and carboxymethyl chitosan (CMCS) using glutaraldehyde as a cross-linking agent.	- Sol-gel transition temperature was nearly body temperature (32-37oC), controlled by the density of CMCS. - The gelation time was around 4.5-8 minutes - Tunable the rate of drug release based on the CMCS content, pluronic F127, and cross-linker	Drug delivery system for local administration	[239]
Chitosan grafted pluronic F127	Hydroxyl group on Pluronic F127 was activated with succinic anhydride, which was reacted with amine groups on chitosan, resulting in	- Gel formed at a concentration >16%, and the phage transition was at 25 °C - The swelling was maintained over ten days - At 20wt%, a storage modulus of about 40 kPa	Cartilage regeneration	[81]

	Chitosan-g-pluronic F127	was achieved, while single pluronic F127 could not. - Pore size ~ 10 μm, suitable for cell migration		
Hyaluronic acid grafted with Pluronic F127	Amine end-capped Pluronic F127 to carboxylic groups of HA using EDC/NHS coupling agents	- HA-g-Pluronic (68.7% Pluronic grafting percent) showed a sol-gel transition temperature similar to F127 at the same concentration. - The impact of the additives could be eliminated in the case of HA-g-Pluronic, while pluronic F127 could not. - HA-g-Pluronic hydrogels exhibited a better mechanical feature than either Pluronic F127 - HA-g-Pluronic hydrogels could maintain a robust gel structure for several weeks.	Cartilage regeneration	[23]
Alginate grafted pluronic F127 (AP)	Pluronic activated with 4-nitrophenyl chloroformate and then reacted with ethylenediamine to form monoamine-terminated PF127 (MATP) Alginate was activated with EDC/NHS and then reacted with MATP, resulting in	- 15wt% was sufficient for AP to exhibit sol-gel transition behavior, while 20 wt% was required for pluronic F127 or a mixture of pluronic F127/ alginate - The sol-gel transition temperature was 30 °C, while pluronic F127 or mixture pluronic F127/ alginate were at 23.7oC. - PF127 exhibited a fibrous structure, while AP showed	Skin regeneration	[237]

	Alginate-g-pluronic F127.	highly porous structures, with pores ranging 10–20 μm in diameter		
Pluronic F127-graft-Carboxymethyl Pullulan (PC)	Pluronic F127 was first activated with 4-nitrophenyl formate and then reacted with ethylenediamine, forming MATP. Carboxymethyl Pullulan was activated with 2-ethoxy-1-ethoxycarbonyl-1,2-dihydroquinoline to react efficiently with MATP at amino motifs.	- The CGC value of grafted copolymer was> 11%, whereas the gelation of poloxamer was not. - The gelation time was correctly adjusted with the participant of Carboxymethyl Pullulan. - PC hydrogel provided the sustained delivery of amoxicillin as compared to the native Pluronic F127	Drug delivery system for local administration	[236]

2.4 Alginate- A Versatile Material For Regenerative Medicine Applications

Sodium alginate is among the most abundant polysaccharides. This polysaccharide is obtained as the waste product after isolating mannitol and iodine from brown algae [102, 235, 244]. The structure of this polysaccharide is constructed from β-mannuronic acid (M) and α-guluronic acid (G) via (1 → 4) glycosidic bonds [242, 245]. However, the organization of these monomers is random; thus, the alginate structure is characterized by the length of segments such as GM, MM, and GG[246]. Because of the abundance of carboxylate groups and hydroxyl groups, the structure of alginate could be modified to make the derivative alginate with the best suitable mechanical feature as well as biological functions by selective crosslinking methods or by the grafting of other polymers [82, 96, 107, 113, 230]. Notably, alginate has the advantages of good biocompatibility, low cost, and mild gel formation conditions and is widely used in biomedical fields [246-251].

Various products based on alginate are already in the market, such as Gaviscon® (for acid reflux), Bisodol® (for heartburn), Algicell® (wound dressing), Comfeel® Plus (wound

dressing), NU-GEL™ (wound dressing), Purilon® gel (diabetic wound), Kaltostat® (wound dressing), Ocusert® (contact lens), etc. In addition, many applications of alginate as an agent for weight control and as temporary acellular scaffolds to mitigate adverse cardiac remodeling are now in clinical trials [102, 241, 242, 246, 249, 252]. Moreover, commercially available tissue engineering alginate products for 3D cell culture include AlgiMatrix from Invitrogen and NOVATACH peptide-coupled alginates from FMC Biopolymers. Along with commercial products and clinical trials, using alginate as a scaffold in tissue regeneration is very attractive [253]. A comprehensive summary of the developed alginate system in tissue regeneration can be found in Table 2.3.

Table 2.3*: Utilization of alginate in tissue regenerative techniques for various tissues/organs*

Alginate form	Cross-linker	Key finding	Potential application	Reference
Alginate bead	$CaCl_2$	- The shear modulus G increased by the increase of alginate concentration, from 5.9 kPa (1% alginate) to 11.4 kPa (2% alginate) - The differentiation of MC3T3-E1 cells was increased with the increase of shear modulus G	Bone	[254]
Hydrogel	$CaCl_2$	- The type of alginate adjusted the stiffness of alginate hydrogel. 2% alginate had E=44.4±3.21 kPa, while the alginate sulfate had E=2.4±0.57 kPa. - The viability of both types of hydrogel was similar - The chondrogenic phenotype was more pronounced on alginate sulfate hydrogels.	Cartilage	[255]
Hydrogel	$CaCl_2$	3% alginate solution with 1% $CaCl_2$ was formed 3D structure	Liver	[256]

		HepG2 laden hydrogel under bio-printing.		
Hydrogel / 3D printing	$CaCl_2$	- The viability of cornea cells was higher in a 0.6% (w/v) alginate than in a 1.2% (w/v) alginate - Increases in the size of internal pores in alginate gels correlate with increases in cell viability - The hybrid system based on alginate and hydroxyethyl cellulose resulted in a suitable compressive modulus for the cornea cells.	Corneal	[257]
Hydrogel/ 3D printing	$CaCl_2$	- 1.5% alginate and 75 mM $CaCl_2$ mixed with adipose-derived stromal vascular fraction (SVF) cells to form the cellular spheroids Via a direct-write bioprinting instrument - SVF cell population remains viable, and the spheroid integrity was maintained for 16 days in suspension culture	Vascular	[257]
Hydrogel	$CaCO_3$	- The stiffness of alginate scaffolds can be varied by tuning the alginate polymer concentration. - The viscoelastic property of the 2wt% alginate disk was matched to the nucleus pulposus.	Intervertebral disc	[258]

		- 2% alginate scaffold no longer matched the stiffness of the nucleus pulposus after 10 days due to the diffusion of calcium ion		
Hydrogel	calcium gluconate	- 1% (wt/vol) alginate and 0.3% (wt/vol) calcium gluconate formed the injectable hydrogel with a 29-gauge needle. - Alginate hydrogel improved left ventricular remodeling and function like neonatal cardiomyocyte transplantation.	Ventricular/ Heart	[259]
Alginate bead	$CaCl_2$	- The alginate hydrogel bead was formed with a final cell concentration of 5×10^6 cells ml^{-1}. - The alginate concentration of 2.2wt% was suitable for differentiating embryonic stem cells to astrocytes and neuronal lineage cells.	Central nervous system	[260]

Alginate facilitates the in situ formation of hydrogels through the cheating agents in mild conditions, including pH and temperature, enabling straightforward cell encapsulation and entrapment [241, 242, 246-248, 253-255, 261]. These hydrogels inherit the natural features of a soft material similar to the many native tissues [233, 242, 260]. Furthermore, the mechanical properties of alginate can be adjusted to cover a spectrum of stiffness representative of various tissues [262]. The mechanical characteristics of hydrogel-based alginate are well-known to depend on the M/G ratios and sequence [262, 263]. The GM block or MM acts as a flexible chain, while the GG block is a stiff chain [264]. Hence, the stiffness of the resulting hydrogel can be easily controlled by carefully selecting M/G ratios and sequences. By changing the alginate with difference M/G ratios or difference MG, MM, and

GG segments, the stiffness of hydrogel-based alginate can shift from 1 to 1000 kPa in terms of compression modulus and from 0.02 to 40 kPa in terms of shear modulus [242, 246, 256, 260, 261, 263, 264]. Further, the modified alginate by chemical reaction, the concentration of alginate, the density, and the type of the cross-liker can be used to modulate the mechanical feature of the resultant alginate hydrogel [263, 264].

Also, alginate benefits from incorporating thermo-responsive polymers to perform thermo-responsive systems [233, 234, 242]. As Lim et al. reported, the combination of alginate and Pluronic resulted in the in situ tissue regeneration scaffold [235]. The introduction of alginate into Pluronic hydrogel significantly improved cell viability, reaching up to 90% [233]. This obtained hydrogel demonstrated the gel's strength improvement due to the alginate concentration. Using 3% alginate, the resultant hydrogel showed an excellent microenvironment for encapsulating cells. Interestingly, the presence of alginate also played a role in controlling the mechanical properties of the Pluronic hydrogel system. However, due to blending techniques, the separation phase between alginate and Pluronic was reported as the main drawback of this system [242]. Similarly, the introduction of alginate as the backbone for PINIPAAM formed the great thermal responsive hydrogel for tissue engineering [265]. A study on swelling kinetics revealed that these hydrogels reached their equilibrium swollen state within 3 hours [88].

Therefore, alginate, through its hybridization with thermo-responsive polymers, emerges as a highly suitable candidate for hybrid thermo-responsive polymer systems. This synergy enables the development of customized bio-scaffolds with optimal gelation temperatures and concentrations, desirable elastic viscosity, and gel strengths.

CHAPTER 3: MATERIALS AND EXPERIMENTAL METHODS

3.1 Materials

3.1.1 Chemical agents

Table 3.1 presents all the information about the chemical agents used in the study, including the origin and the product's code.

Table 3.1: *List of used chemical agents.*

Order number	Chemicals' names	Origin	Note
1	Sodium Alginate	Sigma Aldrich	A2033, medium viscosity
2	Pluronic F127	Sigma Aldrich	F127, P2443
3	Cystamine dihydrochloride	Sigma Aldrich	C121509
4	Peroxidase from horseradish	Sigma Aldrich	HRP enzyme, P6782
5	Resveratrol	Sigma Aldrich	R5010, 99%
6	L-arginine	Sigma Aldrich	99%
7	4-Nitrophenyl chloroformate	Acros Organics	p-NPC,>98%
8	3-ethyl ethyl carbodiimidechloride	Acros Organics	EDC, >97%
9	3-amino-1-propanol	Acros Organics	≥98%
10	3-Hydroxytyramine hydrochloride	Acros Organics	DOPA, >99%
11	Hexadecyltrimethylammonium bromide	Acros Organics	CTAB, >99%
12	Ammonium hydroxide	Acros Organics	28-30 wt%
13	Hemin	Acros Organics	>98%

14	Tetraethyl orthosilicate	Acros Organics	TEOS, >98%
15	Triethyl phosphate	Acros Organics	TEP, 99%)
16	calcium nitrate tetrahydrate	Acros Organics	CaNT, >99%
17	Streptozotocin	Alfa Aesar	STZ, J61601, lot: X16G00
18	2,2-diphenyl-1-picryl-hydrazine-hydrate	TCI, Japan	DPPH, 99%

3.1.2 Others chemical reagents

All the organic solvents used during the synthesized reaction and characterization were HPLC grade and came from Fisher Chemical™. Ethanol and isopropyl alcohol (IPA) were provided from VN-CHEMSOL (Viet Nam). Repligen's Standard Grade Regenerated Cellulose (RC) membrane was used to purify the sample and in the release study.

3.1.3 Reagent for cell culture

The reagents used for in vitro cell assay were summarised in Table 3.2

Table 3.2: *List of used reagents in the cell studies.*

Order number	Chemicals' names	Origin	Note
1	Fibroblast cells, BJ	ATCC	ATCC® CRL-2522™
2	Mesenchymal stem cells, MSCs	Lonza company	
3	Macrophage cell line	ATCC	TIB-71, Raw 264.7 cells
4	Minimum essential medium	Gibco	MEM
5	Dulbecco's modified Eagle's media without the addition of arginine	Gibco	SILAC DMEM Flex Media
6	Dulbecco's modified Eagle's medium	ATCC	DMEM, ATCC
7	Fetal bovine serum	Gibco	FBS, non-US origin
8	Sodium bicarbonate	Sigma Aldrich	
9	Penicillin/streptomycin	Gibco	10,000 units/ml

10	Trypsin-EDTA	Gibco	0.25%
11	Phosphate buffer saline	Gibco	PBS, 1X
12	Lipopolysaccharides	Sigma Aldrich	LPS, from Escherichia coli O111:B4
13	Propidium iodide	Sigma Aldrich	PI, >99%
14	Acridine orange	Alfa Aesar	AO, >99%
15	Alizarin red S	Mackun	
16	Hoestch dye 33342	Invitrogen	
17	DAX-J2™ PON Green 99	AAT Bioquest	16316
18	SRB Assay Kit	Abcam	ab235935
19	MTT Assay Kit	Abcam	ab211091
20	Griess kit assay	Abcam	
21	Cytochrome c reduction assay	Abcam	ab65311
22	2,4,6-trinitrobenzene sulfonic acid or TNBS	Thermo Fisher Scientific	MFCD00064382
23	L-Name	Sigma Aldrich	

3.1.4 Reagent for anti-bacteria

The reagents used for the anti-bacteria assay are listed in Table 3.3

Table 3.3: *List of used reagents for bacteria test*

Order number	Chemicals' names	Origin	Note
1	*Escherichia coli*	ATCC873	
2	*Salmonella typhimurium*	ATCC 14028	
3	*Pseudomonas aeruginosa*	ATCC27853	
4	*Staphylococcus aureus*	ATCC 6538	
5	Methicillin-resistant Staphylococcus aureus – MRSA	ATCC 33592	
6	Agar	Himedia	
7	LB broth	Himedia	
8	Bacitracin disks	Merck	6 mm
9	Penicillin	Sigma Aldrich	

3.1.5 Animal study

The animals used in this study are listed in Table 3.4.

Table 3.4: *List of animals involved in this study.*

Number Order	Animal	Origin	Note
1	Rabbits	Viet Nam	New Zealand White, Male
2	Mice	National Institute of Drug Quality Control, Viet Nam	CD-1 ICR,Coat Color White – Albino

Viet Nam National University, Ho Chi Minh City, approved the animal ethical document, document number 579B/ KHTN-ACUCUS, signed on 30/06/2020.

3.2 Instruments for characterization

The types of equipment used in the study were at the Institute of Applied Materials Science (IAMS) and other national research institutions (Table 3.5)

Table 3.5: *List of used equipment*

Number Order	Equipments' name	Note	Location
1	Transmission electron microscopes	TEM, Jeol JEM-1400	Institute of Materials Sciences
2	Scanning electron microscope equipment with Energy dispersive spectrometry (EDS)	SEM, JSM IT-200 Jeol	
3	X-ray diffraction was performed with D8 Advance ECO	Bruker AXS, Germany	Institute Of Chemistry
4	UV–vis spectrophotometer	UV-1900, Shimadzu, Japan	IAMS
5	Fluoromax Plus C	Horiba-Japan	Institute Of Chemical Technology
6	High-performance liquid chromatography system	Thermal Scientific	IAMS

	equipment with mass spectrometer		
7	Microplate reader	HumaReader HS	IAMS
8	Material Testing Machine	5kN, Shimadzu, Japan	Rubber Research Institute of Vietnam
9	Dragonfly High-Speed Confocal Microscope Systems	Andor	IAMS
10	High-performance liquid chromatography, HPLC, with an evaporative light scattering detector ELSD	Agilent 1100	IAMS
11	Rheometer	- HAAKE 6000, Thermo Fisher Scientific, USA - TA DHR-3 Rheometer, USA	HCM VNU-UT and Thang Long Company
12	FT-IR spectrometer	Horiba, Japan	IAMS
13	NMR Spectrometer	1H-NMR, Brucker, 600HZ	Institute Of Chemistry
14	Nanopartica Series Instruments	Horiba SZ-100	IAMS
15	Ball Milling	Mill PM 100, Germany	IAMS
16	Dialysis tubing cellulose membrane	Biotech Regenerated Cellulose, Repligen, Massachusetts, USA	3.5kDa, 12-14kDa
17	pH Meter	The HI5221, Hanna Instruments, Germany	

3.3 Synthesis of polymer

3.3.1 Preparation of Pluronic precursor

3.3.1.1 Preparation of the mono-activated Pluronic, NPC-F127-OH

Pluronic F127 was melted at 70^{o}C under nitrogen conditions to remove water contamination. After that, a coupling agent (p-nitrophenyl chloroformate, pNPC) (the mol ratio between pluronic and P-NPC was 1:2.5) was added into the melt pluronic F127. The vacuum was connected to this system to increase the reaction yield (removing the by-product, hydrochloric

acid). After six h, the mixture was cooled to 40-45ºC before adding organic solvent (THF, ~30ml). The solution was then returned to room temperature and stirred overnight. 3-amino-1-propanol (the mol ratio with pluronic was 0.5) was drop-wised into the reaction to obtain the mono-activated pluronic F127, NPC-F127-OH. Cold diethyl ether was used to precipitate NPC-F127-OH. The washing step with cold diethyl ether was done at least three times to remove the excess p-NPC. The sign to recognize the final washing step was based on the color of the diethyl ether after adding sodium hydroxyl (1M). The remaining solvent was evaporated under a vacuum. The obtained product was then stored at 4ºC for further study and characterization.

3.3.1.2 Preparation of Pluronic-DOPA (PDA)

The pluronic-dopamine (PDA) derivative was synthesized with the help of p-NPC. Briefly, 20 g of Pluronic F-127 was dissolved in DCM dichloromethane (50 ml). 2.5 mol p-NPC equivalent to Pluronic F127 was prepared in DCM and then dropwised into the reaction. After 24h activation, 4.8 mmol DA was added and reacted for 12 h at room temperature. The DCM was removed by rotary evaporation under vacuum. The chloroform was added to precipitate the free DA. The supernatant was then dropped into the cold (−20 °C) diethyl ether. The precipitate was collected under vacuum filters. The washing step was repeated 4-5 times to remove the excess p-NPC in this reaction. Finally, rotary evaporation under vacuum was applied to obtain the main product, ADA.

3.3.2 Preparation of alginate precursor

3.3.2.1 Preparation of alginate-cystamine

At room temperature, sodium alginate (Na-alg) was dissolved in the mixture solvents (DMSO: water at volume ratio 1:1). The pH value of Na-alg dispersion was adjusted to 5.5 by HCl 1N before activating. 0.00046 mol EDC·HCl for 1 g sodium alginate was dissolved in water (1ml) and then dropped into the reaction. After 15 minutes, 0.00046 mol NHS (the amount for 1 gram of sodium alginate) was added and continued for 30 minutes at RT. 0.00046 mol Cystamine (Cys, the amount of Cys was calculated via the amount of EDC) was added, and the reaction was left for at least five hours. The reaction was then dropped into absolute alcohol. The product, alginate-cystamine (Na-alg-cys), was precipitated. The residue was re-dissolved into water before applying the dialysis method. MES buffer acted as the media for washing the precipitation. The dialysis solution was lyophilized, yielding alginate-cystamine.

3.3.2.2 Preparation of alginate-DOPA

Alginate-DOPA was performed by using the EDC coupling mechanism. Sodium alginate (1g) was dissolved into Mes buffer (pH 6.0, 50ml) before adding EDC (5.22 mmol). After 30 minutes, an equivalent DA to EDC was added to the reaction, and the stirring was maintained

for 3-4 hours. The reaction was then drop-wised into a mixture of solvent, ethanol/IPA (50:50) to collect the sediment. The precipitation was re-dissolved into deionized water following the precipitated step three times to remove excess EDC and DA. Finally, evaporation in the vacuum removed the remaining organic solvent from the precipitation. The obtained product (ADA) was stored at 4 °C for further study.

3.3.3 Preparation of alginate-cystamine –Pluronic

Na-alg-cys was dissolved in water at a fixed concentration (1g/10 ml). NPC-F127-OH was prepared in the cool water at a difference concentration of 5g/100ml and 7g/100ml. NPC-F127-OH solution was dropped into the prepared solution containing Na-alg-cys under stirring conditions at a cool temperature (4^{o}C) for at least five hours. Absolute ethanol was used to purify the product via the dialysis process with cellulose membrane (MWCO 12-14kDa) for the first 2 hours. Then, deionized water (DI) was used for three days before freeze-drying to obtain the ACP copolymer as a white solid.

3.3.4 Characterization technique for the resultant structure

The chemical structure of the products was verified using Fourier transform infrared spectroscopy, proton nuclear resonance, and UV-vis (UV-1900, Shimadzu, Japan). The density of amino groups on the alginate was determined by 2,4,6-trinitrobenzene sulfonic acid (TNBS, Thermo Fisher Scientific) using l-alanine as an internal standard. The substitution degree of DA on alginate or Pluronic was calculated using the monitoring absorbance at 280 nm.

3.4 Preparation of peroxidase mimicking bioglass

3.4.1 Preparation of HNP

Hemin (25mg) was dissolved into 50 ml methanol (HPLC grade, Fisher) following the sonication for 30 min and subsequently transferred to a hydrothermal autoclave reactor (100ml). This reactor was put into Vacuum Oven VOS-210C and heated at 150^{o}C for two hours. The reactor was cooled to room temperature in the oven before taking out. Evaporation was applied to remove the organic solvent. Water was used to dissolve the crude. The obtained products were filtered by 0.22 membrane (FINETECH). The HNP was obtained thrice after centrifugation at 20,000 rpm for 20 minutes.

3.4.2 Preparation of HNP BG

Bioactive glass nanoparticles composed of 64% SiO2–31% CaO–5% P_2O_5 (in mol %) were prepared using the sol-gel process with one-step fundamental catalysis. In brief, CTAB (0.05 M) was dissolved into ethanol and water in the volume ratio 70:30 after adding 5ml ammonium hydroxide. This mixture was stirred at a constant speed (450 rpm) at room temperature for at least 24 hours to allow the stability of the micelles. Next, 0.064 mol TEOS was added to this

mixture. After 30 minutes, 0.005 mol TEP was put into the reaction. 0.031 mol CaNT was dissolved into water and then dropped in. Next, the reaction was performed at 60ºC under vigorous stirring (~1000 rpm) for 48 h. Evaporation was used to form the gel. The obtained gel layer was put into Vacuum Oven VOS-210C at 120 ºC for 12 h to remove the water. The gel was then calcinated at 700 °C for ten h with a 5 °C/min heating rate and cooled down to room temperature with 5 °C/min. The obtained product was then washed with ethanol to remove calcium-rich areas and air-dried before performing the next step.

BG was uniformly dispersed in HNP solution following a 2 hours one-pot reaction in an autoclave at 150 °C. After cooling to RT, the solution was stirred vigorously for another 48 hours. The resulting precipitate (HNP BG) was collected by centrifugation at 10,000 rpm and washed with deionized water. The final product was freeze-dried for 24 hours and stored at room temperature for further use.

3.4.3 Structure characterization

Morphology was done using scanning electron microscopes (SEM, JSM IT-200 Jeol) equipment with energy dispersive spectrometry (EDS) to analyze the element distribution. X-ray diffraction was performed with D8 Advance ECO (Bruker AXS, Germany) to identify the crystallization of products. The UV–vis absorption spectra were recorded in a UV–vis spectrophotometer (UV-1900, Shimadzu, Japan). Fluorescence spectra were recorded by Fluoromax Plus C (Horiba, Japan).

3.5 Peroxidase-like activity test

3.5.1 Pyrogallol assay

Pyrogaollol was prepared with ultrapure water in an amber vial at the concentration of 30 mM for stock solution. Hydrogen peroxide concentration was fixed at 20 mM, which was selected based on the previous study. The stock concentration of HRP enzyme was 1mg/ml prepared in cold water and diluted into 40µg/ml before use. HNP and HNP BG were also prepared using ultrapure water at the design concentration. For the assay, 0.15 ml H2O2 in 3 ml ultrapure water was mixed with 0.3 ml pyrogallol in 4.0 ml quartz-cuvette and was equilibrated at 25 °C in the dark condition. Then 0.05 ml of HRP enzyme or peroxidase mimicking HRP (HNP, HNP BG) was added into cuvettes. The reaction was recorded with UV–vis spectrophotometer (UV-1900, Shimadzu, Japan). In the kinetic study, various concentrations of pyrogallol (0-3mM) were involved. The kinetic mode in UV-1900 was selected to measure the change in the absorbance at 420 nm for 5 minutes. The initial velocity was calculated using the UVProbe. The oxidative pyrogallol activity was determined by measuring the amount of Purpurogallin produced using an extinction coefficient of ε=2460 $M^{-1}.cm^{-1}$. The typical characterization of an enzymatic reaction is the Michaelis-Menten equation, which is V0=Vmax.[S]/([S]+Km).

The turnover number, kcat=Vmax/[E], can be calculated by the Lineweaver-Burk plot (1/ V0 as the y-axis and 1/[S] as the x-axis), which is independent of substrate and enzyme concentration.

3.5.2 Oxidative dopamine reaction

Dopamine (0.4 mM, DA) was prepared in ultrapure water. H_2O_2 (37%) was diluted to 30 mM. For the reaction, 0.5 ml DA was mixed with 0.1 ml H2O2 and then transferred to a cuvette containing 3.0 ml of an aqueous solution containing HNP BG or HRP enzyme. The spectrum of this reaction was measured from 250-700 nm during the 2700s. This oxidation reaction was analyzed with UHPLC ultimate 3000 – MSQ Plus.

3.6 Preparation of hydrogel

3.6.1 Preparation of hydrogel from alginate-cystamine-Pluronic

The ACP copolymer was dissolved in DI water with mild stirring at 10–15 °C. The obtained solution was then stabilized at four °C for 24 h

3.6.2 Preparation of dopamine crosslinking hydrogel

For native PDA hydrogel, a different concentration of PDA was prepared, starting from 20 wt% due to the recommendation of the pure Pluronic F127. All PDA aqueous was kept at 4 ^{C} until it was completely dissolved. The critical concentration for gelation was detected via the tube inversion method. If the solution in the vial cannot flow after inversion, it is classified as a gel.

For cross-linking of PDA by HNP BG, the PDA solution was mixed with HNP BG after adding H_2O_2. Similar to native PDA, the tube inversion was also used to identify the gel concentration of PDA induced by HNP BG.

For dual DA derivative hydrogel, the procedure was identical to that for the PDA hydrogel. Briefly, two solutions, PDA and ADA, were separately prepared. The mixture of PDA and ADA was stirred with a mild speed (~200 rpm) to ignore the bubble. Afterthought, HNP BG was added along with H_2O_2. The effect of ADA on the gelation of PDA was examined via the sol-gel transition under the tube inversion method at different temperatures.

3.7 Characterization of the morphology of the resultant hydrogels

The dry morphology was done by SEM. Briefly, the obtained hydrogels were lyophilized. The hydrogel at the dry stage was put on the conductive carbon adhesive tapes before coating with platinum.

Andor Confocal was involved in the examination of the wet morphology. The hydrogel at the solution stage was mixed with AO dye. The temperature was raised to 40 ºC for 30 minutes.

The washing step to remove the free dye was done at 40 ºC. Then, a confocal microscope was used to observe the specimen at 525nm.

3.8 Thermal responsive testing

3.8.1 Test tube inversion method

The CGC and GT values of the design materials were evaluated with the test tube inversion method via the flow of polymer solution in the tube at the tested temperature and concentration. In brief, the vial (2ml) was loaded with 1ml material solution. This vial was incubated at the design temperature using a water bath. After 10 minutes of equilibration, the vial was invested. If the solution in the vial could not flow to the bottom side within 60 seconds, it was recorded as gel and signed as sol.

3.8.2 Rheological analysis

Rheology was studied with Thermo HAAKE 6000 or TA Discovery HR 30. Both machines were measured with a cone and plate. A cone and plate geometry (40 mm, 2.0º cone plate, Peltier plate Stainless steel) was chosen. The minimum sample volume was 0.585 mL. The truncation gap was 50 µm while the trim gap offset was 20 µm. The oscillation temperature ramp was set up with a range of 5 ºC to 50 ºC (ramp rate: 2.5 ºC/min) or 20 ºC to 50 ºC (1ºC/min). The strain and angular frequency were fixed at 1% and ten rad/s. For the frequency sweep, the strain was set at 1%, and the temperature was at 37 ºC or 20 ºC. For the oscillation amplitude, the function of strain was measured from 0.1 to 200 % at 10 rad/s with a conditioning time of 180 seconds and 5 points per decade. The shear rate for the continuous flow sweep was from 0.1 to 200 (1/s) with 5 points per decade. For cyclic train time sweep, oscillation time sweep (200s) at 0.1% strain, 10 Hz, and then oscillation time sweep (200s) with high strain at 200% strain, 10 Hz. The cycle was repeated 6 times.

3.9 Water uptake and degradation test

The ACP copolymer was weight and was dissolved in different media such as DMEM, PBS 1×, and DI water (the concentration of copolymer was determined at gel concentration via inverted tube method). The mass of vials was recorded and labeled as W. A determined weight of ACP solution (Wi, 0.5ml) was loaded into the vial. The vial was placed in the water bath at a temperature of 37ºC for 30 min before adding 10 ml of DMEM or 1× PBS (these mediums were warmed at 37ºC). At the designed time points, the media was withdrawn, and the cotton paper was included to eliminate the excess water before weighting (Wf). The percentage of water uptake was calculated following the below formula (1):

$$Water\ uptake\ (\%) = 100\ x \frac{W_f - W_i}{W_i - W} \quad (1)$$

The degraded test dissolved ACP copolymer at CGC points (mi) in 0.5 ml media, 1× PBS, or DMEM. After forming the gel stage at 37°C, 10 ml of DMEM or 1× PBS was added. At the determined time points, the medium was withdrawn, and the hydrogel was collected and lyophilized before being weighted (m_t). The degraded level was estimated via the remaining mass percentage of ACP hydrogel following the below formula (2):

$$Remaining\ mass\ percentage = \frac{m_t}{m_i} \times 100\% \quad (2)$$

3.10 Drug encapsulation and in vitro release study

3.11 Drug encapsulation

The encapsulated process was performed using the ball milling method [266].

For resveratrol, resveratrol was mixed with 10 wt% ACP solution and then transferred to a ball milling machine (the ball size was 32mm, the speed was 450 rpm, the duration time was 30 minutes, and no on-off cycle was used). Then, the remaining ACP copolymer was added into the container to make 20wt% ACP in the final concentration. The centrifugation at 2000 rpm at 5oC was used to collect the resveratrol loading ACP hydrogel (R-ACP hydrogel). The pre-test about the loading capacity of hydrogel was done with 500 mg resveratrol. After the collected from the centrifugation, the dialysis in water using a dialysis bag (3.5 kDa) was included to remove the free resveratrol. The temperature was 40°C, and the time was 6 hours. The solution in the bag was collected and then freeze–dried. The obtained products were re-dissolved in isotonic saline. The HPLC was involved in determining the concentration of resveratrol in the hydrogel sample.

For L-arginine, L-arginine was suspended in an isotonic saline solution. The ACP copolymer (20 wt%) was added to this solution. To obtain a hydrogel, this solution was warmed up to 35oC. The identifying concentration of L-arginine was based on the change in pH solution on the DMEM media (using the pH meter) and the toxicity to fibroblasts (following section 3.12.1).

For the resveratrol and L-arginine system, donated AR-ACP hydrogel, resveratrol was first loaded into 10 wt% ACP solution. This prepared solution was transferred into a ball tank with a ball for milling. The determined concentration of L-arginine and the remaining ACP copolymer were added to the ball tank (the final concentration of ACP was 20 wt%). The ball process was similar to R-ACP hydrogel processing. The centrifugation at 2000 rpm, 5°C, was applied to remove the unloaded product and the ball. The resultant product was freeze-dried. The AR-ACP hydrogel was prepared by dissolving the AR-ACP lyophilized product in the isotonic saline.

3.11.1 Released test

The L-arginine and resveratrol were co-detected by using the HPLC method in combination with ELSD. The running program was based on C18 Phenomenex, 5.5 pore size as the stationary phase and the mixture of Acetonitrile and acid water as the mobile phase. The gradient program was applied following the increase of ACN from 0-5% in the first 5 minutes, from 5-70% in the next 7 minutes, and then increased up to 100% ACN in the final 3 minutes. For the release study, the single-loaded hydrogel or dual-loaded hydrogel was placed in the dialysis bag (3.5kDa, 1 ml gel) and then soaked in release media (PBS 1X, pH 7.4). To maintain the good tank condition, the volume of release media was 100 ml. At the determined time, 1 ml released media was withdrawn for analysis while 1 ml fresh media was added into the released vial. According to the standard curve, the concentration of L-arginine and Resveratrol were calculated. The kinetic drug release was recorded by KinetDS 3.0 open-source software.

3.12 Cell Cytotoxic test

The toxicity of the designed hydrogel on the viability of hMSCs cells was tested with 2 methods.

3.12.1 Cytotoxic test with 2D culture

The hydrogel was immersed in MEM media (ratio 1 to 5 in weight). The cell strainer (Biologix, 40μm) was used to collect the extract of hydrogel. The media in 96 well-containing cells (MSC cell, BJ cell, or Raw 264.7 cells) at the density of 1 x 10^3 cells/ml per well was replaced by the extracted solution. At the pre-determined time, an SRB assay was applied to estimate the viability of hMSCs following the manufacturer's guidance.

3.12.2 Cytotoxic test with 3D cell culture

In 3D culture, the materials for making hydrogel were dissolved in the culture media at the determined concentration. The hydrogels were cooled down before mixing with BJ cells or hMSCs cells (the density of 1 x 10^4 cells/ml). This solution was loaded into a 25G needle to transfer to the culture dish, which was heated at 37^{o}C. These culture dishes were incubated at 37^{o}C, 5%CO_2 and 90% humidity. The warm medium was added into each culture dish after 1h marinating. The staining step was applied at the determined time with Hoestch, AO and PI. The cell was then fixed with glutaraldehyde (3%) for 6h. The results were recorded with confocal microscopic at the multi fluorescent channels.

3.12.3 The function of cell-laden in hydrogel

Cell was loaded into hydrogel as the presence in section 3.12.2. The culture plate was placed on the hot plate (37 °C). The cell laden hydrogel was injected on this culture plate via 25 needle. The warm media was added. The plate was placed in the cell incubator. At the

determined time, the staining step was applied. The image was recorded with confocal microscopic at the multi fluorescent channels.

3.13 Anti-bacteria assay

The anti-bacterial was performed with inhibition zone experiments and suspension test via OD 600. The LB plate was coated with 10^6–10^7 colony-forming units (CFU)/ml bacteria for the inhibition zone experiments and incubated for 24h before testing. The tested samples (10ul) were loaded on the Bacitracin disks (6 mm) and then placed on the prepared plate. After 24 incubation at 37°C, the zone from the Bacitracin disks was measured. The positive control was penicillin, while the negative control was PBS 1X pH 7.4. For the suspension test, the viability of bacteria was measured using UV-vis at OD 600nm. Briefly, the LB agar plate was coating the hydrogel layer. These plates were incubated for 24h at 37°C. The agar plate was then collected and mixed with LB solution (0.1g agar/ 20ml LB solution). After 2 h incubating at 37°C, the optical density of the suspension was measured at OD 600 nm. The dead percentage was estimated following the ratio of the OD value of the tested sample to that of the negative control. The negative control was the plate without treatment. The positive control was penicillin. The concentration of penicillin was different between these bacteria trains. For example, *P. aeruginosa* and *S. aureus* were used with 50 ppm, while MRSA was used with 200 ppm. Each experiment was repeated five times.

3.14 Anti-oxidant test

3.14.1 DPPH assay

The concentration of DPPH used in this test was 0.5 mM prepared in methanol. The vial contained 0.3 mL of tested samples. All the samples were incubated at 37°C for at least 30 min before adding 4 mL DPPH. These vials were placed in the dark at 37°C. At each designed time point, the solution in the vial was collected and measured at 517 nm with the help of UV-Vis. The scavenging ability of the tested sample was calculated following the below equation (3):

$$\text{DPPH scavenging effect (\%)} = \frac{\text{ODblank} - \text{ODsample)}}{\text{ODblank}} \quad (3)$$

Where OD_{blank} was the absorbance of non-treated DPPH and OD_{sample} was the absorbance of tested sample. Each experiment was repeated five times.

3.14.2 Superoxide anion assay

This experiment used macrophage-like cells (Raw 264.7 cells) as the model. The culture condition has followed the guidance from ATCC with a bit of change. The culture media was free arginine to test the impact of these biological cues on the behavior of cells. The culture dishes were coated with tested material before seeding cells. The cell density used in this study

was $1x10^6$ cells/well. After allowing the cell to attack the surface, the completed prepared media, including 100 ng/mL of LPS, was added. The superoxide anion ($O^{2\bullet-}$) produced in Raw 264.7 cells was monitored by a cytochrome c reductase kit. The procedure has followed the protocol described in the previous report [30]. The concentration of superoxide was estimated with the reduced cytochrome c extinction coefficient at 550 nm (~28 per mM).

3.14.3 Monitoring the oxidative stress with BMSC cells

This experiment was done with BMSC cells. This cells was induced stress with 100mM H_2O_2 (10 µL/ 2 ml culture media) for 24 hours. Trypsin-EDTA was used to collect all cells. The stressed cells were then seeded on the surface of the tested sample (300 µL of hydrogel). The nitric oxide was measured via Griess kit assay. The culture media was collected and then incubated in this test with Griess kit assay. Sodium nitrite was used to build the standard curve. The amount of superoxide anion was estimated as similar to that described in section 3.14.2. To monitor the formation of peroxynitrite ($ONOO^-$), the cells were stained with DAX-J2™ PON Green 99. The signal of this dye was observed under a confocal microscope with Ex/Em = 480/525 nm. Together with DAX-J2™ PON Green 99, the Hoestch dye 33342 was used to mark the nuclei of BMSC cells.

3.15 Hemolysis assay

The blood compatibility feature of the tested hydrogel was estimated via the hemolysis assay. Briefly, the tested samples were prepared in DI water and then soaked in isotonic saline for 30 minutes. The whole blood collected from mice at the lateral tail vein (0.5ml) was added to each prepared test tube containing the tested sample. The centrifugation (2000 rpm, 5 minutes) was applied to collect the supernatant. The hemolysis of hemoglobin was estimated using the cyanmethemoglobin method. Triton X100 (10mM) was used as the positive control, while isotonic saline was used as the negative control. The hemolysis ratio was determined following the below equation (4):

$$\text{Hemolysis percentage (\%)} = \frac{\text{Hemoglobin in the test sample}}{\text{Total blood hemoglobin sample}} \quad (4)$$

Each experiment was repeated five times.

3.16 Biominimization assay

3.16.1 Biomineralization process in SBF

The hydrogel scaffolds were incubated in SBF to investigate the biomineralization process. Afterward, the remaining hydrogels were collected and lyophilized. SEM investigated the dry samples, and the chemical composition of mineralization products was characterized using EDS analysis during SEM observation. Also, X-ray diffraction (XRD) was performed in a 2θ

range of 10–80° with Cu K radiation to investigate the crystal profiles depositing on the surface of these hydrogels after soaking in SBF.

3.16.2 Osteoinductive assay

hMSCs cells were plated at a density of 1 x 10^4 cells/in 24-well plates. After 24 hours for adhesion, the cells received a completed MEM medium supplemented with hydrogel (10 mg/ml). Alizarin red assay was used to monitor the formation of calcium from the cells. Briefly, Glutaraldehyde (3 vol.%) was used to fix the cell after performing the washed step with 0.15 M PBS (pH 7.2). After fixation, the cells were washed with 0.15 M PBS (pH 7.4) and ultrapure water. Then, 1 mL of alizarin red dye (2%) was added, and the cells were incubated for 15 minutes at room temperature. The excess dye was removed, and the cells were washed with ultrapure water. After that, washing with 0.15 M PBS (pH 7.2) was performed for 15 minutes, followed by rapid washing with ultrapure water and drying at room temperature. Cells were observed under light microscopy.

The control sample was the hMSCs cell culturing in the normal MEM.

3.17 Animal study

The animal study was conducted at the University of Science, Nam National University, Ho Chi Minh City (diabetic mice), and Ho Chi Minh Medicine University (implanted test and skin irritation test). The growth condition obeyed the lab regulations.

Mice were fed a normal diet. For the diabetic mice, water with 5% glucose was supported in the morning (10 A.M. after measuring blood) and afternoon (6 P.M) along with tap water. For normal mice, tap water was only provided during the experiment.

For rabbits, the regular diet was applied. The tap water was supported all day.

3.17.1 Skin irritation test

The protocol was established with the guidance of ISO 10993-10:2010 (E). The hair on the back of rabbit was removed before taking the experiment about 2 days. The tested sample was placed on the rabbit skin. The behavior of skin after dressing was recorded by camera in 5 minutes, and from 1 hour to 10 hours. The irritation level was estimated based on the criteria describing in ISO 10993-10:2010 (E).

3.17.2 Toxicology studies

All mice (CD-1 ICR, Coat Color White – Albino, seven weeks old, 20 - 24 g) come from the National Institute of Drug Quality Control (Viet Nam) and kept in 12 hours of light and 12 hours of dark periods under pathogen-free conditions with adequate food and water.

Hydrogel at different doses (0.2 mL and 0.4 mL) was injected subcutaneously into the hind flank of mice. The skin at the injected site and the physical impairment of mice were tracked daily until the end of the study. At the determined time, the blood test was conducted. The white blood cells (WBC), including granulocytes, monocytes, and lymphocytes, were estimated with Mindray BA-88A (Mindray, China) with the respective kit test (ELITech, France). For C-reactive protein (CRP), CRP ELISA Kit (Mouse) was involved. The procedure followed the guidance of the manufacturer. After 7 days, histopathological analysis was performed using standard laboratory procedures. All mice skins were collected and fixed with 10% (v/v) formalin solution. Slices were stained with hematoxylin–eosin (HE) and examined by a pathologist using an optical microscope.

3.17.3 Establishing the diabetic mice model with STZ

STZ was used to induce diabetic mice. The mice in this experiment was male and had the weight of 30±0.5g. To identify the STZ dose for single intravenous administration, the range of STZ from 100mg/kg to 240 mg/kg was examined with survival analysis (via Kaplan-Meier (KM) model) and blood glucose concentration (Accu Chek Performa). The dose-induced mice with a blood glucose level > 250 mg/dL for over 14 days and >90% survived rate were selected for further study.

3.17.4 Establishing the burn wound model on diabetic mice

A heated metal rod (0.5 cm) made the wounds for the burn wound model. Briefly, ketamine (100 mg/ml) and xylazine (20 mg/ml) were mixed at a ratio of 1:1 in volume. The prepared anesthesia was injected in mice at 0.2 ml/100 g body weight. The mouse's hair on the back was eliminated. 1% polyvinylpyrrolidone iodine was applied to disinfect before applying the heated metal rod. The treatment was performed after 1 day. The tested sample was loaded in a 25G needle. The injection took place on the wound in a cool condition. The dose was 0.4 ml/ wound. The dressing was replaced for each 2 days.

3.17.5 Evaluation of wound healing process

The closure process of wound was recorded in each 2 days. The wound was measured with caliper. The wound closure was identified via the change in wound area before and after treatment. The wound area was estimated following the previous protocol [71, 72].

Histopathological studies were conducted with H&E, and Masson’s trichrome (MT). These studies were done in the Pathology Department- University of Medicine and Pharmacy at Ho Chi Minh City, Vietnam. Zeiss microscopy was used to observe these skin tissues. The re-epithelization was estimated based on the thickness of the epidermal layer with the help of the

AxioVision 3.0 program. The estimation of the collagen fraction was done using ImageJ software. The details of this protocol are presented in **Appendix M1**. Each experiment was repeated three times.

3.18 Data analysis

OrginPro2022B and Graph-Pad Primes 2021 were used to calculate and present the results. All data was collected from 3 replications. The significant difference was concluded if the p-value was lower than 0.05. The selection of the statistical test was detailed in the result section.

CHAPTER 4: CONSTRUCTION OF THERMAL RESPONSIVE HYDROGEL FROM ALGINATE AND PLURONIC VIA GRAFT TECHNIQUES FOR DIABETIC WOUND HEALING

4.1 Characterization of alginate-Pluronic copolymerization

Pluronic F127 was grafted on the alginate backbone via the cystamine bridge as presented in figure 4.1. Cystamine was first introduced on the alginate via the help of EDC/NHS, resulting in the amine functionlized alginate, Na-alg-cys. To graft pluronic on Na-alg-cys at the amino group, the hydroxyl terrminal group of pluronic was activated p-nitrophenyl carbonate, resulting in NPC-F127. The reaction between NPC-F127 and Na-alg-cys was taken place in water at RT condition. The chemical strucutre was analyzed with FT-IR, ^{1}H-NMR and UV-vis.

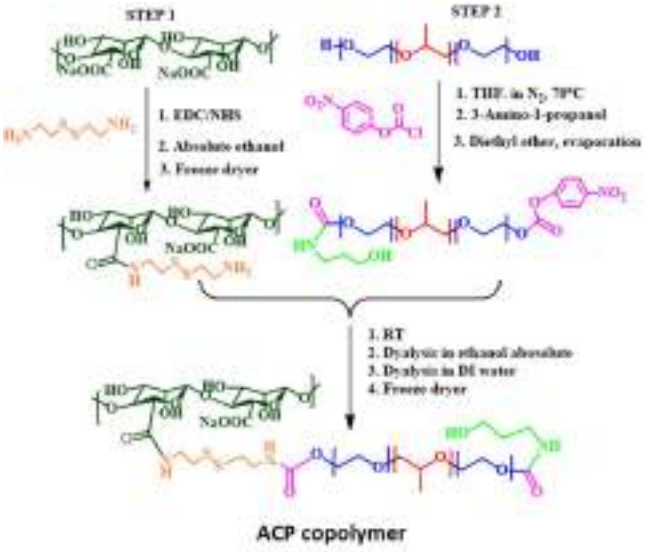

Figure 4.1: *The diagram for making the copolymer from alginate and pluronic F127 in this study.*

4.1.1 Characterization of the precursor alginate, alginate-cystamine

The change in the functional groups of alginate after modifying with cystamine was recorded by FT-IR technique, and the result was presented in Figure 4.2. The FT-IR spectrum of Na-Alg exposes a broad band centered at 3411 cm^{-1} corresponding to the presentation of hydroxyl groups (-OH), the low-intensity bands 2923 cm^{-1} attributing to the symmetric vibration of aliphatic (CH_2), peaks at 1619 cm^{-1} and 1412 cm^{-1} corresponding to symmetric and asymmetric stretching (-COO-), respectively[251]. In the range 1294–815cm^{-1}, some vibrations are assigned to ether functional groups (C-O-C) in glycosidic linkage[267]. The vibration peaks in 890-815 cm^{-1} belong to the C-C and C-O bond in mannuronic acid [250] while the exhibition of the pyranoid ring in guluronic acid is characterized at 1294cm^{-1}-1037cm^{-1} [251]. After

modification with cystamine, the major characterizations of Na-alg (O-H, C=O) are still presented in FT-IR spectra of Na-alg-cys (AC). However, the blue shift is observed for symmetric and asymmetric carboxyl groups compared to the pure Na-Alg, suggesting the interaction of amine groups on carboxylic groups [268]. The spectrum shows the additional peak with strong absorption at 2890 cm^{-1} assigned to the vibration of primary amine, along with a small signal of SH bonding at 2298-1960 cm^{-1}. Along with the shift of carboxylate mode, the FT-IR spectrum of Na-alg-cys is also established by the slight shift of guluronic acid and mannuronic acid. Notably, the anomeric peak of the fingerprint at 1700 cm^{-1} and 1243 cm^{-1} shows the characteristic absorption bands of N-C=O (amine I) and N-H bending vibrations, proposing the amidation of the carboxylic group of alginate molecules.[252] The success of aminated functional Na-alg was further confirmed via ^{1}H-NMR spectra in Figure 3. Both the characteristic proton peaks of Na-alg and cystamine are presented in the ^{1}H-NMR spectra. The spectra display the anomeric proton on the guluronic unit (H1-G) and mannuronic unit (H1-M) at δ =5.05ppm and δ = 4.45ppm [269, 270], respectively. These spectra also show the chemical shift corresponding to proton C-5 of the guluronic unit (H5-G, at δ= 4.37ppm) and mannuronic unit (H5-M, δ=4.20ppm)[245]. In addition, the spectrum exhibits these signals at δ= 3.1 ppm (Ha) and δ= 3.4 ppm (Hb) arising from the respective proton of -$CH_2C\mathbf{H}_2S$- and -$NHC\mathbf{H}_2CH_2S$-, which help to confirm the success of amine functional Na-alg step [249]. Throughout the TNBS assay, the coupled amine content is 54.70±0.36 mg/g of Na-alg-cys, yielding 78.04±2.31%.

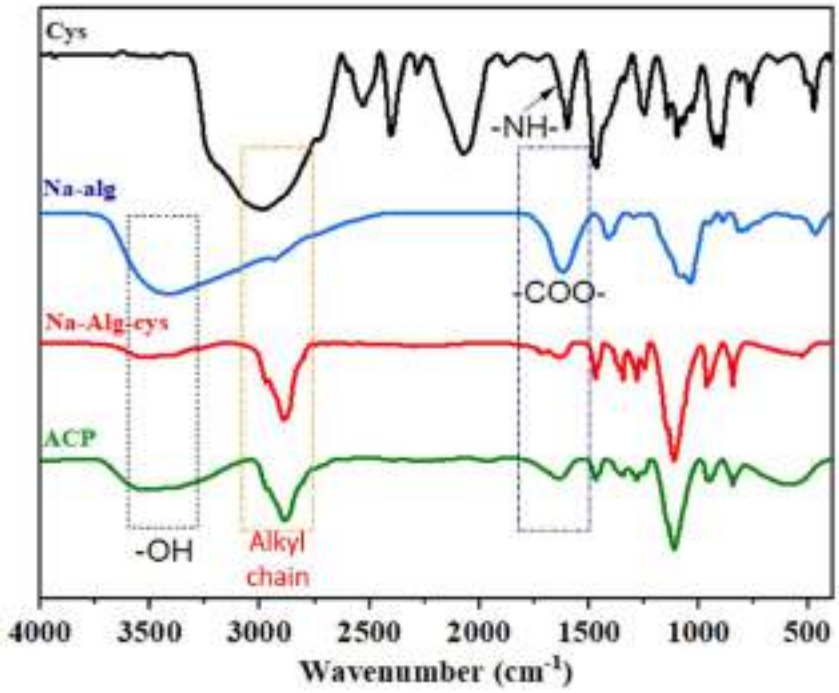

***Figure 4.2**: FT-IR spectra of pure cystamine, Na-alg, Na-alg-cys, and ACP copolymer.*

4.1.2 Characterization of the precursor Pluronic, Pluronic –NPC

The hydroxyl groups on the Pluronic F127 backbone were first activated with p-NPC, and its chemical characterization was presented in Figure 4.3A. This spectrum shows a chemical shift for the protons of the aromatic ring of p-NPC at δ = 7.41 ppm (H2) and δ = 8.29 ppm (H1). The proton signals of PPO blocks of Pluronic F127 are at δ =1.15 ppm (H4, methyl group(-C**H**$_3$)) and δ =3.41ppm (H3, methylene group (>C**H**$_2$), whereas the proton –C**H**$_2$ −CH_2– units of PEO blocks is at δ = 3.67 ppm. In addition, the chemical shift at δ = 4.44 ppm (H5) is assigned to the proton on the methylene group in the ester bond with p-NPC, C**H**$_2$-O-NPC. Also, the peak at δ = 4.22ppm corresponds to methylene protons of C**H**$_2$−CH_2–O-Ami moiety, confirming the success of the second route.

4.1.3 Characterization of alginate-Pluronic copolymerization

Alginate-pluronic (ACP) was formed by conjugating NPC-activated F127 onto the Na-alg-cys. The successful synthesis of ACP was also confirmed by FT-IR (fig 4.2) and ^{1}H-NMR spectra (fig 4.3). ACP copolymer exposes all typical characteristic peaks in the FT-IR spectrum of Na-alg-cys. The introduction of Pluronic on the Na-alg-cys backbone induces the changing intensity of the stretching of ester groups (C=O) and hydroxyl groups (OH). The proof of the covalent chemical bond between Pluronic and Na-alg-cys is the presence of the deformation vibrations of NH bonds and stretching vibrations of CN in the FT-IR spectrum of ACP copolymer. ^{1}H-NMR was used to confirm this result further. As shown in Figure 4.3, along with the anomeric proton signals of Na-alg, this spectrum shows the chemical shifts corresponding to the proton of Pluronic F127. The peak at δ = 1.03 ppm gives evidence of methyl group (-C**H**$_3$) in the PPO block of F127, whereas the peak at δ = 3.70 ppm is corresponding to (–C**H**$_2$ −CH_2–) units of PEO blocks of F127. It can also discern the shift of methylene proton (-C**H**$_2$) in this spectrum, although the intensity of this proton is reduced. The proton signal of methylene in (NHC**H**$_2$-) has disappeared in this spectrum because the characteristic signal for methyl groups on the PPO block is at the same position, δ = 3.40 ppm. These results revealed the formation of ACP. Regarding the remaining amine content calculated by TNBS assay, the activated Pluronic grafting reaction efficiency was about 44.47 ± 0.74%.

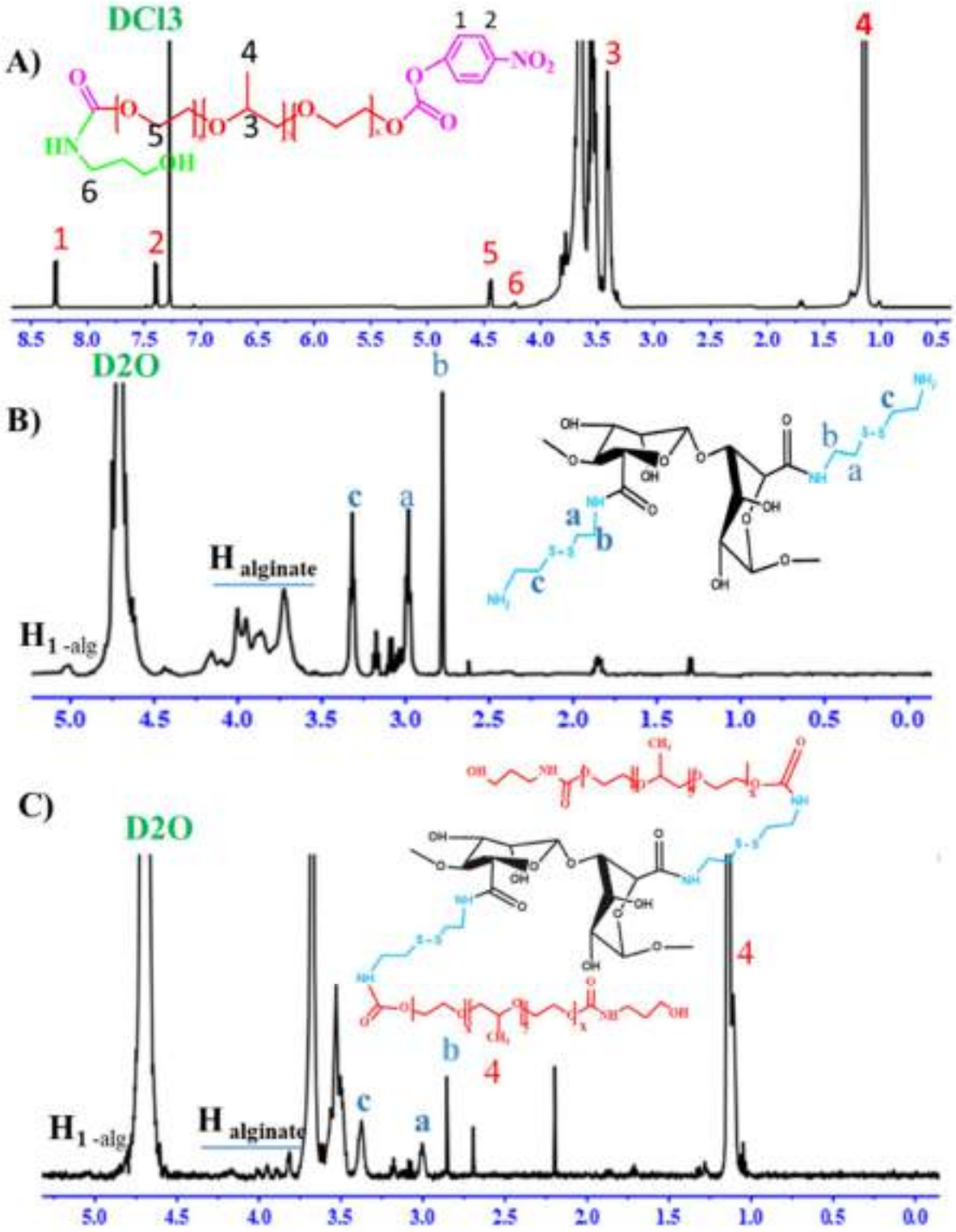

Figure 4.3: *^{1}H-NMR (in DCl_3, 500MHZ) spectrum of A) activated Pluronic F127 and ^{1}H NMR (in D_2O, 500MHZ) characterization of B) Na-Alg-cys and C) ACP copolymer.*

4.2 Preparation of the thermal sensitive hydrogel from alginate-Pluronic copolymerization

4.2.1 The effect of alginate on the thermal sensitive property of the resultant hydrogel

Cohesive energy density is a term in rheology to measure the strength of the internal structure of a material [271, 272]. For hydrogel, this term refers to a measure of the material's elastic strength[272]. This property is associated with the interaction energy between hydrophobic components. Generally, a stronger interaction energy corresponds to a higher level of structural stability. Therefore, the cohesive energy of the grafted copolymer was exploited and compared to pure Pluronic F127 at 20 wt%. As shown in Table 4.1, the cohesive energy of Pluronic F127 was improved after grafting to the alginate backbone. The cohesive energy density of the Pluronic F127 solution (20 wt%) at 35 ^{o}C was 28.8 Pa. After grafting on the alginate backbone (APC with Pluronic accounting for 87.5 % by mass), the cohesive energy was 1655 times improved. It is known that higher cohesive energy density can result from the existence of strong intermolecular interactions[272]. In other words, combining alginate into Pluronic networks could improve the strength of the internal structure. However, when the feed ratio of alginate increased (APC with Pluronic accounting for 83.33% by mass), the cohesive energy density was reduced. It was 158.84 Pa, about 300 times reduction compared to APC from 87.5% Pluronic. This property is associated with the interaction energy between hydrophobic components. Generally, a stronger interaction energy corresponds to a higher level of structural stability. [243, 273].

Table 4.1: *The cohesive energy of tested materials*

Sample 20 wt%	**Cohesive energy at 35^{o}C**
Pure Pluronic F127	28.8 Pa
APC with Pluronic accounting for 87.5% by mass	47 652 Pa
APC with Pluronic accounting for 83.33% by mass	158.84 Pa

The effect of grafting ratio on the sol-gel transition of ACP copolymer was determined by amplitude oscillation sweep, and the results are illustrated in Fig. 4.4. The linear viscoelastic region (LVR) or the region where both moduli and phase angle are independent of applied strains are examined to know the structure of solution at specific temperature. At LVR, G' and G'' are constant and are used presentation for un-disturbed structure[274]. When both moduli tend to decrease, the structure of the sample is disturbed[275]. In other words, the behavior of modulus in LVR gives the information about the structure. The domination of G' suggests the gel-like structure. However, if G" is dominated, the sample is classified as liquid[243]. Due to the purpose of hydrogel for tissue regeneration, the gel stage was required at a temperature

range of 30-37 ºC and liquid at a cool temperature[56, 71, 80, 81]. It was found that viscoelastic parameters are mainly determined by the content of Pluronic F127 in grafting samples. When the feed content of Pluronic F127 is at 83.33%, the LVE region exists at incredibly low shear strain, under 2% for 45 ºC and 4% for 35 ºC. Also, it was observed that ACP copolymer solution at this ratio showed viscoelastic liquid behavior at 35 ºC, suggesting that this solution could not form a gel stage at a temperature below 37 °C even though its copolymer concentration was up to 20 wt% as seen in Fig. 4.4A. A marginal shift in the LVE region was observed when the mass fraction of Pluronic F127 increased to 87.5%. The LVE region was 3.8% at 35ºC and 8.4% at 10ºC. In addition, with 87.5% Pluronic F127 in the grafting reaction, the values of the loss modulus G' were more significant than the value of store modulus G' at 35, confirming that at the beginning of the test, the superstructure formed a consistent, three-dimensional network[243]. These results agreed with cohesive energy density. To better understand the effect of alginate, the critical gel concentration of pure Pluronic F127 was determined. As shown in Appendix A1, the sol-gel transition of Pluronic F127 at 20 wt% was at 20.01ºC. Incorporating alginate, this gel critical temperature (GCT) was shifted to the higher point. For example, with ACP from 83.33% Pluronic, the GCT was at 44.89ºC while ACP from 87.5% Pluronic set up their GCT at 35.1 ºC. The GCT values were depended on the amount of Pluronic F127. It is evident that with an increase in the concentration of alginate, the system becomes more hydrophilic due to the nature of alginate[72, 86]. The higher amount of alginate increases the density of hydrogen bonds with water molecules and then increases the enthalpy of dehydration[24, 233, 234]. The presence of alginate hinders both the initial structural rearrangement of micelles and the subsequent caging to form a packed, ordered gel structure[233, 234] and, consequently, increases the gelation of the temperature. Because only ACP with 87.7% of Pluronic expressed the gel within the range 30-37ºC, this grafted copolymer was used for further study.

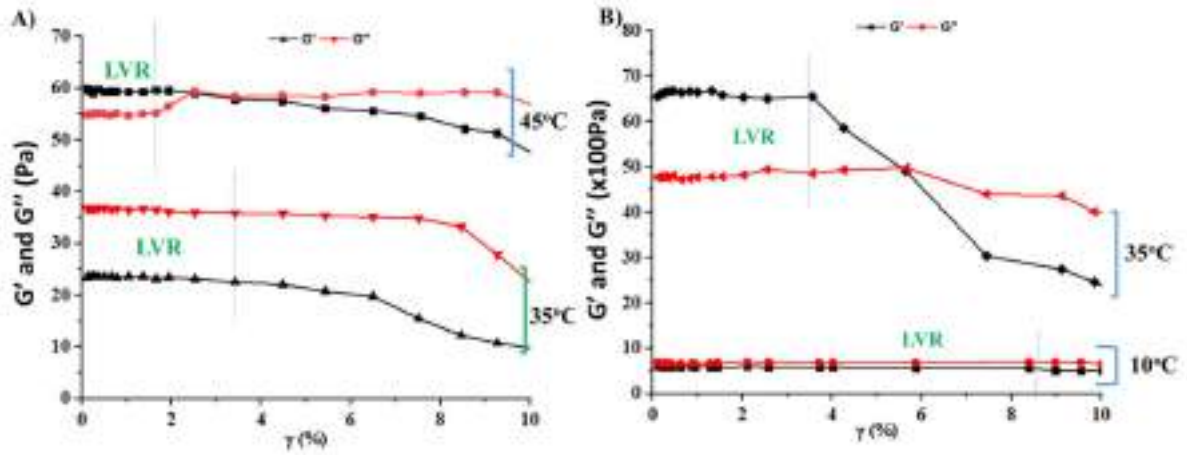

Figure 4.4: *The viscoelastic parameters of two ACP copolymers (20 wt%) at different Pluronic contents.*

A) 83.33 % and B) 87.5 %, as a function of strain amplitude at a fixed angular frequency of 1.0 rad/s in different temperature conditions.

4.2.2 The effect of copolymer concentration on the thermal sensitive property of the resultant hydrogel

The effect of the copolymer concentration on the thermal behavior of the resultant hydrogel through a sol-gel transition was tested and displayed in Figure 4.5. The Tgel was identified with the temperature sweep [276], and the results were presented in Figure 4.5. All the tested ACP concentration ranges showed the crossing-over between G' and G'', confirming the transition of the sol-gel structure.

The sol-gel transition of the ACP copolymer solution was strongly dependent on the concentration of ACP. When the copolymer concentration increased from 13% (wt/wt) to 20% (wt/wt), the temperature-induced Tgel is reduced. Specifically, at 13% (wt/wt), the crossing point is at 41.2 ^{o}C, while it is reduced to 35.1 ^{o}C at 20% (wt/wt). Moreover, the maximum value of G′ followed the order of concentrations, which is attributed to the decrease of copolymer ACP flexibility at higher concentrations[233, 234]. Increasing ACP concentration leads to a higher density of hydrophobic interaction, thus resulting in a higher capacity to build the microstructure. Furthermore, Pluronic's behavior in response to the change in temperature induces the folding of the alginate backbone, creating a more hydrophobic zone[241, 242]. Similar to the jamming-induced gelation in pure Pluronic systems, the thermal gelation in the ACP system could be due to the packing of micelles within the alginate folding pocket[241]. Subsequently, it potentially stores the deformation energy and reduces the isotropic gel[275]. Therefore, the higher concentration of ACP required lower heat energy to introduce the aggregation of ACP, consequently achieving lower Tgel.

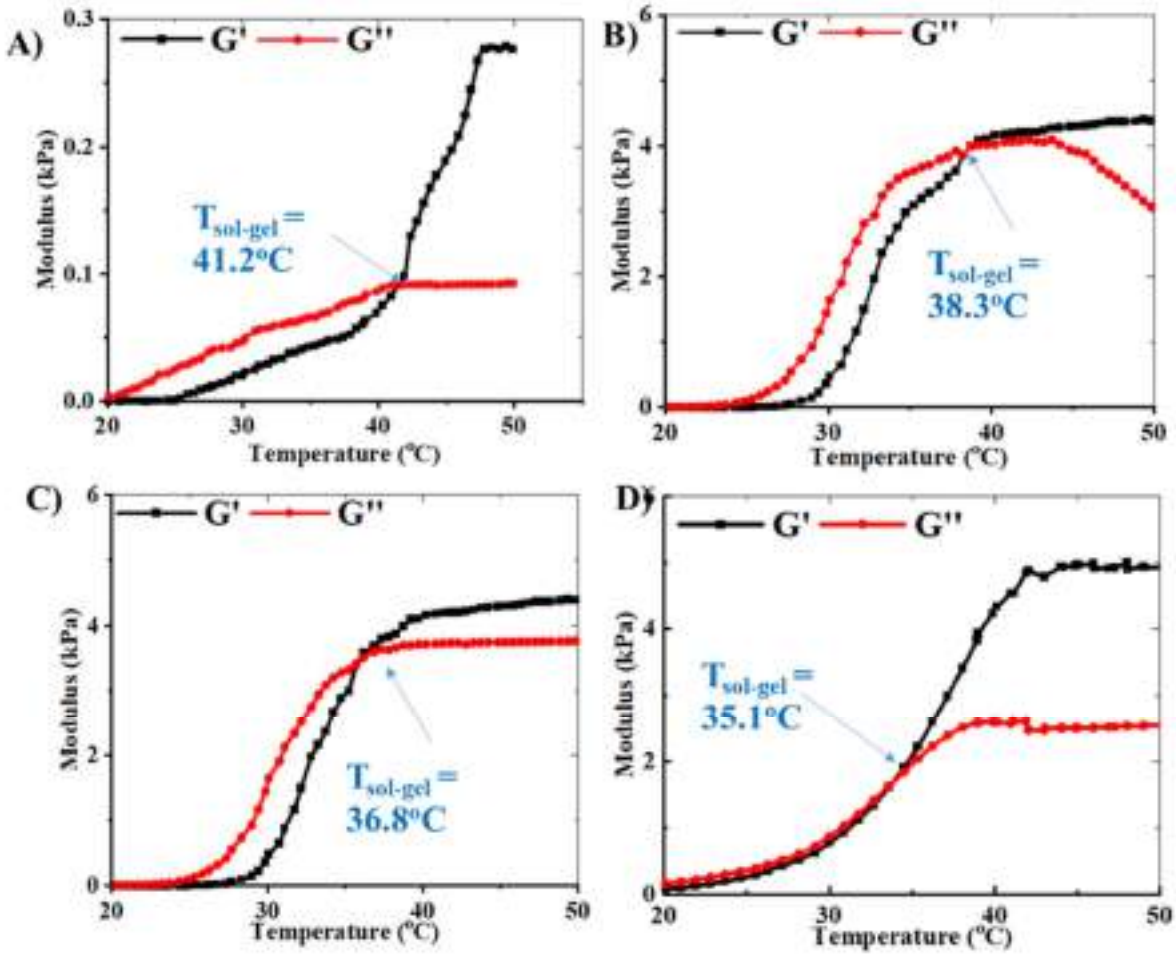

Figure 4.5: *Evolution of the dynamic moduli in temperature sweep experiment of ACP with various concentrations. A) 13 wt%, B) 15 wt%, C) 17 wt% and D) 20 wt%.*

4.2.3 The influence of the physiological solvent on the sol-gel transition of hydrogel

Next, besides the influence of concentration on Tgel, the effect of the aqueous media dissolved ACP copolymer on sol-gel transition temperature was investigated. As shown in Figure 4.6A, at 20 wt% of the copolymer, ACP dissolved in DI water, PBS buffer, or DMEM media undergoes the sol-gel transition in response to the heating condition. Regarding inverted tube methods, there is a non-remarkable difference in the gelation temperature (GT) range of ACP solutions preparing in different mediums (Fig 4.6B). ACP solution (20 wt%) in all tested media appears to be in the gel state at 25°C and complete gel development (G′ over G'' in oscillation rheology) is achieved above 30°C. In terms of rheology, the solvent causes small variations in Tgel values of ACP (Fig 4.6C). ACP dispersed in DI water (20 wt%) undergoes the sol-gel transition at 35.1°C during heating. However, when physiological buffer (PBS 7.4) or culture medium (DMEM) was used to prepare ACP hydrogel (20 wt%), the gelation occurs at a lower temperature as compared to DI water. This may be due to the interaction of Na-alg with ions

in the medium[102, 249, 265, 268]. When ACP polymer is dissolved in this solvent, the cationic ions diffuse into ACP networks and form the ionic inter-chain bridges[234]. Therefore, the lower Tgel induced by medium can be explained by the synergistic effect between the Pluronic copolymers and sodium alginate chains. Due to cationic agents in buffer media, the water surrounding the Pluronic chain may be reduced with the increase of temperature[231], the PPO segments become more hydrophobic and less polar[93], providing a platform for promoting gelation. In the range of concentration and all solvent tested, ACP hydrogel (20%) could be a suitable scaffold for cell encapsulation processes, specialized application in soft tissue such as wound healing.

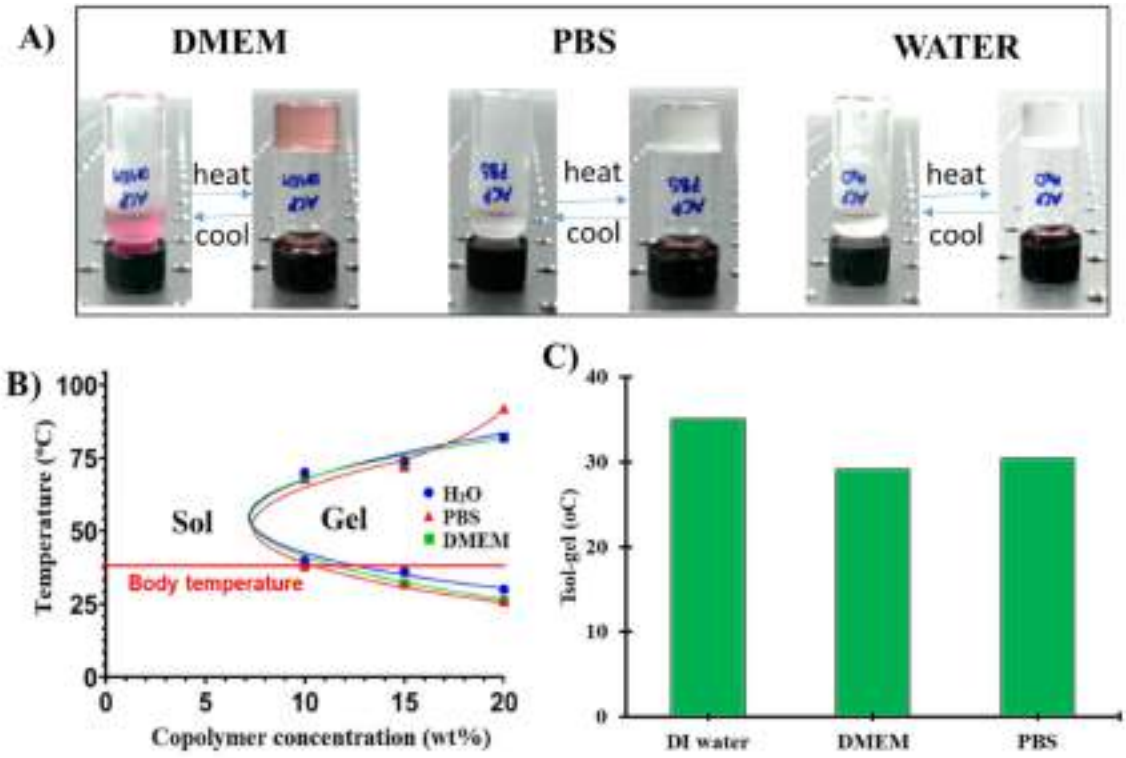

***Figure 4.6**: Thermal responsive via the sol-gel transition of ACP copolymer solution in different solvents (DI water, DMEM, and PBS).*

A) Optical images of inverted glass vials containing ACP copolymer solutions below 20 ºC and above 30 ºC. The sol-gel transition temperature diagram of the ACP hydrogels prepared in different solvents measuring by B) inverted tube method and C) temperature sweep experiment.

4.3 The bio-adhesive property of ACP copolymer

In tissue engineering, hydrogels with adhesive property to the adjacent tissue can avoid detachment of biomaterial from target tissues *in vivo* and eventually promote the potential

biointegration[112, 229, 277]. Herein, we evaluated the adhesive property of ACP with porcine skin. Figure 4.7 indicates that the adhesive strength of ACP hydrogel to porcine tissues significantly increased as amine functionalization Na-alginate increased from 0 to 12.5% (labeled as ACP1, ACP2, and ACP3). The adhesion force for pure Pluronic gel (20 wt%) is eminently fairly, about 0.70 ± 0.16 kPa, but in good agreement with literature reports [135]. The adhesion force increases 233 % (1.63 ± 0.17 kPa) when amine-functionalized alginate cooperating with Pluronic F127 is 5% (ACP3). It is known that alginate alone does not promote cell adhesion because it lacks cell adhesion components[106]. Increasing the feeding AC in ACP copolymer from 5% (ACP3) to 12.5% (ACP1) significantly increased the adhesive strength of ACP hydrogel to 396%, evidencing the critical role of amine functional groups on alginate in tissue adhesion properties.

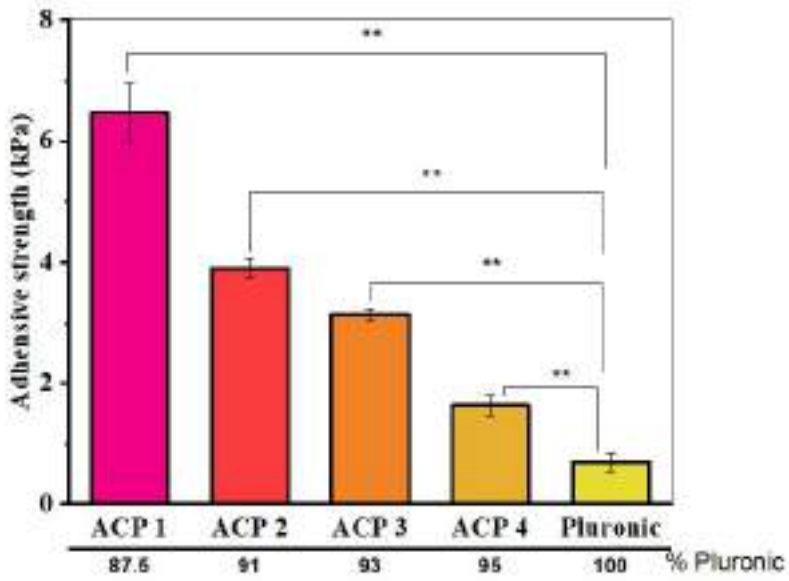

Figure 4.7: *The adhesive strength of ACP hydrogel with various grafted Pluronic F127 (from 87.5% to 100%) to porcine tissue.*

*All tested sample is 20 wt%. The lap-shear adhesion tests at 37oC were repeated three times. **p < 0.05.*

4.4 Morphology of the hydrogel

The morphology of ACP hydrogel was visualized by SEM for dry ACP hydrogel and confocal microscopy for wet hydrogel. ACP hydrogel has a good manifestation of three-dimensional interconnected microstructure in both methods as presented in Figure 4.7A, B. In addition, ACP hydrogel possesses homogeneously distributed pores with a size in the range of 30-80

μm, suggesting that ACP hydrogel may be suitable for cell delivery in tissue engineering[44, 45].

4.5 Swelling and degradation of hydrogel

Along with the required microstructure of hydrogel, the degree and rate of swelling are some of the most critical parameters that affect the release rate of solvents and drugs from polymeric hydrogel networks[44, 46, 55, 57, 75, 80, 113]. Swelling studies were performed in physiological buffer PBS 1X and DMEM. Because the pH of both media was 7.4, the remaining carboxylic groups on the Alg backbone turned to ionize, leading to the increase of repulsion between the carboxylate group [102, 244]; consequently, ACP began to swell at the initial immersed stage. As shown in Figure 4.8C, ACP hydrogel swelled quickly after immersion in both media. Interestingly, the disintegration process did not occur after reaching the maximum point. From the 2^{nd} to the 6^{th} day, ACP hydrogel possessed a high resistance to dissolute. The amount of the uptake water was around 200%, indicating the equilibrium swelling process. Presumably, the ionization of Na-alg may interact with cationic ions in an immersed medium, resulting in the equilibrium in osmotic pressure, thereby controlling the driving force for the penetration of water molecules[248]. However, from the 7^{th} day, the water content in ACP hydrogel decreased in both immersed mediums. This effect is likely resulting from the fact that the density of hydrogen bonds with water molecules within the ACP hydrogel network was exhausted, and the 3D microstructure became damaged [88, 96, 106, 107]. Also, the degradation course of ACP hydrogel in both immersion media was identical (Fig. 4.8D), which agreed with the water uptake ability of ACP in both media. The mass of lyophilized ACP copolymer had been maintained over 7 days (all $p_{values} > 0.1$). The degradation of ACP hydrogel in both media was started on day 8. In PBS media, about 31% of the initial weight of ACP hydrogel was lost, while 28% of ACP hydrogel mass was lost in DMEM. There is a non-remarkable difference in the degradation rate of ACP hydrogels in DMEM or PBS, about 11% per day. After 12 days of immersing in PBS or DMEM solution, the ACP hydrogel could not be recovered, confirming the complete degradation course of ACP hydrogel.

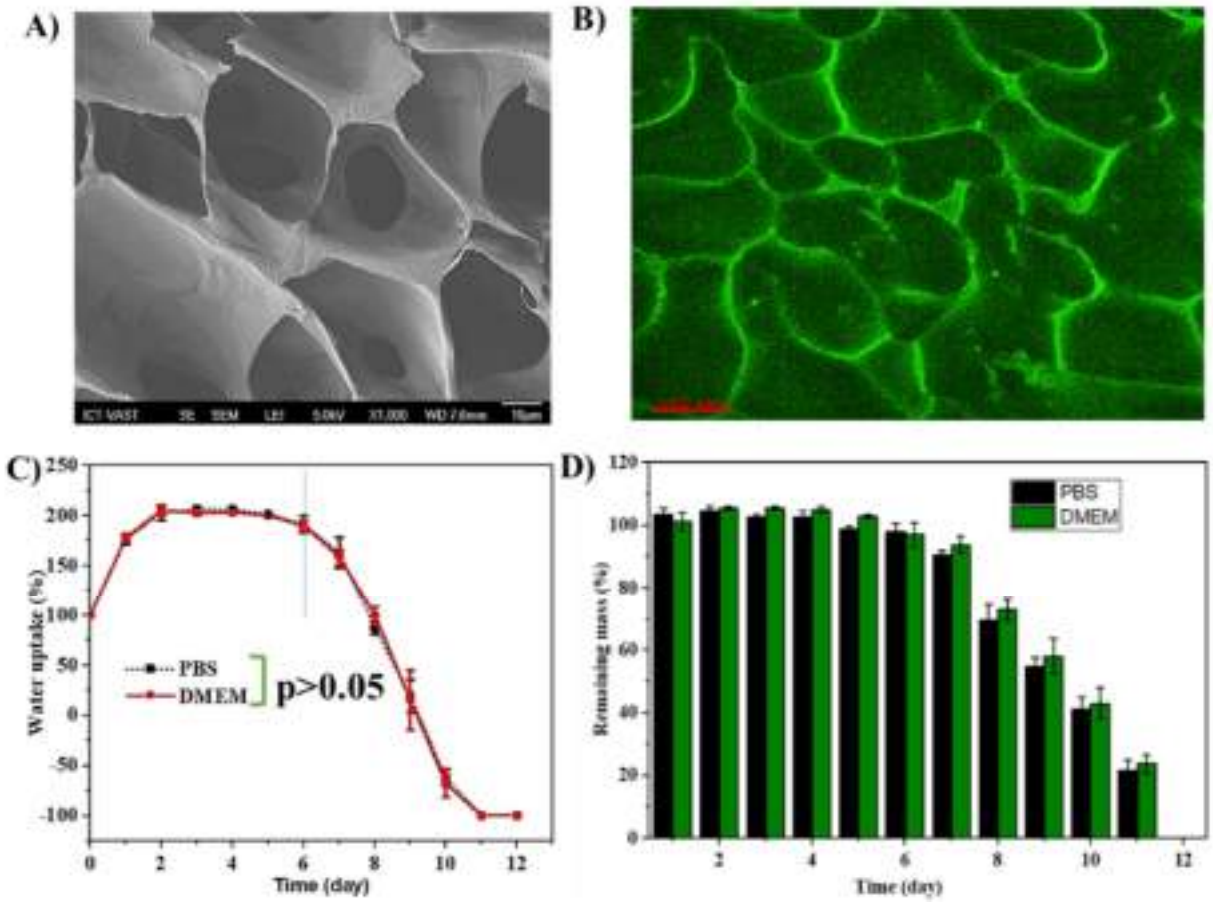

Figure 4.8: *Characterisation of the ACP hydrogel (20 wt%).*

Morphology was observed by A) SEM at the dry stage and B) by confocal for the wet stage. B) The water uptake capacity was measured via the change in the mass of hydrogel before and after immersing in PBS and DMEM. D) The degradation of hydrogel in PBS and DMEM was estimated via the remaining mass

4.6 The cytotoxicity of the resultant hydrogel

Cell vitality is important to conclude whether the material could be applied in tissue engineering and regeneration [46, 47, 55, 86, 229]. Human fibroblast cells were used to evaluate the toxicity profile of the fabricated hydrogel. Culture dishes coated with 0.1% Gelatin were served as the control. Non-significant toxicity effects on BJ cells were observed for both ACP hydrogel and 0.1% gelatin, and above 90% cell viability was achieved, as shown in Figure 4.9A-B. A negative toxicity effect of the ACP coating dish was also proven via live/dead staining. In both coating cases, the green nucleated cells (live cells) due to the presentation of AO are more pronounced while a very small number of cells are dyed with red color (dead) (Fig 4.9C). Fibroblast cells culturing on ACP proliferates quickly that is similar to that on the

gelatin-coating dish (p>0.1, Fig 4.9B). After 48 hours incubation, BJ cells covered approximately 70-80% surface of both coating dishes. In addition, the morphology of fibroblast cells displayed typical elongated and spindle-like -shape on both coating conditions (Fig 4.9C). These results suggest that ACP hydrogel provides a good surface for promoting cell proliferation[55]. In order words, no negative dramatic effect of ACP hydrogel on the proliferation, viability, and morphology of BJ cells, showing the excellent biocompatibility of ACP hydrogel.

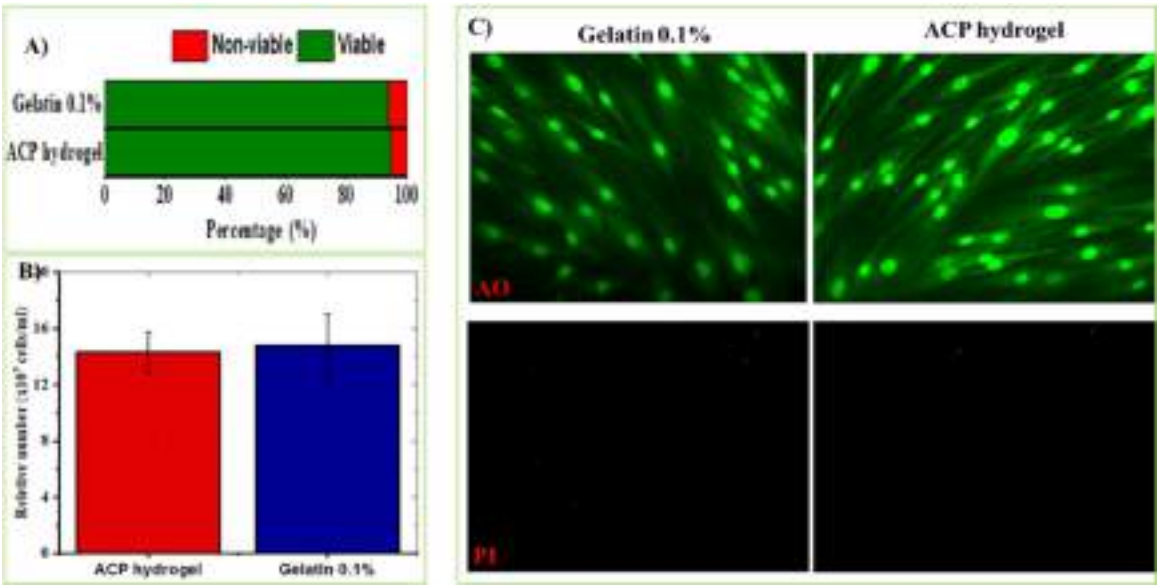

Figure 4.9: *The cell biocompatibility of ACP hydrogel with fibroblast cells, BJ (ATCC® CRL-2522™).*

A) Cell viability was measured with live/dead assay and B) the quantification of cell number was determined by the Trypan Blue technique. D) The live/dead assay image via dual staining AO/PI after 2 days of culture. Scale bar: 100µm. Gelatin 0.1% was used as a control.

4.7 The ability of the ACP hydrogel as a delivery platform for fibroblast cell transplantation

The transplantation of scaffolds containing cells represents a promising approach for regenerating tissues that have sustained damage from injuries or diseases[40]. In treating irreversible tissue damage and functional impairments, cells are typically sourced from biopsied tissue samples taken from the patient's body. These cells are then cultured externally, expanded, and subsequently transplanted, either independently or in conjunction with biomaterials, to facilitate tissue regeneration at the site of injury[45, 51, 75]. To prove the well-designed tissue-specific scaffolding template, fibroblast cells were encapsulated inside the ACP hydrogel matrix. After 48h culture, the viabilities of fibroblast cells were around 96.7 ± 3.5%, estimated by the number of green cells over red cells. For long-term culture, above 90%

of fibroblast cells were primarily stained green which demonstrates that most of the cells are viable. In other words, this indicates that the cells were grown in good culture conditions. After 24 h incubation, BJ cell adhered to the wall of ACP hydrogel proliferated and extended within the ACP scaffolds after 120 hours. The growth of fibroblast cells increased rapidly and created a layered network saturating the hydrogel matrix after 168 hours (Fig 4.10). Furthermore, the morphology of fibroblast cells culturing inside ACP hydrogel was elongated, which is rarely seen under 3D culture conditions[40]. The elongation of fibroblast culturing inside hydrogel has been reported with a hydrogel system forming with biological cues such as alginate hydrogel modified with RGD peptide [41] or a hydrogel system forming with ECM derivative materials such as gelatin[52] or collagen[50]. In this study, the number of elongated fibroblast cells shown at 120 hours and 168 hours was higher compared to the established 3D hydrogel in these studies, confirming that ACP hydrogel mimicked the ECM structure.

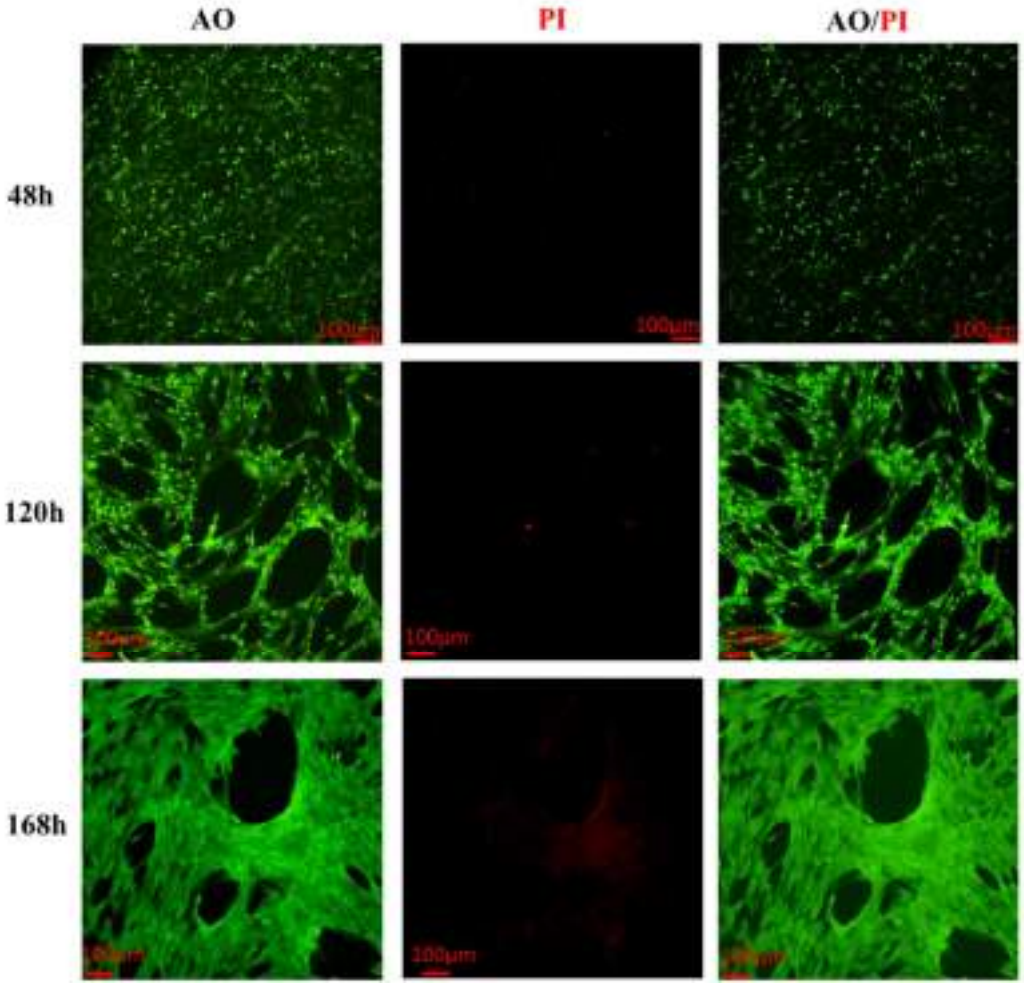

Figure 4.10: *The live/dead image of BJ cells after seeding into ACP hydrogel.*

Human fibroblast encapsulated in ACP hydrogel at 48 h, 120 h, and 168 h. Cells were treated with dual AO/PI. Scale bar: 100µm.

A migration assay was performed to prove that the function of fibroblast cells encapsulated in ACP hydrogel has remained. After 48 hours of incubation, Z-stack imaging exposed the appearance of single cells at the edging ACP cluster (Fig 4.11A) and even more pronounced after 120 h (Fig 4.11B). The outgrowth cells from ACP clusters seemed to be elongated and even longer spindle-like cells after releasing from a cluster. Further, the outgrowth cells established the confluent cell layer on the surface of the culture dish at the 5th-day culture. Upon this observation, this could confirm that the ACP scaffolds provided a favorable microenvironment for cell adhesion, spreading, and proliferation. Therefore, our ACP hydrogel might be applied for tissue engineering with cells as the main composition [278].

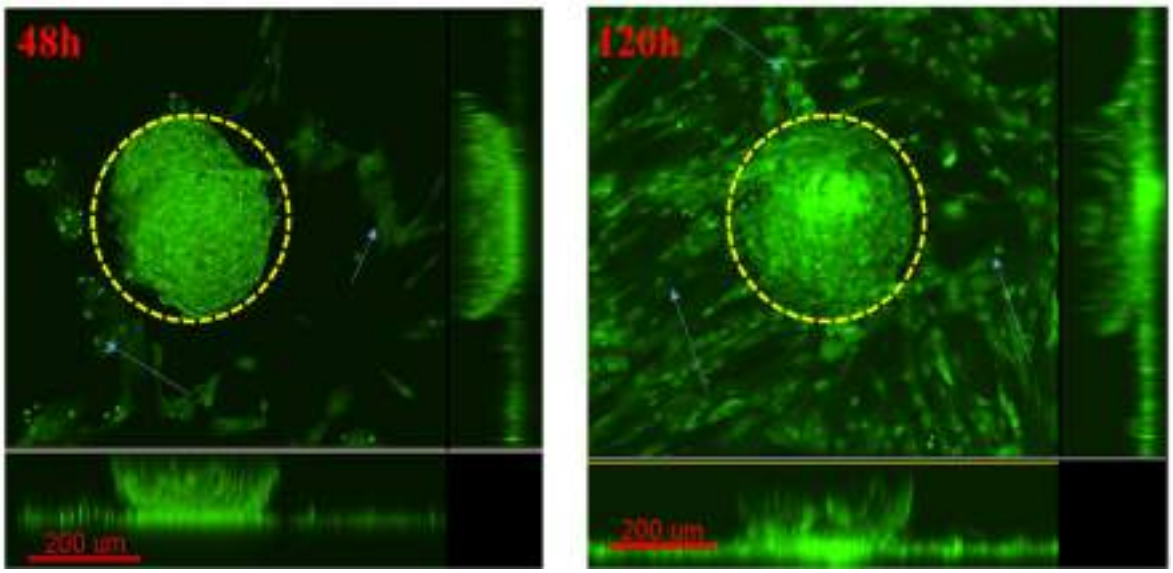

Figure 4.11: *The migration of BJ cells from the ACP hydrogel cluster after 48 hours and 120 hours of culture.*

Z-stack fluorescence images of cells migrating out of an encapsulated hydrogel droplet (20ul) show dual AO/PI staining. A squared dot circle shows the formation of the ACP cluster, and blue arrows identify the outgrowth cell from the ACP hydrogel.

4.8 The ability of the resultant hydrogel in dual active compound incorporation

4.8.1 The reason for selection

Nitric oxide (NO) is a gaseous free radical and natural gasotransmitter that plays a crucial role in wound healing [171, 186, 187, 279]. It is produced from the endogenous amino acid L-arginine (L-Arg) through the catalysis of NO synthase (NOS) enzymes[29, 166-168]. NO functions as a mediator in wound healing and possesses broad-spectrum antibacterial

properties[186]. Its actions include regulating cytokines to initiate the inflammation process, recruiting immune cells to combat microbial infections, and promoting tissue remodeling. Importantly, NO does not induce drug resistance[166]. Studies have shown that the topical application of gaseous NO or artificial NO donors, such as S-nitrosothiols, metal NO complexes, bis-N-nitroso compounds, N-diazeniumdiolates, and Roussin's black salt, can enhance wound healing while preventing bacterial infections [187]. Combining these artificial NO donors with an effective wound dressing system has demonstrated promising potential in wound treatment, serving as a biosafety barrier and facilitating the healing process.[279] For chronic wound, the addition of L-arginine is required to maintaining the immune status[170, 279]. A deficiency in extracellular L-arginine can contribute to the suppression of immune functions, resulting in reduced proliferation of immune cells and diminished production of nitric oxide (NO), which can lead to delay the wound healing process[187]. However, the stimulated macrophage cells during the inflammatory stage induced the massive amount of $O^{2\bullet-}$, which can easily react with iNOS derived NO and form highly reactive ONOO− mediated tissue injury[169, 195]. Therefore, to take the advance of L-arginine therapy in wound healing, the sides of this problematic should be solved.

In order to address the challenges association with L-arginine, the extensive research conducted on polyphenols and antioxidants has consistently shown their ability to prevent endothelial dysfunction caused by oxidative stress[280, 281]. This is primarily achieved through the reduction of cell damage mediated by free radicals. Regulating inflammation is important in reducing the oxidative stress within the wound environment, which in turn aids in the absorption of proliferative drugs by the wound[215, 282, 283]. Among drug/compounds with potential application in wound healing, polyphenol compounds has a lot of interested due to their biological function which can help to regulate the inflammation phages as well as remodeling phages[165, 213, 215]. Resveratrol, a non-flavonoid polyphenol compound derived from plants like grapes, possesses potent antioxidant, anti-inflammatory, and anti-tumor properties[180, 213-215, 220, 282]. Research has demonstrated that Resveratrol promotes angiogenesis and suppresses inflammation in the healing of skin wounds[180]. Also, Resveratrol has been found to inhibit the inflammatory characteristics of macrophages and decrease the secretion of associated inflammatory factors[185, 199]. In addition, Resveratrol increases the production of nitric oxide (NO) in endothelial cells by upregulating the expression of endothelial NO synthase (eNOS), stimulating eNOS enzymatic activity, and preventing eNOS uncoupling[199, 211, 212]. Therefore, the combination of L-arginine and Resveratrol would produce a dual functionality scafffold, where Resveratrol acts as a strong anti-oxidative agent, while L-arginine forms an exogenous substrate for eNOS activity.

4.8.2 Optimization the concentration of L-arginine and resversatrol

ACP hydrogel encapsulated with L-arginine (A-ACP hydrogel) or Resveratrol (R-ACP hydrogel) alone or both (AR-ACP hydrogel) was fabricated by the solid dispersion method with the help of ball milling method. The maximum loading capacity of ACP hydrogel to Resveratrol was 22.12 ± 1.26 %. Further, the cytotoxic of ACP hydrogel with maximum concentration of Resveratrol was non-toxic to fibroblast cells (Fig A2, Appendix). In addition, the addition of Resveratrol was intolerance to sol–gel transition temperature of ACP hydrogel. Therefore, ACP hydrogel was designed with Resveratrol at the concentration of 50 and of 100µg/mg of ACP polymer as R10-ACP and R20-ACP hydrogel, respectively. For L-arginine loading system, various amount of L-arginine (50-200 µg/mL) had been manufactured. However, A-ACP hydrogel induced the cytotoxic to fibroblast cells in a dose-dependent manner. The density as well as the morphology of the fibroblast cells cultured on ACP hydrogel with L- arginine concentration of 50 µg/mL or 100 µg/mL were almost identical to the control sample (Fig A2, Appendix). When the concentration of L-arginine in ACP hydrogel was increased to 150 µg/mL, fibroblast cells showed characteristic changes in morphology, which was similar to the senescence morphology of fibroblast cells induced with oxidative stress [279]. In addition, a massive apoptotic signal was observed. The shrunken and rounded cells with significant cytotoxicity were detected on ACP hydrogel with the highest concentration of L-arginine (200 µg/mL). In addition, the addition of A-ACP hydrogel showed the change in the pH value of culture media as the function of L-arginine. The pH value was 7.2 -7.4 when the concentration of L-arginine in ACP was 50 µg/mL or 100 µg/mL. The higher alkaline environment (pH > 8.0) was recorded with ACP hydrogel containing 150 µg/mL or more. It is well-known the impact of the pH environment of dressing on the wound healing process [280, 281]. The alkaline environments decelerate cell migration, causing prolonged healing time, especially on the wound of hard-to-heal wounds such as diabetic wounds [280]. From the preliminary investigation, the concentration of arginine in all hydrogel dressings was 100µg/ml.

The dual loading systems, donated as AR10-ACP hydrogel and AR20-ACP hydrogel, were fabricated via the pre-determined loading concentration. In difference, in a single loading system, the color of the resultant ACP solution was shifted to a dark brown color (Fig 4.12A). The retention time of L-arginine and Resveratrol in a dual system was identical to a single one on the HPLC chromatogram (Fig A3, Appendix), confirming that there was no chemical reaction between L-arginine and Resveratrol. From some of the literature reviews about Resveratrol [282] as well as arginine [283, 284], the change in the color of the dual system might be due to the hydrogen bond between the methylene bridge in Resveratrol and guanidino group of arginine. Notably, all the extracted hydrogels did not induce any toxicity to fibroblast

cells (Fig A4, Appendix). The density as well as the morphology of fibroblast was similar to the control sample. Therefore, it could be concluded that the concentration of these biological cues could be used for further study.

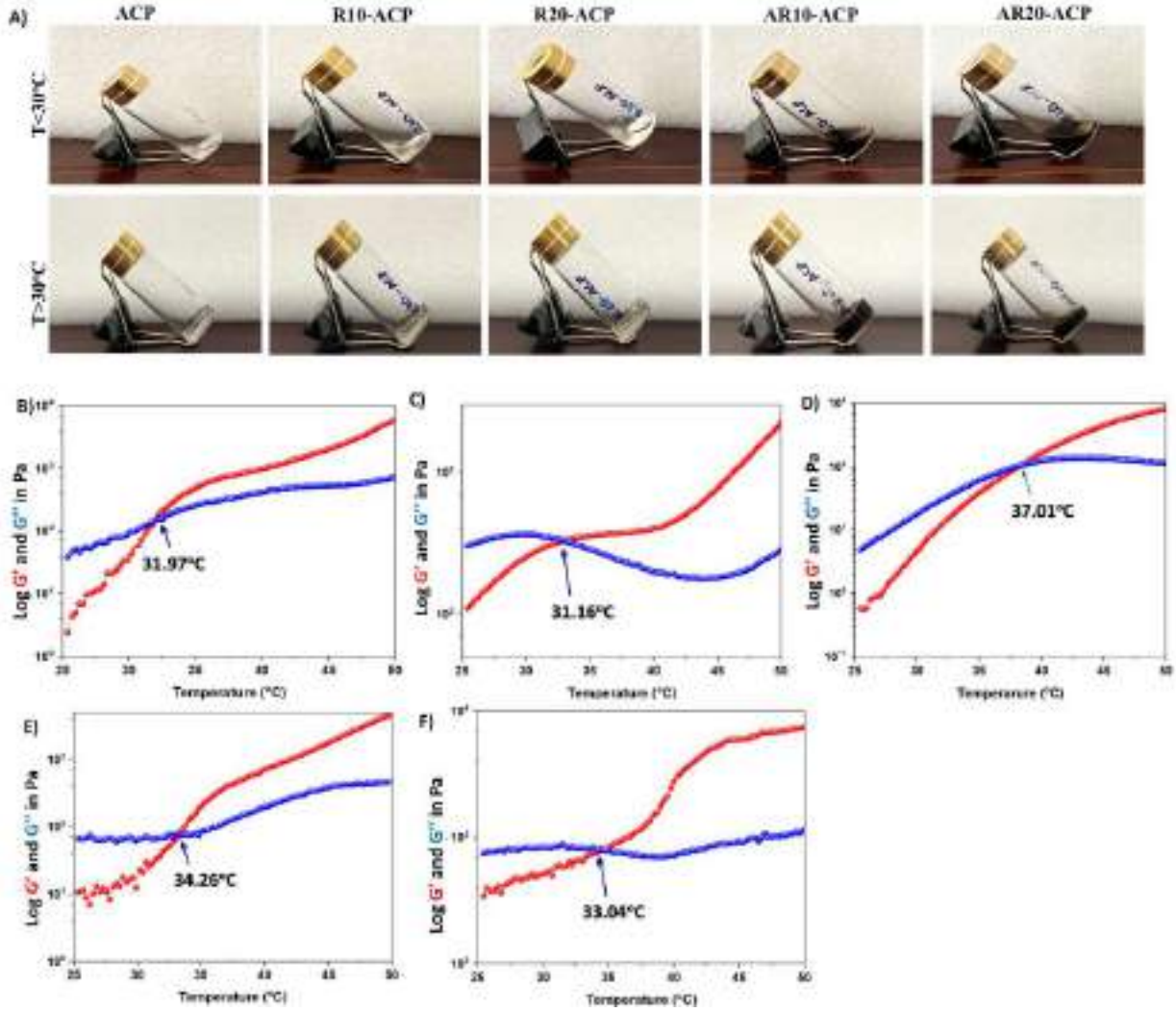

Figure 4.12: *The effect of the biological cues (L-arginine and resveratrol) on the sol-gel transition of ACP hydrogel.*

A) Photographs showing reversible sol–gel transition behavior of ACP hydrogel with different loading agents in ACP hydrogel and its rheological study under oscillation temperature ramp (strain =1% and frequency = 10rad/s): B) A-ACP hydrogel; C) R10- ACP hydrogel; D) R20 - ACP hydrogel; E) AR10 – ACP hydrogel; F) AR20 – ACP hydrogel.

4.8.3 Characterization of thermal behavior of AR-ACP hydrogel

In term of thermal gelling behavior, AR10-ACP hydrogel and AR20- ACP hydrogel showed sol-gel transition when the temperature surpassed 30°C and conversion to flowable sol upon

cooling (Fig. 4.12A). This result was also authenticated by rheological behavior (fig 4.12 B-F). However, the biological cues expressed the impact on the rheological property of ACP hydrogel. The incorporation of Resveratrol reduced the critical sol-gel transition temperature. The gel–sol transition was shifted from 34.83 ºC (Fig 4.12B) to 31.97ºC (Fig 4.12B) when the amount of Resveratrol in ACP was 50 µg/mg. This pattern was clearly confirmed with ACP hydrogel containing a higher amount of Resveratrol (fig 4.12C). In addition, the storage modulus was drastically increased following the incorporation of Resveratrol as similar as hydrogel encapsulating hydrophobic molecules [29, 72, 285]. Increased storage moduli in the liquid phase and reduced gelation temperatures as Resveratrol concentration rises imply a possible decrease in the distance between the clusters of the aggregated PPO segments due to the multiple hydrophobic sites [72, 285]. In contrast, the incorporation of L-arginine induced a higher gelation temperature (fig 4.12D). L-arginine is a hydrophilic and positively-charged amino acid [166, 286, 287]. L-arginine causes the electrostatic interaction with the carboxylate group on alginate in the ACP copolymer. The reduction in elastic moduli confirmed that the ionic strength was strong enough to suppress temperature-dependent solubility of PPO in water [285]. Therefore, a higher temperature was required for the sol-gel transition. Intriguingly, the modeling behavior of ACP hydrogel in a dual-loading system was adjusted by L-arginine and Resveratrol. The gelation temperature R10-ACP was increased from 31.97 ºC to 34.04 ºC following the support of L-arginine ((fig 4.12E). For relatively higher Resveratrol, R20-ACP, these phenomena were similar (fig 4.12F). In other words, in the presentation of Resveratrol, the PPO segments might be manageable to close-packed to overlap the hydrophilic density [72]. Adding hydrophobic Resveratrol might reduce the influence of the electrostatic interaction between alginate and L-arginine. The thermogelling behavior of A-ACP hydrogel was decreased in the suitable application.

The scanning electron microscopic image of these hydrogels is presented in Fig. 4.13A. The porous structure of the ACP hydrogel was maintained despite adding different loading agents. Due to the difference in properties of arginine and Resveratrol, the interconnected compact morphology with different pores was observed. With the addition of L-arginine, some of the fibril bundles are exposed in the interpenetrating channel, revealing the ionic coordination bonds between the alginate backbone and L-arginine. In the case of Resveratrol, the internal arrangements of the ACP network remained; however, there was a more compact porous structure than that of the pure one. This may result from the addition of the hydrophobic intermolecular fashion of Resveratrol and the hydrophobic zone of the ACP hydrogel network, consequently causing the tighter cross-linking between these micelles.

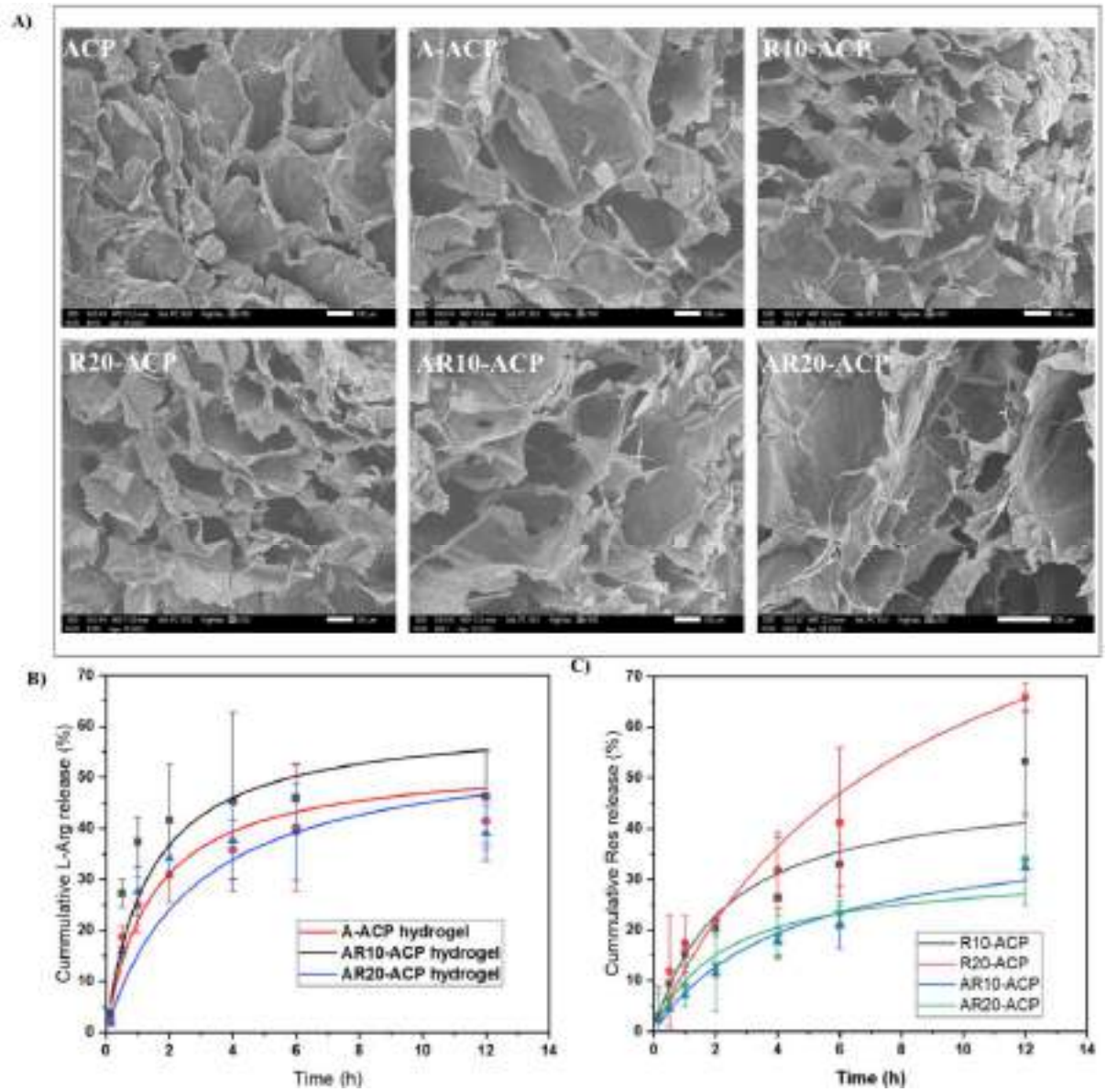

Figure 4.13: *Characterisation of ACP hydrogel with the biological cues: Morphology and release pattern.*

A) The morphology of these hydrogel was obtained by SEM techniques with magnification = 100, SED = 10KeV. The release profiles of B) arginine and C) Resveratrol from ACP hydrogel was monitored during the first 12h. Data was presented as mean ± SD (n=4).

4.8.4 The release behavior of L-arginine and Resveratrol from AR-ACP hydrogel

The release profiles of both arginine and Resveratrol were extensively investigated (Fig. 4.13 B-C). The kinetic released models for drug release from the polymeric matrix [288, 289] such as zero order, first order, Higuchi, Hixson-Crowell, Korsmeyer-Peppas and its modified form with time lag were presented in table A1 (Appendix). Both arginine and Resveratrol had a

comparatively rapid release in the first 2 hours and then showed a sustained release. As shown in Table A1, the modified Korsmeyer-Peppas has a greater potential to be employed as a predictive model for Arginine from ACP hydrogel. Of note, L-arginine is hydrophilic molecules. L-arginine molecules are preferred to locate at or near the hydrogel surface. Therefore, about 30-40% arginine was leaked from the ACP system during 2 hours of immersion. After burst release, ACP with arginine showed a sustained pattern after that. The introduction of L-arginine induced more coordinative bonds due to the protonation of L-arginine and a deprotonating carboxylic group on ACP leading to control amount of L-arginine diffusing in the network. Similar, the arginine from the dual loading system, modified Korsmeyer-Peppas was outperformed all exanimated models. The use of Resveratrol along with L- arginine did not influence the initial release time (t_{lag} for A-ACP, AR10-ACP, and AR20-ACP were 0.23 hours, 0.26 hours, and 0.24 hours, respectively). The diffusional exponent n was below 0.45 in all cases, confirming the L-arginine release mechanism's similarity. Interestingly, the kinetic coefficient k value was much lower for arginine from the dual system as compared to the single system, confirming the influence of Resveratrol in decelerating L-arginine release. For Resveratrol system, Zero-order and Korsmeyer-Peppas models and its modified Korsmeyer-Peppas models appeared to trend with the experimental data. By comparing the Akaike Information Criterion (AIC) value, Zero-order and Korsmeyer-Peppas models were the preferred models. Because all the diffusional exponent n for R10-ACP and R20- ACP were in the range 0.43−0.85, the release of Resveratrol was influenced by both diffusion and swollen matrix [288]. The drug release models to describe Resveratrol release behavior from dual loading systems, AR10-ACP, and AR20- ACP, were similar to R10-ACP and R20-ACP hydrogel. Also, the diffusional exponent suggested that Resveratrol release from a variety of dual systems relies on non-Fickian diffusion ($0.43<n<0.85$) [289]. However, the transport constants (K) were much higher for a single Resveratrol loading system than for Resveratrol from a dual system. This phenomenon was similar to the release of L-arginine from a dual system. For the R-ACP system, the density of the hydrophobic zone in the ACP hydrogel increased following the encapsulation of Resveratrol [113]. After immersion in a release buffer, water diffused into the network, causing the hydration of these zones; consequently, Resveratrol could easily escape [72]. The support of L-arginine in the microstructure might provide more of a cage for Resveratrol. Therefore, the release profiles of Resveratrol in the dual system have been adjusted suitably.

4.8.5 The synergic of L-arginine and Resveratrol dual loading ACP hydrogel in anti-oxidation activity

4.8.5.1 L-arginine controls the scavenging rate of Resveratrol in the manner way

The 1,1-diphenyl-2-picrylhydrazine (DPPH) radical assay was first carried out to estimate the antioxidant properties of hydrogels from the adsorption peak of 517 nm. Due to the participation of sulphhydryl molecules in the ACP copolymer structure, which are effective free radical scavengers[290, 291], the resultant ACP hydrogels exhibited promising antioxidant capacity. It was found that the addition of Resveratrol or L-arginine displayed more remarkable scavenging capacity than those native ACP hydrogels (Fig. 4.14A-B). Besides, a deep purple color of pure DPPH (0.5mM) vanished following the increase of incubation time (Fig. 4.14A) with the loading system, revealing the enhanced antioxidant property as a result of the compound release. For 4 hours of incubation, all types of ACP hydrogel exposed the ability to cancel the radical agent of DPPH with a similar rate (all $p<0.05$). The scavenging function of loading factors was evident after 8 hours. Hydrogel with Resveratrol showed an excellent DPPH clearance rate compared to others. The combination of Resveratrol and arginine seemed to be antagonistic; 22.38±3.49% or 26.55±3.96% of DPPH radical was scavenged by R10-ACP hydrogel or R20-ACP at 8 hours. However, with the addition of L-arginine, the scavenging rate was nearly two orders of magnitude lower than that of the single system ($p= 0.00248$, R10-ACP vs AR10-ACP; $p=0.00493$, R20-ACP vs AR20-ACP). During 24 hours, ACP with Resveratrol removes over 50% of radicals in the solution, while the AR system removes about 40% of DPPH. However, the effective scavenging activity of AR-ACP hydrogel and R-ACP hydrogel was comparable after 96 hours of incubation ($p=0.11688$, R10-ACP vs AR10-ACP; $p=0.62544$, R20-ACP vs AR20-ACP). In addition, the scavenging abilities against DPPH radicals of ACP hydrogel with L-arginine were increased over time. In the first 8h incubation, the DPPH scavenging efficiency of A-ACP hydrogel was identical to that of native ACP hydrogel (all $p>0.05$). The antioxidant response to prevent radical agents of L-arginine in A-ACP hydrogel was observed at 24 hours ($p= 0.00322$, A-ACP vs control). Therefore, arginine does not block the effect of Resveratrol in removing radicals. According to the release pattern of Resveratrol in the dual loading system, the reduction in DPPH scavenging capacity of AR-ACP hydrogels could be explained. Many studies demonstrate the importance of radical agents in wound healing [128-129]. On the one hand, a low amount of radical agents aid in defence of wounds against microbial infections and promotes vascularization by activating multiple cellular signalling pathways [127]. On the other hand, The extensive production of ROS in diabetic patients impedes the wound healing process by blocking the normal physiological metabolism[169, 170, 185, 186]. Failure to perform radical detoxification in a timely manner can often result in the wound becoming non-healing and

chronic, thereby posing significant challenges for treatment. [10-21]. Therefore, the combination between L-arginine and Resveratrol provided an effective radical detoxifying strategy.

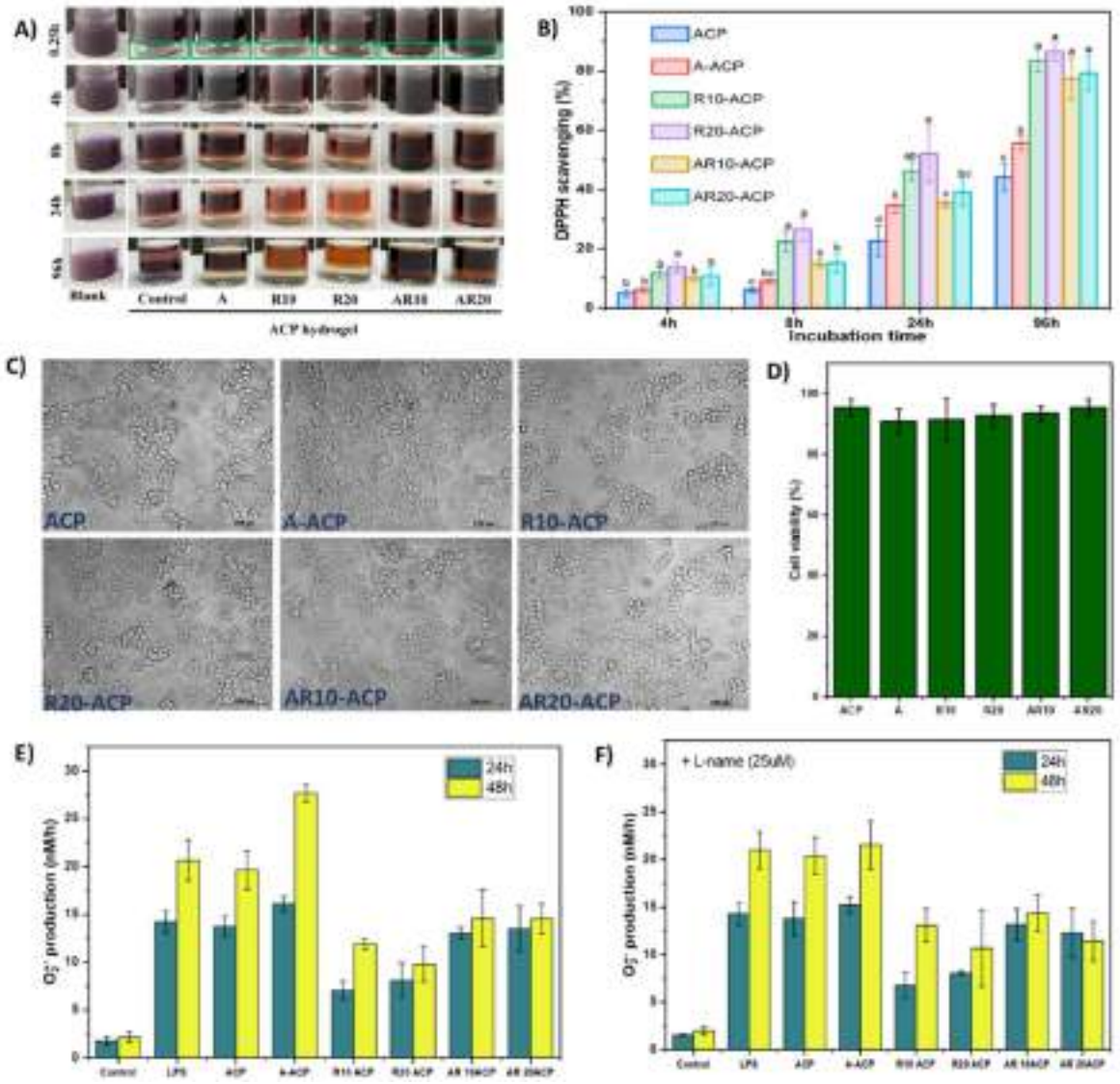

Figure 4.14*: Characterisation of the ROS scavenging capacity of ACP hydrogel with biological cues: DPPH assay and superoxide anion.*

A) Photographs of DPPH (0.5 mM) adding into various ACP hydrogels at different time points (green box indicated hydrogel layer). B) The percentage free DPPH radical scavenged by ACP hydrogels as compared to non-treated sample (bars with different letters of alphabets have values that are statistically significant ($p<0.05$)). Superoxide anion ($O^{2\bullet-}$) was investigate with Raw 264.7 cells. C) Morphology and D) the viability of Raw 264.7 cells were first accessed. $O^{2\bullet-}$ production in RAW 264.7 cells treating with ACP hydrogels in two time points: 24 hours

and 48h E) without NOS inhibitors and F) with NOS inhibitors (L-name). Data was presented as mean ± SD (n=5). ACP blank (control), A (A-ACP), R10 (R10-ACP), R20 (R20-ACP), AR10 (AR10-ACP), AR20 (AR20-ACP).

4.8.5.2 Resveratrol prevents the generation of $O^{2\bullet-}$ production in the active immune cells.

$O^{2\bullet-}$ is the first ROS produced by macrophages upon contact with various activating stimuli (e.g., LPS, cytokines, growth factors, and fragments of bacterial membranes)[170, 185, 199]. Therefore, to verify whether the designed hydrogel could have the ability to eliminate intracellular ROS activity, the consumption of $O^{2\bullet-}$ production in stimulated Raw 264.7 cells was performed. Before the assay, the toxic profile induced by all ACP samples on Raw 264.7 cells was assessed (Fig. 4.14 C-D). During the 48h incubation of ACP or on ACP hydrogel with a loading agent, the density of Raw 264.7 cells was very high (Fig. 4.14C). Over 90% of cells were alive, as estimated by MTT assay (Fig. 4.14D), suggesting that all ACP samples were not toxic to cells after 48h of incubation. The cytochrome c reduction assay was used to assess the level of $O^{2\bullet-}$ production. The $O^{2\bullet-}$ formation was very high in the stimulated macrophage cells (Fig. 4.14E). After 24h of LPS stimulation, macrophages produced relatively high amounts of $O^{2\bullet-}$ production (14.2 ±1.1nM/h), about eight times higher than that of unstimulated cells ($p<0.05$), which then increased up to 20.6 ±2.2nM/h at 48 hours ($p<0.01$). The effect of the native ACP hydrogel on the production of $O^{2\bullet-}$ could be ignored due to indistinguishable values compared to control LPS. At the same time, other ACP samples induced strong effects on the synthesis of this radical. According to Figure 4E, there was a massive increase in $O^{2\bullet-}$ production in the stimulated cells incubated with A-ACP hydrogel, from 16.1±0.8 nM/h at 24 hours h to 27.7±0.9nM/h at 48 hours, relative to 134.3% in LPS-stimulated cells ($p<0.05$). In contrast, ACP hydrogel with Resveratrol leads to a marked reduction of $O^{2\bullet-}$ production. The concentration of $O^{2\bullet-}$ in both R10-ACP hydrogel and R20-ACP hydrogel was halved over A-ACP hydrogel ($p<0.05$) or stimulated cells ($p<0.05$) after 24 hours. Interestingly, the longer culture time did not seem to affect the level of $O^{2\bullet-}$ in the case of ACP hydrogel supplemented with Resveratrol ($p>0.05$). Presumably, as an effect of Resveratrol, dual AR-ACP hydrogels suppressed the amount of $O^{2\bullet-}$ compared to single L-arginine-loaded ACP hydrogels only. From 24 to 48 hours, the amount of $O^{2\bullet-}$ in the cell media containing AR10-ACP hydrogel or AR20-ACP hydrogel was maintained at around 14–15nM/h. To further define the importance of Resveratrol in the depletion of superoxide anion production in bacterial endotoxin-stimulated macrophages cultured with the A-hydrogel, the analog of L-arginine (L-NAME)- known as NOS inhibitor [198] was added to the culture medium (Fig. 4.14F). We found that the treatment of RAW 264.7 cells with L- NAME resulted in incomparable changes in $O^{2\bullet-}$ formation in the case of LPS-stimulated cells, R-ACP

hydrogels, or ACP hydrogels, except for the ACP hydrogel containing L-arginine. NOS inhibitors administered with A-ACP hydrogel did not affect $O^{2\bullet-}$ production within the first 24 hours of incubation. However, after 48h of incubation, more than 22% of $O^{2\bullet-}$ production was blocked when NOS inhibitors were used along with A-ACP hydrogel. This result confirmed the problem of the utilization of L-arginine in wound healing[195]. Importantly, NOS inhibitors did not influence the concentration of $O^{2\bullet-}$ from AR-ACP hydrogel groups. The O2 •− production level was in the range of 14–15 nM/h, similar to the levels shown with the non-inhibitor supplemented in the medium. The results suggested that adding Resveratrol could help control the extracellular ROS induced by extracellular L-arginine availability in treatment.

4.8.5.3 Resveratrol helps to prolong the stability of nitric oxide generated from L-arginine in oxidative stress.

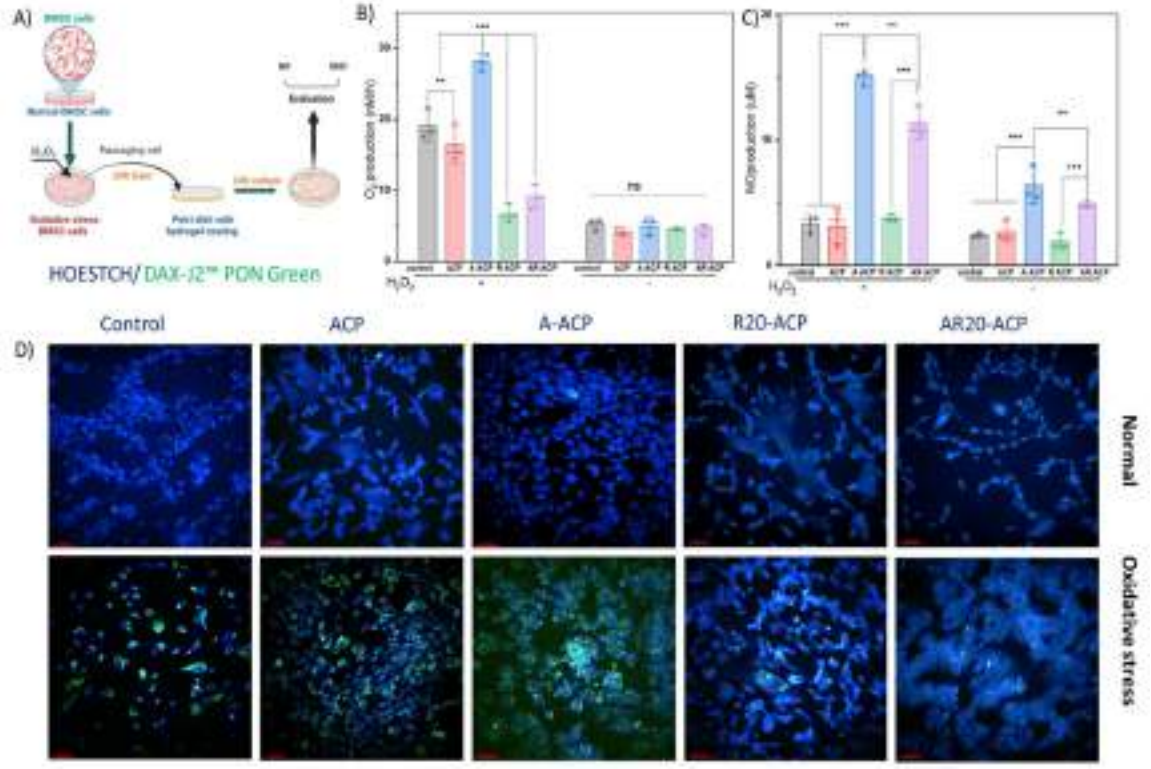

Figure 4.15: *The effect of an ACP hydrogel with dual biological cues on the oxidative stress cells model of H_2O_2-induced oxidative.*

A) The illustration of the cell model. B) The concentration of $O^{2\bullet-}$ and C) NO release from normal and oxidative stress cells with different treatments after 24h culture (n = 3 individual experiments). D) The cells stained with DAX-J_2 PON (Green) to peroxynitrite (ONOO−) and Hoestch (Blue) to Nucleus. Data are expressed as mean ± SEM. Significant differences were

*detected by one-way ANOVA with Tukey's multiple comparisons test, *p<0.05, **p<0.01, ***p<0.001.*

Further, the cellular models of oxidative stress were established to support evidence about the synergy of L-arginine and Resveratrol in the anti-oxidative process. The BMSC cells were treated with a strong oxidant (H_2O_2) for 24 hours to treat oxidative stress in BMSC cells (Fig. 4.15A). After subculturing established cells, $O^{2\bullet-}$ was overproduced in stress cells ($p>0.05$) (Fig. 4.15B). Consistent with DPPH results, the formation of $O^{2\bullet-}$ was gradually weakened compared to non-treated stress cells ($p=0.0023$). Like LPS-activating macrophage cells treated with A-ACP hydrogels, the intracellular $O^{2\bullet-}$ level was significantly increased in the oxidative stress cells (28.1±2.2 nM/h). Replacing L-arginine as Resveratrol in ACP hydrogel was proven to be an effective strategy to eliminate massive ROS from stress cells. Also, the use of Resveratrol and L-arginine in the combined therapy hydrogel had a prominent effect similar to that of Resveratrol single loading hydrogels. The concentration of endogenous NO released from BMSC cells was monitored (Fig. 4.15C). Despite evidence of the stimulation of Resveratrol in response to endothelial NO synthase (eNOS)[212], the endogenous NO release from oxidative stress sBMSC treated with R-ACP hydrogel was comparable to that of non-treated cells or to bare ACP hydrogel. The nitric oxide (NO) level was only dominated in the cells culturing on the hydrogel with L-arginine (Fig. 4.15C). In the normal cell condition, NO was also strongly generated from the cells seeded on A-ACP or AR-ACP hydrogel surfaces (all $p<0.05$) compared to other types, revealing the function of arginine as a nitric oxide donor compound However, if NO is present nearby, the production of $O^{2\bullet-}$ could combine with NO to form peroxynitrite ($ONOO^-$) - a strong a short-lived oxidant that pplaysa critical role for host defense [184, 186]. The massive amount of ONOO- would delay the healing time, though, due to the prolonged inflammatory phage time [28]. Therefore, the fluorescent probe of peroxynitrite (DAX-J2 PON (Green)) was used to monitor the presentation of ONOO- in the cytoplasm of BMSC cells. For the normal BMSC cells, the signal of the peroxynitrite probe was absent in all treated samples (Fig. 3.15D). However, in the oxidative stress cells, the green signal was detected inside the cytoplasm of almost all cells. The cell model cultured on native ACP form did not show a decrease in the density of cells with green fluorescent compared to non-treated. With the support of L-arginine, the ONOO- signals were strongly displayed, confirming the concern of L-arginine therapy. Interestingly, the green fluorescence was significantly dismutated upon treatment with hydrogels containing Resveratrol. Only slight ONOO– generation was found for R-ACP hydrogels, which could be attributed to the reactions with endogenic NO or $O^{2-\bullet}$. Taking the example of Resveratrol, despite the high amount of NO liberation from cells treated with AR-ACP hydrogel, intracellular ONOO generation was

very smaminimaler words, the antioxidant capacity of Resveratrol on suppressing intracellular ONOO- generation can help to maintain the NO concentration that would benefit angiogenesis and tissue repair during the wound healing process.

4.8.6 Hemolysis property, skin irritation tests, and antibacterial activity of AR-ACP hydrogels

Along with cell biocompatibility, haemocompatibility is another essential factor for biomaterials used in wound healing[292]. The behavior of red blood cells in different treated trials (saline - negative control, triton X-100 - positive control, bare ACP hydrogel, and AR-ACP hydrogel) is displayed in Figure 4.16A. The color of the supernatant in the hydrogel was clear, transparent with blood coagulation, and comparable to the negative control. The hemolysis ratios of all hydrogel groups were lower than 5% (Fig. 4.16A), revealing that ACP hydrogel systems are highly haemocompatible according to international biomaterials standards.

NO in wound healing therapy has two sides[171, 184, 187, 198]. Inadequate levels of NO can potentially result in the development of persistent wounds, particularly in individuals with diabetes, as NO plays a crucial role as a gasotransmitter in promoting the healing of wounds[169]. On the other hand, excessive NO exacerbates wound inflammation, leading to a delay in the healing process and potential skin irritation among patients[198]. Therefore, a skin irritation test for the ACP hydrogel formulation was performed on rabbits. Skin irritation, redness, or dehydration was not detected on the rabbit skin, even after 10 hours of being covered by ACP hydrogels or AR-ACP hydrogels (Fig. 4.16B). The calculation of the Primary Dermal Irritation Index and the Grading of Irritancy Potential [293] suggested that the ACP hydrogel or AR-ACP hydrogel had no irritation to the rabbit's skin (the index was 0). Hence, the hydrogel formulation appeared to be biocompatible, safe, and suitable for use as a wound dressing.

Given that Resveratrol and L-arginine have an intrinsic anti-bacterial activity[166, 213], the antibacterial ability of AR-ACP hydrogel was investigated via a zone of inhibition test with some common bacterial strains isolated from infected wounds (the gram-negative bacterial *P. aeruginosa*, gram-positive bacterial *S. aureus* and Methicillin-Resistant *Staphylococcus aureus* - MRSA). As shown in Figure 4.16C-D, the antibacterial feature of ACP hydrogel was strong and prominently efficacy against all tested bacterial strains. The zone of clearance for *S. aureus* was observed in the following order: AR-ACP hydrogel ~ positive control ($p=0.624$) > ACP hydrogel ($p<0.05$). The order was substantially different to *P. aeruginosa*, AR-ACP hydrogel > positive control ($p=0.0024$) ~ ACP hydrogel ($p=0.12$). For MRSA, the sensitivity of penicillin was remarkably lower than AR-ACP hydrogel or even blank ACP hydrogel. Interestingly, the efficacy against all bacterial strains with different ACP hydrogel types was

similar (all $p>0.05$). To verify the antibacterial effects of the ACP hydrogel as well as its derivative form, the quantification of the bacteria incubated overnight on the surface of hydrogels was conducted. The solid media containing bacteria was then dissolved in LB broth and incubated for 2 hours before the optical density of the bacterial suspension was measured. The relative viability of bacteria was achieved by comparing the OD value at 600 nm between non-treated and treated samples. As shown in Figure 4.16E, hydrogel coating agar surfaces remarkably influenced the antibacterial activity against gram-negative and gram-positive strains. The reduction in the viability of *S. aureus* and *P. aeruginosa* count by nearly 95% was similar to that of the positive control ($p>0.05$). However, the relative viability of these cells remained above 50% for penicillin treatment, even at the highest concentration (200 ppm). The effectiveness of ACP hydrogel against MRSA was outstanding with the loading agents. AR-ACP hydrogel reduced the number of viable MRSA cells by 96.87±0.89%, while a 71.53±10.33% reduction was recorded with blank ACP hydrogel. The antibacterial ability of ACP hydrogel had been proven in a previous study via the performance of cystamine. However, in this study, the antibacterial activities of ACP hydrogels could be due to their stiffness. Because the solidity of ACP hydrogel was lower than that of agar and this solid stage could be easily disturbed by temperature, the adhesion of bacteria onto the surface of the plate was prevented. The antibacterial natures of L-arginine and Resveratrol have been well-established in various studies [33-35]. The release of L-arginine would increase the alkalinity of the environment, resulting in challenging conditions for the growth of bacteria. In addition, because L-arginine is positively charged, this compound might interact with the bacterial cell membrane, limiting antibacterial activity. Further, the nitric oxide released from L-arginine can quickly diffuse into bacterial cells, causing oxidative damage to the cells [33]. In addition, Resveratrol can help block the redox homeostasis of bacteria by protecting it against exogenous NO. The data demonstrated that the dual loading of L-arginine and Resveratrol in ACP hydrogel synergistically facilitated wound disinfection, leading to a sustainable wound healing effect.

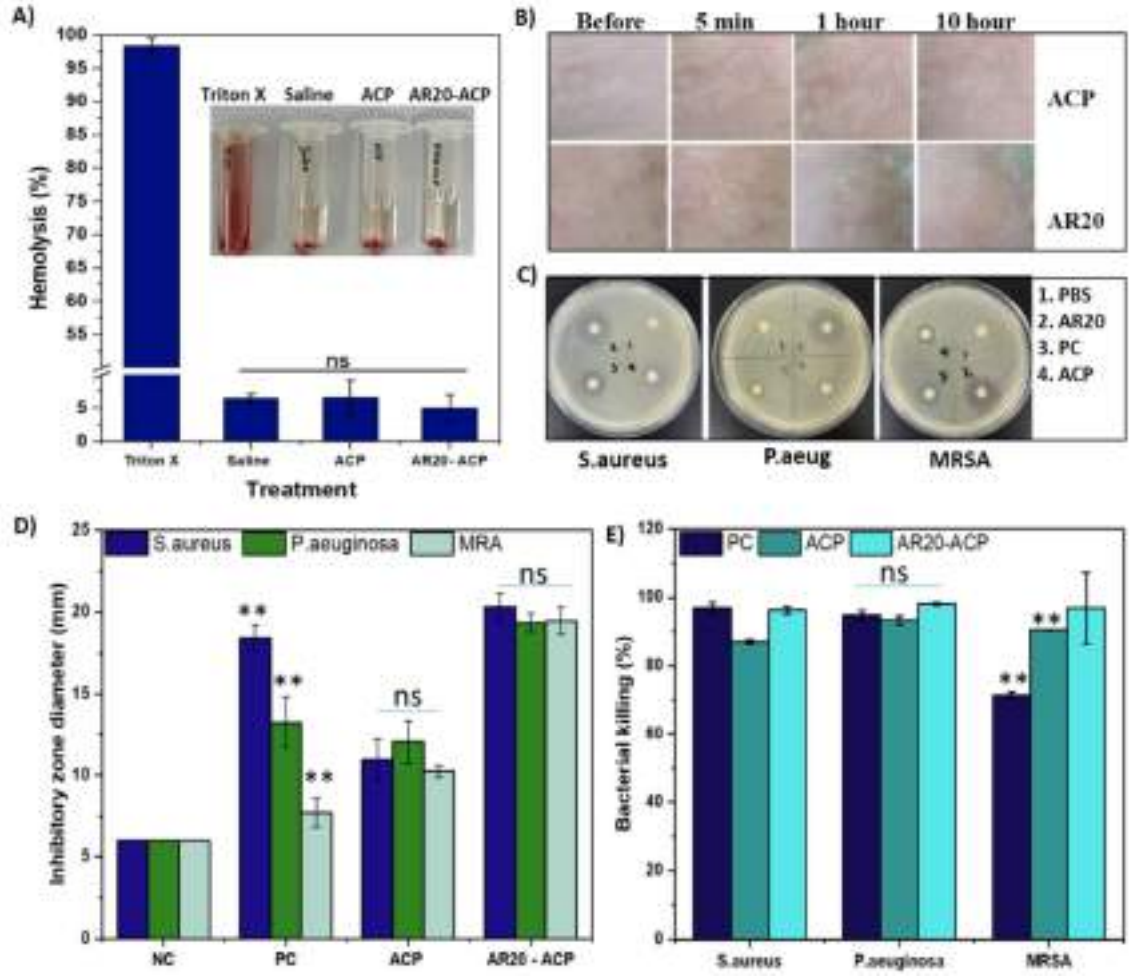

Figure 4.16: *Biosafety (hemocompatibility and irritation) and anti-bacterial activity of result hydrogel.*

4.9 In vivo diabetic wound healing performance of the functional ACP hydrogels

Encouraged by the above results, the *in vivo* performance as an ideal wound dressing based on AR-ACP hydrogel in promoting diabetic wound healing using a mouse model with induced STZ (Fig. 4.17) was included.

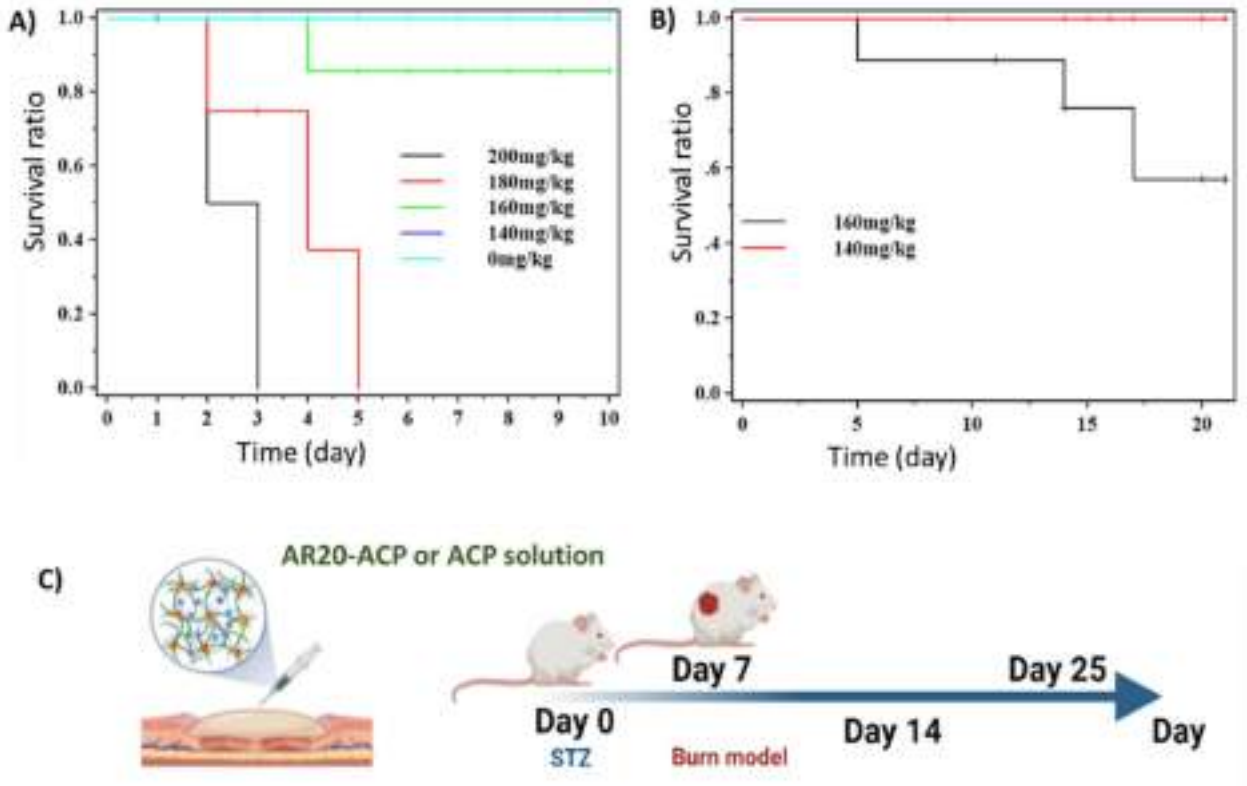

Figure 4.17: *The selection of STZ dose in building diabetic mice model.*

Kaplan–Meier plot for STZ admiration at different doses: A) 0mg/kg-200mg/kg and B) 140-160mg/kg. C) In vivo burn wound healing on diabetic mice model.

4.9.1 Evaluation of the diabetic model

Various concentrations, from 0 to 200 mg/kg, were first used in this study. As shown in Figure 4.17 A, the high STZ doses (over 150 mg/kg) recommended in some studies consistently achieved a diabetic state with a high mortality rate. 100% of mice died during the first week with a dose over 160mg/kg. Mice models with STZ dose at 160 mg/kg had a success rate of 80% for the first 10 days of the experiment. However, nearly 40% of mice died at this dose for a long time. According to the Kaplan–Meier plot (Fig 4.17B), the median survival was 17.57±1.76 days in mice given 160mg/kg. The survival rate in STZ-induced diabetic mice by 140mg/kg dose was 100%. Also, the blood glucose examination in this group was significantly higher than the normal blood (the normal blood for mice is 140-160 mg/dl)[294]. To better conclude the model, the blood glucose level of mice receiving 140mg/kg STZ was examined daily.

The data showed that all mice rapidly developed diabetes after a 2-day injection of STZ at 140mg/kg, and the proportion of mice that survived with no complications was 100%. All mice

experienced their first blood glucose level exceeding 250 mg/dL for 3 consecutive readings. The mice were not considered to have established our model until they were determined to be severely diabetic (>400 mg/dL). On day 7, the peak blood glucose was between 250 and 300 mg/dL in 30% of mice, 400 and 450 mg/dl in 65% of mice, and ≥ 500 mg/dl in 5%. The symptoms of hyperglycemia in the selected mice were maintained over 21 days. Therefore, a dose of 140 mg/kg STZ was chosen for study, and the wound healing process was evaluated for 21 days.

The burn wound was generated in diabetic mice following the previous study [27]. Based on the examination of the damaged tissue by H&E staining, it was concluded that the wounds were third-degree burns. The burn wounds generated in diabetic mice were treated topically with AR20-ACP hydrogel by needle injection (Fig.3.17C) on the wound, and their assistance in the wound healing process was compared to control groups, which were treated with isotonic saline and native ACP hydrogel.

4.9.2 Evaluation of the wound closure

Digital photographs of the wounds in each group are shown at different time points in Figure 4.18 A, and the wound healing progress was determined by measuring the wound area over 14 days (Fig. 4.18 B). On day 3, wounds in the 3 groups demonstrated non-distinct appearances. The wound size was expanded by over 100%. The saline-treated group did not demonstrate comparable wound closure by the end of the first week. Also, the condition of wounds in saline groups was aggravated. These wounds are still red and swollen, with a small amount of bleeding after nine days. A significant difference in wound healing in this group was only identified at the end of the experiment. The wound became dry with the formation of an abnormal scab. The hydrogel-treated groups displayed extraordinary wound appearance. The phenomenon of the inflammation stage (redness and swelling) was exhibited on day 3. After 5 days of treatment, the advance of the wound dressing-based ACP hydrogel system was observed. Wounds dressed with native ACP hydrogel were kept moist, leading to a bright color on the wound surface. The wound edge started the contracted process, and the average maximum wound area exhibited a reduction of 14.43±2.35% compared to the 3rd day. AR20-ACPOn caused changes to both the speed and pattern of re-epithelialization, the healthy granulation tissue on the center of the wound, and the formation of a scar in the wound edge, which was readily apparent on visual inspection on day 5. In addition, AR20-ACP hydrogel exhibited great accelerated wound closure with 77.23±5.23% remaining wound area. Despite the good closure rate (23.7%) on day 9, the wound was dark red in the native ACP-treated group. This phenomenon was eliminated in the case of AR20-ACP hydrogel dressing. Also, the wounds in this group exhibited significantly more contraction than their bare form of ACP-

treated counterparts. However, no differences in the approximate rates of wound closure were observed among the hydrogel groups after day 15 (Fig. 4.18C). Thus, histological analyses were carried out to clarify the tendencies of wound healing among the different groups.

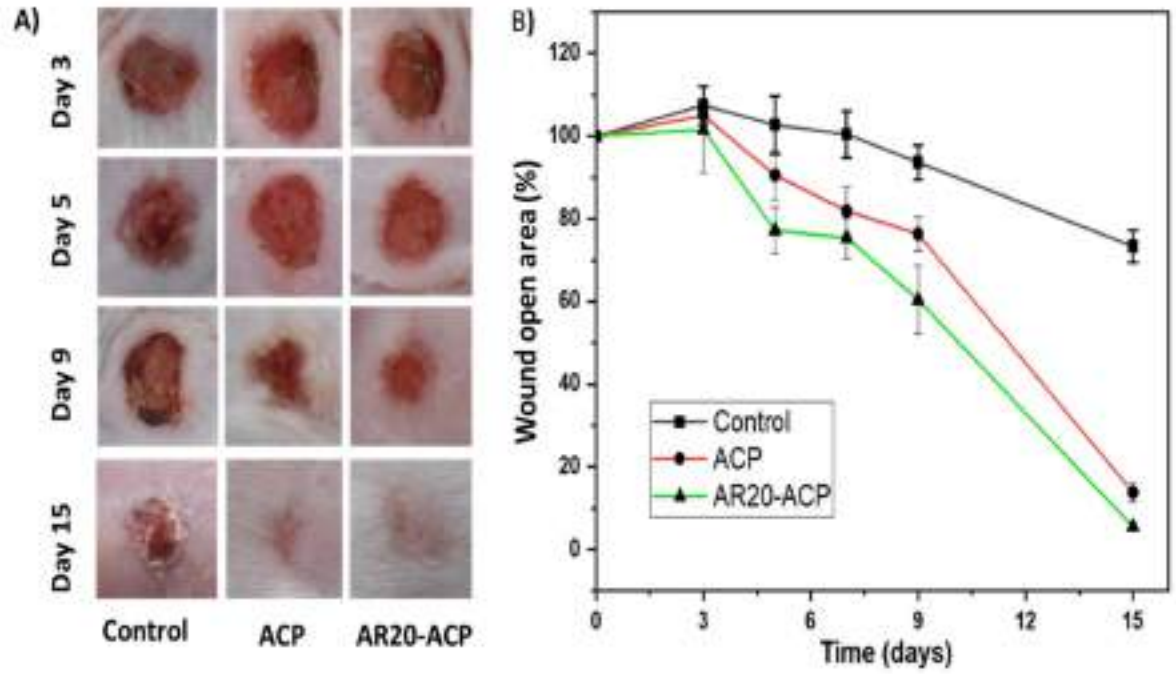

Figure 4.18: *In vivo burn wound healing on diabetic mice model with AR20-ACP hydrogel compared to ACP hydrogel and non-treated group (control).*

A) The photographs and B) the statistical analysis of wound closure (n=3) of the burn wounds (100mm) at the given time.

4.9.3 Evaluation of the regeneration of damaged skin

The skin biopsies for histological examination were taken on the 10^{th} and 18^{th} days after treatment. H&E staining revealed changes in the skin layers during the healing process (Fig. 4.19), while the Masson's trichrome (MT)-stained technique was involved in evaluating the remodeling process of collagen matrix (fig 4.20). The enlarged images for H&E and MT were also presented in Appendix A5 and A6, respectively.

On day 10, H&E staining (Fig. 4.19A and A5) showed that the re-epithelialization was discernible within the wound edges (labeled A1 and A3) in the control groups. Figure 4.19B showed that the epidermal thickness of the advancing epithelial tongue was 5–6-fold increase as compared to the length of epidermis in the normal skin region (labelled N). However, the centre of the wound (labelled A2) in the control groups contained large numbers of necrotic and dermal cells. In addition, neutrophil infiltration, which is representative of severe allergic reactions, as well as serious bleeding and other inflammatory cells, was observed in the wound

area. Similar to controls, the administration of ACP hydrogel appeared to alter the regeneration process in the wound edges rather than that in the center of the wound, but with more incredible velocity. The change in epidermal thickness to the normal skin was smaller than in the control group ($p=0.013$). Also, the affiliated skin organs, such as hair follicles and sebaceous glands, appeared at the edge, which was missing in the control. Histological analysis indicated that only the animals treated with AR20-ACP hydrogel had fully restored the epidermis in all examined areas. The epithelial thickness was comparable to wound edges or the wound center (all $p>0.2$). Further, the epidermis of the whole wound region was fully stratified, including terminally differentiated stratum corneum, through the vast majority of the wound surface. Together with epithelial coverage formation, neovascularisation is a crucial advantage of the AR20-ACP hydrogel. The density of newly formed blood vessels was 37.12 ±11.4% in the wound when AR20-ACP hydrogel was applied, nearly nine times higher than that of the native ACP hydrogel group. Specifically, the angiogenesis process was shown on most wounds with AR20-ACP but occurred only on the edges of the wounds treated with ACP hydrogel and was limited in the control groups.

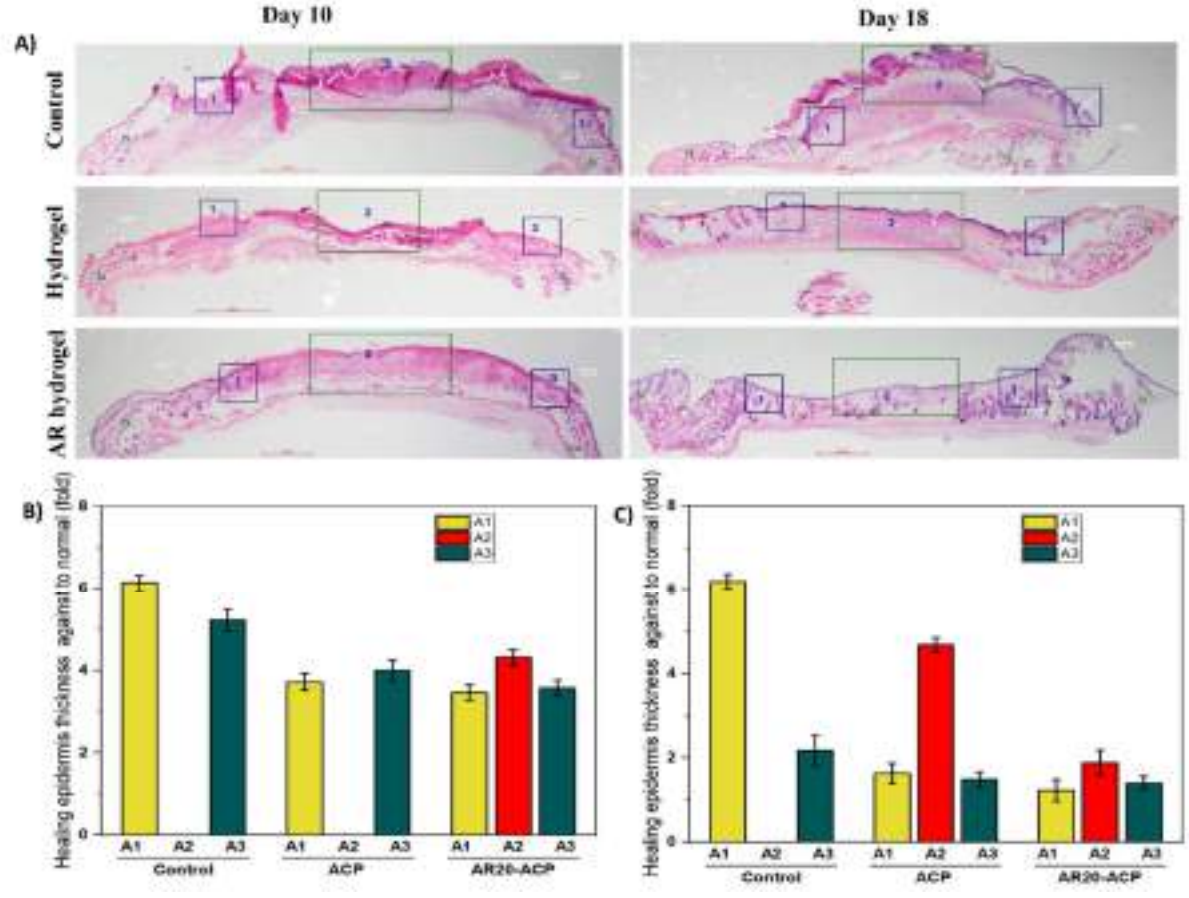

Figure 4.19: *The evaluation of the re-epithelialization process of the diabetic wound.*

A) H&E staining images of diabetic wound tissues on the 10th and 18th day after different treatments, respectively. The rectangle indicates the wound edge (A1 and A3) and the center (A2) of the wound bed. The percentage of epithelialization (n = 3) at B) day ten and C) day 18 post-wounding.

By day 18, the restoration of wound skin structure was significantly different in three groups (Fig. 4.19C). The centers of control wounds with saline treatment had no epithelial coverage after 18 days. The remodeling process in the edges wound was also unequal. The hemorrhaging and infiltration of inflammation cells appeared in A2 under the immature epidermis. In contrast, the full re-epithelialization of most wound-administered ACP hydrogel or AR20-ACP hydrogel was concluded by day 18. The significantly more effective re-modeling process was detected in the AR20-ACP hydrogel group. The epidermis thickness of wounds was comparable to that of undamaged skin. Notably, in the AR20-ACP hydrogel treatment, mice with complete wound closure also exhibited hair regrowth at the wound edges. Meanwhile, hair follicles and sebaceous glands were discerned in the dermal layer of the wound center, which was missing from other groups. These results demonstrated a well-organized wound-healing process with AR20-ACP hydrogel.

To further clarify the advantages of AR20-ACP hydrogels in the diabetic wound healing process, Masson's trichrome-stained tissue sections of wounds with different treatments were set up (Fig. 4.20 and A6). There was no significant difference in the organization of the fibrous matrix in the dermal layer among the three groups in the wound edge at day 10 (Fig. 4.20A). However, integrated collagen was observed only in the AR20-ACP group in the wound center. The level of collagen deposition in AR20-ACP at day 10 reached 30–40% compared to undamaged skin (Fig. 4.20B). The denser and better arrangement, appearing as regularly organized bundles, was seen on day 18 in all experimental groups, especially for ordered collagen bundles in AR20-ACP hydrogel (Fig. 4.20C). Wounds with saline treatment displayed a higher cellular and vascularised granulation following the rapid increase in myofibroblasts compared to day 10, proposing the formation of scarring. However, the epidermis of these wounds did not completely close, which increased the risk of skin barrier dysfunction. With ACP hydrogels, the epidermis of the wound was re-generated; however, cellularity in the dermis was still high, and increased scarring was possible. As expected, the infiltration of cells in the dermal layer was absent. The collagen deposition in AR20-ACP-treated wounds showed a more fibrillar morphology in the dermal layer than the dense irregular collagenous connective tissue feature of the normal skin. Therefore, AR20-ACP hydrogels were validated to be effective in accelerating wound healing and skin regeneration in a diabetic mouse model. Moreover, regarding inflammatory relief, granulation tissue formation, re-

epithelialization, remodeling, and collagen deposition, the more rapid wound healing and more advanced skin regeneration over the whole healing process strongly demonstrated the efficacy and potential of AR20-ACP hydrogel in burn wound healing.

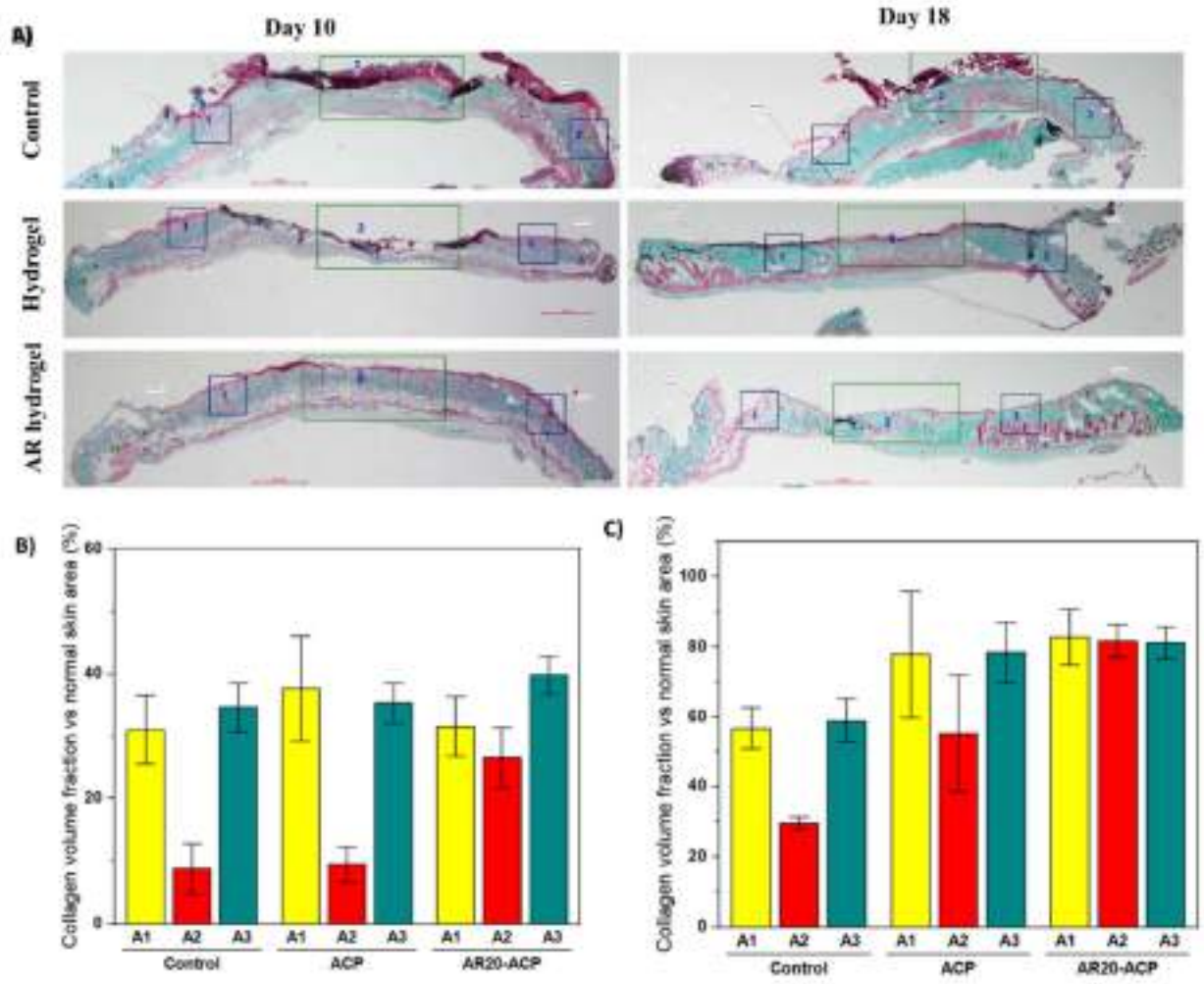

Figure 4.20: *The regeneration of the structure of dermal collagen fibers.*

A) Representative trichrome images of wounds on the 10th and 18th day post-treatment. Collagen is stained green. Scale bars = 100 µm. Collagen staining is quantified for B) day 10 and C) day 18.

4.10 Conclusion

Thermal-sensitive hydrogel-based alginate-cystamine-Pluronic was successfully prepared via copolymerization techniques. Cystamine was introduced to the alginate backbone through the "activated ester" method, forming an alginate-cystamine linker (AC). The hydroxyl group of Pluronic F127 was activated with nitrophenyl ester. The nitrophenyl ester groups were easy to replace by amino groups on AC, resulting in the formation of the new copolymer, Alginate-

cystamine-Pluronic (ACP). This copolymer inherited the thermal responsive feature of Pluronic. ACP hydrogel exposed reversible sol-to-gel transition in the response to temperature. The hydrogel exhibited excellent cytocompatibility. Because of their temperature sol-gel transitions, ACP copolymer has allowed facile encapsulation and controllable release of fibroblast cells. The gelation temperature is in the wide range (from 25^{o}C to under 37^{o}C) with mild conditions, envisioning the suitable 3D encapsulation of cells. The outgrowth cells from the cluster form the cell layer on the surface of the culture dish, which is similar to a 2D culture. Also, the ACP copolymerization was used as the carrier to combine a bio-safe NO donor L-Arginine and ROS scavenging compound Resveratrol for rapidly treating wound burns in a diabetic model. The incorporation of L-arginine could re-design the release profiles of Resveratrol sustainably. Notably, the dual incorporation of Resveratrol and L-arginine gave the thermally sensitive ACP hydrogel a prominent anti-oxidative capacity. ROS activity was very high when the macrophage cells or stress cells were cultured with a single L-arginine-based system or native ACP hydrogel. NO, a vital gasotransmitter that stimulates wound repair, was only formed with the L-arginine system. In addition, the formation of peroxynitrite, a powerful oxidant that is toxic to cells due to the combination of ROS agents and NO, was relatively high. The co-loading with Resveratrol as a ROS scavenging constituent helped to reduce the superoxide anion and the production of stress cells, consequently maintaining the stability of NO induced by L-arginine. In addition, the AR-ACP hydrogel system efficiently inhibited the growth of some common bacteria on wound sites due to a synergistic effect of L-arginine and Resveratrol. Hemolysis and skin irritation measurements confirmed the biocompatibility of the AR-ACP system. *In vivo* experiments indicated that the system promoted wound healing in the diabetic mouse model. Histological analyses revealed that the system facilitated the formation of collagen fibers and blood vessels and recruited a large number of macrophages, which indicated an accelerated repair process for the wound tissue. Our work provides an alternative strategy for wound management with dual-function hydrogel dressing, ROS scavenging, and NO signaling, which prevents pathogen infections and promotes wound healing sustainably, possibly providing a solution for diabetic wound therapy in clinical or household settings (schematic 4.1)

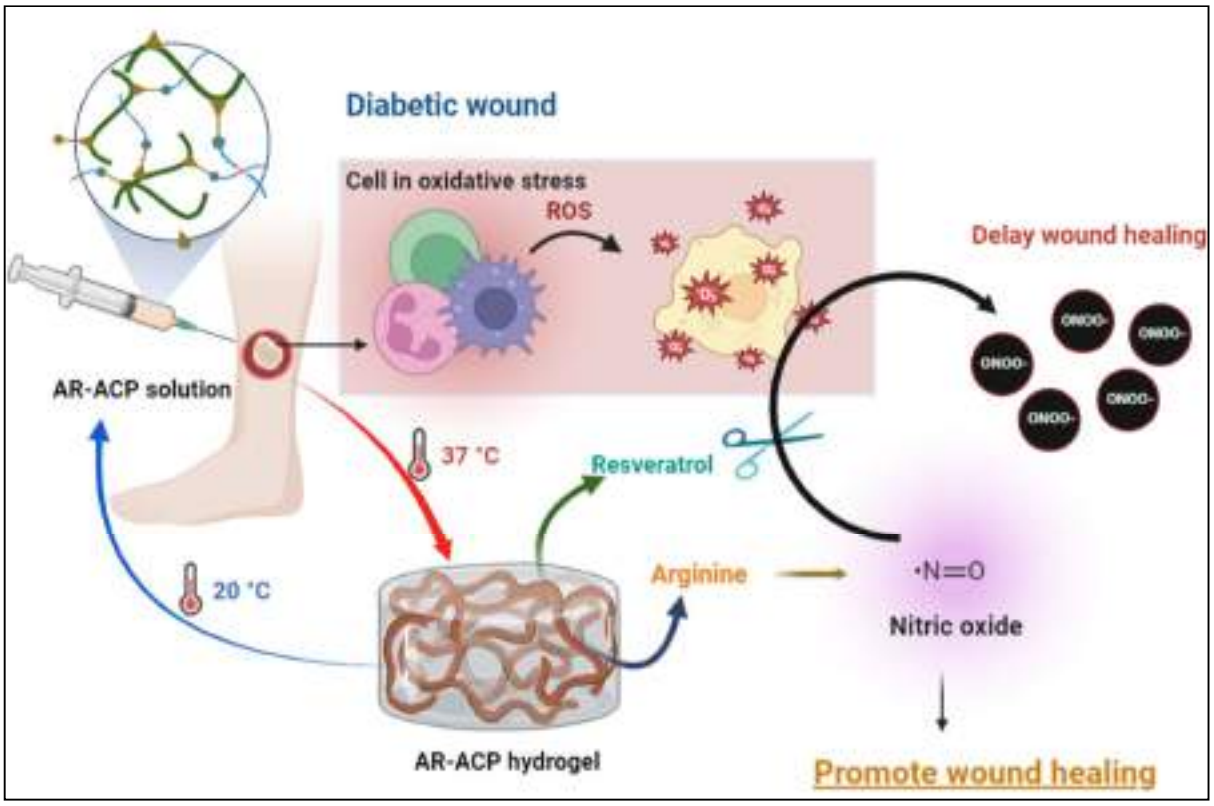

Schematic 4.1: *Schematic illustration of a reasonable design of the AR-ACP hydrogel dressing for diabetic wound.*

CHAPTER 5: CONSTRUCTION OF THERMAL RESPONSIVE HYDROGEL FROM ALGINATE AND PLURONIC VIA CROSS-LINKING TECHNIQUE FOR BONE REGENERATION

5.1 Critical thinking for development

Alginate is favoured for repairing cancellous bone due to its similarity to natural tissue structure[251]. The affinity of alginate for cations, particularly Ca^{2+}, leads to supersaturation within confined spaces in the alginate structure[102]. This phenomenon governs the location and polymorphism of crystals, thereby conferring biomineralization capabilities to the alginate scaffold [246]. Moreover, alginate has received human applications approval from the United States Food and Drug Administration (FDA), indicating its safety [234, 235, 249, 251, 265]. In this context, thermal-responsive hydrogels based on sodium alginate and Pluronic F127 have gained significant attention.

There is substantial interest in designing and developing hybrid polymers by chemical crosslinking[140]. Incorporating the interfacial modifiers as crosslinking agents presents a straightforward approach, as it builds upon readily available commercial polymers and processing equipment[133, 136, 137]. Among the various crosslinking agents, the catechol group has garnered attention as a non-toxic option for creating in situ hydrogels[136]. Catechols can be readily oxidized to form reactive o-quinones, which undergo secondary reactions to establish covalent crosslinks[137]. Also, inspired by the impressive adhesive properties of marine mussels on wet or moist surfaces, the catechol motif has been identified for its potential to enhance adhesion[138]. The amino acid 3,4-dihydroxy-L-phenylalanine (DOPA), containing numerous ortho-dihydroxyphenyl (catechol) functional groups, is abundantly present in mussel adhesion proteins[295]. These catechol groups can form robust covalent and noncovalent bonds with organic and inorganic surfaces[136].

The focus of most investigations into the crosslinking methods for hydrogel-based DOPA has centered around the coordination of ionic bonds between catechol groups and transition metal ions[137], particularly Fe3+, as well as covalent crosslinking through the utilization of oxidizing agents, notably $NaIO_4$[138]. However, the broader applications of these techniques have been hindered by challenges related to poor biocompatibility and limited stability within biological environments [136, 137]. These challenges are effectively addressed through the presence of peroxidase enzymes.

Despite the advancements mentioned earlier, two significant challenges persist in the context of native peroxidase-catalyzed in situ hydrogel formation based on catechol oxidation[110]. The favourable pH condition for oxidation can disrupt the protein scaffolds, potentially leading to a loss of peroxidase function[112]. Moreover, peroxidase has been identified as having the potential to trigger immune responses in humans and other mammals due to its protein

sequence[296]. To surmount these limitations, substantial efforts have been dedicated to the development of peroxidase-mimicking enzymes[144, 225, 297]. This innovative approach aims to overcome the challenges associated with native peroxidase by creating enzyme-analogue material that replicates the catalytic activity of peroxidase[141, 143]. By doing so, researchers aim to achieve improved control over the oxidative catechol crosslinking process, addressing the pH sensitivity and immune response issues and enabling the broader use of mussel-inspired hydrogel systems in various biomedical applications.

In addition to injectability, adhesiveness, and self-healing properties, ideal hydrogels for bone regeneration should also exhibit osteoconductivity[50, 298]. Bioactive glass (BG) has gained prominence in this field due to its potential to induce new bone formation by promoting hydroxyapatite formation, providing infection protection through released metallic ions, and showing anticancer properties[174, 222]. The inclusion of BGs within hydrogels can significantly enhance their osteogenic activity[27]. Notably, BGs can exhibit various functionalities based on their composition[174]. By drawing inspiration from the peroxidase-like function of cerium oxide, the co-synthesis of ceria and bioglass has been used to govern the enzymatic activity of hybrid nanoparticles[299, 300]. In another study by Ziqi Xu[225], incorporating gold nanoclusters into the BG network showcased a novel function for BG: peroxidase-like catalytic activity. Therefore, BGs with peroxidase-mimicking properties could be more effective strategies for designing mussel-inspired hydrogels with injectability, adhesiveness, and enhanced bioactivity.

Hemin, an iron porphyrin compound with biological activity, possesses an analogous catalytic centre to horseradish peroxidase (HRP)[141, 142]. Its remarkable catalytic performance has garnered significant attention in peroxidase-mimicking enzymes[141]. Employing a ‘bottom-up’ approach, researchers have successfully fabricated hemin-based peroxidase mimetic catalysts[142]. This method emulates catalytic functions and replicates the active sites of natural peroxidases, offering a deeper comprehension of the origins of natural enzymes[141, 297, 299].

Therefore, in this study, the peroxidase mimicking bioglass based on hemin nanoparticles was developed and then using as the catalyst for crosslinking dopamine derivative alginate and dopamine derivative Pluronic resulting in the multifunctional thermal sensitive hydrogel for bone regeneration.

5.2 Characterization of the bioglass as a catalyst for catechol crosslinking

5.2.1 Preparation of HNP BG

5.2.1.1 Preparation of HNP nanoparticles

Hemin first underwent a solvothermal carbonization reaction in methanol to make HNPs. The TEM images show that the HNPs have a dispersive and uniform morphology (Fig. 5.1A). The DLS results showed that the average hydrodynamic diameter of HNPs was about 33.4 nm. However, the PDI value of HNPs indicated that the system had a highly polydispersed and moderately dispersed distribution. Encouragingly, a function of the delay time of HNPs in water is deconvoluted into a single exponential (Fig. 5.1C), confirming a single broad population. HNP solution (Fig. 5.1D) was clear and transparent after dissolving in water, confirming the highly dispersive property of HNPs. The ultraviolet–visible (UV–vis) spectrum of hemin in NaOH displays two split Soret bands at 360 and 385.5 nm and Q bands at 500 nm [142]. Under the carbonization, the absorption peak of hemin was unchanged but showed a redshift (Fig. 5.1E). It was observed that HNPs had another absorption peak at 266 nm, which was derived from the n–π* transition of the functional groups with a lone pair of electrons [301]. In addition, HNPs displayed fluorescent emission, whereas the raw material hemin had none, which agrees with some reports [142, 301]. Under UV light, the color of the HNP solution changed from yellow to green (Fig. 5.1D). The fluorescent properties of HNPs were then examined in water. HNPs showed excitation-dependent emission features. As shown in Fig. 5.1F at the excitation wavelength of 470 nm, the HNPs showed a strong fluorescent emission at 500 nm, corresponding to the green color, similar to previous reports. Based on these results, it can be deduced that the solvothermal reaction carbonized hemin and successfully produced hemin in the nanosized particles with a new physical property (fluorescent emission).

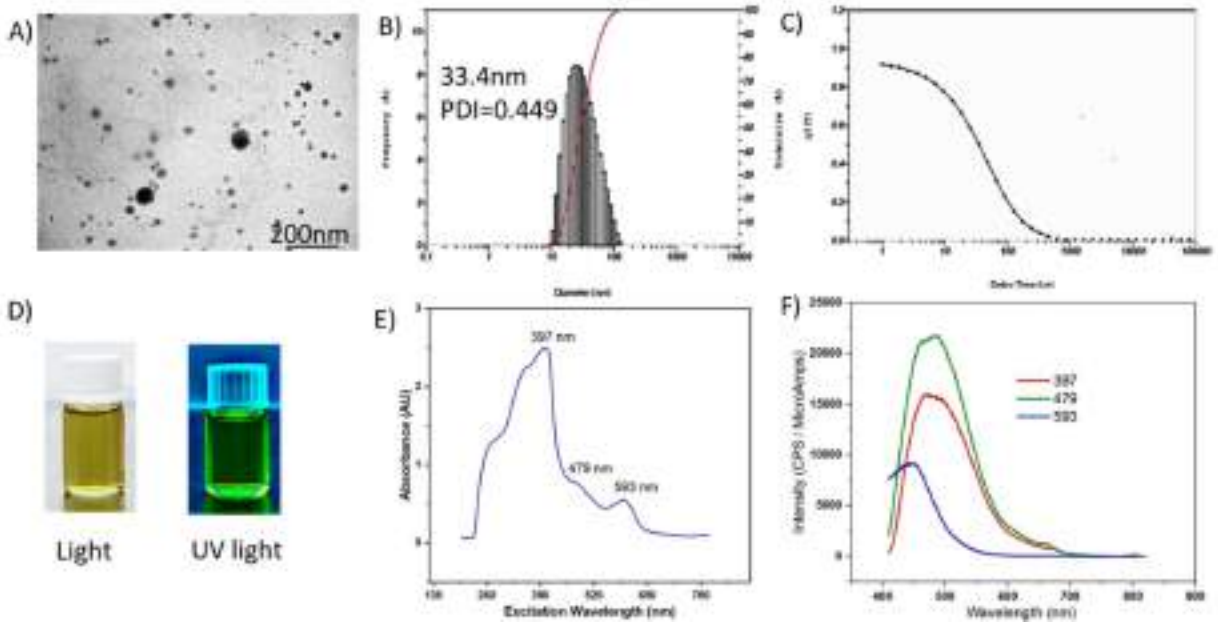

Figure 5.1: *Characterisation of hemin nanoparticles, HNPs.*

A) The typical TEM image, B) the hydrodynamic size in water and C) the DLS autocorrelation functions of the synthesised HNPs. D) The photo image of vials containing HNP solution under white and UV light. E) The absorbance wavelength and F) emission (Em) spectra of HNPs in water at different excitation wavelengths.

5.2.1.2 Preparation of HNP BG

The bioglass (BG) was synthesised via the sol–gel method. Figure 5.2A shows the size, morphology, and distribution using the SEM images and elemental analysis using the EDS spectrum of synthesised BG. BG was observed to be a size of around ∼150 nm with dense, spherical, and monodispersed particles. According to the EDS mapping (Fig. 5.2B, C), the three main elements in BG, Si, Ca and P, are uniformly distributed in the BG. The addition of HNPs did not influence the size or morphology of BG (Fig. 5.2D). Compared to native BG, the EDS mapping (Fig. 4.2E), as well as the spectrum of HNP BG (Fig. 5.2F), displayed the new element signal corresponding to Fe, accounting for 0.77% by mass. Intriguingly, HNP BG showed a strong fluorescence emission at 500 nm when excited at 479 nm (Fig. 5.2G), similar to HNPs. Confocal microscopy was conducted to support this evidence (Fig. 5.2H). The green fluorescent signal was emitted from HNP BG under the excitation of λ = 480nm. The XRD patterns of native BG and HNP BG are compared in Figure 5.2I. As expected, the BG and HNP BG were approximately amorphous. However, some crystallisation had occurred in HNP BG. The identified crystalline phases were calcite (ICDD: 01-072-1937). In addition, the board diffraction peak in the XRD pattern of BG was a hypsochromic shift from the region of 20–

25° to 23–32°, confirming the mixture of crystalline regions of hemin into a crystalline phase of BG [225, 300]. According to the results obtained from the reported analysis, it can be concluded that the HNP BG was successfully synthesised in this study.

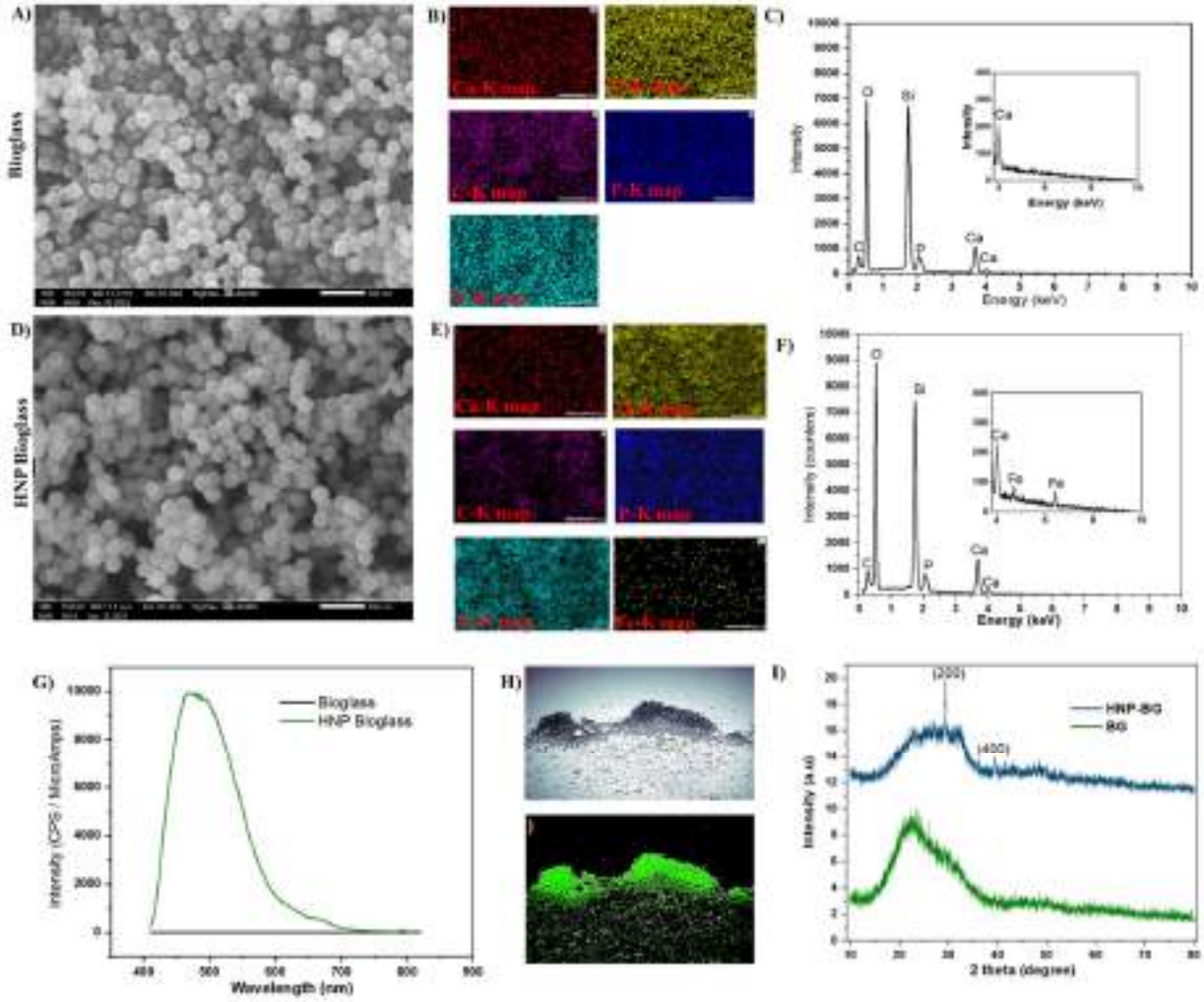

Figure 5.2: *Characterisation of HNP BG.*

SEM image in combination with its surface mapping EDS for characteristic main elements (C, O, Ca, P, Si and Fe) of distribution and whole EDS of native bioglass BG (A, B, C) and HNP BG (D, E, F). G) The emission (Em) spectra of HNP BG and BG nanoparticles in water at excitation 479 nm. H) The figure of HNP BG under bright light and fluorescent light (Ex = 480, Em = 525). I) The XRD pattern of BG and its derivative HNP BG.

5.2.2 Peroxidase-mimicking function of HNP BG

To go one step further, the possibility of peroxidase-mimicking characteristics of HNP BG was studied. Pyrogallol was used as the substrate for the peroxidase activity measurements. The

peroxidase-like oxidation of pyrogallol yields purpurogallin, whose formation can be monitored by UV–vis spectroscopy or visual observation. In the presence of an oxidant such as hydrogen peroxide (H_2O_2), the colourless pyrogallol converts to a yellow product, purpurogallin. The signal of purpurogallin was undetectable in the case of pure BG (Fig. 5.3A, B), even with longer incubation. Purpurogallin was immediately formed with the addition of HRP enzyme, HNPs or HNP BG, confirming that peroxidase-mimicking activity was related to HNP only. In the catalytic course of HNP BG, shown in Figure 3A, the intensity of purpurogallin was increased following the increase of HNP BG concentration. Therefore, to pinpoint the catalytic selectivity of these design materials as HRP enzymes, the reactions with various concentrations of HNPs or its derivative HNP BG were carried out at a constant pyrogallol (2.5 mM) and a hydrogen peroxide concentration of 20 mM. With a similar number of active sites to the HRP enzyme, the absorbance at 420 nm induced by oxidation of pyrogallol using 4 ng/ml HNPs could not be detected. When the number of active sites in the HNP solution was more than 50 times that of HRP, the intensity at 420 nm was nearly comparable to the native enzyme (Fig. 5.3B). The analysis of the performance of HNPs in the pyrogallol oxidation reaction followed the conventional enzymatic dynamic regulation of the Michaelis–Menten equation (Fig. 5.3C). The obtained Lineweaver–Burk plots of HNPs or HRP were a nearly perfect linear relationship. The Km value of HNPs was 3.932 mM, two orders of magnitude better than that of HRP (Fig. 5.3D). This result was consistent with previous reports; the binding affinity of hemin to the substrate is more pronounced than that of HRP enzyme, which is significantly related to the high-index surface of the active site[142, 302]. The active site of the HRP enzyme is a groove in the polypeptide pocket, while the active site in HNPs is naked. Therefore, the affinity of H_2O_2 for HNPs is stronger than the heme group within the HRP enzyme. Despite the lower turnover frequency (Kcat), the catalytic efficiency (Kcat/Km) of HNPs (235.7 $mM^{-1}.min^{-1}$) is also about 1.73 orders of magnitude better than that of the natural enzyme HRP.

Based on the pyrogallol reaction with HNPs, the HNP BG concentration started from 1 mg/ml. However, the UV–vis results from the addition of HNP BG samples in Figure 5.3B did not yield conclusive results. The absorbance of the peak present at ~420 nm of 1 mg/ml HNP BG does not precisely match the same amount of native HNP solution (40 µg/ml). The absorbance at 420 nm was below 0.5 under the catalytic 1mg/ml HNP BG, which was three times lower than 40 µg/ml HNPs. Also, the yellow colour intensity of the reaction with HNP BG was significantly weaker than that of native HNPs. The reduction in the catalytic ability of HNPs after processing in BG could be explained due to the hinder interaction between the substrate and catalyzer [141-143, 225, 302]. The matching of the catalytic performance to 40 µg/ml

HNPs was observed when the concentration of HNP BG was 5 mg/ml. The affinity of HNP BG for pyrogallol was similar to native HNPs. The rate of the catalysing reaction by HNP BG (Vmax = 0.33 min^{-1}) was comparable to that of the HNPs (Vmax = 0.31 min^{-1}) at a concentration of 40 µg/ml. This rate was also identical to the native HRP enzyme. Along with the similar catalytic activity as native HRP enzyme, HNP BG could be an effective method to promote peroxidase-like activity over a wide range of temperatures. Almost all natural enzymes work effectively only within a narrow temperature range [302]. In our case, the catalytic activity of the HRP enzyme was decreased tremendously by increasing the temperature from 25 to 80ºC (Fig. 5.3E) HRP enzyme could not perform its catalytic activity when the temperature was over 80 ºC, suggesting complete denaturation. Like HRP, other peroxidase mimics (for example, Fe_3O_4 [303], graphene oxide[304], gold nanoparticles[305], etc.) only worked effectively within a narrow temperature range (i.e., inactive at high temperatures). Intriguingly, in contrast to natural enzymes, the relative activity for the oxidation of HNP BG was independent of temperature. The amount of purpurogallin remained unchanged as the temperature increased from 25 to 100 °C. These results further confirmed that natural enzymes could easily lose catalytic activity when the environment changes, whereas HNP BG has excellent stability under stringent conditions.

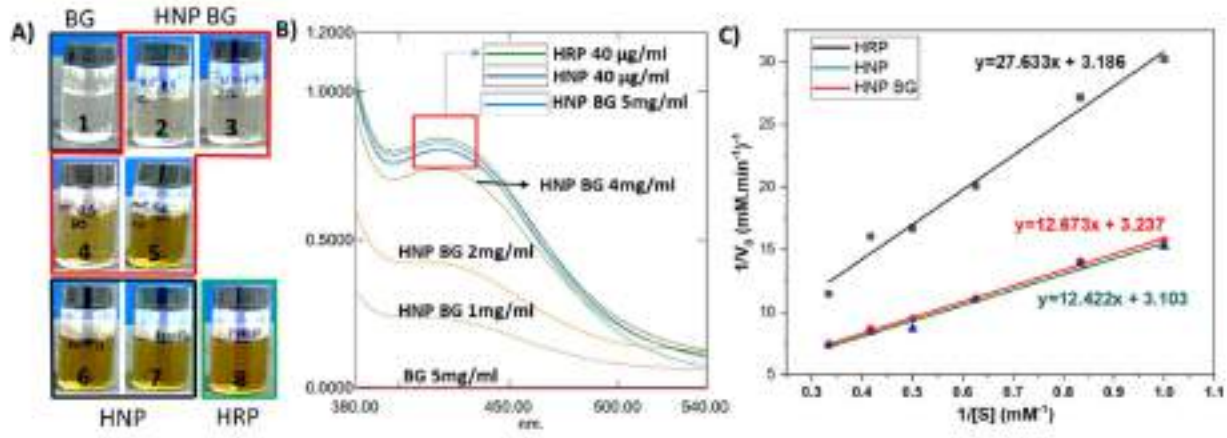

D)

Parameter	Type of catalyst		
	HRP	HNP	HNP BG
Km (mM)	8.673	3.932	4.003
Kcat (min^{-1})	1177	926.8	9.667
Kcat/km ($mM^{-1}.min^{-1}$)	135.7	235.7	2.415

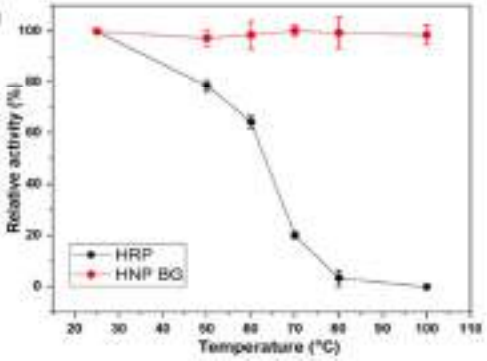

Figure 5.3: *The catalyst activity of design systems (HNP, HNP BG) under the oxidative reaction of pyrogallol compared to native HRP enzyme.*

A) The picture and B) their UV–vis spectrum of the oxidative pyrogallol reaction under different types of catalyst reagents after 5 min incubation. 1. BG 5 mg/ml; 2. HNP BG 1 mg/ml; 3. HNP BG 2 mg/ml; 4. HNP BG 4 mg/ml; 5. HNP BG 5 mg/ml; 6. HNPs 20 µg/ml; 7. HNPs 40 µg/ml; 8. HRP enzyme 40µg/ml. $V_{catalyst}$ *= 20µl,* V_{total} *= 3ml. C) Lineweaver–Burk plot of the pyrogallol oxidation catalyzed by HRP (40 µg/ml, black line, and completed square), HNPs (HNPs 40 µg/ml, red line, and completed circle), HNP BG (5 mg/ml, cyan line and completed triangle) and D) their corresponding kinetic parameters. [pyrogallol] = 1–3 mM,* $[H_2O_2]$ *= 20 mM, T = 25* ^oC*. The relative activity of HRP enzyme and HNP BG following the increase in temperature (E). Data was presented as mean ± SD, n = 4.* ε*= 2460* $M^{-1}.cm^{-1}$.

5.2.3 The potential of HNP BG as a catalyst for catechol crosslinking

Dopamine (DA) is a member of the catechol compounds[136, 295]. It serves various essential functions in the brains and bodies of animals as a neurotransmitter belonging to the catecholamine and phenethylamine families. Oxidation of DA leads to the formation of the corresponding dopamine-o-quinone (DQ), followed by a further cyclization step and its subsequent oxidation to monochrome (AC)[137]. The rearrangement reaction, which involves AC to form 5, 6-dihydroxyindole (DHI) or 5,6-indole-quinone (IQ), forms covalent bonds between monomers and their subsequent polymerization products[134]. Inspired by oxidative crosslinking to form polydopamine, DA has been used instead of conventional crosslinkers for making the composite hydrogel [26]. The HRP/H_2O_2 couple is frequently chosen as a biomimetic oxidizing agent for catechol crosslinking hydrogels. Before fabricating mussel-inspired catechol-functionalization hydrogel, the polymerization process of DA was studied based on variations of UV–vis spectra in response to oxidation with H_2O_2 with the help of the HRP enzyme (Fig. 4.4A) or HNP BG (Fig. 5.4B). Similar to previous oxidative test functions, HNP BG has the ability to catalyze the H_2O_2-driven oxidation of DA to monochrome (AC), in analogy to HRP. Pristine DA exhibited characteristic peaks at 280 nm corresponding to the molecular electronic transition in phenolic catechol amines. Adding H_2O_2 did not induce any change in the UV–vis spectrum of DA over 1 hour. Upon adding HRP or HNP BG, the peak at 280 nm immediately intensified and red-shifted to ~300 nm. In comparison, a broad shoulder in the visible region (~400 nm) appeared, confirming the formation of different DA-derived quinones, as described in the literature [306, 307]. With the increase of the incubation time, the absorbance due to the formation of the dopachrome intermediate DQ at 300 nm increased while the absorbance at 400 nm tended to broaden in the range of 400–600 nm, suggesting

further transformation to the indole family. To confirm the UV–vis result, the behaviour of chromatographic retention and product ion spectra of oxidative DA were studied. Under the selected HPLC–MS analytical conditions, the peak retention time due to the reaction of DA and H_2O_2 under HNP BG was the same as the HRP enzyme (Fig. 5.4C), suggesting that the oxidation course of HNP BG is identical to the HRP enzyme. Further verifying the presence of the polydopamine structure, a rapid liquid chromatography/tandem mass spectrometry (LC–MS/MS) method has been developed. In fact, various polydopamine monomers are generated during the oxidative reaction. Oxidative coupling of DA units connecting two or more benzene rings by the formal loss of two hydrogen atoms is a well-known reaction for polydopamine. Based on the molecular weight of the possible building blocks proposed in Figure 5.4D, 5,6-indol-quinone (m/z 147) was selected as the monomer in this study, defined as M. Gratifyingly, the mass peaks could be detected for oligomers with different degrees of saturation from dimer to nonamer, as depicted in Figure 4E. The first one is the m/z dimer peak of 299.14 (2M + 6H) or 338.09 (2M + 6H + Ca^{2+}). The appearance of the peak at m/z 456.98 was assigned for the trimer oligomers (3M + 18). In addition, the tetramer (4M) was exhibited in the mass spectrum, which predicted the origin from the covalent bonding between trimer and pyrrole-carboxylic acid ($C_4H_{14}NO_3^+$) moieties derived from the oxidative degradation of indole units. Moreover, the positive spectra of the various polydopamines with higher repeating building block hybrids with calcium ions from HNP BG, such as pentamers (5M + 20 + Ca^{2+}), hexamer (6M + 30 + $2Ca^{2+}$), etc., were proposed in this study. Altogether, the results revealed the possible strategy of HNP BG as the alternative catalyst for DA crosslinking hydrogel.

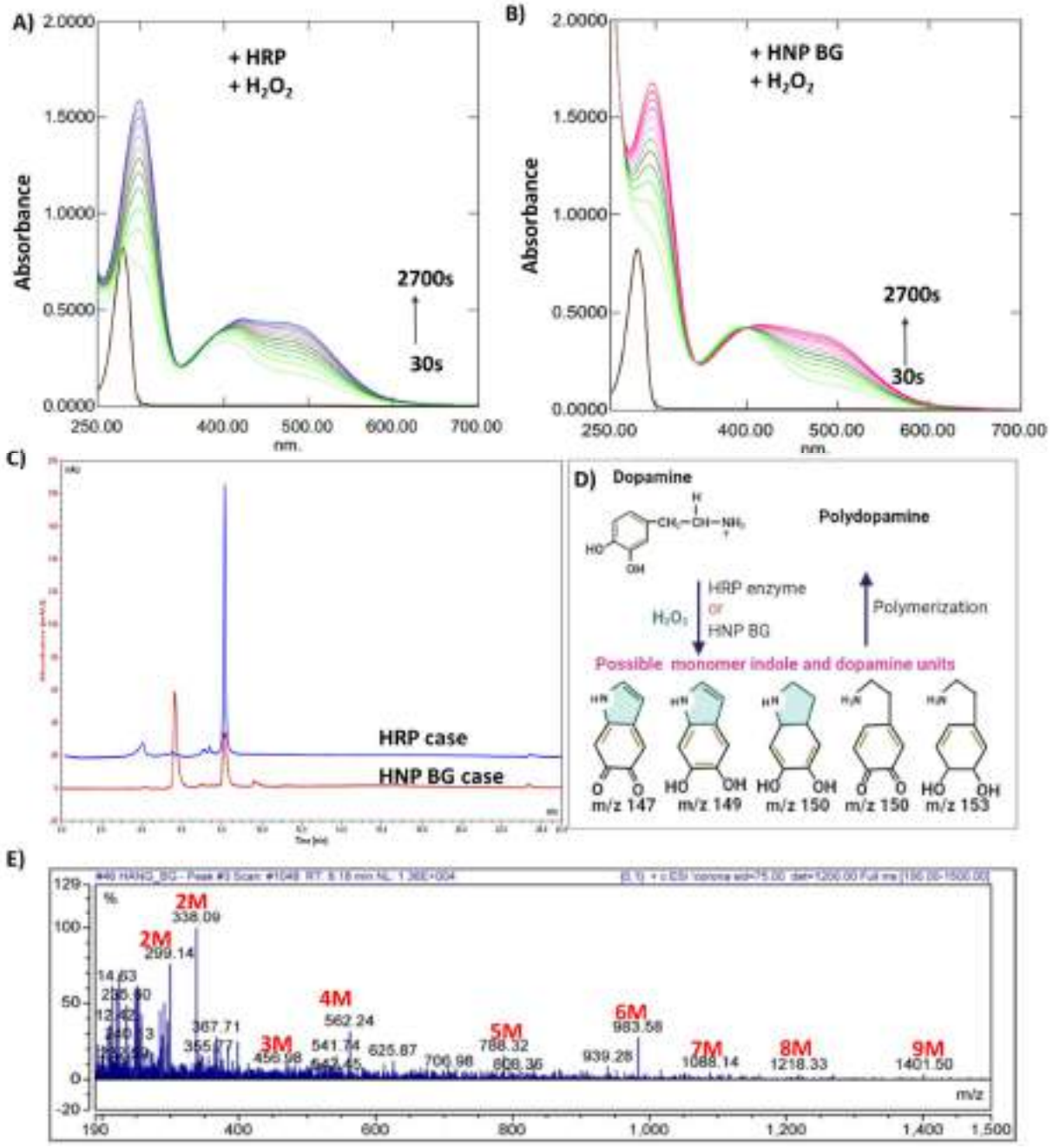

Figure 5.4: *The oxidative pathway of DA under the catalyst of HRP enzyme or HNP BG in DI water.*

UV–vis spectrum of DA solution after addition of H_2O_2 and catalyst, A) HRP enzyme and B) HNP BG recording within 2700 s. C) The reaction was then analysed with LC−MS (ESI+) analysis. D) The suggested monomer forming after the oxidative reaction was used to identify the self-polymerisation of the DA product. E) The mass spectrum of oxidative DA under the catalyst of HNP BG.

5.3 Preparation of catechol precursor based on alginate and Pluronic

Figure 5.5A presents the fabrication process of these precursor polymers. The conjugation of catechol hydroxyl-phenols on the alginate backbone (ADA) was performed via the carbodiimide coupling reagent. In the case of Pluronic F127, the hydroxyl group at both terminal ends was first activated with p-nitrophenyl chloroformate to generate 4-nitrophenyl carbamates as a specific site for substitution of amino motifs on DA, resulting in the coupling of a catechol group to both ends of Pluronic F127 (ADA). Both native sodium alginate and Pluronic did not show absorption bands in the 250–800 nm (Fig. 5.5B). After conjugating dopamine, UV–vis spectra of ADA and PDA show absorption bands at λmax = 280 nm corresponding to the L_a–L_b transitions in phenolic catecholamines in pristine DA. From UV–vis spectroscopy, Beer's law was used to calculate the amount of catecholic anchor on the polymer backbone. The conjugation efficiencies for alginate and Pluronic F127 were 13.91 ± 2.55% (30.7 ± 0.02 mg catechol/g alginate derivative) and 94.78 ± 3.22% (23.02 ± 0.78 mg catechol/g Pluronic derivative).

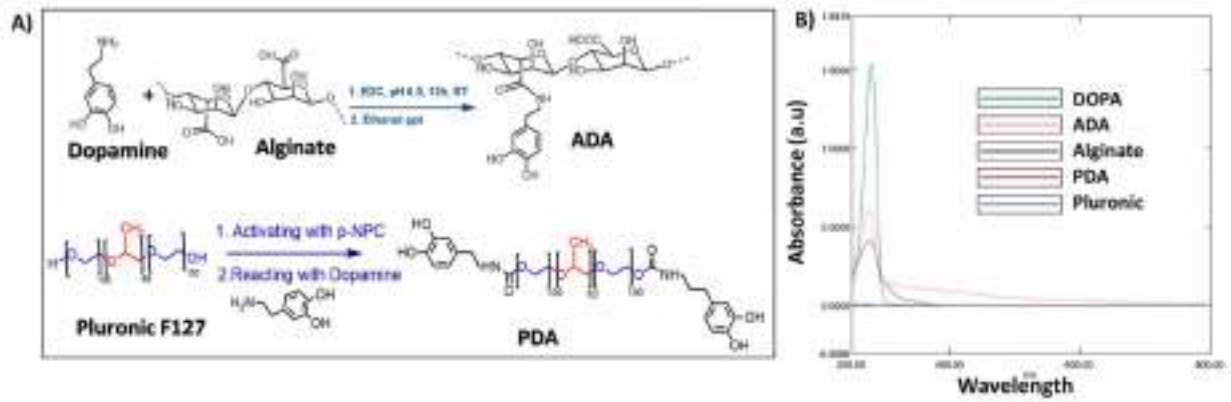

Figure 5.5: *Preparation of catecholic anchor precursor polymers.*

A) The synthesis route of catecholic anchor (DA) polymers, alginate–dopamine (ADA) and Pluronic F127–dopamine (PDA) and B) their UV–vis spectra along with precursor reactants (DA, sodium alginate and Pluronic F127).

5.4 Preparation of the thermal responsive hydrogel based catechol chemistry

5.4.1 The formation of catechol crosslinking between two catechol precursors

UV–vis spectroscopy was used to track the change in catecholic anchor (DA) polymers during the reaction process to investigate the gelation mechanism. The UV–vis results from the polymer-based DA solution samples in Figure 5.6C yielded conclusive results about the formation of catechol−catechol adducts between polymer-based DA triggered by H_2O_2 and HNP BG. For single DA derivative polymers, the quinone peak (λmax = 401 nm) appeared

immediately after the addition of HNP BG, indicating the rapid oxidation of DA polymers in the presence of oxidants (Fig. 5.6C). Following that, the absorption peaks at 401 nm showed the bathochromic shift to 500 nm, possibly resulting from dicatechol formation, suggesting the formation of 5,5'-di(3,4-dihydroxyphenylalanine) (DA in dimer form) as the possible coupling mechanism through aryloxy radical formation on the DA phenyl ring (fig 5.6 B). These UV–vis profiles were matched precisely with the oxidation pristine DA shown in Figure 4.4B. Oxidation of dual DA derivatives showed results in the same spectra as a single derivative. However, the red-shifted quinone peak was quicker than that of the single one. Along with the main peaks comparing favourably with DA chrome, the peak at λmax = 300 nm was the emergence, which is believed to be a precursor to the formation of melanins, high molecular weight polymers crosslinked from catecholamines. The results described here indicate that dual DA derivative polymers, ADA and PDA, are capable of rapid gelation in situ under mild physical conditions.

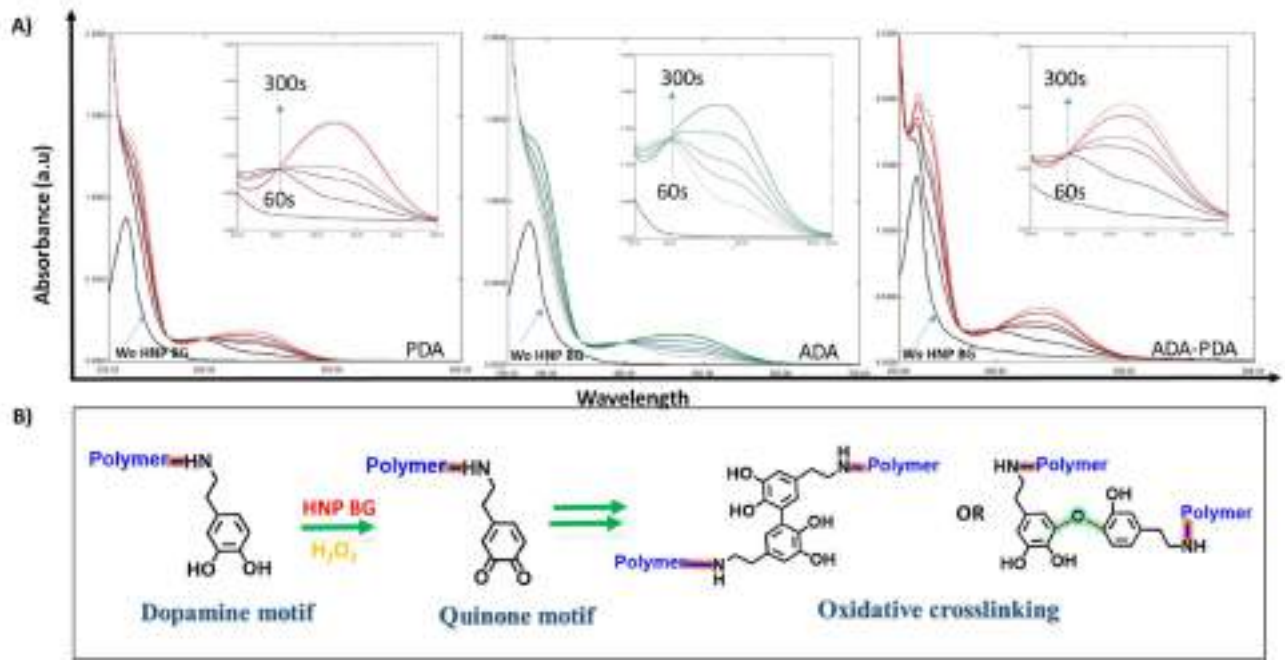

Figure 5.6: *Characterisation of oxidative reaction of catecholic polymer in the presentation of HNP BG.*

A) The function of HNP BG in performance of the crosslinking between catecholic polymers. The real-time evolution of UV–vis spectra for PDA, ADA and the mixture ADA–PDA (1:1) solutions with the addition of HNP BG 5 mg/ml recording from 250 nm to 800 nm. B) The illustration of the formation crosslinking between dopamine motif on each polymer backbone.

5.4.2 Preparation of the hydrogel

Next, hydrogel formation based on DA derivative polymers in single or dual combination was studied via the sol–gel transition; the results are presented in Figure 5.7. Consistent with previous reports showing the formation of DA derivative Pluronic F127 hydrogels, a higher concentration was required for hydrogel formation than that of the bare Pluronic.

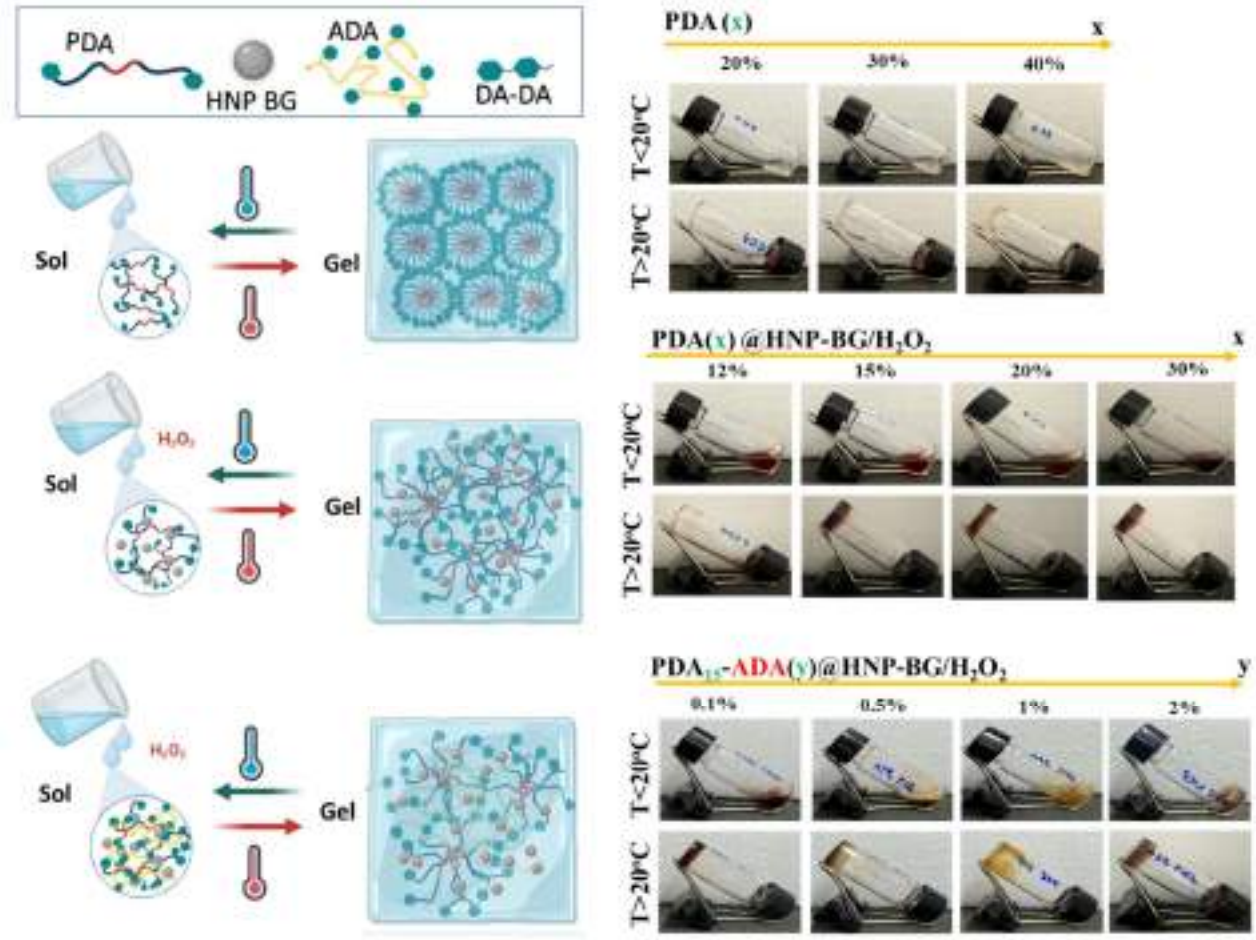

Figure 5.7: *Thermal responsive behavior of the resultant hydrogel via the oxidative reaction of catechol under the help of HNP BG.*

The tube inversion method for sol–gel conversion of PDA with/without HNP BG/H2O2 and the mixture PDA–ADA. x and y denote the concentrations of PDA and ADA, respectively.

The addition of DA to the Pluronic F127 showed sol–gel transition properties significantly shift to the left with an increase to 40 wt%, whereas Pluronic F127 was ~16 wt%. It is known that the Pluronic copolymers aggregate with increasing temperature in the form of spherical micelles by enhanced hydrophobic interactions between PPO middle blocks of the copolymers. Above a critical concentration, the self-assembling Pluronic micelles are closely packed to

Generate a physically crosslinked hydrogel structure. The additional presence of a catechol group moiety at the PEO distal end of Pluronic F127 might disturb the well-ordered micellar integrity as well as the packing density due to the variation in hydrophilic/hydrophobic balance of Pluronic F127, thereby raising the gelation concentration [56]. With the addition of HNP BG along with H_2O_2, the gelation of PDA was shifted to a lower concentration regime. The gelation concentration of PDA was detected at 15 wt% at temperatures higher than 30 ºC. The gelation was reversible between 4 ºC and 30 ºC similar to the bare Pluronic hydrogel. This behavior was proved with the temperature sweep test. As shown in figure 4.8A, 15% PDA the formulation was observed to regain its solution state, reaching almost the same start-up values of G' and G''. When HNP BG and H2O2 was added along PDA_{15}, the viscoelastic response of PDA_{15} was significant changed (fig 4.8B). Upon heating from 5°C, only G'' was detected, confirming the liquid stage of the sample. From 25ºC, the solution showed the ability to store energy elastically. After this point, G' is one order of magnitude higher than G'', inferring gel structure formation. In addition, the color of the PDA solution was changed from colorless to dark brown, confirming the oxidative process of the catechol group [302, 306, 307]. HNP BG induced the oxidation of the DA motif and subsequent self-crosslinking between Pluronic micelles, which generated loops and tails on the shell layer of the packed Pluronic micelles, providing physically and chemically interconnected, tightly bound junctions between them. Therefore, the PDA_{15} with HNP BG/H2O2 indicated a predominant viscoelastic behavior typical of hydrogels, while pure PDA15 was typically observed for viscous solutions.

The 15% PDA and 0.1% ADA mixture formed hydrogels within 60 s. The mixmix PDA–ADA maintained sol-like behavior at cool conditions and returned to the gel stage at warm temperatures (T > 30 C30 ºC). Figure 5.8 B showed that G′ and G″ of $\underline{PDA_{15}\text{-}ADA_{0.1}@HNP}$ BG/H_2O_2 followed the function of temperature. The drastic change in elastic modulus and crossover between G′ and G″ at ca. 22.61 °C is characteristic of a sol–gel phase transition [274]. In contrast to $\underline{PDA_{15}@HNP}$ BG/H_2O_2, the elastic portion of the viscoelastic behavior appeared in the initial temperature testing condition, suggesting links inside the material, for example chemical bonds or physical-chemical interactions [226]. Increase the concentration of ADA to 0.5%, the sol-gel phase transition was unchanged (fig 5.8C). However, the G'' values of $\underline{PDA_{15}\text{-}ADA_{0.1}@HNP}$ BG/H_2O_2 was higher than $\underline{PDA_{15}\text{-}ADA_{0.5}@HNP}$ BG/H_2O_2 after reaching the phase transition. This confirmed that the more interaction forces in $\underline{PDA_{15}\text{-}ADA_{0.5}@HNP}$ BG/H_2O_2 than that of $\underline{PDA_{15}\text{-}ADA_{0.1}@HNP}$ BG/H_2O_2. The existence of high density of crosslinking prevent the transformation of deformation energy into heat energy, suggesting the ideally elastic hydrogel [226]. However, at ADA concentrations at 1 wt%, we did not observe any significant sol–gel transition properties. In agreement to inverted tube

method, the crossover between measured G′ and G″ curves of $\underline{PDA_{15}\text{-}ADA_1@HNP}$ BG/H_2O_2 were undetectable (fig 5.8E). Obviously, the G′ of this hydrogel was always higher than G″ at all temperature. Interestingly, increase the temperature, both G' and G'' were increased very obvious, indicating the sensitivity of this system to temperature. After 22-23°C, the viscosity of the composite system tends to be stable in the process of increasing the temperature. It was known that ADA alone became a gel state at 1% following the addition of HNP BG. This is not only the result of oxidative crosslinking of DA but also the result of the 'egg-box' model of the alginate backbone with bivalent cations that release from BG [241, 242]. Therefore, the higher the concentration of ADA, the density of crosslinking due to ADA is sufficient, and the disruption of micelles entanglement due to the PPO segment in PDA is offset; consequently, sol–gel transition due to temperature is eliminated.

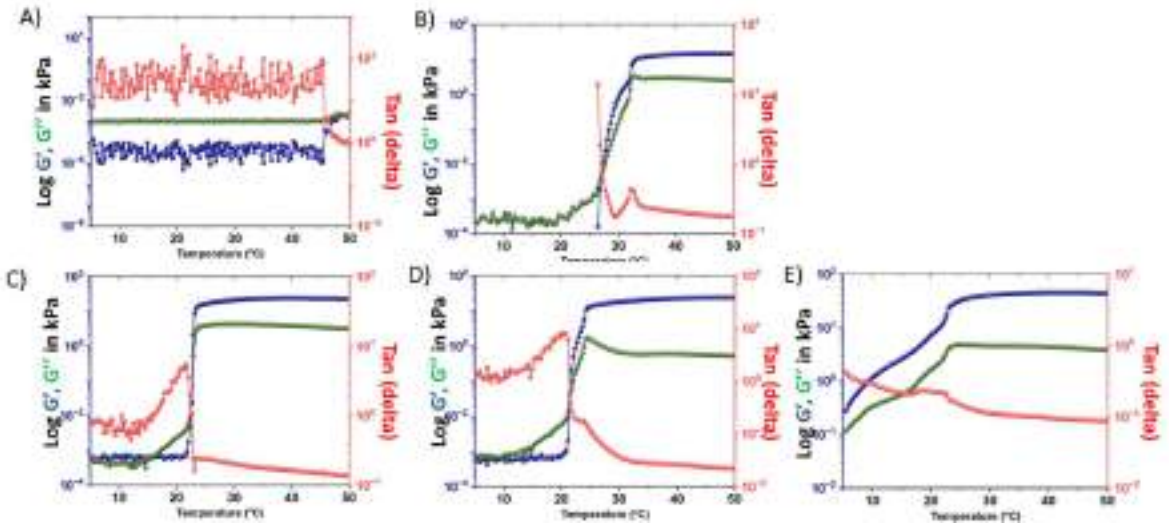

Figure 5.8: *Rheological behavior of the resultant hydrogel.*

Temperature sweep test at y= 1% and f= 1Hz of A) PDA_{15}, B) PDA_{15}+ HNP BG/H2O2, C) $PDA_{15}ADA_{0.1}$ + HNP BG/H2O2, D) $PDA_{15}ADA_{0.5}$ + HNP BG/H2O2, E) $PDA_{15}ADA_1$ + HNP BG/H2O2.

5.4.3 Morphology of hydrogel

The morphology of resultant hydrogels was accessed by SEM technique using freeze-dried samples. The cross-section of PDA hydrogel at 40% wt possessed a honeycomb-like structure with a relatively dense porous structure (figure 5.9). The pore size became larger with the reduction in PDA concentration to 15 wt%. This hydrogel demonstrated a tubular and reticular network morphology with lower interconnected pores within the hydrogel matrix, confirming the pseudo-gel stage.

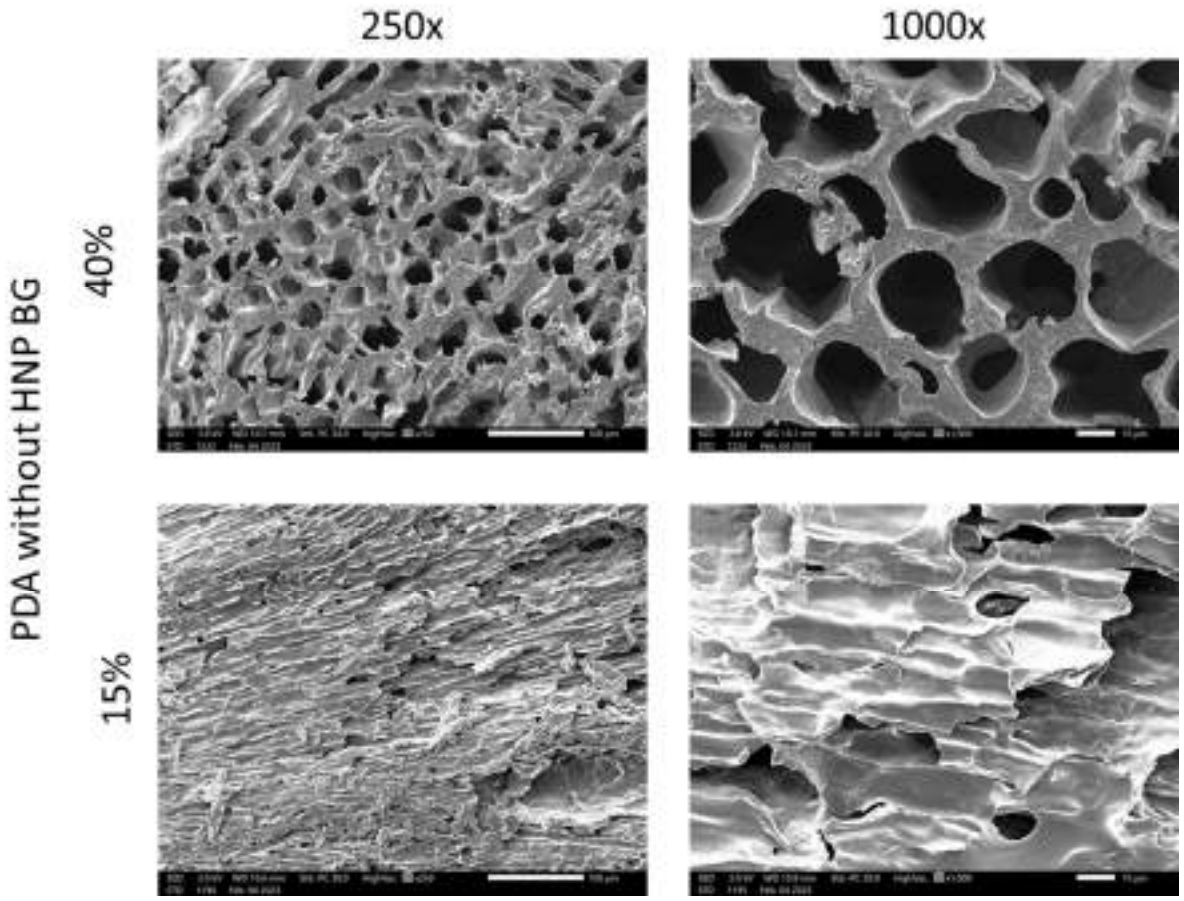

Figure 5.9: *Morphology of PDA hydrogel without HNP BG at 40% wt and 15% wt.*

In contrast, the introduction of chemical crosslinking in PDA 15 wt% under the catalytic activity of HNP BG (PDA_{15}@HNP BG/ H_2O_2) led to the spontaneous formation of a three-dimensional (3D) porous structure (Fig 5.10). It indicated that the mechanism of crosslinking accompanied by reaction-induced phase separation leads to diverse morphologies of the resulting porous structure of crosslinked hydrogel [40, 54, 55, 75]. When 0.1% ADA solution was applied along with PDA 15 wt% ($\underline{PDA_{15}\text{-}ADA_{0.1}@HNP}$ BG/H_2O_2), the composite hydrogel showed a similar macroscopic structure as single PDA@HNP BG/H_2O_2, but with a high degree of interconnectivity. It was observed that the perfect miscibility was between these compositions as one phase with the absence of a separation zone. The increase in the concentration of ADA, a sponge-like network k structure, was observed in $\underline{PDA_{15}\text{-}ADA_{0.1}@HNP}$ BG/H_2O_2, but with relatively smaller pore size. Also, the walls of the micropores were much thicker, proposing a longer time for degradation. The highly interconnected structure in $\underline{PDA_{15}\text{-}ADA_{0.1}@HNP}$ BG/H_2O_2 hydrogel provides the necessary scaffold to retain tissue fluid and possess high oxygen and nutrient permeability[50, 52, 112].

Therefore, the design of hydrogels might be suitable for cell attachment and three-dimensional cell growth.

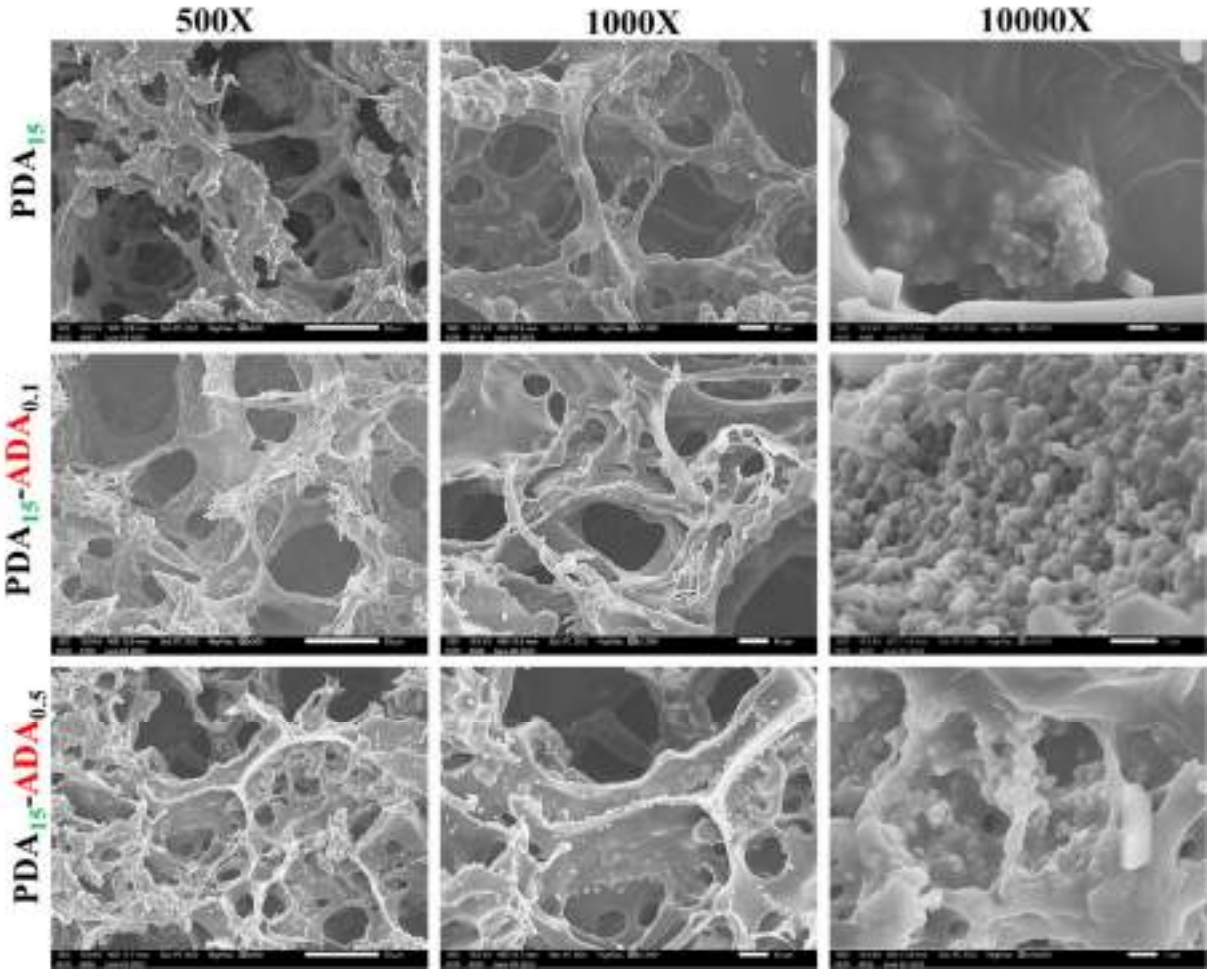

Figure 5.10*: The morphology of the obtained hydrogel from PDA and the mixture between PDA and ADA with the help of HNP BG/ H_2O_2*

5.4.4 Injectable property of hydrogel

Next, an evaluation to ascertain if designed hydrogels displayed the essential mechanical characteristics required for the creation of a clinically applicable drug delivery platform was performed via rheology. Due to the sol-gel transition behavior, PDA_{15}-$ADA_{0.5}$@HNP BG/H_2O_2 could be injectable following the change of temperature. Frequency sweeps provide a relative ranking of elastic and viscous properties under constant strain. Increasing frequencies decrease relaxation times and favor elastic properties (G′, storage modulus) over viscous properties (G′′, loss modulus) as there is minimal time for energy to dissipate or for hydrogels to flow during testing[308]. These results indicate that the PDA_{15}-$ADA_{0.5}$@HNP BG/H_2O_2 as solid-like characteristics (e.g., G' greater than G'') over a broad range of frequencies when 37^oC was applied (fig 8A). In contrast, when PDA_{15}-$ADA_{0.5}$@HNP BG/H_2O_2 was at 20^oC, no hydrogel was formed and rheological characterization revealed the mixture

exhibited liquid-like properties over physiologically relevant frequencies (Supplemental Figure S3). These results indicate that PDA_{15}-$ADA_{0.5}$@HNP BG/H_2O_2 hydrogel was easier to inject at the cool condition (T<20°C). Therefore, it is highly desirable to apply this scaffold at low temperature. Further, the injectability of PDA_{15}-$ADA_{0.5}$@HNP BG/H_2O_2 sample at gel condition was accessed. Analyzing the strain sweep at 37°C, it becomes evident that the hydrogel undergoes a significant reduction in both storage and loss moduli beyond a specific yield strain, signifying material yielding (fig 8B)[309]. When evaluating injectability using rheological data, the shear-thinning characteristic is of paramount importance[310]. Shear-thinning hydrogels experience a decrease in viscosity under the influence of shear forces, a feature made possible by reversible cross-linking mechanisms[308]. As shown in figure 8C, the viscosity of PDA_{15}-$ADA_{0.5}$@HNP BG/H_2O_2 hydrogel dropped approximately 7000 orders of magnitude as shear rate as shear rate increases from 0.1 to 200 (1/s), demonstrating that this material is extremely injectable[308, 311]. The strong decline in viscosity implies that the internal framework of the PDA_{15}-$ADA_{0.5}$@HNP BG/H_2O_2 network was disrupted under high-shear conditions. To regain its solid form after injection, the network structure would need to spontaneously regenerate[312]. To determine the ability for PDA_{15}-$ADA_{0.5}$@HNP BG/H_2O_2 to self-heal, the cyclic train time sweep where material underwent multiple cycles of high and low strain conditions was applied. When applied strain at 200%, the G′ was lower than the G″, representing a gel-sol transformation behavior. The modulus of PDA_{15}-$ADA_{0.5}$@HNP BG/H_2O_2 rapidly and repeatedly restored to original levels once low stain condition (0.1%) was applied, confirming the rapid self-healing properties of this hydrogel. This also indicates injectability of PDA_{15}-$ADA_{0.5}$@HNP BG/H_2O_2 at critical gel temperature[308].

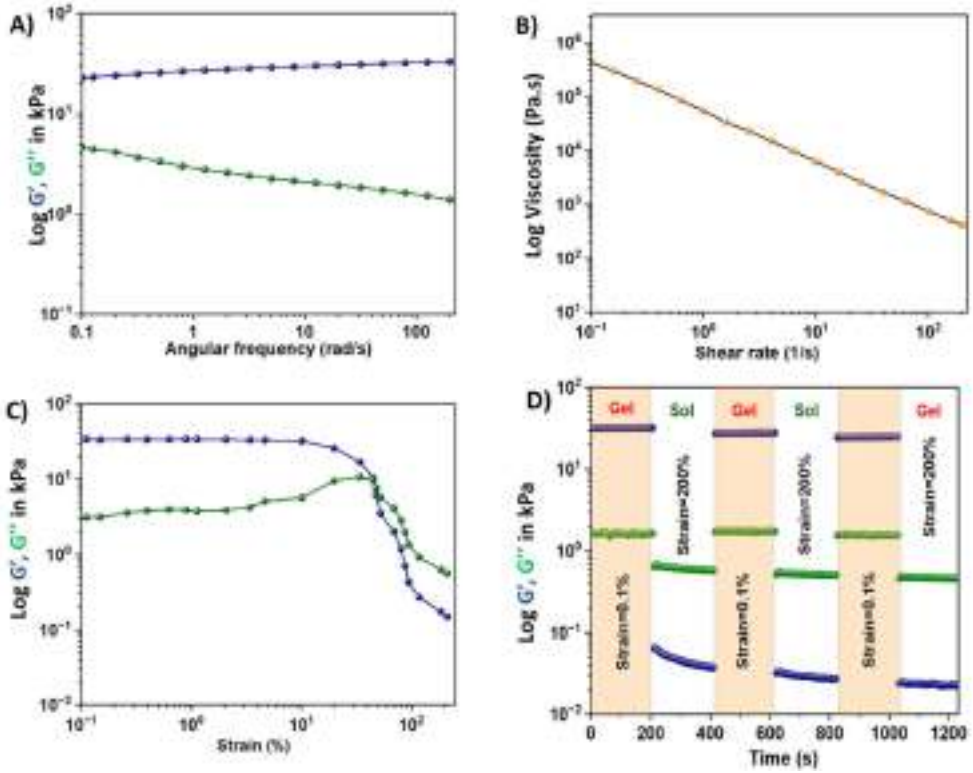

Figure 5.11: PDA_{15}-$ADA_{0.5}$@HNP BG/H_2O_2 hydrogel exposes its rheological behavior that enables injection through needles.

A) Oscillatory frequency rheology, B) Continuous flow, C) oscillatory amplitude rheology and cyclic train time sweep rheology for PDA_{15}-$ADA_{0.5}$@HNP BG/H_2O_2 at 37°C.

5.4.5 The cytotoxic of the resultant hydrogel

The potential toxicity of the hydrogel needed to be tested. In 2D culture, the viability of hMSCs cultured with the extracted hydrogel solution was over 90% compared to non-treated cells (Fig. 5.12A) at all culture times, indicating that the effect of the hydrogel degraded processes could be ignored. The potential toxicity of PDA_{15}-$ADA_{0.5}$@HNP BG was also tested with 3D culture. For this, hMSCs were laden in a hydrogel network, and a live–dead fluorescence assay was performed to observe and analyze the differences more intuitively. The live/dead staining images showed that most cells encapsulated in the tested hydrogels were viable (green) even at day 20 (Fig. 5.12B). However, some cells remained round after 5-day encapsulation. The number of spreading cells and their spreading extension increased with the incubation time. Finally, cells in the composite hydrogels developed into a typical spindle shape, in which pseudopods were visible. Altogether, PDA_{15}-$ADA_{0.5}$@HNP BG displayed superior biocompatibility.

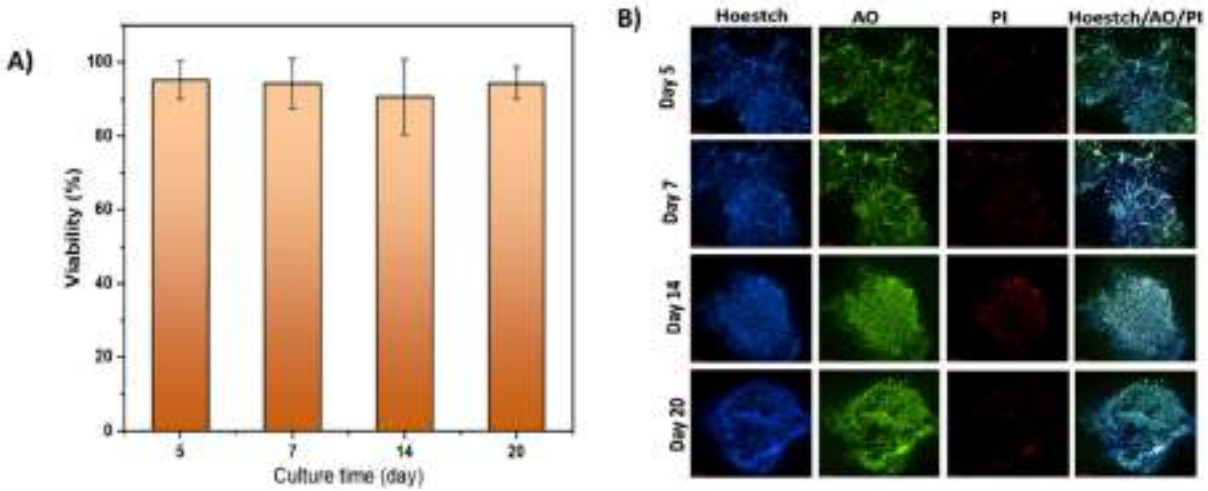

Figure 5.12: *The cytotoxicity of the resultant hydrogel.*

A) The viability of hMSCs with the hydrogel-extracted solution (10 mg/ml) was assessed with an SRB assay compared to non-treated cells at different culture times. B) Live/dead staining of hMSCs laden with hydrogel was performed with Propidium Iodide (PI, red, dead cells), Acridine Orange (AO, green, live cells) and Hoechst 33342 (blue, cell nucleus).

5.5 The potential of catechol hydrogel-based HNP BG for bone regeneration.

5.5.1 In vitro biomineralisation

Bioactivity is one of the most essential characteristics of the material for bone regeneration, which can be confirmed by monitoring the growth of hydroxycarbonate apatite (HCA) layers after immersing material in SBF for defined periods. SEM observed the apatite-deposited surfaces with chemical compositions–EDS analysis, as shown in Figure 5.13. Microscopic observations by SEM revealed that the PDA scaffolds' surface remained unchanged, depicting a relatively flat surface with a shallow signal of Ca and P elements after seven days of SBF immersion. After 14 days of mineralization of SBF, the supersaturated ions in the SBF continued to precipitate on the surface of PDA. The EDS mapping suggested that the ratio of Ca/P on PDA was 6. However, from the XRD analysis (Fig. 5.13C, D), it was found that the deposited material on the PDA was not apatite. In the case of hydrogel with HNP BG, HNP BG was observed on the surface of scaffolds with cauliflower-like structures. The surface was almost entirely covered by a large amount of tiny crystals when incubated longer in SBF. Further, the EDS map images (Fig. 5.13B) proved that HNP derivative hydrogel surface composition was found to be Ca and P elements with a higher Ca/P ratio over 2.0, predicting the presence of HA and another form of calcium, such as calcite. As per the reference from JCPDS no. 09-0432, the XRD pattern of hydrogel forming with HNP BG concluded that these precipitated crystals belonged to HA. It was also observed that the glass transformed into a nearly amorphous phase after 14 days of immersion. The glass had become more amorphous, and the HA peaks at $2\theta = 28.35°$ (1 0 2) and $2\theta = 39.8^{o}$ (1 1 3) became sharper, indicating the formation of crystalline HCA. Along with the HCA signal, diffraction spectra of the HNP BG-driven hydrogel shown in Figure 8C, D confirmed the appearance of calcite. However, the diffraction intensity of these peaks was higher in $\underline{PDA_{15}\text{-}ADA_{0.5}@HNP\ BG/H_2O_2}$ than in the single PDA hydrogel. Compared to native HNP BG (Fig. 5.12F), EDS mapping results showed that increased aggregation of Ca and P was observed on dual DA derivatives after 7 days of soaking, and these signals were identical to PDA_{15}@HNP BG. The aggregation of the new Ca and P on PDA was observed on the surface of PDA_{15}@HNP BG when the soaking time was extended to 14 days. In other words, ADA might help to increase the driving force of the crystallisation process resulting in an increase in biomineralisation. This is because alginate matrices contain carboxylate groups, which can interact with diffusing solutes such as Ca^{2+} from the SBF medium or the HNP BG, consequently increasing the supersaturation concerning the promotion of the nucleation of apatite or calcite structures on the surface of the PDA–ADA composite hydrogel in the early time as compared to HNP BG only [247, 261]. Therefore, the bioactivity of PDA_{15}-$ADA_{0.5}$@HNP BG/ H_2O_2 was extensively higher than that of others.

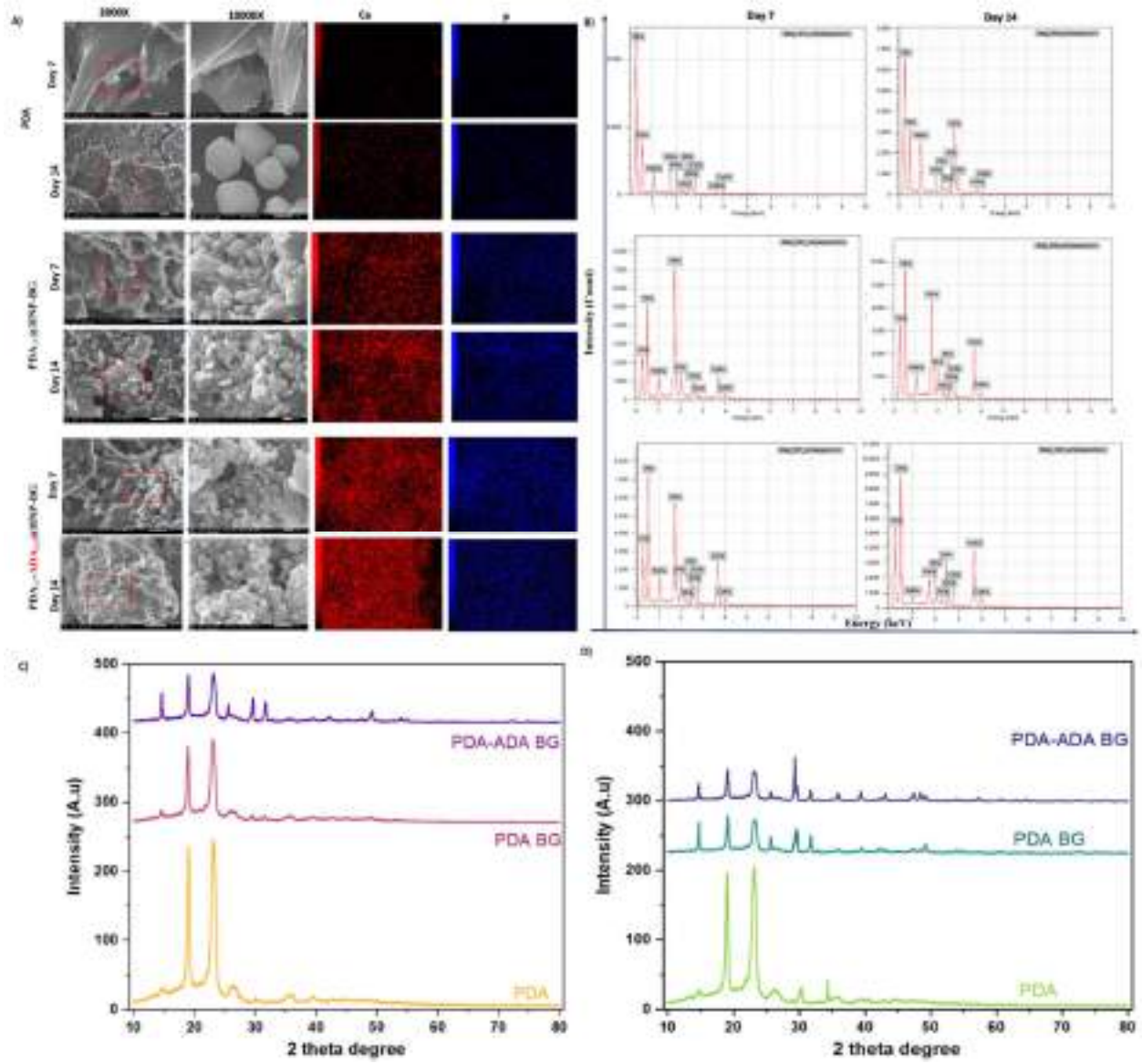

***Figure 5.13**: In vitro biomineralisation promotive property of the design hydrogel.*

A) The surface of this hydrogel at different magnifications (2000 X and 10.000 X) following the characteristic elements of Ca and P distribution and their corresponding EDS spectra (B) X-ray diffractometer patterns after C) 7 days and D) 14 days immersion in SBF at 37 °C.

5.5.2 Osteoinductive potential

Bone mineralization resulting from calcium deposition is a late marker in osteogenic differentiation. hMSCs were used to test whether PDA_{15}-$ADA_{0.5}$@HNP BG induced osteogenic differentiation. Calcium mineralization was detected via Alizarin Red S staining. As shown in Figure 5.14, calcium nodules were produced in the PDA_{15}-$ADA_{0.5}$@HNP BG on day 7, while this phenomenon was lacking in the control hMSCs. The Alizarin Red staining of

hMSCs cultured with hydrogel composite appeared more extensive at day 14 of differentiation, while the mineralization of nearly the entire well was observed in control.

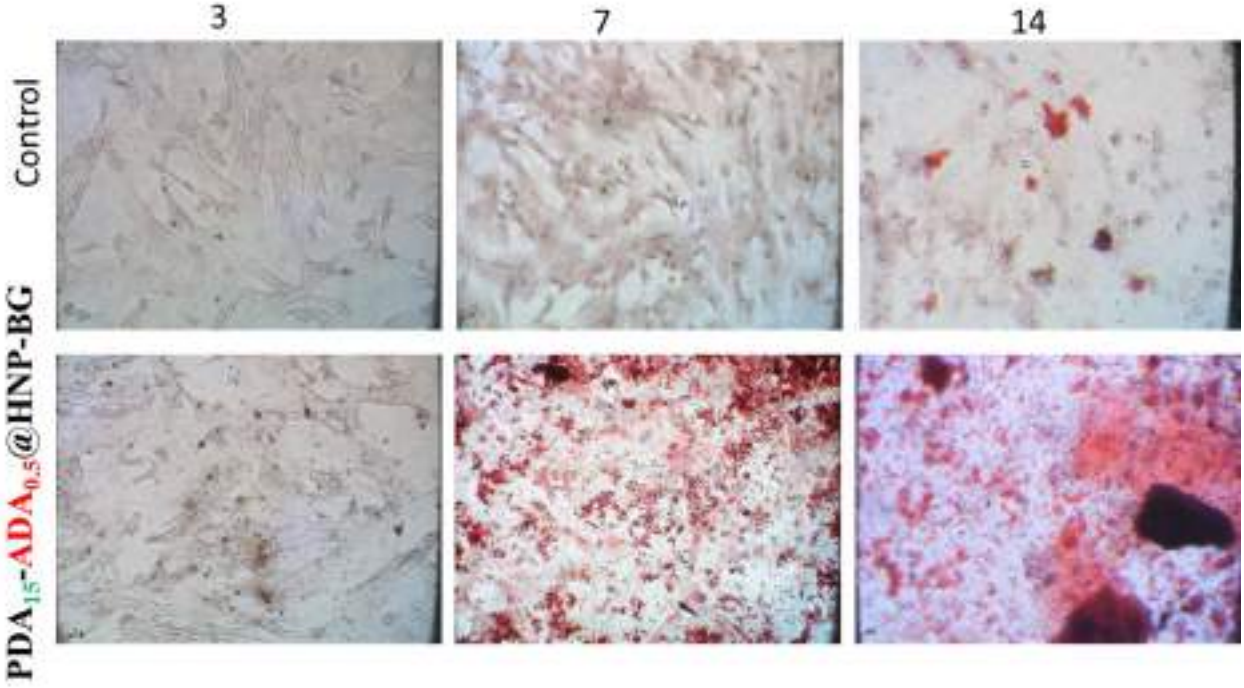

Figure 5.14: *Osteoinductive potential of PDA_{15}-$ADA_{0.5}$@HNP BG hydrogel in an hMSC model.*

Alizarin Red staining of hMSCs in culture with PDA_{15}-$ADA_{0.5}$@HNP BG hydrogel after 3, 7 and 14 days of culture.

5.5.3 Anti-bacteria

As an effective material for combating infection and stabilising the chemical internal environment of bone defect sites, the antibacterial properties of the PDA_{15}-$ADA_{0.5}$@HNP BG hydrogel were also implemented in this study. The PDA_{15}-$ADA_{0.5}$ formed by the HRP enzyme and H_2O_2 was used for comparison purposes, defined as the control sample. *S. aureus* and *E. coli* were selected as models in this experiment, and the results are displayed in Figure 5.15. It was possible to verify that the PDA_{15}-$ADA_{0.5}$ hydrogel without HNP BG does not possess antimicrobial activity. The bacterium growth increased in the first 24 h (10^9 CFU/mL, $p < 0.0001$), remaining stable at high bacterial concentrations during the rest of the assay period. When the bacterium was exposed to PDA_{15}-$ADA_{0.5}$@HNP BG hydrogel, a remarkable decrease in the bacterium growth was detected. The hydrogel reduced the bacterial levels to lower than 10^2 CFU/mL, and ≥ 99% of *S. aureus* and *E. coli* were killed. Overall, the bacteria seem to be susceptible to HNP BG. It is well known that bioglass has intrinsic bacteria. The

exchange of network-modifier ions in bioglass with hydrogen ions from the media causes an increase in pH and chaos in the osmotic pressure consequently inhibiting bacterial growth [30, 33, 174]. Therefore, PDA_{15}-ADA_3@HNP BG hydrogels showed higher levels of antibacterial activity than the hydrogel formed with the HRP enzyme. Therefore, PDA_{15}-$ADA_{0.5}$@HNP BG is an ideal material for bone regeneration applications.

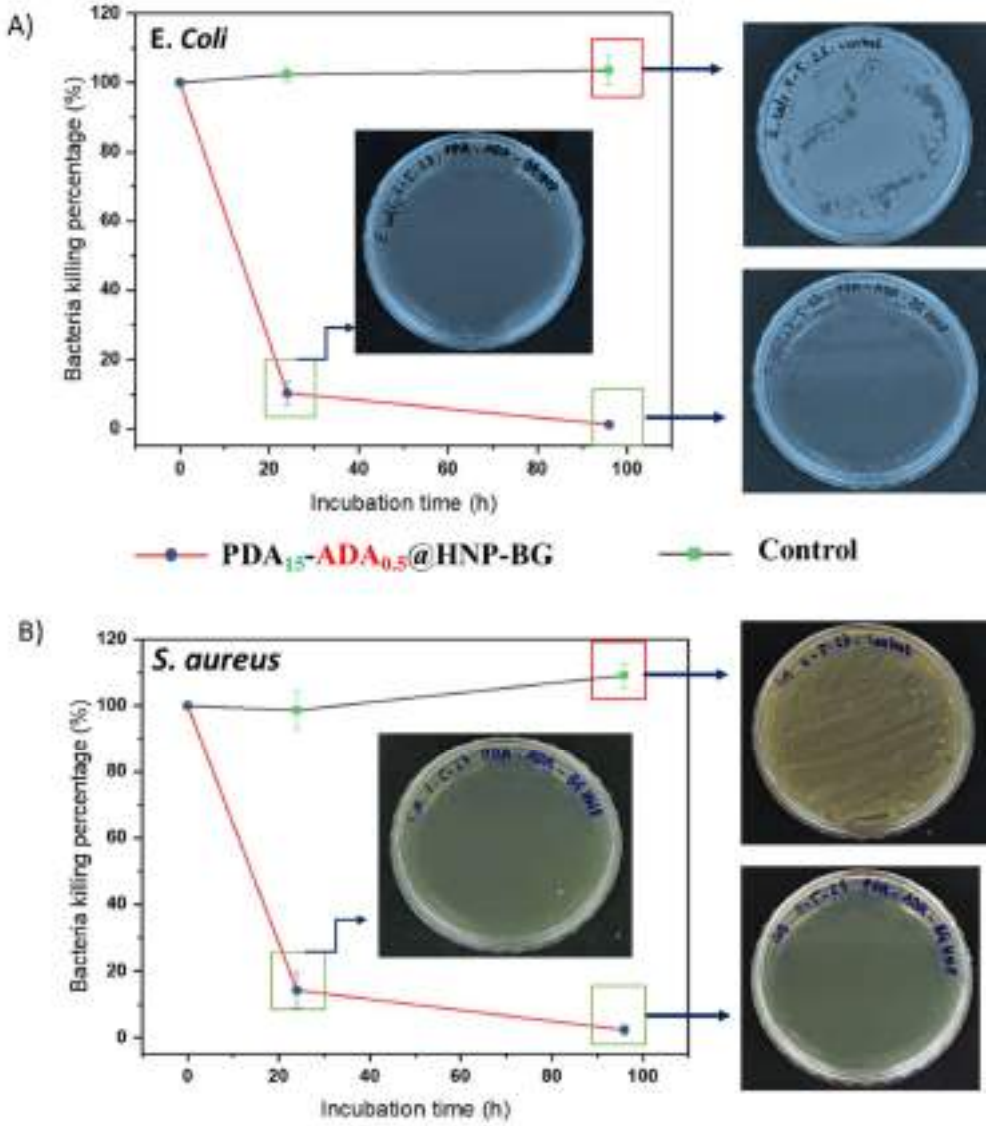

Figure 5.15: *Antibacterial activity evaluation of PDA_{15}-ADA_3@HNP BG hydrogel.*

Evaluation of the inhibition of hydrogels on the growth of A) E. coli and B) S. aureus at 24 h and 96 h incubation. The figure embeds images of surviving bacterial clones on agar plates.

5.5.4 The immunological responsive to implanted hydrogel

It is well-known that, upon implantation, materials and devices would trigger the local inflammation which may cause a breakdown of the implant or the leaching of toxic species into the tissue from the underlying layers[308, 313, 314]. Therefore, the performance of the PDA_{15}-$ADA_{0.5}$@HNP BG hydrogel was assessed in vivo in mice. In this study, hydrogel with two difference doses (0.2 mL and 0.4 mL) was delivered to the subcutaneous injection site through a 28 gauge needle. The tissue response to the implant was studied with the blood test as well as histopathological data as shown in figure 5.16. Upon injecting PDA_{15}-$ADA_{0.5}$@HNP BG, both groups displayed a red nodule at the injection site (Fig 5.16A). The red nodule generally tends to resolve. None of the complications ranging from necrosis to any inflammatory changes such as edema, bruising, and erythema were observed during follow-up periods. In addition, hydrogel could be observed under the skin over the course of the following week. No mice showed signs of discomfort or distress, a change in behavior, or a change in physical impairment, confirming hydrogel induced no signs of toxicity[314]. To determine the magnitude of the systemic inflammatory response to PDA_{15}-$ADA_{0.5}$@HNP BG hydrogels after implantation, the level of C-reactive protein (CRP) and the concentration of white blood cells (immune cells) were accessed. CRP, categorized as a pentraxin, functions as an extensively employed marker for inflammation in clinical contexts[315]. CRP plays an active role in the innate immune response by binding to microorganisms and damaged cellular components via phosphocholine interactions[316]. Consequently, this instigates complement activation and initiates the process of phagocytosis[315]. In other words, elevated CRP levels are detected in conditions that trigger an inflammatory reaction along with the concentration of white blood cells[317]. The normal level of CRP in mice serum was 2.25 ±0.33 µg/mL (IQR: 1.89-2.56 µg/mL) (fig 5.16B). As shown in figure 5.16C, CRP levels rapidly rise within the first 6h implantation in both groups compared with the normal group (0.2 mL vs normal, $t=13.79$, $p<0.0001$, 95%CI=5.16-7.24; 0.4 mL vs normal, $t=11.3$, $p=1.42\text{x}10^{-4}$, 95%CI=4.69 -7.10). Similarly, 100% mice with hydrogel implants encountered significant leukocytosis, which is characterized by a WBC count increase of ≥50% (fig 5.16 D-E). Hydrogel dose, however was clearly non-correlated with increased WBC count (0.2 mL vs 0.4 mL: 17.0 ± 1.7 G/L vs 17.2 ±1.2 G/L, p=0.835). The level of CRP and WBC in blood serum started declining. The CRP levels returned to baseline levels (1.89-2.56 µg/mL) from day 3 (72h) post-injection and was remain so over a 168 h period. In term of white blood cells, all compositions (monocytes, lymphocytes, granulocytes) in the implanted groups were within the range of the normal mice after 3 days. These mice were continuing to be monitored by histological sections of tissues surrounding PDA_{15}-$ADA_{0.5}$@HNP BG hydrogel implants (fig 5.16 F). Neither hemorrhage nor necrosis was identified in skin sections after 7 subcutaneous implantation with differencdifferentn addition, there was no evidence of tissue injury observed in remote muscle fibers at the implantation site. Examination of skin sections through H&E staining with higher magnification in both dose displayed a small influx of cells into the biomaterial. Intriguingly, these cellular infiltrates were primarily concentrated along the strands of extracellular matrix (ECM) deposited within the hydrogel. Notably, at both tested doses, the hydrogel did not significantly elicit a foreign response when compared to the control group without implantation. There

were minimal evidence of typical fibrosis near the interface between the hydrogel and host tissue, and multi-nucleated foreign body giant cells were conspicuously absent in these samples. These findings indicate that the formulated hydrogel exhibited outstanding biocompatibility[314]. Together with intrinsic anti-bacteria property, this research showcases the biocompatibility of PDA_{15}-$ADA_{0.5}$@HNP BG hydrogel implants as a successful scaffold for bone regeneration.

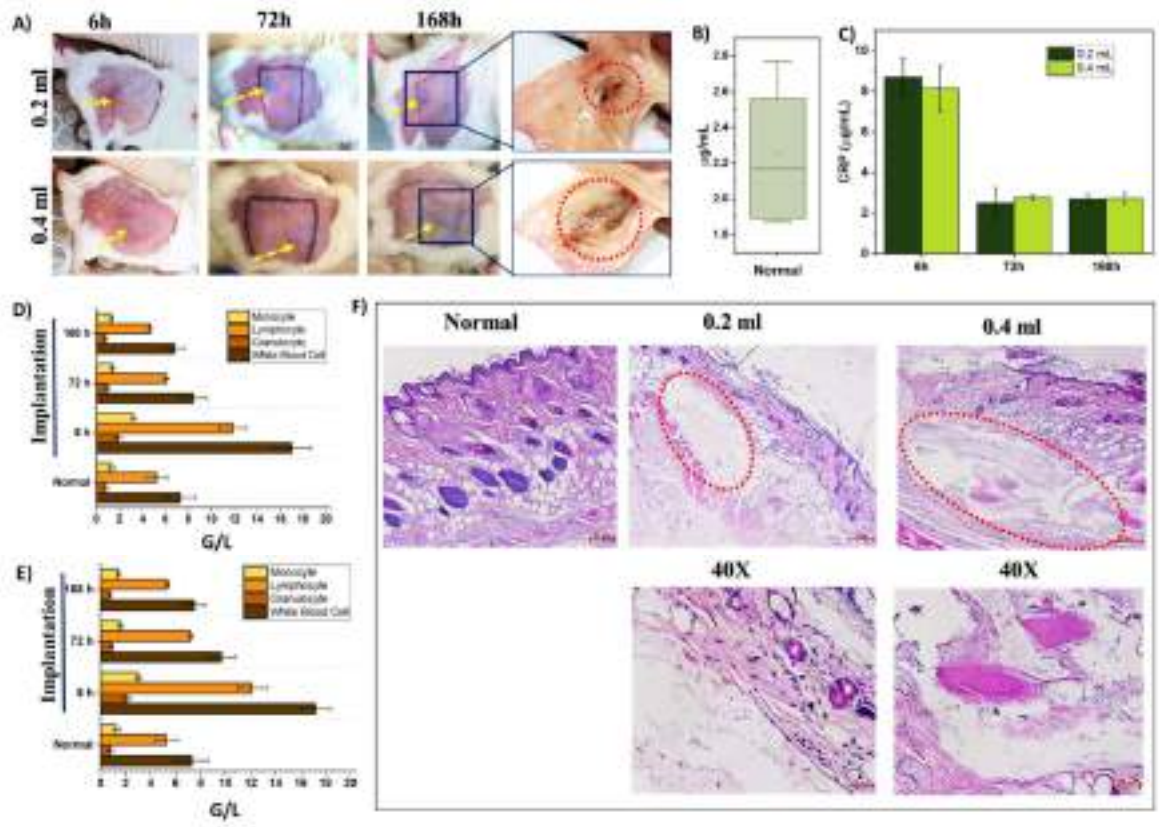

Figure 5.16*: In vivo immunological response to the implanted designed hydrogel.*

A) Representative images of hydrogels with 2 doses (0two2ml and 0.4ml) following subcutaneous injection into mice at different time intervals. B) Serum CRP content in normal mice and C) in the mice with the hydrogel. In vivo whole white blood analysis following hydrogel implantation at different time intervals with dose of doses: 2ml and E) 0.4ml. Data was presented as mean ± SD, n = 4. F) Representative hematoxylin and eosin-stained sections of PDA_{15}-$ADA_{0.5}$@HNP BG hydrogel implants with surrounding tissue after seven days (168h). H denotes the hydrogel. Red eclipse with dash line are the tissue surrounding and the zoomed areas—scale bars: 20 µm.

5.6 Conclusion

In summary, given the outstanding versatility of peroxidase-mimicking material, we present a new strategy for developing nanozyme-based bioglass (HNP BG) by introducing HNPs on the bioglass network. Due to the surficial hemin particles, HNP BG shows a peroxidase-like activity similar to the HRP enzyme. Intriguingly, the catalytic activity of HNP BG was over a broader temperature range than that of the native enzyme. Further, HNP BG performed its catalyst activity in the oxidation of DA to aminochrome, consequently forming polydopamine. This perspective shows that HNP BG is the alternative catalyst for dopamine crosslinking hydrogel based on alginate and Pluronic. Moreover, due to oxidative DA and intermolecular complexes between the alginate backbone and ions released from HNP BG, the resultant hydrogel had many interconnections via covalent bonding. This hydrogel also showed thermo-sensitivity and injectable properties, ideal for in situ bioscaffold systems. Testing with hMSCs in both 2D and 3D cultures, the bioscaffolds exhibited biocompatibility. More importantly, the HNP BG endows the hydrogel with osteogenic activity and is antibacterial. It is believed that such an intelligent artificial enzyme-based bioglass will bring exciting new opportunities for making in situ injectable bioscaffold-based catechol derivative polymers for bone regeneration (schematic 5.1).

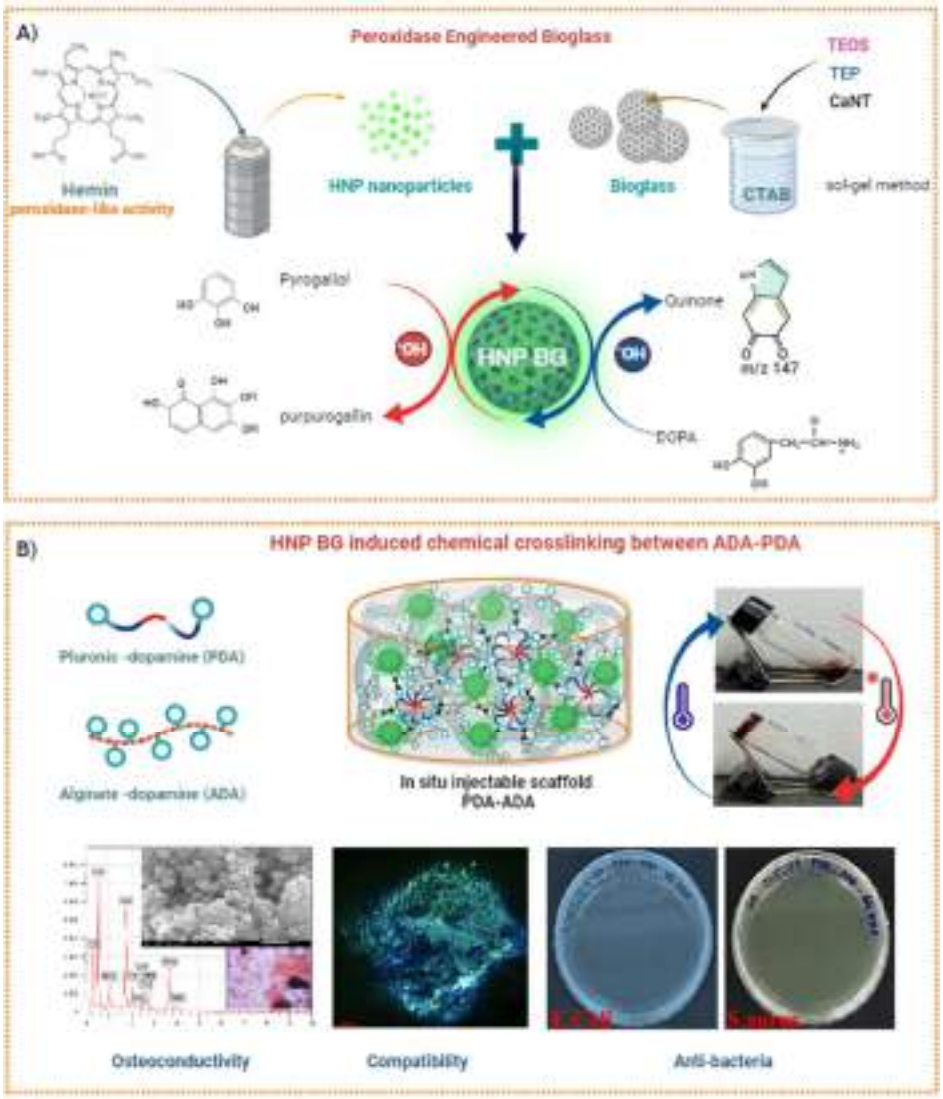

Schematic 5.1*: A) The illustration of the peroxidase mimicking bioglass based on hemin nanoparticles (HNP BG) and B) its potential application in making injectable catechol based hydrogel from dopamine derivative polymer.*

CHAPTER 6: CONCLUDING REMARKS

6.1 Concluding remarks

This work developed injectable hydrogels comprising thermally responsive polymer, Pluronic F127, and alginate using different methods. It also provided the functional scaffold with on-demand biological cues for specific tissue regeneration.

- The first aim of this work, which involved the design of the thermal responsive hydrogel based on grafting techniques, was successfully approached. The coupling method was used to synthesize the copolymer, alginate-cystamine-pluronic F127. This copolymer inherited the thermal responsive feature of Pluronic with the adjustment via the density of alginate. With grafting approaching with coupling chemistry, the grafted copolymer was ready for homogenous processing in fabricating hydrogel; consequently, the morphology of the resultant hydrogel in both the wet stage and dry stage presented a typical interconnected and porous microstructure with uniformly arranged pores intended for efficient transport and permeation of oxygen and nutrients as well as for the exchange of tissue fluid waste. ACP hydrogel exposed reversible sol-to-gel transition in response to temperature without the separation phage. The hydrogel exhibited excellent cytocompatibility. Because of their temperature sol-gel transitions, ACP copolymer has allowed for facile encapsulation and controllable release of fibroblast cells. The gelation temperature is in the wide range (from 25^{o}C to under 37^{o}C) with mild conditions, envisioning the suitable for 3D encapsulation of cells. The outgrowth cells from the cluster form the cell layer on the surface of the culture dish, which is similar to a 2D culture. These studies demonstrate the tunability of the hydrogel system and the potential for minimally invasive tissue regeneration applications. Further, the stiffness of hydrogel via rheology suggests the potential application to soft tissue, suggesting its application in wound healing.

The ACP copolymerization was used as the carrier to combine a safe NO donor (L-Arginine) and ROS scavenging compound (Resveratrol) for on-demand therapeutic treatment of wound burns in a diabetic model. The addition of these biological cues should be carefully examined in terms of sol-gel transition and cytotoxicity. The addition of these biological cues showed a strong effect on the thermal responsive ACP hydrogel. Therefore, it needed to be managed to happen within a restricted temperature interval. A higher temperature of 37^{o}C would reduce the application of this hydrogel. As expected, dual L-arginine and resveratrol at the suitable dose showed excellent performance in the wound healing process with the diabetic mice model. My work provides an alternative strategy for wound management with dual-function hydrogel dressing, ROS scavenging, and NO signaling, which prevents pathogen infections

and promotes wound healing in a sustainable way, possibly providing a solution for diabetic wound therapy in clinical or household settings.

- The second aim of this work focused on the design the thermal responsive hydrogel based on enzyme crosslinking techniques. Compared to grafting techniques, this strategy was easy to formulate – a responsive scaffold from combining polysaccharide and thermal-responsive polymer. Inspired by the catechol cross-linking chemistry, 3,4-dihydroxyphenylalanine (DOPA) was selected as the cross-linker model. The introduction of DOPA in the alginate backbone (ADA) was synthesized via the EDC/NHS coupling reaction. In contrast, the replaced hydroxyl group on the Pluronic F127 backbone (PDA) was done by p-NPC coupling reaction. Following the advance of enzymatic crosslinking of polymer–catechol conjugates in the presence of peroxidase and H_2O_2, we propose a new strategy to engineer BG with peroxidase-mimic hemin (HNP BG), thus achieving the synergistic effect, for catalyst in crosslinking reaction and bioactive agents to reinforce the function of the resultant hydrogel. Incorporating HNPs into the BG network endows HNP BG with a new function, the catalytic activity of a peroxidase enzyme. Also, HNP BG promoted the crosslinking between two catechol derivative polymers, ADA and PDA, resulting in the formation of a biomimetic hydrogel suitable for bone regeneration in terms of stiffness and biological environment. The chemical crosslinking density needs to be controlled to retain the sol-gel transition. At 15% wt PDA and 0.5% wt ADA, the obtained hydrogel had injectability following a thermal-responsive gelling system with a microporous architecture. In addition, incorporating HNP BG can effectively manipulate the capability of the mineralization process, which remarkably promotes new bone formation, accelerates bone regeneration in situ, and has antibacterial properties. Therefore, this work provided a new strategy for synthesizing the bio-scaffold for bone regeneration via combining biological cues as a catalyst for forming the crosslinking catechol-based polymer.

The overall conclusions derived from this work are that injectable, in situ forming hydrogels based alginate and Pluronic F127 with different chemical crosslinking strategies can be developed for tissue engineering applications. The grafting approach and crosslinking techniques can be designed for the hybrid thermal responsive hydrogel based on alginate and Pluronic F127. Both resultant hydrogels are liquids at cool temperatures for injectable administration, rapidly forming three-dimensional and nonshrinking hydrogel networks in situ to stabilize and contour to irregular defect shapes, enable simple and localized delivery of cells, and finally, degrade to allow for tissue growth. By adding bioactive agents such as L-arginine, Resveratrol, or BG, alginate-pluronic hydrogels become attractive platforms for new tissue regeneration intentions. These intelligent hydrogels can afford a safer, successful,

and potential alternative for many implementations in biomedicine including but not limited to early detection of diseases, disease control, and tissue engineering.

6.2 Future perspective

These research expansions encompass the different methods for the development of different hybrid hydrogels, which similarly points to the elaboration of novel technicalities of the extrinsic stimuli-responsive hydrogels. Despite the exciting outlook of designing thermal responsive hydrogel as the alternative EMC scaffold, numerous tasks will be done to gain a deeper scientific understanding, technological maturation, and eventual translation, adoption, and commercialization of the product.

First, future research should focus on the scaling ability of the synthesis process to estimate the potential transferred techniques to the industry. In other words, the optimization process to increase the pilot of the study should be clarified. Second, the stability of the product should be approached to understand its storage condition and aging information. Although animals were used in this study, the mice's skin or mice’s immunological systems are quite different from humans; large animals such as dogs and pigs, … should be used in the future. In addition, the hydrogel was well-adapted to cells. The evidence for the application of cell-laden hydrogels will be further studied to provide information on their application in the multifunctional tissue engineering field. For example, further research should be considered with individualized tissue regeneration using cell therapy combined with the designed scaffold. Furthermore, the standardized criteria for evaluating these hydrogels should be conducted to bring the product to clinical trials.

LIST OF PUBLICATIONS

1. **Le Hang Dang**, Phuong Doan, Tran Thi Yen Nhi, Dinh Trung Nguyen, Bich Tram Nguyen, Thi Phuong Nguyen, and Ngoc Quyen Tran. "Multifunctional injectable Pluronic-cystamine-alginate-based hydrogel as a novel cellular delivery system towards tissue regeneration." International Journal of Biological Macromolecules 185 (2021): 592-603.
2. Vo Le, Tuong Van, Ngoc Quyen Tran, **Dang Le Hang**, Thanh Tuyen Nguyen, Quynh Anh Bui, Nguyen Dinh Trung, Nguyen Dat Thinh et al. "Impacting different structures of injectable Pluronic-conjugated alginate (chitosan) hydrogels on their physicochemical characteristics and morphological fibroblast behavior." International Journal of Polymer Analysis and Characterization 27, no. 3 (2022): 205-219.
3. **Le Hang Dang**, Hong Tuoi Do, Kim Tram Pham, Phuong Thu Ha, Thi Phuong Nguyen, Tan Phat Dao, Ngoc Quyen Tran. "Injectable thermogel incorporating reactive oxygen species scavenger and nitric oxide donor to accelerate the healing process of diabetic wounds". International Journal of Pharmaceutics 648 (2023): 123576.
4. **Le Hang Dang,** Vu Nhu Quynh, Thuy Tien Nguyen, Thi Hong Tuoi Do, Thi Kim Tram Pham, and Ngoc Quyen Tran. "Thermally-responsive and reduced glutathione-sensitive folate-targeted nanocarrier based on alginate and pluronic F127 for on-demand release of methotrexate." International Journal of Biological Macromolecules 263 (2024): 130227.
5. **Đặng Thị Lệ Hằng,** Trần Ngọc Quyển, National Patent (VN 1-2021-01465): QUY TRÌNH TỔNG HỢP HYDROGEL NHẠY NHIỆT TỪ VẬT LIỆU ALGINAT-CYS-PLURONIC, cấp năm 2024.

Other related publications

1. **Le Hang Dang**, Thai Tuan Tran, Minh Tuan Nguyen, Thao- Han Luong, Dat Thinh Nguyen, Minh-Dung Truong, Phuong Le, Hai Khoa Le, Thuy-Tien Dang, Ngoc Quyen Tran. "Syringeable hydrogel based β-cyclodextrin and mixed micelles for Methotrexate delivery". Journal of Drug Delivery Science and Technology, 92 (2023), 105299.

REFERENCES

[1] P. Zarrintaj, M. Khodadadi Yazdi, M. Youssefi Azarfam, M. Zare, J.D. Ramsey, F. Seidi, M. Reza Saeb, S. Ramakrishna, M. Mozafari, Injectable Cell-Laden Hydrogels for Tissue Engineering: Recent Advances and Future Opportunities, Tissue Eng Part A, 27 (2021) 821-843.
[2] W. Yang, J. Chen, Z. Zhao, M. Wu, L. Gong, Y. Sun, C. Huang, B. Yan, H. Zeng, Recent advances in fabricating injectable hydrogels via tunable molecular interactions for bio-applications, J Mater Chem B, (2023).
[3] V. Uppuluri, S. Thukani Sathanantham, S.K. Bhimavarapu, L. Elumalai, Polymeric Hydrogel Scaffolds: Skin Tissue Engineering and Regeneration, Adv Pharm Bull, 12 (2022) 437-448.
[4] I.H. Kim, M. Jeon, K. Cheon, S.H. Kim, H.S. Jung, Y. Shin, C.M. Kang, S.O. Kim, H.J. Choi, H.S. Lee, K.E. Lee, J.S. Song, In Vivo Evaluation of Decellularized Human Tooth Scaffold for Dental Tissue Regeneration, Appl Sci (Basel), 11 (2021).
[5] J. Vanderburgh, J.A. Sterling, S.A. Guelcher, 3D Printing of Tissue Engineered Constructs for In Vitro Modeling of Disease Progression and Drug Screening, Ann Biomed Eng, 45 (2017) 164-179.
[6] F. Messner, Y. Guo, J.W. Etra, G. Brandacher, Emerging technologies in organ preservation, tissue engineering and regenerative medicine: a blessing or curse for transplantation?, Transpl Int, 32 (2019) 673-685.
[7] C. Thomson, J.M. Schneider, U. Pohl, D.M. Power, Failed Acellular Nerve Allografts: A Critical Review, Ann Plast Surg, 89 (2022) 63-71.
[8] A. Mardomi, S.B. Naderi, S.Z. Vahed, M. Ardalan, New insights on the monitoring of solid-organ allografts based on immune cell signatures, Transpl Immunol, 70 (2022) 101509.
[9] H.M. Blau, J.H. Pomerantz, Re"evolutionary" regenerative medicine, JAMA, 305 (2011) 87-88.
[10] C.R. Lynch, P.P.D. Kondiah, Y.E. Choonara, Advanced Strategies for Tissue Engineering in Regenerative Medicine: A Biofabrication and Biopolymer Perspective, Molecules, 26 (2021).
[11] A. Hassanpour, T. Talaei-Khozani, E. Kargar-Abarghouei, V. Razban, Z. Vojdani, Decellularized human ovarian scaffold based on a sodium lauryl ester sulfate (SLES)-treated protocol, as a natural three-dimensional scaffold for construction of bioengineered ovaries, Stem Cell Res Ther, 9 (2018) 252.
[12] F. Asgari, H.R. Asgari, M. Najafi, B.S. Eftekhari, M. Vardiani, M. Gholipourmalekabadi, M. Koruji, Optimization of decellularized human placental macroporous scaffolds for spermatogonial stem cells homing, J Mater Sci Mater Med, 32 (2021) 47.
[13] J.C. Huling, A. Atala, J.J. Yoo, Chapter 42 - Decellularized Whole Organ Scaffolds for the Regeneration of Kidneys, in: M.H. Little (Ed.) Kidney Development, Disease, Repair and Regeneration

2016, Pages Elsevier2016, pp. 569-578.
[14] R.K. da Palma, P. Fratini, G.S. Schiavo Matias, A.D. Cereta, L.L. Guimaraes, A.R.A. Anunciacao, L.V.F. de Oliveira, R. Farre, M.A. Miglino, Equine lung decellularization: a potential approach for in vitro modeling the role of the extracellular matrix in asthma, J Tissue Eng, 9 (2018) 2041731418810164.

[15] A.M. Rosales, K.S. Anseth, The design of reversible hydrogels to capture extracellular matrix dynamics, Nat Rev Mater, 1 (2016).
[16] J. Lou, D.J. Mooney, Chemical strategies to engineer hydrogels for cell culture, Nat Rev Chem, 6 (2022) 726-744.
[17] S. Salehi, S.M. Naghib, H.R. Garshasbi, S. Ghorbanzadeh, W. Zhang, Smart stimuli-responsive injectable gels and hydrogels for drug delivery and tissue engineering applications: A review, Front Bioeng Biotechnol, 11 (2023) 1104126.
[18] A.P. Mathew, S. Uthaman, K.H. Cho, C.S. Cho, I.K. Park, Injectable hydrogels for delivering biotherapeutic molecules, Int J Biol Macromol, 110 (2018) 17-29.
[19] E. Zeimaran, S. Pourshahrestani, A. Fathi, N. Razak, N.A. Kadri, A. Sheikhi, F. Baino, Advances in bioactive glass-containing injectable hydrogel biomaterials for tissue regeneration, Acta Biomater, 136 (2021) 1-36.
[20] M. Radivojsa, I. Grabnar, P. Ahlin Grabnar, Thermoreversible in situ gelling poloxamer-based systems with chitosan nanocomplexes for prolonged subcutaneous delivery of heparin: design and in vitro evaluation, Eur J Pharm Sci, 50 (2013) 93-101.
[21] B. Vigani, S. Rossi, G. Sandri, M.C. Bonferoni, C.M. Caramella, F. Ferrari, Recent Advances in the Development of In Situ Gelling Drug Delivery Systems for Non-Parenteral Administration Routes, Pharmaceutics, 12 (2020).
[22] K.A. Soliman, K. Ullah, A. Shah, D.S. Jones, T.R.R. Singh, Poloxamer-based in situ gelling thermoresponsive systems for ocular drug delivery applications, Drug Discov Today, 24 (2019) 1575-1586.
[23] H. Lee, T.G. Park, Photo-crosslinkable, biomimetic, and thermo-sensitive pluronic grafted hyaluronic acid copolymers for injectable delivery of chondrocytes, J Biomed Mater Res A, 88 (2009) 797-806.
[24] M. Prabaharan, J.F. Mano, Stimuli-responsive hydrogels based on polysaccharides incorporated with thermo-responsive polymers as novel biomaterials, Macromol Biosci, 6 (2006) 991-1008.
[25] F. Pati, D.H. Ha, J. Jang, H.H. Han, J.W. Rhie, D.W. Cho, Biomimetic 3D tissue printing for soft tissue regeneration, Biomaterials, 62 (2015) 164-175.
[26] F. Causa, P.A. Netti, L. Ambrosio, A multi-functional scaffold for tissue regeneration: the need to engineer a tissue analogue, Biomaterials, 28 (2007) 5093-5099.
[27] H. Hu, H. Zhang, Z. Bu, Z. Liu, F. Lv, M. Pan, X. Huang, L. Cheng, Small Extracellular Vesicles Released from Bioglass/Hydrogel Scaffold Promote Vascularized Bone Regeneration by Transferring miR-23a-3p, Int J Nanomedicine, 17 (2022) 6201-6220.
[28] D.Q. Wu, J. Zhu, H. Han, J.Z. Zhang, F.F. Wu, X.H. Qin, J.Y. Yu, Synthesis and characterization of arginine-NIPAAm hybrid hydrogel as wound dressing: In vitro and in vivo study, Acta Biomater, 65 (2018) 305-316.
[29] A. Mohandas, J. Rangasamy, Nanocurcumin and arginine entrapped injectable chitosan hydrogel for restoration of hypoxia induced endothelial dysfunction, Int J Biol Macromol, 166 (2021) 471-482.
[30] X. Wu, H. Li, Incorporation of Bioglass Improved the Mechanical Stability and Bioactivity of Alginate/Carboxymethyl Chitosan Hydrogel Wound Dressing, ACS Appl Bio Mater, 4 (2021) 1677-1692.
[31] I. De Luca, F. Di Cristo, R. Conte, G. Peluso, P. Cerruti, A. Calarco, In-Situ Thermoresponsive Hydrogel Containing Resveratrol-Loaded Nanoparticles as a Localized Drug Delivery Platform for Dry Eye Disease, Antioxidants (Basel), 12 (2023).

[32] A. Joseph, A. Balakrishnan, P. Shanmughan, B. Maliakel, K. Illathu Madhavamenon, Micelle/Hydrogel Composite as a "Natural Self-Emulsifying Reversible Hybrid Hydrogel (N'SERH)" Enhances the Oral Bioavailability of Free (Unconjugated) Resveratrol, ACS Omega, 7 (2022) 12835-12845.
[33] Q. Zeng, Y. Han, H. Li, J. Chang, Design of a thermosensitive bioglass/agarose-alginate composite hydrogel for chronic wound healing, J Mater Chem B, 3 (2015) 8856-8864.
[34] Z. Sun, X. Wang, J. Liu, Z. Wang, W. Wang, D. Kong, X. Leng, ICG/l-Arginine Encapsulated PLGA Nanoparticle-Thermosensitive Hydrogel Hybrid Delivery System for Cascade Cancer Photodynamic-NO Therapy with Promoted Collagen Depletion in Tumor Tissues, Mol Pharm, 18 (2021) 928-939.
[35] L.C. Shanley, O.R. Mahon, D.J. Kelly, A. Dunne, Harnessing the innate and adaptive immune system for tissue repair and regeneration: Considering more than macrophages, Acta Biomater, 133 (2021) 208-221.
[36] M. Karin, H. Clevers, Reparative inflammation takes charge of tissue regeneration, Nature, 529 (2016) 307-315.
[37] P.V. Giannoudis, I. Pountos, Tissue regeneration. The past, the present and the future, Injury, 36 Suppl 4 (2005) S2-5.
[38] N. Muzzio, S. Moya, G. Romero, Multifunctional Scaffolds and Synergistic Strategies in Tissue Engineering and Regenerative Medicine, Pharmaceutics, 13 (2021).
[39] L. Cui, Y. Saeed, H. Li, J. Yang, Regenerative medicine and traumatic brain injury: from stem cell to cell-free therapeutic strategies, Regen Med, 17 (2022) 37-53.
[40] R. Takahashi, H. Miyazako, A. Tanaka, Y. Ueno, Dynamic Creation of 3D Hydrogel Architectures via Selective Swelling Programmed by Interfacial Bonding, ACS Appl Mater Interfaces, 11 (2019) 28267-28277.
[41] K. Bott, Z. Upton, K. Schrobback, M. Ehrbar, J.A. Hubbell, M.P. Lutolf, S.C. Rizzi, The effect of matrix characteristics on fibroblast proliferation in 3D gels, Biomaterials, 31 (2010) 8454-8464.
[42] A.C. Alavarse, E.C.G. Frachini, R. da Silva, V.H. Lima, A. Shavandi, D.F.S. Petri, Crosslinkers for polysaccharides and proteins: Synthesis conditions, mechanisms, and crosslinking efficiency, a review, Int J Biol Macromol, 202 (2022) 558-596.
[43] A. Podevyn, S. Van Vlierberghe, P. Dubruel, R. Hoogenboom, Design and Synthesis of Hybrid Thermo-Responsive Hydrogels Based on Poly(2-oxazoline) and Gelatin Derivatives, Gels, 8 (2022).
[44] A. Shafiee, A. Atala, Tissue Engineering: Toward a New Era of Medicine, Annu Rev Med, 68 (2017) 29-40.
[45] V.P. Ribeiro, J.M. Oliveira, R.L. Reis, Special Issue: Tissue Engineered Biomaterials and Drug Delivery Systems, Pharmaceutics, 14 (2022).
[46] N.D. Caprio, J.A. Burdick, Engineered biomaterials to guide spheroid formation, function, and fabrication into 3D tissue constructs, Acta Biomater, 165 (2023) 4-18.
[47] M. Toledano, M. Toledano-Osorio, A. Carrasco-Carmona, C. Vallecillo, R. Toledano, A.L. Medina-Castillo, R. Osorio, State of the Art on Biomaterials for Soft Tissue Augmentation in the Oral Cavity. Part II: Synthetic Polymers-Based Biomaterials, Polymers (Basel), 12 (2020).
[48] X. Li, J. Shan, X. Chen, H. Cui, G. Wen, Y. Yu, Decellularized diseased tissues: current state-of-the-art and future directions, MedComm (2020), 4 (2023) e399.

[49] M. Kasravi, A. Ahmadi, A. Babajani, R. Mazloomnejad, M.R. Hatamnejad, S. Shariatzadeh, S. Bahrami, H. Niknejad, Immunogenicity of decellularized extracellular matrix scaffolds: a bottleneck in tissue engineering and regenerative medicine, Biomater Res, 27 (2023) 10.
[50] M.B. Oliveira, C.A. Custodio, L. Gasperini, R.L. Reis, J.F. Mano, Autonomous osteogenic differentiation of hASCs encapsulated in methacrylated gellan-gum hydrogels, Acta Biomater, 41 (2016) 119-132.
[51] L. Serpico, S. Dello Iacono, A. Cammarano, L. De Stefano, Recent Advances in Stimuli-Responsive Hydrogel-Based Wound Dressing, Gels, 9 (2023).
[52] J.T. Koivisto, C. Gering, J. Karvinen, R. Maria Cherian, B. Belay, J. Hyttinen, K. Aalto-Setala, M. Kellomaki, J. Parraga, Mechanically Biomimetic Gelatin-Gellan Gum Hydrogels for 3D Culture of Beating Human Cardiomyocytes, ACS Appl Mater Interfaces, 11 (2019) 20589-20602.
[53] A. Bagheri, C.M. Fellows, C. Boyer, Reversible Deactivation Radical Polymerization: From Polymer Network Synthesis to 3D Printing, Adv Sci (Weinh), 8 (2021) 2003701.
[54] C. Lin, P. Zhao, F. Li, F. Guo, Z. Li, X. Wen, Thermosensitive in situ-forming dextran–pluronic hydrogels through Michael addition, Materials Science and Engineering: C, 30 (2010) 1236-1244.
[55] M. Ross, N. Amaral, A. Taiyab, H. Sheardown, Delivery of Cells to the Cornea Using Synthetic Biomaterials, Cornea, 41 (2022) 1325-1336.
[56] A.A.H. Abdellatif, A. Al-Subaiyel, A.M. Mohammed, Thermosensitive polymers-based injectable hydrogels: a quantitative validations design utilized for controlled delivery of gefitinib anticancer drug, Eur Rev Med Pharmacol Sci, 27 (2023) 2646-2658.
[57] J.D. Tang, C. Mura, K.J. Lampe, Stimuli-Responsive, Pentapeptide, Nanofiber Hydrogel for Tissue Engineering, J Am Chem Soc, 141 (2019) 4886-4899.
[58] A. Shit, S. Park, Y. Lee, B. Ryplida, N. Morgan, Y.C. Jang, E.J. Jin, S.Y. Park, Stimuli-responsive pressure-strain sensor-based conductive hydrogel for alleviated non-alcoholic fatty liver disease by scavenging reactive oxygen species in adipose tissue, Acta Biomater, (2023).
[59] H. Zhou, G. Dong, G. Gao, R. Du, X. Tang, Y. Ma, J. Li, Hydrogel-Based Stimuli-Responsive Micromotors for Biomedicine, Cyborg Bionic Syst, 2022 (2022) 9852853.
[60] R. Cheng, F. Meng, C. Deng, H.A. Klok, Z. Zhong, Dual and multi-stimuli responsive polymeric nanoparticles for programmed site-specific drug delivery, Biomaterials, 34 (2013) 3647-3657.
[61] A.I. Visan, R. Cristescu, Polysaccharide-Based Coatings as Drug Delivery Systems, Pharmaceutics, 15 (2023).
[62] C.L. Ward, M.A. Cornejo, S.H. Peli Thanthri, T.H. Linz, A review of electrophoretic separations in temperature-responsive Pluronic thermal gels, Anal Chim Acta, 1276 (2023) 341613.
[63] W.H. Abuwatfa, N.S. Awad, W.G. Pitt, G.A. Husseini, Thermosensitive Polymers and Thermo-Responsive Liposomal Drug Delivery Systems, Polymers (Basel), 14 (2022).
[64] G. Gardoni, N. Manfredini, G. Bagnato, M. Sponchioni, D. Moscatelli, Role of the Polymer Microstructure in Controlling Colloidal and Thermo-Responsive Properties of Nano-Objects Prepared Via RAFT Polymerization in a Non-polar Medium, Langmuir, 39 (2023) 10133-10144.

[65] X. Guan, M. Avci-Adali, E. Alarcin, H. Cheng, S.S. Kashaf, Y. Li, A. Chawla, H.L. Jang, A. Khademhosseini, Development of hydrogels for regenerative engineering, Biotechnol J, 12 (2017).
[66] U.C.L.t.a.u.a.u. Tim Arnett, https://boneresearchsociety.org/resources/image/12/.
[67] Y. Fu, X. Fan, C. Tian, J. Luo, Y. Zhang, L. Deng, T. Qin, Q. Lv, Decellularization of porcine skeletal muscle extracellular matrix for the formulation of a matrix hydrogel: a preliminary study, J Cell Mol Med, 20 (2016) 740-749.
[68] M. Kamalvand, E. Biazar, M. Daliri-Joupari, F. Montazer, M. Rezaei-Tavirani, S. Heidari-Keshel, Design of a decellularized fish skin as a biological scaffold for skin tissue regeneration, Tissue and Cell, 71 (2021) 101509.
[69] D. Nordsletten, A. Capilnasiu, W. Zhang, A. Wittgenstein, M. Hadjicharalambous, G. Sommer, R. Sinkus, G.A. Holzapfel, A viscoelastic model for human myocardium, Acta Biomater, 135 (2021) 441-457.
[70] E. Kargar-Abarghouei, Z. Vojdani, A. Hassanpour, S. Alaee, T. Talaei-Khozani, Characterization, recellularization, and transplantation of rat decellularized testis scaffold with bone marrow-derived mesenchymal stem cells, Stem Cell Res Ther, 9 (2018) 324.
[71] L.H. Dang, T.H. Nguyen, H.L.B. Tran, V.N. Doan, N.Q. Tran, Injectable Nanocurcumin-Formulated Chitosan-g-Pluronic Hydrogel Exhibiting a Great Potential for Burn Treatment, J Healthc Eng, 2018 (2018) 5754890.
[72] L. Pham, L.H. Dang, M.D. Truong, T.H. Nguyen, L. Le, V.T. Le, N.D. Nam, L.G. Bach, V.T. Nguyen, N.Q. Tran, A dual synergistic of curcumin and gelatin on thermal-responsive hydrogel based on Chitosan-P123 in wound healing application, Biomed Pharmacother, 117 (2019) 109183.
[73] N. Yang, M. Zhu, G. Xu, N. Liu, C. Yu, A near-infrared light-responsive multifunctional nanocomposite hydrogel for efficient and synergistic antibacterial wound therapy and healing promotion, J Mater Chem B, 8 (2020) 3908-3917.
[74] D.I.U. Edirisinghe, A. D'Souza, M. Ramezani, R.J. Carroll, Q. Chicon, C.L. Muenzel, J. Soule, M.B.B. Monroe, A.E. Patteson, O.V. Makhlynets, Antibacterial and Cytocompatible pH-Responsive Peptide Hydrogel, Molecules, 28 (2023).
[75] Y. Zhang, X. Gao, X. Tang, L. Peng, H. Zhang, S. Zhang, Q. Hu, J. Li, A dual pH- and temperature-responsive hydrogel produced in situ crosslinking of cyclodextrin-cellulose for wound healing, Int J Biol Macromol, 253 (2023) 126693.
[76] J.H. Ryu, Y.H. Lee, W.H. Kong, T.G. Kim, T.G. Park, Bio-inspired tissue adhesive chitosan/pluronic composite hydrogel, J Control Release, 152 Suppl 1 (2011) e236-237.
[77] M. Abbasian, B. Massoumi, R. Mohammad-Rezaei, H. Samadian, M. Jaymand, Scaffolding polymeric biomaterials: Are naturally occurring biological macromolecules more appropriate for tissue engineering?, Int J Biol Macromol, 134 (2019) 673-694.
[78] A.A. Aldana, S. Houben, L. Moroni, M.B. Baker, L.M. Pitet, Trends in double networks as bioprintable and injectable hydrogel scaffolds for tissue regeneration, ACS Biomater. Sci. Eng. , 7 (2021) 4077–4101.
[79] S. Correa, A.K. Grosskopf, H. Lopez Hernandez, D. Chan, A.C. Yu, L.M. Stapleton, E.A. Appel, Translational Applications of Hydrogels, Chem Rev, 121 (2021) 11385-11457.
[80] B. Tian, J. Liu, Smart stimuli-responsive chitosan hydrogel for drug delivery: A review, Int J Biol Macromol, 235 (2023) 123902.

[81] K.M. Park, S.Y. Lee, Y.K. Joung, J.S. Na, M.C. Lee, K.D. Park, Thermosensitive chitosan-Pluronic hydrogel as an injectable cell delivery carrier for cartilage regeneration, Acta Biomater, 5 (2009) 1956-1965.
[82] J.H. Kim, S.B. Lee, S.J. Kim, Y.M. Lee, Rapid temperature/pH response of porous alginate-g-poly(N-isopropylacrylamide) hydrogels, Polymers, 43 (2002).
[83] A. Lupu, I. Rosca, V.R. Gradinaru, M. Bercea, Temperature Induced Gelation and Antimicrobial Properties of Pluronic F127 Based Systems, Polymers (Basel), 15 (2023).
[84] S. Li, C. Yang, J. Li, C. Zhang, L. Zhu, Y. Song, Y. Guo, R. Wang, D. Gan, J. Shi, P. Ma, F. Gao, H. Su, Progress in Pluronic F127 Derivatives for Application in Wound Healing and Repair, Int J Nanomedicine, 18 (2023) 4485-4505.
[85] Z.H. Zhou, J.G. Zhang, Q. Chen, Y.L. Luo, F. Xu, Y.S. Chen, Temperature and Photo Dual-Stimuli Responsive Block Copolymer Self-Assembly Micelles for Cellular Controlled Drug Release, Macromol Biosci, 21 (2021) e2000291.
[86] S. Kotova, S. Kostjuk, Y. Rochev, Y. Efremov, A. Frolova, P. Timashev, Phase transition and potential biomedical applications of thermoresponsive compositions based on polysaccharides, proteins and DNA: A review, Int J Biol Macromol, 249 (2023) 126054.
[87] S. Rittikulsittichai, A.G. Kolhatkar, S. Sarangi, M.A. Vorontsova, P.G. Vekilov, A. Brazdeikis, T. Randall Lee, Multi-responsive hybrid particles: thermo-, pH-, photo-, and magneto-responsive magnetic hydrogel cores with gold nanorod optical triggers, Nanoscale, 8 (2016) 11851-11861.
[88] N. Yu, G. Li, Y. Gao, H. Jiang, Q. Tao, Thermo-sensitive complex micelles from sodium alginate-graft-poly(N-isopropylacrylamide) for drug release, Int J Biol Macromol, 86 (2016) 296-301.
[89] Y. Liu, W.L. Lu, J.C. Wang, X. Zhang, H. Zhang, X.Q. Wang, T.Y. Zhou, Q. Zhang, Controlled delivery of recombinant hirudin based on thermo-sensitive Pluronic F127 hydrogel for subcutaneous administration: In vitro and in vivo characterization, J Control Release, 117 (2007) 387-395.
[90] J.M. Brunet-Maheu, J.C. Fernandes, C.A. de Lacerda, Q. Shi, M. Benderdour, P. Lavigne, Pluronic F-127 as a cell carrier for bone tissue engineering, J Biomater Appl, 24 (2009) 275-287.
[91] I.M.A. Diniz, C. Chen, X. Xu, S. Ansari, H.H. Zadeh, M.M. Marques, S. Shi, A. Moshaverinia, Pluronic F-127 hydrogel as a promising scaffold for encapsulation of dental-derived mesenchymal stem cells, J Mater Sci Mater Med, 26 (2015) 153.
[92] B. Shriky, A. Kelly, M. Isreb, M. Babenko, N. Mahmoudi, S. Rogers, O. Shebanova, T. Snow, T. Gough, Pluronic F127 thermosensitive injectable smart hydrogels for controlled drug delivery system development, J Colloid Interface Sci, 565 (2020) 119-130.
[93] M.S. Akash, K. Rehman, N. Li, J.Q. Gao, H. Sun, S. Chen, Sustained delivery of IL-1Ra from pluronic F127-based thermosensitive gel prolongs its therapeutic potentials, Pharm Res, 29 (2012) 3475-3485.
[94] R.N. Shamma, R.H. Sayed, H. Madry, N.S. El Sayed, M. Cucchiarini, Triblock Copolymer Bioinks in Hydrogel Three-Dimensional Printing for Regenerative Medicine: A Focus on Pluronic F127, Tissue Eng Part B Rev, 28 (2022) 451-463.
[95] A. Arranja, A.G. Denkova, K. Morawska, G. Waton, S. van Vlierberghe, P. Dubruel, F. Schosseler, E. Mendes, Interactions of Pluronic nanocarriers with 2D and 3D cell cultures: Effects of PEO block length and aggregation state, J Control Release, 224 (2016) 126-135.

[96] R. Tan, Z. She, M. Wang, Z. Fang, Y. Liu, Q. Feng, Thermo-sensitive alginate-based injectable hydrogel for tissue engineering, Carbohydrate Polymers, 87 (2012).
[97] R. Parhi, Cross-Linked Hydrogel for Pharmaceutical Applications: A Review, Adv Pharm Bull, 7 (2017) 515-530.
[98] E.G. Ertugral-Samgar, A.M. Ozmen, O. Gok, Thermo-Responsive Hydrogels Encapsulating Targeted Core-Shell Nanoparticles as Injectable Drug Delivery Systems, Pharmaceutics, 15 (2023).
[99] I. Ortiz de Solorzano, T. Alejo, M. Abad, C. Bueno-Alejo, G. Mendoza, V. Andreu, S. Irusta, V. Sebastian, M. Arruebo, Cleavable and thermo-responsive hybrid nanoparticles for on-demand drug delivery, J Colloid Interface Sci, 533 (2019) 171-181.
[100] S. Chen, J. Shi, X. Xu, J. Ding, W. Zhong, L. Zhang, M. Xing, L. Zhang, Study of stiffness effects of poly(amidoamine)-poly(n-isopropyl acrylamide) hydrogel on wound healing, Colloids Surf B Biointerfaces, 140 (2016) 574-582.
[101] Q. Dong, D. Wu, M. Li, W. Dong, Polysaccharides, as biological macromolecule-based scaffolding biomaterials in cornea tissue engineering: A review, Tissue Cell, 76 (2022) 101782.
[102] T. Andersen, P. Auk-Emblem, M. Dornish, 3D Cell Culture in Alginate Hydrogels, Microarrays (Basel), 4 (2015) 133-161.
[103] A.K. Singh, R. Malviya, Graft Copolymers of Polysaccharide: Synthesis Methodology and Biomedical Applications in Tissue Engineering, Curr Pharm Biotechnol, 24 (2023) 510-531.
[104] F. Nagler, C. Schiller, C. Kropf, F.H. Schacher, Amphiphilic Graft Copolymers for Time-Delayed Release of Hydrophobic Fragrances, ACS Appl Mater Interfaces, 14 (2022) 56087-56096.
[105] N.R. Gupta, P.P. Ghute, M.V. Badiger, Synthesis and characterization of thermo-sensitive graft copolymer of carboxymethyl guar and poly(N-isopropylacrylamide), Carbohydr. Polym., 83 (2011) 74-80.
[106] K.Y. Lee, D.J. Mooney, Alginate: properties and biomedical applications, Prog Polym Sci, 37 (2012) 106-126.
[107] S. Pentlavalli, P. Chambers, B.N. Sathy, M. O'Doherty, M. Chalanqui, D.J. Kelly, T.H.-. Donahue, H.O. McCarthy, N.J. Dunne, Simple radical polymerization of poly(Alginate-Graft-N-Isopropylacrylamide) injectable thermoresponsive hydrogel with the potential for localized and sustained delivery of stem cells and bioactive molecules, Moleculecular Bioscience, 17 (2017) 1-12.
[108] P. Purohit, A. Bhatt, R.K. Mittal, M.H. Abdellattif, T.A. Farghaly, Polymer Grafting and its chemical reactions, Front Bioeng Biotechnol, 10 (2022) 1044927.
[109] Y. Zhong, B.J. Zeberl, X. Wang, J. Luo, Combinatorial approaches in post-polymerization modification for rational development of therapeutic delivery systems, Acta Biomater, 73 (2018) 21-37.
[110] Y. Chainani, G. Bonnanzio, K.E. Tyo, L.J. Broadbelt, Coupling chemistry and biology for the synthesis of advanced bioproducts, Curr Opin Biotechnol, 84 (2023) 102992.
[111] M. Banik, M. Oded, R. Shenhar, Coupling the chemistry and topography of block copolymer films patterned by soft lithography for nanoparticle organization, Soft Matter, 18 (2022) 5302-5311.
[112] M. D'Ischia, D. Ruiz-Molina, Bioinspired Catechol-Based Systems: Chemistry and Applications, Biomimetics (Basel), 2 (2017).

[113] L.H. Dang, P. Doan, T.T.Y. Nhi, D.T. Nguyen, B.T. Nguyen, T.P. Nguyen, N.Q. Tran, Multifunctional injectable pluronic-cystamine-alginate-based hydrogel as a novel cellular delivery system towards tissue regeneration, Int J Biol Macromol, 185 (2021) 592-603.
[114] T. Schleeh, M. Madau, D. Roessner, Two competing reactions of tetrabutylammonium alginate in organic solvents: Amidation versus gamma-lactone synthesis, Carbohydr Polym, 138 (2016) 244-251.
[115] B.A.G. de Melo, M.H.A. Santana, Structural Modifications and Solution Behavior of Hyaluronic Acid Degraded with High pH and Temperature, Appl Biochem Biotechnol, 189 (2019) 424-436.
[116] M. De Nicola, E. Bruni, E. Traversa, L. Ghibelli, Slow release of etoposide from dextran conjugation shifts etoposide activity from cytotoxicity to differentiation: A promising tool for dosage control in anticancer metronomic therapy, Nanomedicine, 13 (2017) 2005-2014.
[117] A.R. Choppin, E.L. Compere, Kinetics of the thermal decomposition of isopropyl chlorocarbonate, J Am Chem Soc, 70 (1948) 3797-3801.
[118] R. Axen, S. Ernback, Chemical fixation of enzymes to cyanogen halide activated polysaccharide carriers, Eur J Biochem, 18 (1971) 351-360.
[119] V. Ravichandran, G.P. Kothandaraman, C. Bories, P.M. Loiseau, A. Jayakrishnan, Synthetic Polysaccharides as Drug Carriers: Synthesis of Polyglucose-Amphotericin B Conjugates and In Vitro Evaluation of Their Anti-Fungal and Anti-Leishmanial Activities, J Nanosci Nanotechnol, 18 (2018) 2405-2414.
[120] B. Balakrishnan, S. Lesieur, D. Labarre, A. Jayakrishnan, Periodate oxidation of sodium alginate in water and in ethanol-water mixture: a comparative study, Carbohydr Res, 340 (2005) 1425-1429.
[121] V. Ravichandran, A. Jayakrishnan, Synthesis and evaluation of anti-fungal activities of sodium alginate-amphotericin B conjugates, Int J Biol Macromol, 108 (2018) 1101-1109.
[122] M. Gericke, T. Heinze, E. Members of European Polysaccharide Network of, Homogeneous tosylation of agarose as an approach toward novel functional polysaccharide materials, Carbohydr Polym, 127 (2015) 236-245.
[123] T. Zhou, J. Li, X. Jia, X. Zhao, P. Liu, pH/Reduction Dual-Responsive Oxidized Alginate-Doxorubicin (mPEG-OAL-DOX/Cys) Prodrug Nanohydrogels: Effect of Complexation with Cyclodextrins, Langmuir, 34 (2018) 416-424.
[124] Y. Yang, H.B. Jones, T.P. Dao, C.A. Castaneda, Single Amino Acid Substitutions in Stickers, but Not Spacers, Substantially Alter UBQLN2 Phase Transitions and Dense Phase Material Properties, J Phys Chem B, 123 (2019) 3618-3629.
[125] Y. Oishi, A. Onozuka, H. Kato, N. Shimura, S. Imai, T. Nisizawa, The effect of amino acid spacers on the antigenicity of dimeric peptide--inducing cross-reacting antibodies to a cell surface protein antigen of Streptococcus mutans, Oral Microbiol Immunol, 16 (2001) 40-44.
[126] L.M. Nong, D. Zhou, D. Zheng, Y.Q. Jiang, N.W. Xu, G.Y. Zhao, H. Wei, S.Y. Zhou, H. Han, L. Han, The effect of different cross-linking conditions of EDC/NHS on type II collagen scaffolds: an in vitro evaluation, Cell Tissue Bank, 20 (2019) 557-568.
[127] F. He, Y. Chai, Z. Zeng, F. Lu, H. Chen, J. Zhu, Y. Fang, K. Cheng, E. Miclet, V. Alezra, Y. Wan, Rapid Formation of Intramolecular Disulfide Bridges using Light: An Efficient Method to Control the Conformation and Function of Bioactive Peptides, J Am Chem Soc, (2023).

[128] J. Zhang, J. Nie, X. Zhu, Surface-Selective Grafting of Crosslinking Layers on Hydrogel Surfaces via Two Different Mechanisms of Photopolymerization for Site-Controllable Release, Macromol Rapid Commun, 39 (2018) e1800144.
[129] S. Mao, Y. Ren, S. Chen, D. Liu, X. Ye, J. Tian, Development and characterization of pH responsive sodium alginate hydrogel containing metal-phenolic network for anthocyanin delivery, Carbohydr Polym, 320 (2023) 121234.
[130] W. Hu, Z. Wang, Y. Xiao, S. Zhang, J. Wang, Advances in crosslinking strategies of biomedical hydrogels, Biomater Sci, 7 (2019) 843-855.
[131] C. Schatz, S. Lecommandoux, Polysaccharide-containing block copolymers: synthesis, properties and applications of an emerging family of glycoconjugates, Macromol Rapid Commun, 31 (2010) 1664-1684.
[132] L.S. Teixeira, J. Feijen, C.A. van Blitterswijk, P.J. Dijkstra, M. Karperien, Enzyme-catalyzed crosslinkable hydrogels: emerging strategies for tissue engineering, Biomaterials, 33 (2012) 1281-1290.
[133] V.G. Muir, J.A. Burdick, Chemically Modified Biopolymers for the Formation of Biomedical Hydrogels, Chem Rev, 121 (2021) 10908-10949.
[134] H.A. Lee, E. Park, H. Lee, Polydopamine and Its Derivative Surface Chemistry in Material Science: A Focused Review for Studies at KAIST, Adv Mater, 32 (2020) e1907505.
[135] Y. Lee, H.J. Chung, S. Yeo, C.-H. Ahn, H. Lee, P.B. Messersmith, T.G. Park, Thermo-sensitive, injectable, and tissue adhesive sol–gel transition hyaluronic acid/pluronic composite hydrogels prepared from bio-inspired catechol-thiol reaction, Soft Matter, 6 (2010) 977-983.
[136] R. Pinnataip, B.P. Lee, Oxidation Chemistry of Catechol Utilized in Designing Stimuli-Responsive Adhesives and Antipathogenic Biomaterials, ACS Omega, 6 (2021) 5113-5118.
[137] J. Yang, M.A.C. Stuart, M. Kamperman, Jack of all trades: versatile catechol crosslinking mechanisms, Chem Soc Rev, 43 (2014) 8271-8298.
[138] Y.J. Oh, I.H. Cho, H. Lee, K.J. Park, H. Lee, S.Y. Park, Bio-inspired catechol chemistry: a new way to develop a re-moldable and injectable coacervate hydrogel, Chem Commun (Camb), 48 (2012) 11895-11897.
[139] J.A. Hammer, A. Ruta, J.L. West, Using Tools from Optogenetics to Create Light-Responsive Biomaterials: LOVTRAP-PEG Hydrogels for Dynamic Peptide Immobilization, Ann Biomed Eng, 48 (2020) 1885-1894.
[140] S. Choi, H. Ahn, S.-H. Kim, Tyrosinase-mediated hydrogel crosslinking for tissue engineering, Applied Polymer Science, 139 (2021) 51887.
[141] C. Chen, M. Vazquez-Gonzalez, M.P. O'Hagan, Y. Ouyang, Z. Wang, I. Willner, Enzyme-Loaded Hemin/G-Quadruplex-Modified ZIF-90 Metal-Organic Framework Nanoparticles: Bioreactor Nanozymes for the Cascaded Oxidation of N-hydroxy-l-arginine and Sensing Applications, Small, 18 (2022) e2104420.
[142] Y. Yuan, R. Yuan, Y. Chai, Y. Zhuo, X. Ye, X. Gan, L. Bai, Hemin/G-quadruplex simultaneously acts as NADH oxidase and HRP-mimicking DNAzyme for simple, sensitive pseudobienzyme electrochemical detection of thrombin, Chem Commun (Camb), 48 (2012) 4621-4623.
[143] H. Li, J. Chang, T. Hou, F. Li, HRP-Mimicking DNAzyme-Catalyzed in Situ Generation of Polyaniline To Assist Signal Amplification for Ultrasensitive Surface Plasmon Resonance Biosensing, Anal Chem, 89 (2017) 673-680.

[144] M. Bardor, C. Faveeuw, A.C. Fitchette, D. Gilbert, L. Galas, F. Trottein, L. Faye, P. Lerouge, Immunoreactivity in mammals of two typical plant glyco-epitopes, core alpha(1,3)-fucose and core xylose, Glycobiology, 13 (2003) 427-434.
[145] Dheeraj, L. Rana, G. Hundal, New bis[MoO(2)] and [MoO(O(2))] compounds: An artificial enzyme with peroxidase activity against o-phenylenediamine and dopamine, J Inorg Biochem, 244 (2023) 112231.
[146] K. Arda, N. Ciledag, E. Aktas, B.K. Aribas, K. Kose, Quantitative assessment of normal soft-tissue elasticity using shear-wave ultrasound elastography, AJR Am J Roentgenol, 197 (2011) 532-536.
[147] R. Pozzi, I. Parzanese, A. Baccarin, M. Giunta, C.B. Conti, P. Cantu, G. Casazza, A. Tenca, R. Rosa, D. Gridavilla, G. Casella, D. Conte, M. Fraquelli, Point shear-wave elastography in chronic pancreatitis: A promising tool for staging disease severity, Pancreatology, 17 (2017) 905-910.
[148] A.E. Samir, A.S. Allegretti, Q. Zhu, M. Dhyani, A. Anvari, D.A. Sullivan, C.A. Trottier, S. Dougherty, W.W. Williams, J.L. Babitt, J. Wenger, R.I. Thadhani, H.Y. Lin, Shear wave elastography in chronic kidney disease: a pilot experience in native kidneys, BMC Nephrol, 16 (2015) 119.
[149] D.E. Discher, D.J. Mooney, P.W. Zandstra, Growth factors, matrices, and forces combine and control stem cells, Science, 324 (2009) 1673-1677.
[150] Z. Ma, S. Hu, J.S. Tan, C. Myer, N.M. Njus, Z. Xia, In vitro and in vivo mechanical properties of human ulnar and median nerves, J Biomed Mater Res A, 101 (2013) 2718-2725.
[151] H.H. Savelberg, J.G. Kooloos, R. Huiskes, J.M. Kauer, Stiffness of the ligaments of the human wrist joint, J Biomech, 25 (1992) 369-376.
[152] C. Pailler-Mattei, S. Bec, H. Zahouani, In vivo measurements of the elastic mechanical properties of human skin by indentation tests, Med Eng Phys, 30 (2008) 599-606.
[153] O. Chaudhuri, L. Gu, D. Klumpers, M. Darnell, S.A. Bencherif, J.C. Weaver, N. Huebsch, H.P. Lee, E. Lippens, G.N. Duda, D.J. Mooney, Hydrogels with tunable stress relaxation regulate stem cell fate and activity, Nat Mater, 15 (2016) 326-334.
[154] Z. Xuan, Q. Peng, T. Larsen, L. Gurevich, J. de Claville Christiansen, V. Zachar, C.P. Pennisi, Tailoring Hydrogel Composition and Stiffness to Control Smooth Muscle Cell Differentiation in Bioprinted Constructs, Tissue Eng Regen Med, 20 (2023) 199-212.
[155] C. Zhou, C. Wang, K. Xu, Z. Niu, S. Zou, D. Zhang, Z. Qian, J. Liao, J. Xie, Hydrogel platform with tunable stiffness based on magnetic nanoparticles cross-linked GelMA for cartilage regeneration and its intrinsic biomechanism, Bioact Mater, 25 (2023) 615-628.
[156] Y. Liang, S. Li, Y. Li, M. Li, X. Sun, J. An, Q. Xu, Z. Chen, Y. Wang, Impact of hydrogel stiffness on the induced neural stem cells modulation, Ann Transl Med, 9 (2021) 1784.
[157] K.L. Wu, R.C. Bretherton, J. Davis, C.A. DeForest, Pharmacological regulation of protein-polymer hydrogel stiffness, RSC Adv, 13 (2023) 24487-24490.
[158] M.M. Hasan, A.C. Dunn, Fewer polymer chains but higher adhesion: How gradient-stiffness hydrogel layers mediate adhesion through network stretch, J Chem Phys, 159 (2023).
[159] I. Levental, P.C. Georges, P.A. Janmey, Soft biological materials and their impact on cell function, Soft Matter, 3 (2007) 299-306.
[160] R.R. Chaturvedi, T. Herron, R. Simmons, D. Shore, P. Kumar, B. Sethia, F. Chua, E. Vassiliadis, J.C. Kentish, Passive stiffness of myocardium from congenital heart disease and implications for diastole, Circulation, 121 (2010) 979-988.

[161] J.Y. Rho, R.B. Ashman, C.H. Turner, Young's modulus of trabecular and cortical bone material: ultrasonic and microtensile measurements, J Biomech, 26 (1993) 111-119.
[162] S.F. Bensamoun, L. Robert, G.E. Leclerc, L. Debernard, F. Charleux, Stiffness imaging of the kidney and adjacent abdominal tissues measured simultaneously using magnetic resonance elastography, Clin Imaging, 35 (2011) 284-287.
[163] J.A. Last, S.M. Thomasy, C.R. Croasdale, P. Russell, C.J. Murphy, Compliance profile of the human cornea as measured by atomic force microscopy, Micron, 43 (2012) 1293-1298.
[164] J. Matalia, M. Francis, P. Gogri, P. Panmand, H. Matalia, A. Sinha Roy, Correlation of Corneal Biomechanical Stiffness With Refractive Error and Ocular Biometry in a Pediatric Population, Cornea, 36 (2017) 1221-1226.
[165] A.S. Arellano Buendia, J.G. Juarez Rojas, F. Garcia-Arroyo, O.E. Aparicio Trejo, F. Sanchez-Munoz, R. Arguello-Garcia, L.G. Sanchez-Lozada, R. Bojalil, H. Osorio-Alonso, Antioxidant and anti-inflammatory effects of allicin in the kidney of an experimental model of metabolic syndrome, PeerJ, 11 (2023) e16132.
[166] E. Arribas-Lopez, N. Zand, O. Ojo, M.J. Snowden, T. Kochhar, The Effect of Amino Acids on Wound Healing: A Systematic Review and Meta-Analysis on Arginine and Glutamine, Nutrients, 13 (2021).
[167] Y. Zhou, G. Liu, H. Huang, J. Wu, Advances and impact of arginine-based materials in wound healing, J Mater Chem B, 9 (2021) 6738-6750.
[168] M. Sun, Y. Cao, Y. Xing, X. Mu, Y. Hao, J. Yang, X. Niu, D. Li, Effects of L-Arginine and Arginine-Arginine dipeptide on amino acids uptake and alphaS1-casein synthesis in bovine mammary epithelial cells, J Anim Sci, (2023).
[169] C. Tu, H. Lu, T. Zhou, W. Zhang, L. Deng, W. Cao, Z. Yang, Z. Wang, X. Wu, J. Ding, F. Xu, C. Gao, Promoting the healing of infected diabetic wound by an anti-bacterial and nano-enzyme-containing hydrogel with inflammation-suppressing, ROS-scavenging, oxygen and nitric oxide-generating properties, Biomaterials, 286 (2022) 121597.
[170] A. Sadhu, Y. Moriyasu, K. Acharya, M. Bandyopadhyay, Nitric oxide and ROS mediate autophagy and regulate Alternaria alternata toxin-induced cell death in tobacco BY-2 cells, Sci Rep, 9 (2019) 8973.
[171] L.M. House, 2nd, R.T. Morris, T.M. Barnes, L. Lantier, T.J. Cyphert, O.P. McGuinness, Y.F. Otero, Tissue inflammation and nitric oxide-mediated alterations in cardiovascular function are major determinants of endotoxin-induced insulin resistance, Cardiovasc Diabetol, 14 (2015) 56.
[172] R. Sergi, D. Bellucci, V. Cannillo, A Review of Bioactive Glass/Natural Polymer Composites: State of the Art, Materials (Basel), 13 (2020).
[173] A. Dreanca, M. Muresan-Pop, M. Taulescu, Z.R. Toth, S. Bogdan, C. Pestean, S. Oren, C. Toma, A. Popescu, E. Pall, B. Sevastre, L. Baia, K. Magyari, Bioactive glass-biopolymers-gold nanoparticle based composites for tissue engineering applications, Mater Sci Eng C Mater Biol Appl, 123 (2021) 112006.
[174] E. Daskalakis, B. Huang, C. Vyas, A.A. Acar, A. Fallah, G. Cooper, A. Weightman, B. Koc, G. Blunn, P. Bartolo, Novel 3D Bioglass Scaffolds for Bone Tissue Regeneration, Polymers (Basel), 14 (2022).
[175] A. Can Karaca, E. Assadpour, S.M. Jafari, Plant protein-based emulsions for the delivery of bioactive compounds, Adv Colloid Interface Sci, 316 (2023) 102918.

[176] Y. Chen, W. Yu, H. Cao, Arginine-Functionalized Thin Film Composite Forward Osmosis Membrane Integrating Antifouling and Antibacterial Effects, Membranes (Basel), 13 (2023).
[177] H. Cao, L. Duan, Y. Zhang, J. Cao, K. Zhang, Current hydrogel advances in physicochemical and biological response-driven biomedical application diversity, Signal Transduct Target Ther, 6 (2021) 426.
[178] L. He, J. Yin, X. Gao, Additive Manufacturing of Bioactive Glass and Its Polymer Composites as Bone Tissue Engineering Scaffolds: A Review, Bioengineering (Basel), 10 (2023).
[179] M.E.V. Barreto, R.P. Medeiros, A. Shearer, M.V.L. Fook, M. Montazerian, J.C. Mauro, Gelatin and Bioactive Glass Composites for Tissue Engineering: A Review, J Funct Biomater, 14 (2022).
[180] M. Bi, Y. Qin, L. Wang, J. Zhang, The protective role of resveratrol in diabetic wound healing, Phytother Res, (2023).
[181] Z. Chen, D. Ceballos-Francisco, F.A. Guardiola, D. Huang, M.A. Esteban, The alleviation of skin wound-induced intestinal barrier dysfunction via modulation of TLR signalling using arginine in gilthead seabream (Sparus aurata L), Fish Shellfish Immunol, 107 (2020) 519-528.
[182] Y. Wen, J.K. Oh, Recent strategies to develop polysaccharide-based nanomaterials for biomedical applications, Macromol Rapid Commun, 35 (2014) 1819-1832.
[183] Y.J. Kuo, C.H. Chen, P. Dash, Y.C. Lin, C.W. Hsu, S.J. Shih, R.J. Chung, Angiogenesis, Osseointegration, and Antibacterial Applications of Polyelectrolyte Multilayer Coatings Incorporated With Silver/Strontium Containing Mesoporous Bioactive Glass on 316L Stainless Steel, Front Bioeng Biotechnol, 10 (2022) 818137.
[184] S. Myronchenko, T. Zvyagintseva, N. Gridina, N. Kytsiuk, Y. Zhelnin, The Role of Nitric Oxide and Peroxynitrite in the Erythemal Period of Ultraviolet-Induced Skin Damage, Wiad Lek, 76 (2023) 1737-1741.
[185] A.K. Pinheiro, D.A. Pereira, J.L. Dos Santos, F.B. Calmasini, E.C. Alexandre, L.O. Reis, A.L. Burnett, F.F. Costa, F.H. Silva, Resveratrol-nitric oxide donor hybrid effect on priapism in sickle cell and nitric oxide-deficient mouse, PLoS One, 17 (2022) e0269310.
[186] R.L. Mokry, B.S. O'Brien, J.W. Adelman, S. Rosas, M.L. Schumacher, A.D. Ebert, S.S. Terhune, Nitric Oxide Attenuates Human Cytomegalovirus Infection yet Disrupts Neural Cell Differentiation and Tissue Organization, J Virol, 96 (2022) e0012622.
[187] A.J. Kutner, A.J. Friedman, Use of nitric oxide nanoparticulate platform for the treatment of skin and soft tissue infections, Wiley Interdiscip Rev Nanomed Nanobiotechnol, 5 (2013) 502-514.
[188] S.E. Maloney, C.A. Broberg, Q.E. Grayton, S.L. Picciotti, H.R. Hall, S.M. Wallet, R. Maile, M.H. Schoenfisch, Role of Nitric Oxide-Releasing Glycosaminoglycans in Wound Healing, ACS Biomater Sci Eng, 8 (2022) 2537-2552.
[189] A. Sirsjo, M. Karlsson, A. Gidlof, O. Rollman, H. Torma, Increased expression of inducible nitric oxide synthase in psoriatic skin and cytokine-stimulated cultured keratinocytes, Br J Dermatol, 134 (1996) 643-648.
[190] X. Tang, L. Yang, K.L. Sung, [Advance of researches in nitric oxide biological function on wound repair], Sheng Wu Yi Xue Gong Cheng Xue Za Zhi, 27 (2010) 211-214.

[191] B. Stallmeyer, H. Kampfer, N. Kolb, J. Pfeilschifter, S. Frank, The function of nitric oxide in wound repair: inhibition of inducible nitric oxide-synthase severely impairs wound reepithelialization, J Invest Dermatol, 113 (1999) 1090-1098.
[192] A. Soneja, M. Drews, T. Malinski, Role of nitric oxide, nitroxidative and oxidative stress in wound healing, Pharmacol Rep, 57 Suppl (2005) 108-119.
[193] A. Stancic, A. Jankovic, A. Korac, B. Buzadzic, V. Otasevic, B. Korac, The role of nitric oxide in diabetic skin (patho)physiology, Mech Ageing Dev, 172 (2018) 21-29.
[194] M. Miao, Y. Niu, T. Xie, B. Yuan, C. Qing, S. Lu, Diabetes-impaired wound healing and altered macrophage activation: a possible pathophysiologic correlation, Wound Repair Regen, 20 (2012) 203-213.
[195] S. Eligini, B. Porro, J.P. Werba, N. Capra, S. Genovese, A. Greco, V. Cavalca, C. Banfi, Oxidative Stress and Arginine/Nitric Oxide Pathway in Red Blood Cells Derived from Patients with Prediabetes, Biomedicines, 10 (2022).
[196] D.D. Thomas, M.G. Espey, L.A. Ridnour, L.J. Hofseth, D. Mancardi, C.C. Harris, D.A. Wink, Hypoxic inducible factor 1alpha, extracellular signal-regulated kinase, and p53 are regulated by distinct threshold concentrations of nitric oxide, Proc Natl Acad Sci U S A, 101 (2004) 8894-8899.
[197] S. Frank, B. Stallmeyer, H. Kampfer, N. Kolb, J. Pfeilschifter, Nitric oxide triggers enhanced induction of vascular endothelial growth factor expression in cultured keratinocytes (HaCaT) and during cutaneous wound repair, FASEB J, 13 (1999) 2002-2014.
[198] H. Iqbal, P. Yadav, A.K. Verma, D. Mishra, B. Vamadevan, D. Singh, S. Luqman, A.S. Negi, D. Chanda, Anti-inflammatory, anti-oxidant and cardio-protective properties of novel fluorophenyl benzimidazole in L-NAME-induced hypertensive rats, Eur J Pharmacol, 929 (2022) 175132.
[199] Y. Takizawa, Y. Kosuge, H. Awaji, E. Tamura, A. Takai, T. Yanai, R. Yamamoto, K. Kokame, T. Miyata, R. Nakata, H. Inoue, Up-regulation of endothelial nitric oxide synthase (eNOS), silent mating type information regulation 2 homologue 1 (SIRT1) and autophagy-related genes by repeated treatments with resveratrol in human umbilical vein endothelial cells, Br J Nutr, 110 (2013) 2150-2155.
[200] J. Jensen, D. Packert, C. Miller, G. Packert, J. Hanft, S. Jensen, Discovery and Development of Gaseous Nitric Oxide Under Increased Atmospheric Pressure as an Antimicrobial: In Vitro and In Vivo Testing of Nitric Oxide Against Multidrug-Resistant Organisms, Clin Podiatr Med Surg, 37 (2020) 231-246.
[201] T. Treadwell, Use of Topical Gaseous Nitric Oxide/Plasma Energy in the Treatment of Recalcitrant Wounds, Surg Technol Int, 43 (2023).
[202] A. Ghaffari, C.C. Miller, B. McMullin, A. Ghahary, Potential application of gaseous nitric oxide as a topical antimicrobial agent, Nitric Oxide, 14 (2006) 21-29.
[203] A. Ghaffari, R. Jalili, M. Ghaffari, C. Miller, A. Ghahary, Efficacy of gaseous nitric oxide in the treatment of skin and soft tissue infections, Wound Repair Regen, 15 (2007) 368-377.
[204] M. Wu, Z. Lu, K. Wu, C. Nam, L. Zhang, J. Guo, Recent advances in the development of nitric oxide-releasing biomaterials and their application potentials in chronic wound healing, J Mater Chem B, 9 (2021) 7063-7075.
[205] M. Pekarova, A. Lojek, H. Martiskova, O. Vasicek, L. Bino, A. Klinke, D. Lau, R. Kuchta, J. Kadlec, R. Vrba, L. Kubala, New role for L-arginine in regulation of inducible

nitric-oxide-synthase-derived superoxide anion production in raw 264.7 macrophages, ScientificWorldJournal, 11 (2011) 2443-2457.
[206] T.S. Lai, A. Hausladen, T.F. Slaughter, J.P. Eu, J.S. Stamler, C.S. Greenberg, Calcium regulates S-nitrosylation, denitrosylation, and activity of tissue transglutaminase, Biochemistry, 40 (2001) 4904-4910.
[207] L.E. Laverman, A. Wanat, J. Oszajca, G. Stochel, P.C. Ford, R. van Eldik, Mechanistic studies on the reversible binding of nitric oxide to metmyoglobin, J Am Chem Soc, 123 (2001) 285-293.
[208] J. Kim, G. Saravanakumar, H.W. Choi, D. Park, W.J. Kim, A platform for nitric oxide delivery, J Mater Chem B, 2 (2014) 341-356.
[209] L. Tie, H.Q. Yang, Y. An, S.Q. Liu, J. Han, Y. Xu, M. Hu, W.D. Li, A.F. Chen, Z.B. Lin, X.J. Li, Ganoderma lucidum polysaccharide accelerates refractory wound healing by inhibition of mitochondrial oxidative stress in type 1 diabetes, Cell Physiol Biochem, 29 (2012) 583-594.
[210] A. Jankovic, C. Ferreri, M. Filipovic, I. Ivanovic-Burmazovic, A. Stancic, V. Otasevic, A. Korac, B. Buzadzic, B. Korac, Targeting the superoxide/nitric oxide ratio by L-arginine and SOD mimic in diabetic rat skin, Free Radic Res, 50 (2016) S51-S63.
[211] N. Xia, U. Forstermann, H. Li, Resveratrol and endothelial nitric oxide, Molecules, 19 (2014) 16102-16121.
[212] A. Gonzalez-Vicente, P.D. Cabral, J.L. Garvin, Resveratrol increases nitric oxide production in the rat thick ascending limb via Ca2+/calmodulin, PLoS One, 9 (2014) e110487.
[213] Z. Ghaeini Hesarooeyeh, A. Basham, M. Sheybani-Arani, M. Abbaszadeh, A. Salimi Asl, M. Moghbeli, E. Saburi, Effect of resveratrol and curcumin and the potential synergism on hypertension: A mini-review of human and animal model studies, Phytother Res, (2023).
[214] I. Datseris, N. Bouratzis, C. Kotronis, I. Datseris, M.E. Tzanidaki, A. Rouvas, N. Gouliopoulos, One-year outcomes of resveratrol supplement with aflibercept versus aflibercept monotherapy in wet age-related macular degeneration, Int J Ophthalmol, 16 (2023) 1496-1502.
[215] M. Paczkowska-Walendowska, A. Miklaszewski, B. Michniak-Kohn, J. Cielecka-Piontek, The Antioxidant Potential of Resveratrol from Red Vine Leaves Delivered in an Electrospun Nanofiber System, Antioxidants (Basel), 12 (2023).
[216] M.D. Knutson, C. Leeuwenburgh, Resveratrol and novel potent activators of SIRT1: effects on aging and age-related diseases, Nutr Rev, 66 (2008) 591-596.
[217] L. Ciccone, E. Piragine, S. Brogi, C. Camodeca, R. Fucci, V. Calderone, S. Nencetti, A. Martelli, E. Orlandini, Resveratrol-like Compounds as SIRT1 Activators, Int J Mol Sci, 23 (2022).
[218] Y. Wang, X. Zhao, D. Shi, P. Chen, Y. Yu, L. Yang, L. Xie, Overexpression of SIRT1 promotes high glucose-attenuated corneal epithelial wound healing via p53 regulation of the IGFBP3/IGF-1R/AKT pathway, Invest Ophthalmol Vis Sci, 54 (2013) 3806-3814.
[219] X. Huang, J. Sun, G. Chen, C. Niu, Y. Wang, C. Zhao, J. Sun, H. Huang, S. Huang, Y. Liang, Y. Shen, W. Cong, L. Jin, Z. Zhu, Resveratrol Promotes Diabetic Wound Healing via SIRT1-FOXO1-c-Myc Signaling Pathway-Mediated Angiogenesis, Front Pharmacol, 10 (2019) 421.
[220] N. Tamura, N. Heidari, R.G.A. Faragher, R.K.W. Smith, J. Dudhia, Effects of resveratrol and its analogues on the cell cycle of equine mesenchymal stem/stromal cells, J Equine Sci, 34 (2023) 67-72.

[221] A. Aldhaher, F. Shahabipour, A. Shaito, S. Al-Assaf, A.A.M. Elnour, E.B. Sallam, S. Teimourtash, A.A. Elfadil, 3D hydrogel/ bioactive glass scaffolds in bone tissue engineering: Status and future opportunities, Heliyon, 9 (2023) e17050.
[222] X. Zhang, J. Cui, L. Cheng, K. Lin, Enhancement of osteoporotic bone regeneration by strontium-substituted 45S5 bioglass via time-dependent modulation of autophagy and the Akt/mTOR signaling pathway, J Mater Chem B, 9 (2021) 3489-3501.
[223] M. Li, A. Zhang, J. Li, J. Zhou, Y. Zheng, C. Zhang, D. Xia, H. Mao, J. Zhao, Osteoblast/fibroblast coculture derived bioactive ECM with unique matrisome profile facilitates bone regeneration, Bioact Mater, 5 (2020) 938-948.
[224] N. Attik, R. Gauthier, M. Ahmed, Bioactive Glass-Based Materials for Soft and Hard Tissue Regeneration: A New Future for Dental and Biomedical Applications, Materials (Basel), 16 (2023).
[225] Z. Xu, T. Wang, Y. Li, M. Wen, K. Liang, C. Ruan, L. Zhang, Y. Xue, L. Shang, Nanozyme-Engineered Bioglass through Supercharged Interface for Enhanced Anti-Infection and Fibroblast Regulation, Advance Functional Materials, 33 (2023).
[226] J. Sun, J. Yang, D. Jeon, D. Park, J.W. Kim, Shear-Responsive Sol-Gel Transition of Phase Change Material Emulsions for an Injectable Thermal Insulation Platform, Small, (2023) e2304120.
[227] A. Zambon, G. Malavasi, A. Pallini, F. Fraulini, G. Lusvardi, Cerium Containing Bioactive Glasses: A Review, ACS Biomater Sci Eng, 7 (2021) 4388-4401.
[228] I. Atkinson, A.M. Seciu-Grama, S. Petrescu, D. Culita, O.C. Mocioiu, M. Voicescu, R.A. Mitran, D. Lincu, A.M. Prelipcean, O. Craciunescu, Cerium-Containing Mesoporous Bioactive Glasses (MBGs)-Derived Scaffolds with Drug Delivery Capability for Potential Tissue Engineering Applications, Pharmaceutics, 14 (2022).
[229] C.F. de Freitas, J. de Araujo Santos, D.S. Pellosi, W. Caetano, V.R. Batistela, E.C. Muniz, Recent advances of Pluronic-based copolymers functionalization in biomedical applications, Biomater Adv, 151 (2023) 213484.
[230] F. Kalogeropoulou, D. Papailiou, C. Protopapa, A. Siamidi, L.A. Tziveleka, N. Pippa, M. Vlachou, Design and Development of Low- and Medium-Viscosity Alginate Beads Loaded with Pluronic((R)) F-127 Nanomicelles, Materials (Basel), 16 (2023).
[231] Y. Petkova-Olsson, C. Oelschlaeger, H. Ullsten, L. Jarnstrom, Structural, microrheological and kinetic properties of a ternary silica-Pluronic F127-starch thermosensitive system, J Colloid Interface Sci, 514 (2018) 459-467.
[232] E. Gioffredi, M. Boffito, S. Calzone, S.M. Giannitelli, A. Rainer, M. Trombetta, P. Mozetic, V. Chiono, Pluronic F127 Hydrogel Characterization and Biofabrication in Cellularized Constructs for Tissue Engineering Applications, Procedia CIRP, 49 (2016) 125-132.
[233] A. Dalmoro, A.A. Barba, M. Grassi, G. Grassi, G. Lamberti, In situ coronary stent paving by Pluronic F127-alginate gel blends: Formulation and erosion tests, J Biomed Mater Res B Appl Biomater, 104 (2016) 1013-1022.
[234] M.T. Cidade, D.J. Ramos, J. Santos, H. Carrelo, N. Calero, J.P. Borges, Injectable Hydrogels Based on Pluronic/Water Systems Filled with Alginate Microparticles for Biomedical Applications, Materials (Basel), 12 (2019).
[235] S.I.H. Abdi, J.Y. Choi, J.S. Lee, H.J. Lim, C. Lee, J. Kim, H.Y. Chung, J.O. Lim, In Vivo study of a blended hydrogel composed of pluronic F-127-alginate-hyaluronic acid for its cell injection application, Tissue Engineering and Regenerative Medicine, 9 (2012) 1-9.

[236] M. Constantin, B. Cosman, M. Bercea, G.L. Ailiesei, G. Fundueanu, Thermosensitive Poloxamer-graft-Carboxymethyl Pullulan: A Potential Injectable Hydrogel for Drug Delivery, Polymers (Basel), 13 (2021).
[237] C.C. Chen, C.L. Fang, S.A. Al-Suwayeh, Y.L. Leu, J.Y. Fang, Transdermal delivery of selegiline from alginate-Pluronic composite thermogels, Int J Pharm, 415 (2011) 119-128.
[238] J.H. Ryu, Y. Lee, W.H. Kong, T.G. Kim, T.G. Park, H. Lee, Catechol-functionalized chitosan/pluronic hydrogels for tissue adhesives and hemostatic materials, Biomacromolecules, 12 (2011) 2653-2659.
[239] S. Khan, N. Akhtar, M.U. Minhas, Fabrication, rheological analysis, and in vitro characterization of in situ chemically cross-linkable thermogels as controlled and prolonged drug depot for localized and systemic delivery, polymer advanced technologies, 30 (2019) 755-771.
[240] Q. Yang, J. Peng, H. Xiao, X. Xu, Z. Qian, Polysaccharide hydrogels: Functionalization, construction and served as scaffold for tissue engineering, Carbohydr Polym, 278 (2022) 118952.
[241] G. Grassi, A. Crevatin, R. Farra, G. Guarnieri, A. Pascotto, B. Rehimers, R. Lapasin, M. Grassi, Rheological properties of aqueous Pluronic-alginate systems containing liposomes, J Colloid Interface Sci, 301 (2006) 282-290.
[242] S. Kuncorojakti, W. Rodprasert, S. Yodmuang, T. Osathanon, P. Pavasant, S. Srisuwatanasagul, C. Sawangmake, Alginate/Pluronic F127-based encapsulation supports viability and functionality of human dental pulp stem cell-derived insulin-producing cells, J Biol Eng, 14 (2020) 23.
[243] K. Chen, C. Zhou, L. Yao, M. Jing, C. Liu, C. Shen, Y. Wang, Phase morphology, rheological behavior and mechanical properties of supertough biobased poly(lactic acid) reactive ternary blends, Int J Biol Macromol, 253 (2023) 127079.
[244] R.S. Ashton, A. Banerjee, S. Punyani, D.V. Schaffer, R.S. Kane, Scaffolds based on degradable alginate hydrogels and poly(lactide-co-glycolide) microspheres for stem cell culture, Biomaterials, 28 (2007) 5518-5525.
[245] M. Tian, H. Li, L. Ma, Z. Gu, X. Qi, X. Li, H. Tan, C. You, Long-term and oxidative-responsive alginate-deferoxamine conjugates with low toxicity for iron overload, RSC Adv, 6 (2016) 32471-32479.
[246] Y. Li, Z. Xu, J. Wang, X. Pei, J. Chen, Q. Wan, Alginate-based biomaterial-mediated regulation of macrophages in bone tissue engineering, Int J Biol Macromol, 230 (2023) 123246.
[247] N. Czaplicka, D. Konopacka-Lyskawa, A. Nowotnik, A. Mielewczyk-Gryn, M. Lapinski, R. Bray, Precipitation of calcium carbonate in the presence of rhamnolipids in alginate hydrogels as a model of biomineralization, Colloids Surf B Biointerfaces, 218 (2022) 112749.
[248] Y.N. Dai, P. Li, J.P. Zhang, A.Q. Wang, Q. Wei, Swelling characteristics and drug delivery properties of nifedipine-loaded pH sensitive alginate-chitosan hydrogel beads, J Biomed Mater Res B Appl Biomater, 86 (2008) 493-500.
[249] Y. Zhao, S.G.S. Zhao, Y. Li, L. Cheng, J. Li, Y. Yin, Synthesis and characterization of disulfide-crosslinked alginate hydrogel scaffolds, Mater. Sci. Eng. C, 32 (2012) 2153-2162.
[250] E. Gómez-Ordóñez, P. Rupérez, FTIR-ATR spectroscopy as a tool for polysaccharide identification in edible brown and red seaweeds, Food Hydrocollidal 25 (2011) 1514-1520.

[251] W. Wan, Q. Li, H. Gao, L. Ge, Y. Liu, W. Zhong, J. Ouyang, M. Xing, BMSCs laden injectable amino-diethoxypropane modified alginate-chitosan hydrogel for hyaline cartilage reconstruction, J Mater Chem B, 3 (2015) 1990-2005.
[252] F. Laffleur, P. Kuppers, Adhesive alginate for buccal delivery in aphthous stomatitis, Carbohydr Res, 477 (2019) 51-57.
[253] G. Cattelan, A. Guerrero Gerboles, R. Foresti, P.P. Pramstaller, A. Rossini, M. Miragoli, C. Caffarra Malvezzi, Alginate Formulations: Current Developments in the Race for Hydrogel-Based Cardiac Regeneration, Front Bioeng Biotechnol, 8 (2020) 414.
[254] B.H. Lee, B. Li, S.A. Guelcher, Gel microstructure regulates proliferation and differentiation of MC3T3-E1 cells encapsulated in alginate beads, Acta Biomater, 8 (2012) 1693-1702.
[255] R. Mhanna, A. Kashyap, G. Palazzolo, Q. Vallmajo-Martin, J. Becher, S. Moller, M. Schnabelrauch, M. Zenobi-Wong, Chondrocyte culture in three dimensional alginate sulfate hydrogels promotes proliferation while maintaining expression of chondrogenic markers, Tissue Eng Part A, 20 (2014) 1454-1464.
[256] H. Jeon, K. Kang, S.A. Park, W.D. Kim, S.S. Paik, S.H. Lee, J. Jeong, D. Choi, Generation of Multilayered 3D Structures of HepG2 Cells Using a Bio-printing Technique, Gut Liver, 11 (2017) 121-128.
[257] B. Wright, R.A. Cave, J.P. Cook, V.V. Khutoryanskiy, S. Mi, B. Chen, M. Leyland, C.J. Connon, Enhanced viability of corneal epithelial cells for efficient transport/storage using a structurally modified calcium alginate hydrogel, Regen Med, 7 (2012) 295-307.
[258] S.K. Williams, J.S. Touroo, K.H. Church, J.B. Hoying, Encapsulation of adipose stromal vascular fraction cells in alginate hydrogel spheroids using a direct-write three-dimensional printing system, Biores Open Access, 2 (2013) 448-454.
[259] J.L. Bron, L.A. Vonk, T.H. Smit, G.H. Koenderink, Engineering alginate for intervertebral disc repair, J Mech Behav Biomed Mater, 4 (2011) 1196-1205.
[260] N. Landa, L. Miller, M.S. Feinberg, R. Holbova, M. Shachar, I. Freeman, S. Cohen, J. Leor, Effect of injectable alginate implant on cardiac remodeling and function after recent and old infarcts in rat, Circulation, 117 (2008) 1388-1396.
[261] S. Sancilio, M. Gallorini, C. Di Nisio, E. Marsich, R. Di Pietro, H. Schweikl, A. Cataldi, Alginate/Hydroxyapatite-Based Nanocomposite Scaffolds for Bone Tissue Engineering Improve Dental Pulp Biomineralization and Differentiation, Stem Cells Int, 2018 (2018) 9643721.
[262] M.I. Neves, L. Moroni, C.C. Barrias, Modulating Alginate Hydrogels for Improved Biological Performance as Cellular 3D Microenvironments, Front Bioeng Biotechnol, 8 (2020) 665.
[263] A.M. Smith, J.J. Senior, Alginate Hydrogels with Tuneable Properties, Adv Biochem Eng Biotechnol, 178 (2021) 37-61.
[264] S.J. Bidarra, C.C. Barrias, P.L. Granja, Injectable alginate hydrogels for cell delivery in tissue engineering, Acta Biomater, 10 (2014) 1646-1662.
[265] F. Charbonier, D. Indana, O. Chaudhuri, Tuning Viscoelasticity in Alginate Hydrogels for 3D Cell Culture Studies, Curr Protoc, 1 (2021) e124.
[266] A. Ahmad, R. Prakash, M.S. Khan, N. Altwaijry, M.N. Asghar, S.S. Raza, R. Khan, Enhanced Antioxidant Effects of Naringenin Nanoparticles Synthesized using the High-Energy Ball Milling Method, ACS Omega, 7 (2022) 34476-34484.

[267] M. Steigedal, H. Sletta, S. Moreno, M. Maerk, B.E. Christensen, T. Bjerkan, T.E. Ellingsen, G. Espin, H. Ertesvag, S. Valla, The Azotobacter vinelandii AlgE mannuronan C-5-epimerase family is essential for the in vivo control of alginate monomer composition and for functional cyst formation, Environ Microbiol, 10 (2008) 1760-1770.
[268] M. Kuzmanovic, D.K. Božanic, D. Milivojevic, D.M. Culafic, S. Stankovic, C. Ballesteros, J. Gonzalez-Benito, Sodium-alginate biopolymer as a template for the synthesis of nontoxic red emitting Mn 2 -doped CdS nanoparticles, RSC Adv, 7 (2017) 53422-53432.
[269] X.C. M Tian, H Li, L Ma, Z Gu, X Qi, X Li, H Tan, C You, Long-term and oxidative-responsive alginate-deferoxamine conjugates with low toxicity for iron overload, RSC Adv., 6 (2016) 32471-32479.
[270] R. Mahou, F. Borcard, V. Crivelli, E. Montanari, S. Passemard, F. Noverraz, S. Gerber-Lemaire, L.o. Bühler, C. Wandrey, Tuning the properties of hydrogel microspheres by adding chemical cross-linking functionality to sodium alginate, Chemistry of Materials, 27 (2015) 4380-4389 %@ 0897-4756.
[271] D. Bhati, B. Singh, A. Singh, S. Sharma, R. Pandiselvam, Assessment of physicochemical, rheological, and thermal properties of Indian rice cultivars: Implications on the extrusion characteristics, J Texture Stud, 53 (2022) 854-869.
[272] Y. Ji, W. Kang, S. Liu, R. Yang, H. Fan, The relationships between rheological rules and cohesive energy of amphiphilic polymers with different hydrophobic groups, Journal of Polymer Research, 22 (2015).
[273] S. Desai, B.J. Carberry, K.S. Anseth, K.M. Schultz, Characterizing rheological properties and microstructure of thioester networks during degradation, Soft Matter, (2023).
[274] H. Herrada-Manchon, M.A. Fernandez, E. Aguilar, Essential Guide to Hydrogel Rheology in Extrusion 3D Printing: How to Measure It and Why It Matters?, Gels, 9 (2023).
[275] S. Unterman, L.F. Charles, S.E. Strecker, D. Kramarenko, D. Pivovarchik, E.R. Edelman, N. Artzi, Hydrogel Nanocomposites with Independently Tunable Rheology and Mechanics, ACS Nano, 11 (2017) 2598-2610.
[276] T.B.T. Nguyen, L.H. Dang, T.T.T. Nguyen, D.L. Tran, D.H. Nguyen, V.T. Nguyen, C.K. Nguyen, T.H. Nguyen, V.T. Le, N.Q. Tran, Green processing of thermosensitive nanocurcumin-encapsulated chitosan hydrogel towards biomedical application, Green Processing and synthesis, 5 (2016) 511-520 %@ 2191-9550.
[277] T.T. Lau, D.A. Wang, Bioresponsive hydrogel scaffolding systems for 3D constructions in tissue engineering and regenerative medicine, Nanomedicine (Lond), 8 (2013) 655-668.
[278] C.N.M. Ryan, M.N. Doulgkeroglou, D.I. Zeugolis, Electric field stimulation for tissue engineering applications, BMC Biomedical Engineering, 3 (2021).
[279] A. Zainuddin, K.H. Chua, N. Abdul Rahim, S. Makpol, Effect of experimental treatment on GAPDH mRNA expression as a housekeeping gene in human diploid fibroblasts, BMC Mol Biol, 11 (2010) 59.
[280] A.G. Guex, D.J. Poxson, D.T. Simon, M. Berggren, G. Fortunato, R.M. Rossi, K. Maniura-Weber, M. Rottmar, Controlling pH by electronic ion pumps to fight fibrosis, Applied Materials Today, 22 (2021) 100936.
[281] C.R. Kruse, M. Singh, S. Targosinski, I. Sinha, J.A. Sorensen, E. Eriksson, K. Nuutila, The effect of pH on cell viability, cell migration, cell proliferation, wound closure, and wound reepithelialization: In vitro and in vivo study, Wound Repair Regen, 25 (2017) 260-269.

[282] N. Poklar Ulrih, R. Opara, M. Korosec, M. Wondra, V. Abram, Part II. Influence of trans-resveratrol addition on the sensory properties of 'Blaufrankisch' red wine, Food Chem Toxicol, 137 (2020) 111124.
[283] Z. Zhang, T. Wei, Y. Chen, T. Chen, B. Chi, F. Wang, X. Chen, A polydiacetylenes-based colorimetric and fluorescent probe for l-arginine and l-lysine and its application for logic gate, Sensors and Actuators B: Chemical, 225 (2018) 2211-2217.
[284] L. Zeußel, P. Mai, S. Sharma, A. Schober, S. Ren, S. Singh, Colorimetric Method for Instant Detection of Lysine and Arginine Using Novel Meldrum's Acid-Furfural Conjugate, Chemistry Select 6(2021) 6834-6840.
[285] S.M. Hashemnejad, A.Z.M. Badruddoza, B. Zarket, C. Ricardo Castaneda, P.S. Doyle, Thermoresponsive nanoemulsion-based gel synthesized through a low-energy process, Nat Commun, 10 (2019) 2749.
[286] K.L. Schneider, N. Yahia, Effectiveness of Arginine Supplementation on Wound Healing in Older Adults in Acute and Chronic Settings: A Systematic Review, Adv Skin Wound Care, 32 (2019) 457-462.
[287] H. Jiang, Q. Xu, X. Wang, L. Shi, X. Yang, J. Sun, X. Mei, Preparation of Antibacterial, Arginine-Modified Ag Nanoclusters in the Hydrogel Used for Promoting Diabetic, Infected Wound Healing, ACS Omega, 8 (2023) 12653-12663.
[288] I.Y. Wu, S. Bala, N. Skalko-Basnet, M.P. di Cagno, Interpreting non-linear drug diffusion data: Utilizing Korsmeyer-Peppas model to study drug release from liposomes, Eur J Pharm Sci, 138 (2019) 105026.
[289] S. Unal, G. Varan, J.M. Benito, Y. Aktas, E. Bilensoy, Insight into oral amphiphilic cyclodextrin nanoparticles for colorectal cancer: comprehensive mathematical model of drug release kinetic studies and antitumoral efficacy in 3D spheroid colon tumors, Beilstein J Org Chem, 19 (2023) 139-157.
[290] L.F. Ferreira, M.B. Reid, Muscle-derived ROS and thiol regulation in muscle fatigue, J Appl Physiol (1985), 104 (2008) 853-860.
[291] M. Conrad, I. Ingold, K. Buday, S. Kobayashi, J.P. Angeli, ROS, thiols and thiol-regulating systems in male gametogenesis, Biochim Biophys Acta, 1850 (2015) 1566-1574.
[292] H. Shokrani, A. Shokrani, F. Seidi, M.T. Munir, N. Rabiee, Y. Fatahi, J. Kucinska-Lipka, M.R. Saeb, Biomedical engineering of polysaccharide-based tissue adhesives: Recent advances and future direction, Carbohydr Polym, 295 (2022) 119787.
[293] P.J. Dykes, R. Marks, An evaluation of the irritancy potential of povidone iodine solutions: comparison of subjective and objective assessment techniques, Clin Exp Dermatol, 17 (1992) 246-249.
[294] M. Wei, D. Feng, Y. Zhang, Y. Zuo, J. Li, L. Wang, P. Hu, Effect and Correlation of Rosa roxburghii Tratt Juice Fermented by Lactobacillus paracasei SR10-1 on Oxidative Stress and Gut Microflora Dysbiosis in Streptozotocin (STZ)-Induced Type 2 Diabetes Mellitus Mice, Foods, 12 (2023).
[295] S. Lee, S. Kim, J. Park, J.Y. Lee, Universal surface modification using dopamine-hyaluronic acid conjugates for anti-biofouling, Int J Biol Macromol, 151 (2020) 1314-1321.
[296] J.L. Durosoir, A. Thabaut, C. Laverdant, [Letter: Use of peroxidase-labelled globulins in parasitological immunology], Nouv Presse Med, 3 (1974) 1507.
[297] Y. Wang, J. Wang, Y. Jiao, K. Chen, T. Chen, X.P. Wu, X. Jiang, W. Bu, C. Liu, X. Qu, Redox-Active Polyphenol Nanoparticles Deprive Endogenous Glutathione of Electrons for ROS Generation and Tumor Chemodynamic Therapy, Acta Biomater, (2023).

[298] Y. Wang, Z. Yang, X. Chen, X. Jiang, G. Fu, Silk fibroin hydrogel membranes prepared by a sequential cross-linking strategy for guided bone regeneration, J Mech Behav Biomed Mater, 147 (2023) 106133.
[299] A.M. Deliormanli, Synthesis and characterization of cerium- and gallium-containing borate bioactive glass scaffolds for bone tissue engineering, J Mater Sci Mater Med, 26 (2015) 67.
[300] A. El-Fiqi, R. Allam, H.W. Kim, Antioxidant cerium ions-containing mesoporous bioactive glass ultrasmall nanoparticles: Structural, physico-chemical, catalase-mimic and biological properties, Colloids Surf B Biointerfaces, 206 (2021) 111932.
[301] J. Yang, L. Xiong, M. Li, J. Xiao, X. Geng, B. Wang, Q. Sun, Preparation and Characterization of Tadpole- and Sphere-Shaped Hemin Nanoparticles for Enhanced Solubility, Nanoscale Res Lett, 14 (2019) 47.
[302] J.H. Ryu, Y. Lee, M.J. Do, S.D. Jo, J.S. Kim, B.S. Kim, G.I. Im, T.G. Park, H. Lee, Chitosan-g-hematin: enzyme-mimicking polymeric catalyst for adhesive hydrogels, Acta Biomater, 10 (2014) 224-233.
[303] Y.Q. Almulaiky, S.A. Al-Harbi, A novel peroxidase from Arabian balsam (Commiphora gileadensis) stems: Its purification, characterization and immobilization on a carboxymethylcellulose/Fe(3)O(4) magnetic hybrid material, Int J Biol Macromol, 133 (2019) 767-774.
[304] Y. Tao, Y. Lin, Z. Huang, J. Ren, X. Qu, Incorporating graphene oxide and gold nanoclusters: a synergistic catalyst with surprisingly high peroxidase-like activity over a broad pH range and its application for cancer cell detection, Adv Mater, 25 (2013) 2594-2599.
[305] X. Ji, Q. Li, R. Su, Y. Wang, W. Qi, Peroxidase-Mimicking Hierarchically Organized Gold Particles for Glucose Detection, Langmuir, 39 (2023) 3216-3224.
[306] Y. Ouyang, M. Fadeev, P. Zhang, R. Carmieli, Y.S. Sohn, O. Karmi, Y. Qin, X. Chen, R. Nechushtai, I. Willner, Aptamer-Functionalized Ce(4+)-Ion-Modified C-Dots: Peroxidase Mimicking Aptananozymes for the Oxidation of Dopamine and Cytotoxic Effects toward Cancer Cells, ACS Appl Mater Interfaces, 14 (2022) 55365-55375.
[307] R.P. Bacil, L. Chen, S.H.P. Serrano, R.G. Compton, Dopamine oxidation at gold electrodes: mechanism and kinetics near neutral pH, Phys Chem Chem Phys, 22 (2020) 607-614.
[308] Y. Zhao, Z. Li, Y. Jiang, H. Liu, Y. Feng, Z. Wang, H. Liu, J. Wang, B. Yang, Q. Lin, Bioinspired mineral hydrogels as nanocomposite scaffolds for the promotion of osteogenic marker expression and the induction of bone regeneration in osteoporosis, Acta Biomaterialia, 113 (2020) 614-626.
[309] L. Pham, L.H. Dang, M.D. Truong, T.H. Nguyen, L. Le, N.D. Nam, L.G. Bach, V.T. Nguyen, N.Q. Tran, A dual synergistic of curcumin and gelatin on thermal-responsive hydrogel based on Chitosan-P123 in wound healing application, Biomedicine & Pharmacotherapy, 117 (2019) 109183.
[310] J. Sun, J. Yang, D. Jeon, D. Park, J.W. Kim, Shear-Responsive Sol–Gel Transition of Phase Change Material Emulsions for an Injectable Thermal Insulation Platform, Small, 2023 (2023) 2304120.
[311] I.M. Diniz, C. Chen, X. Xu, S. Ansari, H.H. Zadeh, M.M. Marques, S. Shi, A. Moshaverinia, Pluronic F-127 hydrogel as a promising scaffold for encapsulation of dental-derived mesenchymal stem cells, Journal of Materials Science: Materials in Medicine, 26 (2015) 1-10.

[312] A. Manzar, X. Ruirui, Z. Ning, Z. Qianli, Y. Xuehai, Antitumor Photodynamic Therapy Based on Dipeptide Fibrous Hydrogels with Incorporation of Photosensitive Drugs, ACS Biomater. Sci. Eng., 4 (2018) 2046-2052.
[313] J. Fischer, A. Kolk, C. Pautke, P.H. Warnke, C. Plank, R. Smeets., Future of local bone regeneration–protein versus gene therapy, Journal of Cranio-Maxillofacial Surgery, 39 (2011) 54-64.
[314] A.A. Kareem, D. Victoria, O. Boris, K. Jackie, S. Morris, A. Nissan, A. Rubinstein, Biocompatibility evaluation of crosslinked chitosan hydrogels after subcutaneous and intraperitoneal implantation in the rat, Journal of Biomedical Materials Research Part A: An Official Journal of The Society for Biomaterials, The Japanese Society for Biomaterials, and The Australian Society for Biomaterials and the Korean Society for Biomaterials, 83 (2007) 414-422.
[315] A.u. Rahman, S. Rashid, R. Noon, Z.S. Samuel, B. Lu, W.S. Borgnakke, R.C. Williams, Prospective evaluation of the systemic inflammatory marker C-reactive protein in patients with end-stage periodontitis getting teeth replaced with dental implants: a pilot investigation, Clinical Oral Implants Research, 16 (2005) 128-131.
[316] S. Gor, S.-H. Kim, K. Yein, J. Michael, E. Price, C-Reactive protein rise in rheumatology patients following COVID-19 vaccination Rheumatology Advances in Practice, 7 (2023) i2-i5.
[317] N. Heim, V. Wiedemeyer, R.H. Reich, M. Martini, The role of C-reactive protein and white blood cell count in the prediction of length of stay in hospital and severity of odontogenic abscess, Journal of Cranio-Maxillofacial Surgery, 46 (2018) 2220-2226.

APPENDIX

A1: Rheology of Pluronic F127 at 20wt%

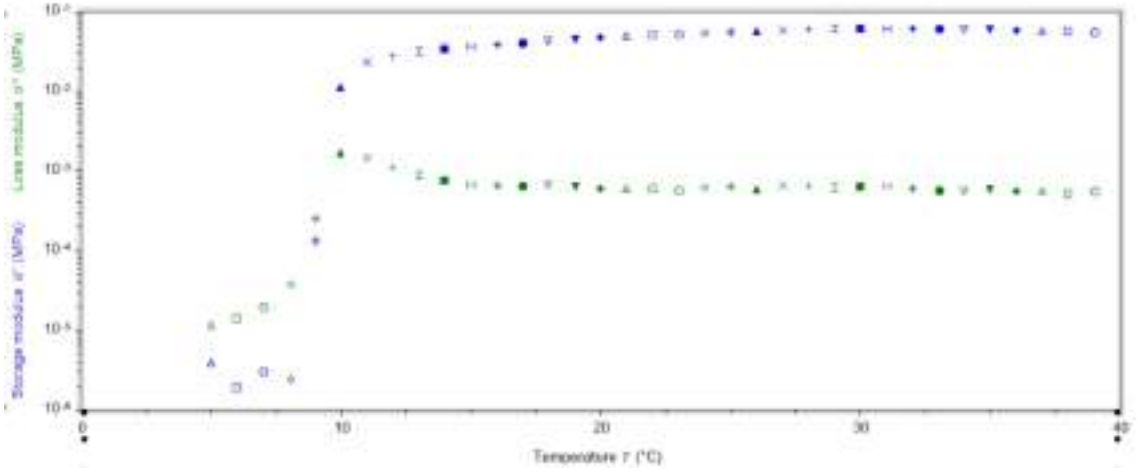

Figure A1: Temperature sweep function of pure Pluronic F127 at 20 wt%.

A2: Live/dead assay for screening single loading agents.

Experimental procedure:

Human fibroblast cells, BJ cells (ATCC® CRL-2522™) were used for cytotoxicity evaluation following the previous study (Dang et. al., 2021) In this study, all hydrogels were plated onto a 35 mm culture dish separately. These ACP dishes were incubated at 4 °C for 4 h before incubating at 37 °C overnight. Ultraviolet (UV)-light was involved to sterilize. 2×10^5 BJ cells/ml suspended in complete DMEM (10% FBS and 0.1% penicillin-streptomycin) were seeded on these dishes. The live/dead assay was performed based on the dual staining acridine orange (AO)/propidium iodide (PI) method. The morphology of BJ cells was observed under a confocal microscope (Andor) with dual laser channels.

Result:

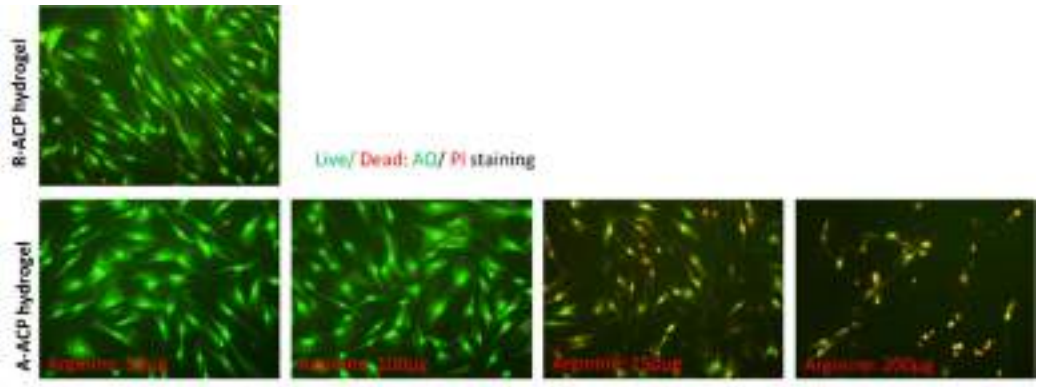

Figure A1: The live/dead image via dual AO/PI staining technique for human dermal fibroblast (BJ cell) at 24 h cultured on different single loading ACP hydrogel system.

A3. HPLC chromatogram for the released data

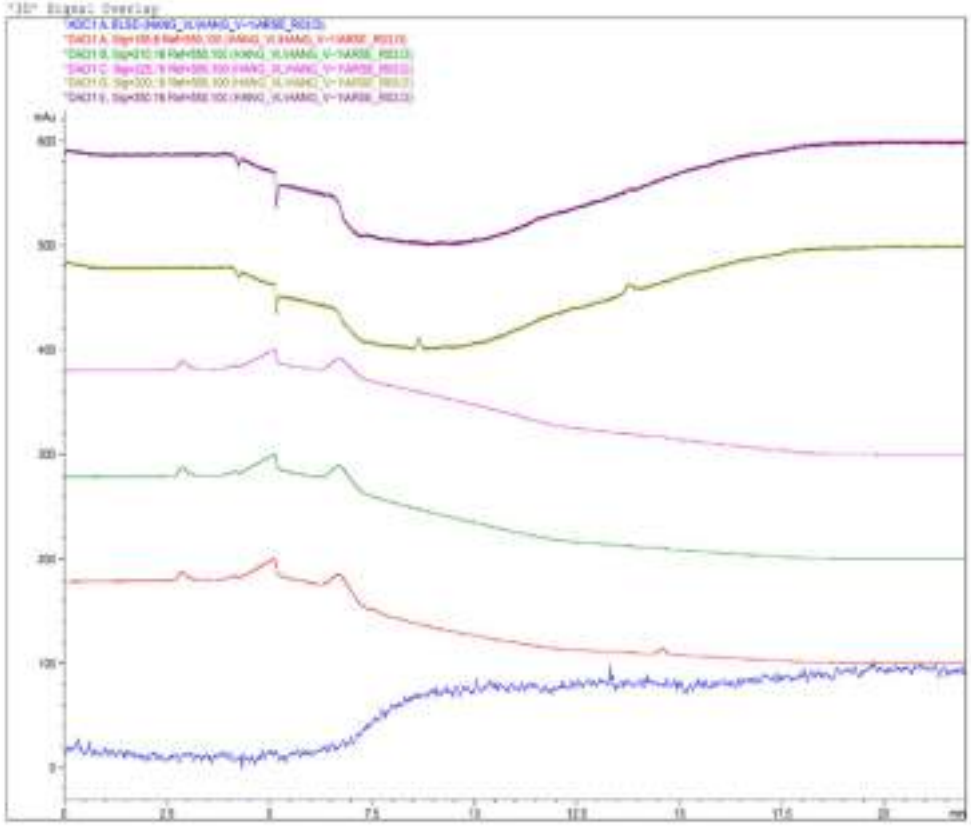

Figure A3A: HPLC chromatogram of blank ACP hydrogel

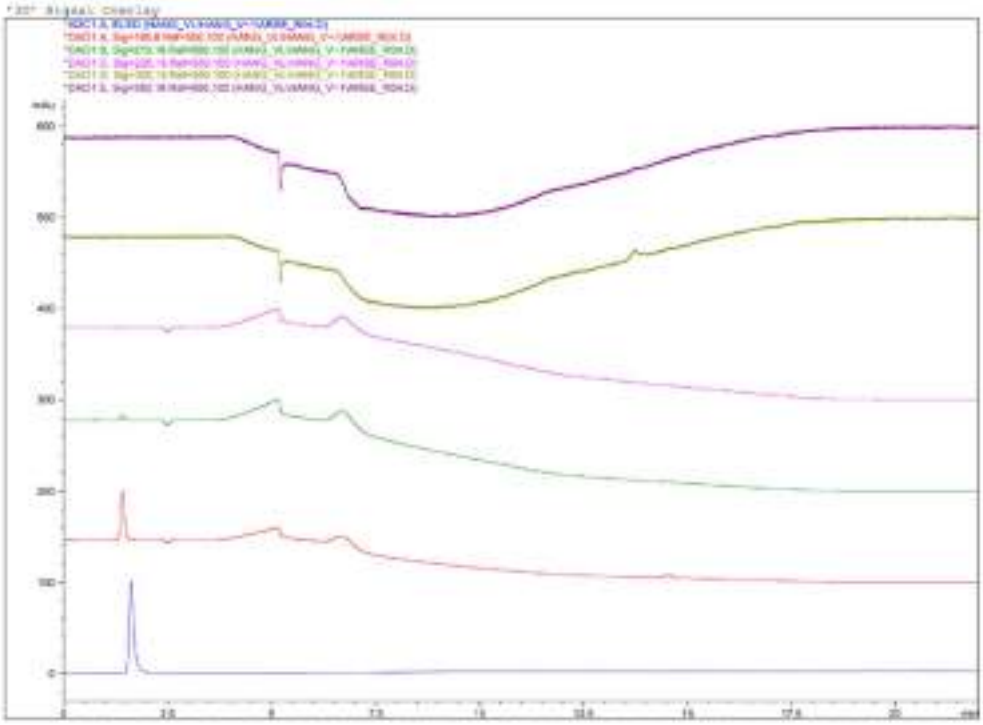

Figure A3B: HPLC chromatogram of L-arginine in ACP hydrogel

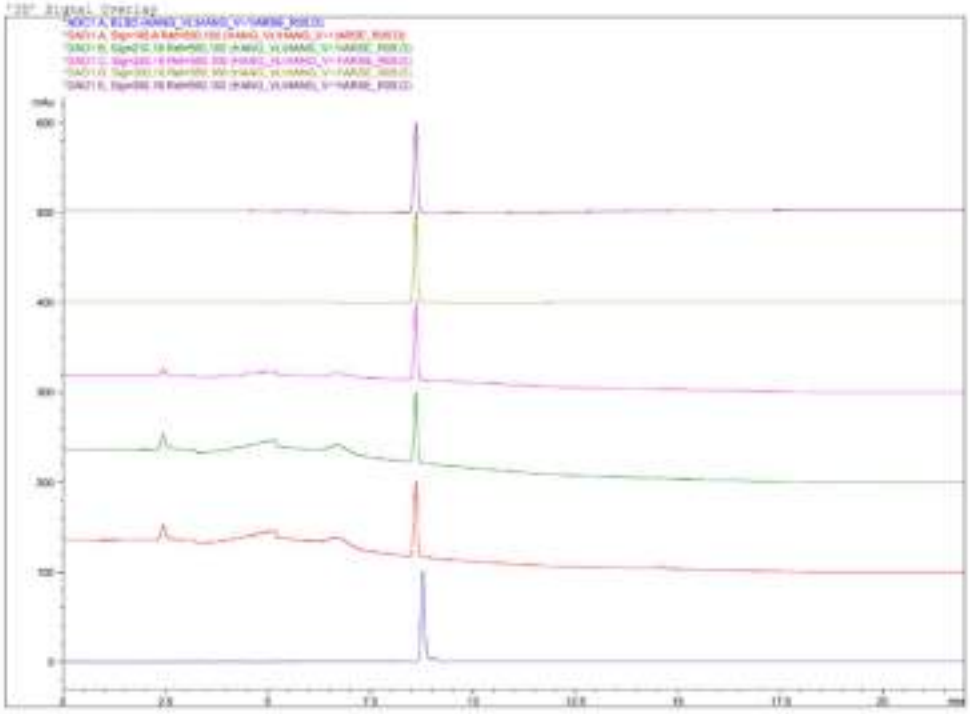

Figure A3C: HPLC chromatogram of Resveratrol in ACP hydrogel

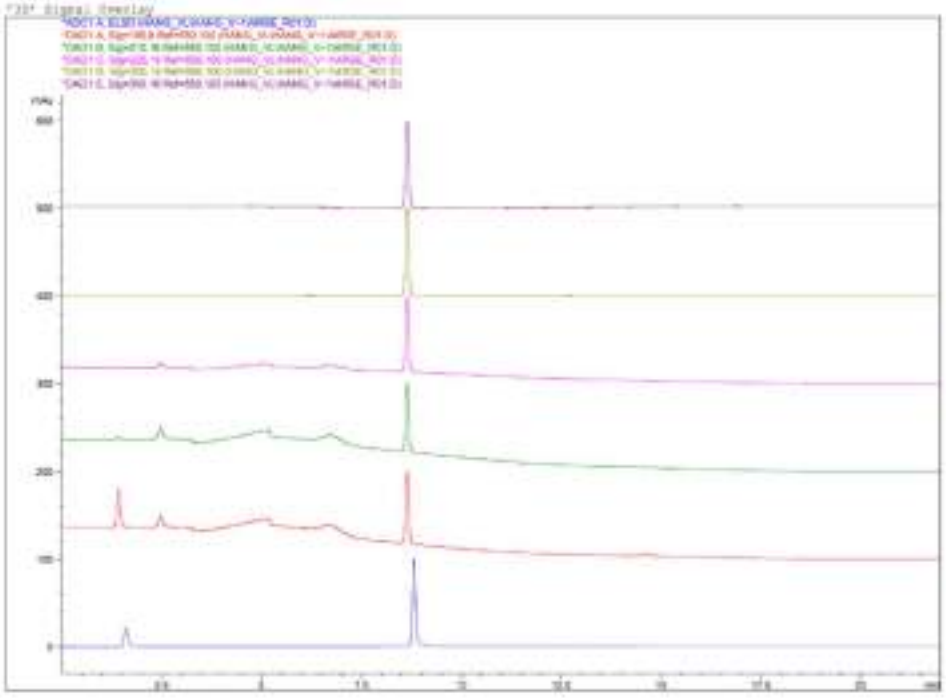

Figure A3D: HPLC chromatogram of Resveratrol in combination with L-arginine in ACP hydrogel.

A4. The cytotoxicity of the extracted hydrogel on fibroblast.

Experimental procedure:

All type hydrogels were weighted to make the determined concentration. After allowing gelation, the gel was minced with culture media. The cell strainer (40 µm) was used to collect the extracted liquid. Fibroblast (BJ cells) was seeded on 96 well plate with density of $2x10^3$ cells/well. After 5h maintain in CO_2 incubator, the older media was withdrawn and then replaced by the media containing extracted liquid. At the determine time, MTT assay (ab211091) was applied to calculated the viability. The procedure was followed the guidance of manufactory. In addition, live/dead assay was applied with dual AO/PI staining to observe the change in morphology of fibroblast cells.

Result:

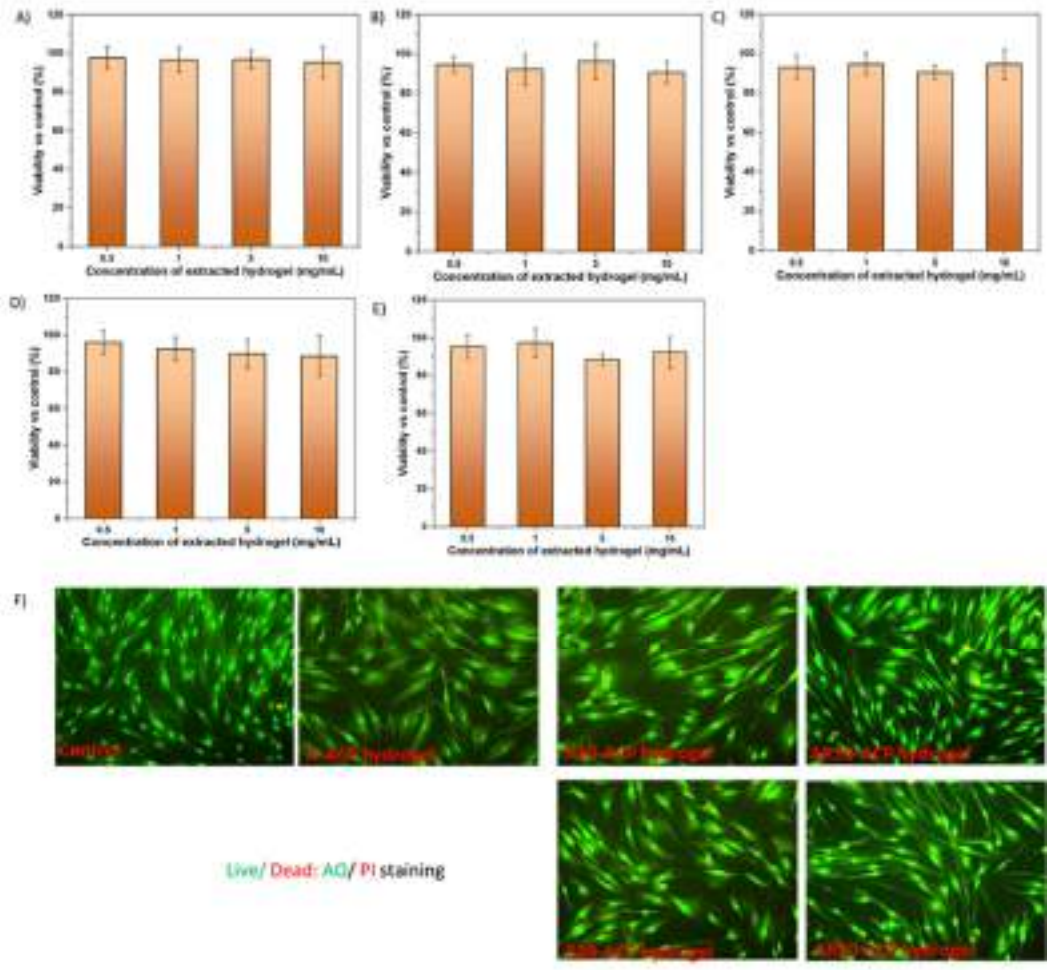

Figure A4: The viability of fibroblast cells (BJ cells) in respective to control was determined by MTT assay after 48h treatment with the indicated concentration of extracted

hydrogel samples: A) R10-ACP hydrogel; B) R-20 ACP hydrogel; C) A-ACP hydrogel; D) AR10-ACP hydrogel and E) AR20- ACP hydrogel. Results are expressed as the mean ± SEM of 3 independent experiments. The live/dead assay via dual staining AO/PI was performed with the BJ cell culturing with 10 mg/mL extracted hydrogel.

A5. The HE staining image at 10th day and 18th day

Dark line: epidermis layer

Red line: muscle layer

Green arrow: sebaceous gland

Yellow arrow: blood vessle

Blue arrow: the inflitration of immune cells

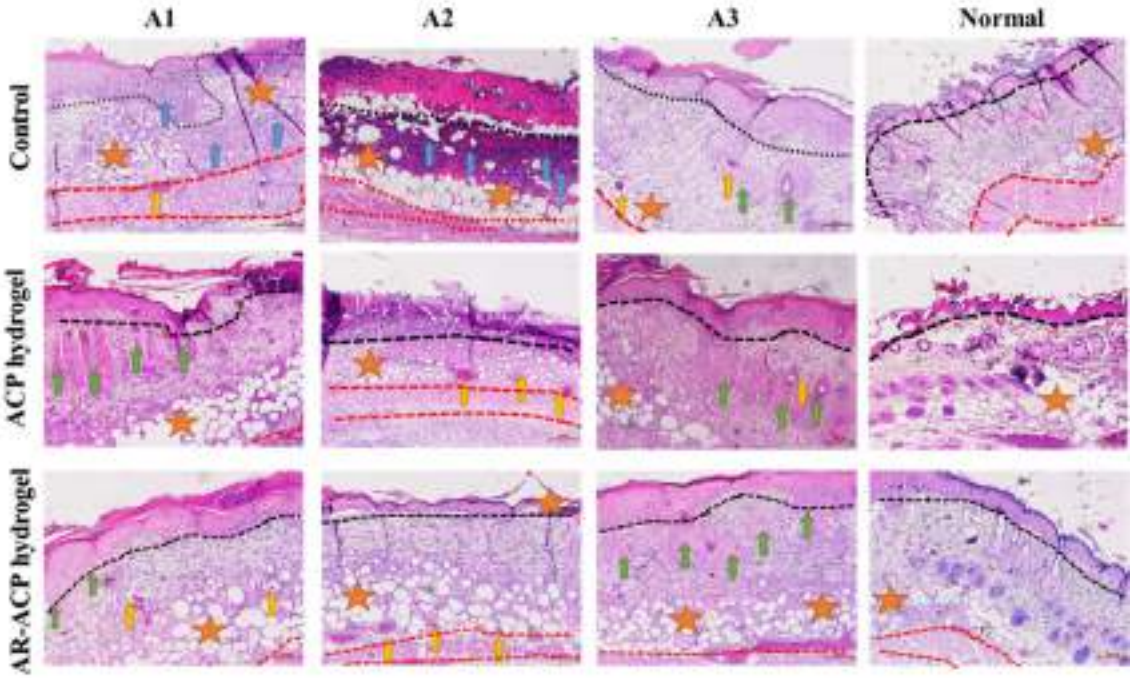

Figure A5A: H&E staining images of diabetic wound tissues at 10th day after different treatments, respectively. Wound edge (A1 and A3) as well as the center (A2) of wound bed.

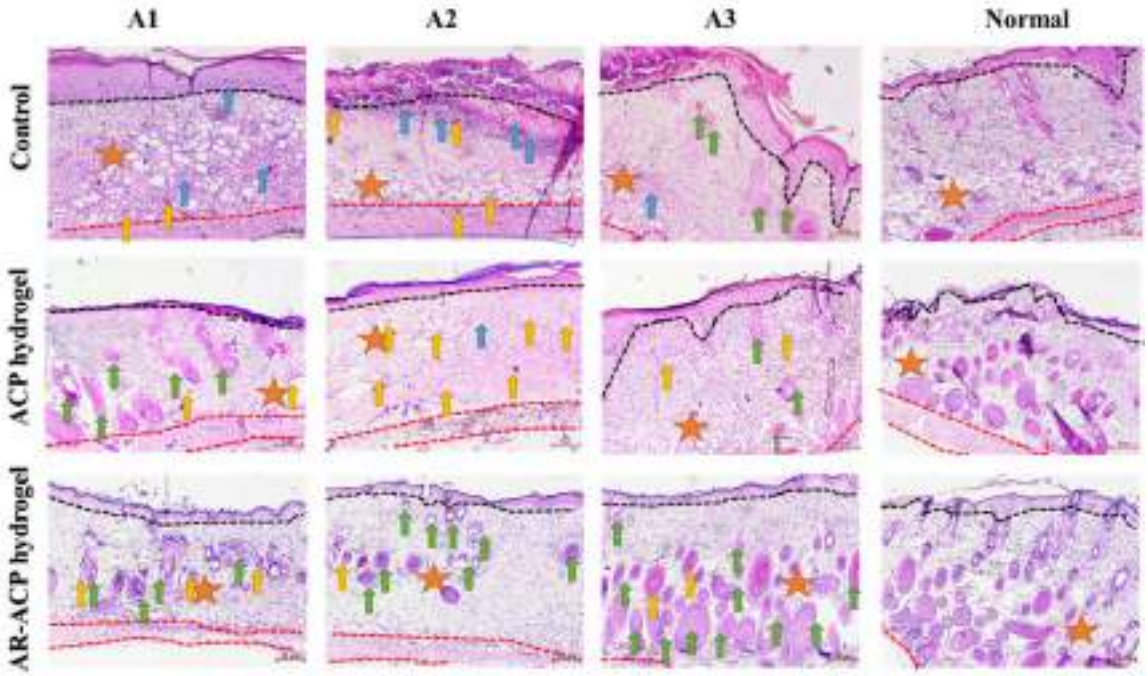

Figure A5B: H&E staining images of diabetic wound tissues at 18th day after different treatments, respectively. Wound edge (A1 and A3) as well as the center (A2) of wound bed

A6: The MT Staining image at 10th day and 18th day

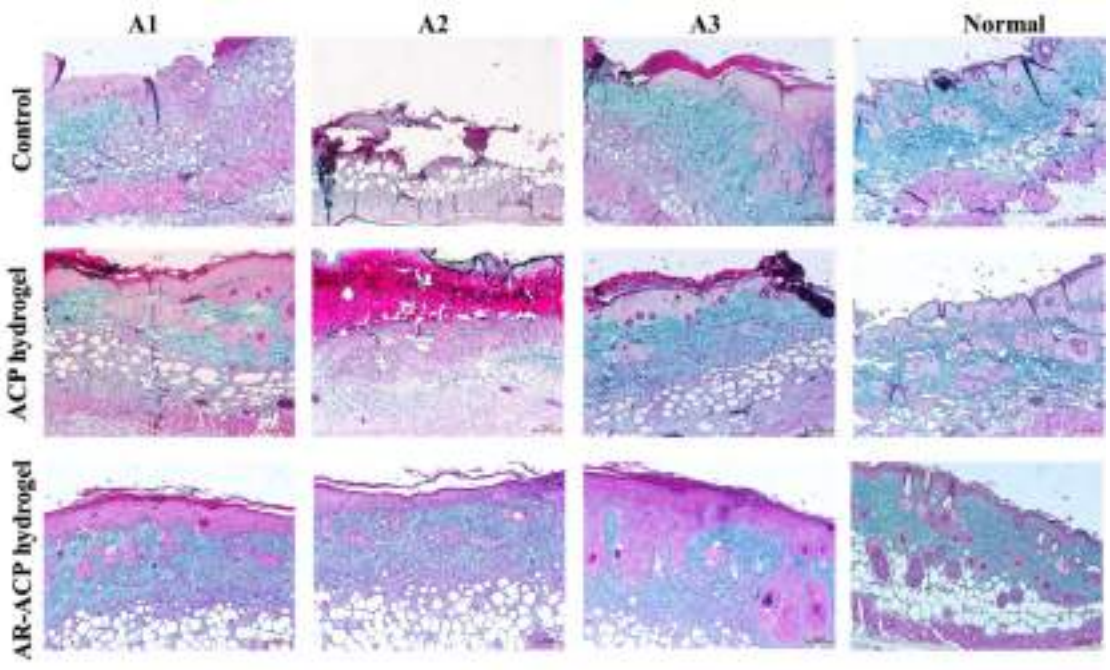

Figure A6A: Representative trichrome images of wounds at 10th day post treatment. Wound edge (A1 and A3) as well as the center (A2) of wound bed.

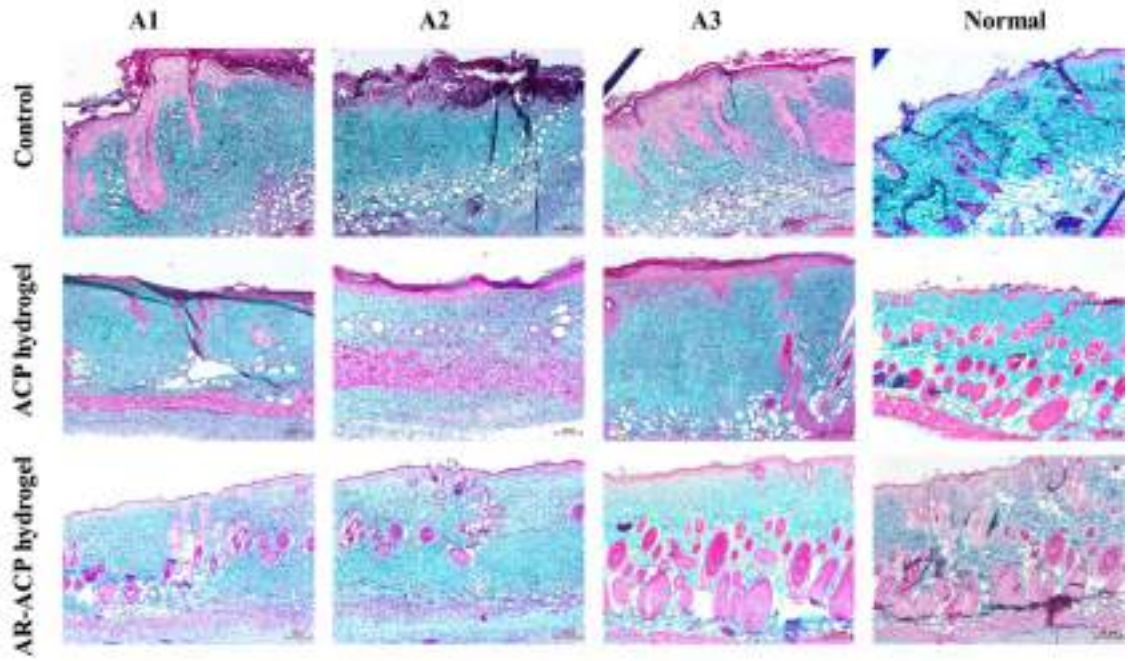

Figure A6B: Representative trichrome images of wounds at 10th day post treatment. Wound edge (A1 and A3) as well as the center (A2) of wound bed.

Table A1: The kinetic release model of L-arginine and Resveratrol from difference type of ACP hydrogel.

Resveratrol			Arginine		Biological cues	Release Data Info
AR20-ACP	AR10-ACP	R20- ACP	R10- ACP	AR20-ACP	AR10-ACP	A-ACP	Sample	
0,95	0,99	0,96	0,95	0,45	0,57	0,37	R^2	Zero Order
0,73	0,72	0,59	0,62	0,28	0,31	0,23	R^2	First Order
0,99	0,99	0,94	0,96	0,74	0,76	0,67	R^2	KP*
8,907	7,200	13,03	11,66	n/a	n/a	n/a	K	
0,54	0,62	0,68	0,67	0,66	0,58	0,49	n	
0,99	0,93	0,88	0,90	0,49	0,62	n/a	R^2	Higuchi
0,82	0,82	0,7617	0,76	0,33	0,39	0,27	R^2	Hixson-Crowell
0,79	0,79	0,94	0,92	0,98	0,99	0,98	R^2	Modifed KP*
0,53	0,61	0,48	0,47	0,24	0,26	0,23	n	
0,003	0,002	0,14	0,13	0,15	0,15	0,15	t_{lag}	
8,94	7,22	18,09	15,19	24,307	24,67	32,57	K	

*KP: Korsmeyer-Peppas; n/a: non observation.

Appendix M1: Procedure for processing images with ImageJ for histology staining analysis. A) Scale setting, B) Color setting, C) Color deconvolution